Department of Civil and Environmental Engineering

PhD Civil Engineering

May 2024

Synergistic Effect of Hydration and Carbonation on the Development of MgO-Based Cementitious Materials

Shuang Liang

1900559

A thesis submitted to the Brunel University London in partial fulfilment of the requirements for the degree of Doctor of Philosophy

Brunel University London
Uxbridge
Middlesex
UB8 3PH
United Kingdom

Abstract

Portland cement (PC) production is accountable for 5-8% of anthropogenic carbon dioxide (CO_2) emissions. The concrete and construction industries have been under increasing pressure to develop alternative materials and technologies that produce fewer CO_2 emissions and potentially absorb CO_2, resulting in an increased interest in sustainable practices. Compared to cement clinker, reactive MgO (RM) from calcining $MgCO_3$ has a lower calcination temperature (700–900 °C vs. 1450 °C needed for calcining $CaCO_3$). It can gain strength by permanently sequestering CO_2, and it can be largely recycled after completing its lifecycle. This thesis investigates four major aspects related to using reactive magnesia in the construction industry: (1) Enhancement of carbon sequestration and mechanical properties of reactive magnesia-based cements under 15% of CO_2 and ambient curing; (2) The effectiveness of amino acids on controlling performance of magnesium-based carbonate; (3) The feasibility of using magnesium-based carbonate in Portland metakaolin cement blends; and (4) The role of magnesia in alumina/silicate hydrate binder systems.

The first and second investigations (i.e. Chapter 4) involved the evaluation of the influence of amino acids (i.e. L-arginine (L-Arg) and L-aspartic (L-Asp)) on the performance of reactive magnesia-based mixes. The results of this research were presented in terms of hardened properties such as bulk density and compressive strength. The mechanisms of hydration and carbonation and microstructural characterization of the mixes were also studied. The results revealed that the use of amino acids as additives resulted in the formation of unstable nesquehonite ($MgCO_3·3H_2O$) and maintained its polymorph during the carbonation of MgO. Additionally, the carbonated composites produced with amino acids had a higher carbonation degree and higher stability, compared to the base batch without amino acids. The presence of amino acid resulted in the formation of denser carbonation products with a different morphology than those in the control mix, leading to significantly enhanced

carbonation and compressive strength.

Chapter 5 (third aspect) investigated the influence of carbonates (limestone, magnesite, various hydrated magnesium carbonates (HMCs), and lab-produced HMCs) and non-carbonate (quartz) on the performance of Portland metakaolin cement binder. The mixtures exhibited a distinct difference in strength at early ages (i.e. from 3 to 7 days), while at the late ages (after 28 days) compressive strengths were comparable call the binders. Also, the microstructure of the mixtures was densified by the lab-produced HMCs. The synergistic reaction between metakaolin and high-reactivity carbonate produced carboaluminates, which may explain the observed increase in strength. Moreover, the observed increase in strength cannot solely be attributed to the carboaluminates; other hydration products may also play a role. strätlingite and C-A-S-H gel) also play an important role.

Based on the findings from the last two chapters, which approved the feasibility of magnesia-based materials in the alumina/silicate hydrate binders, Chapter 6 investigated the practical applications for magnesia in alumina/silicate hydrate binder systems. The study introduced reactive magnesia (i.e. MgO) and sodium carbonate, together with an early-age oven curing regime, as an approach to clay solidification. The results indicated that incorporating MgO effectively solidified the clay by providing additional Mg^{2+} and OH^- ions. The morphology of hydration phases plays a more important role than their contents and porosity in strength development.Another investigation conducted in this thesis is to replace microsilica with waste glass for preparing $MgO-SiO_2$ formulations to form magnesium silicate hydrate (M-S-H). The results suggested that waste glass can partially replace microsilica (i.e. up to 50 wt.% replacement level) in $MgO-SiO_2$ formulations without sacrificing the compressive strength, whereas the complete replacement with waste glass did not reveal favourable outcomes in terms of performance. The reactivity and solubility of the silica source played a key role in the formation of M-S-H, which contributed to the strength development in samples containing microsilica.

This study is original as it was the first in the literature to introduce amino acids into reactive magnesia mixes to control the polymorphs of HMCs in carbonated magnesia composites to develop low carbon MgO-clay binder systems via the use of the polymorphs controlled HMCs. The findings have suggested the high potential of reactive magnesia-based formulations to be used in various building applications based on their ability to gain strength via the sequestration of CO_2 and their lower sensitivity to impurities, enabling the utilization of large quantities of industrial waste.

Authorship Attribution Statement

This thesis contains material from 3 papers published in the following peer-reviewed journals/conference where I was the first and/or second author.

Section 4.1 is published as **Liang, S**., Zhou, X., & Hou, P. (2023). Impact of amino acids as performance-controlling additives on the hydration of reactive MgO. In Journal of Physics: Conference Series (Vol. 2423, No. 1, p. 012029). IOP Publishing.

Chapter 6 is published as [1] **Liang, S**., Zhou, X., Ruan, S., Kastiukas, G., & Sun, Y. (2023). Milled Waste Glass Powder in Magnesium-Silicate-Hydrate Cement: Technical and Environmental Assessment. Journal of Materials in Civil Engineering, 35(1), 04022379. [2] Ruan, S., **Liang, S**., Kastiukas, G., Zhu, W., & Zhou, X. (2020). Solidification of waste excavation clay using reactive magnesia, quicklime, sodium carbonate and early-age oven curing. Construction and Building Materials, 258, 120333.

Working papers:
1. **Liang, S**., Zhou, X., Hou, P. Synergetic regulation of hydration and carbonation of reactive MgO cement by amino acids. Ready to submit.

2. **Liang, S.**, Zhou, X., Hou, P., Sun, Y., Niu, Z., & Liu, M. Understanding the role of Hydrated magnesium carbonates in cementitious systems with reactive aluminosilicates. In preparation.

Acknowledgements

First and foremost, I would like to take this opportunity to express my deepest sense of gratitude to my principal supervisor, Professor Xiangming Zhou, for giving me the opportunity to study at Brunel University London, and also for his patience, motivation, enthusiasm, and immense knowledge. His excellent guidance helped me in the investigation and writing of this thesis. I am also grateful for his encouragement to present my work at international scientific conferences, allowing me to broaden my horizons.

I would like to thank Zhongyuan University of Technology (ZUT) for providing a Ph.D. scholarship to me to conduct this study at Brunel University London. Also from ZUT, thanks go to Professor Yuzhou Sun, who was very supportive of my work. Special thanks go to Professor Pengkun Hou, Dr Tao Zhao, Dr Shaoqin Ruan and Dr Gediminas Kastiukas, who shared experience and knowledge with me.

I greatly appreciate the support from the staff at Brunel University London the staff at the Joseph Lowe, the Experimental Techniques Centre (ETC) and the Wolfson Centre for sharing their discussions, experiences, and knowledge during the time of my study. Thanks to Mr Neil Macfadyen, Mr Charles Morrison, Mr Richard Parish, Mr Abdul Ghani, Dr Uchechukwu Onwukwe, Dr Nicholas Nelson, Dr Ashley Howkins, Dr Sophia Haghani, and Dr Lorna Anguilano for their expertise and assistance to support the research work.

Thanks to Mr Zhonghao Niu, Mr Ziyan Fu, Dr Enshen Lu, Mr Yichen Zhang, and Mr Mingqing Liu for their friendship and help.

Finally, my most sincere gratitude goes to my father Mr Hongzhi Liang and my mother Ms Jiaxiang Wang. Without your unconditional and endless love and support, it would be not possible for me to overcome the difficulties and complete the study. Thank you are always with me and support me all the time.

Contents

List of Figures

List of Tables

1. Chapter 1 Introduction

1.1. Research Background

The construction industry is one of the fastest growing industries, and its importance has made the net-zero carbon emission of buildings in service more and more popular in recent decades. From 1950 to 2017, global cement consumption has increased tenfold, making it the world's most widely used building material [1]. According to predictions, the world's cement demand represents a 4.7% annual growth rate [2]. For instance, there was a 0.2 billion tonnes increase observed from 2020 to 2021, as shown in **Fig. 1.1.** The booming demand for cement in recent years has led the sector to become one of the largest energy consumers and the most significant greenhouse gas (GHG) emitter. For example, cement production accounted for 22% (i.e. 2.2 Gt) of global greenhouse gas emissions in 2014 [3]. The cement industry, which is associated with around 5-8% of the total global anthropogenic CO_2 emission, is one of the highest carbon-intensive industries in the world [4]. Approximately 1 tonne CO_2 is released by the production of 1 tonne of cement. It is estimated that the increase in emissions would result in an additional 85–105 Gt of CO_2eq, based on current emission factors [1]. As a result, the EU is targeting to reduce greenhouse gas emissions by at least 80% by 2050 compared with that of 1990 [5].

Cement plants emit approximately 60 wt.% of their CO_2 emissions because of calcining limestone (i.e. the decomposition of $CaCO_3$ into CaO while releasing CO_2), while the rest is associated by the energy consumed in this process [6]. CO_2 emissions are strongly influenced by the manufacturing method and the type of fuel used in the production of cement [7]. In addition to CO_2, the production of cement releases sulphur oxides (SOx), cement kiln dust (CKD), and nitrogen oxides (NOx) into the environment, which are considered harmful substances [8,9]. In Europe, 0.6 kg of SO_2, 2.4 kg of NO_x and 2.7 Kg of CKD are emitted from the production of 1 tonne of Type I Portland cement

(PC) [7]. Besides the environmental impact of cement, the quantity and range of hazardous solid waste generated by the cement industry and its impact on human health are also beginning to be of concern to many people. Among them, the environmental impact of waste disposal is particularly valued, which has led to a search for a new and more sustainable route. It has been enforced to make some changes concerning sustainability.
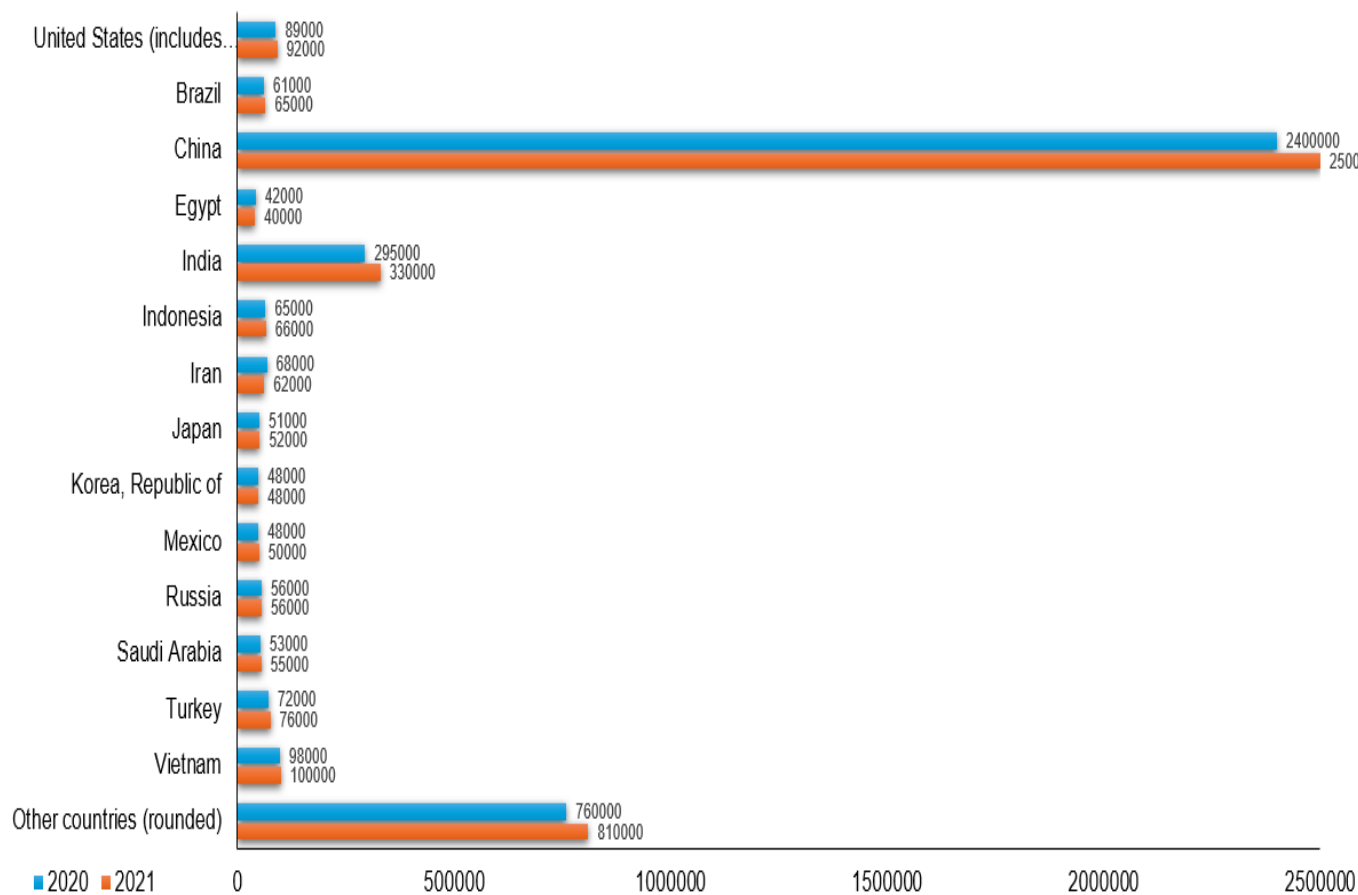
Fig. 1.1 The worldwide cement production (Thousand metric tons) [8]

The cement energy technology roadmap published by the International Energy Agency (IEA) estimates that the cement industry could reduce its direct emissions by 18% from current levels by 2050 [3]. Some of the solutions, such as adopting new curing technologies new additives and using new

14

binder systems to improve the carbon-capture ability of cementitious products, have been adopted to reduce the environmental impact of concrete [9]. For instance, a strategy being employed is the development of alternative binders to reduce the temperature of calcination, as around 60% of the CO_2 emitted by cement plants is derived from the calcination of limestone. Alternatively, the adoption of carbon capture and storage technologies in cement manufacture is becoming an increasingly attractive research area for reducing CO_2 emissions.

In recent decades, the reactive magnesium oxide (MgO) used as a construction material has been regarded as a promising technique to further reduce the composite's overall environmental impact and improve its performance from certain perspectives. The reactive magnesia can participate in the strength development and hydration reactions of cement to improve the carbon-capture ability [10]. The light-burned MgO with relatively lower calcination temperatures of 700-1000 ^{o}C shows high reactivity. Because the production of MgO-based cement requires lower temperatures than that of Portland cement (1450 ^{o}C). The production of MgO-based cement therefore saves energy, envisioning it as an important role in the future of environmentally conscious cement production. Moreover, the ability of MgO to absorb CO_2 to form a wide variety of hydrated magnesium carbonates (HMCs) should be highlighted, which could potentially result in the absorption of as much CO_2 during their service life as being emitted during their production. Additionally, RMC-based binders can gain strength by absorbing CO_2, as HMCs are considered to contribute more to strength gain than brucite, which is the main hydration product in magnesium-based binder systems [11].

1.2. Objectives and Structure of This Thesis

This thesis innovatively proposed a method to improve the carbonation of MgO and subsequently enhance its mechanical properties by using amino acids. The reason for applying amino acids is that they have been widely used to control the structure and properties of the $CaCO_3$ minerals, specifically, to

stabilize typical metastable amorphous calcium carbonate (ACC), aragonite, and vaterite polymorphs. Considering that $MgCO_3$ is also a type of alkaline-earth carbonate, this study hypothesizes that amino acids can enhance the performance of these composites by altering the polymorphs of HMCs. Furthermore, this study also investigated the effectiveness of controlling polymorphs of the carbonation products. After that, the feasibility of amino acid-modified carbonated magnesia in the alumina-silicate binder system (i.e. Portland metakaolin cement) was assessed. Moreover, alumina and /or silicate-based solid construction waste such as waste excavation clay and waste glass were processed or reused by magnesia. This study is novel since, to the best of the author's knowledge, there are no studies that have been conducted to investigate the effects of amino acids on controlling the performance of magnesia mixes. The objectives and structure of the thesis are outlined below.

1. To examine the effects of additives (i.e. amino acids) on the hydration and carbonation of magnesia in terms of bulk density, strength development, and carbon sequestration. The effectiveness of amino acids on the HMCs' polymorphs controlling will be assessed through a series of characterization and microstructure analysis. The amount of CO_2 captured by MgO-amino acids mixtures will be calculated according to thermogravimetric results. Besides, the mechanism of amino acids to enhance carbonation of magnesia will also be investigated. (Chapter 4)

2. To investigate the impact of the presence of different carbonates (i.e. calcium-based carbonate and magnesium-based carbonates) or non-carbonate (quartz) powders alongside PC and metakaolin (i.e. Portland metakaolin cement) on the mechanical performance, water absorption, density, microstructure, and carbonation depth. Additionally, the performance-controlled HMCs obtained from the previous study will be used as the carbonate source to replace the limestone in Portland metakaolin cement and be subsequently assessed in terms of compressive strength and microstructure. The hydration mechanism and

the reaction between magnesium ions and alumina-silicate binder will be systematically studied. (Chapter 5)

3. To explore the feasibility of using magnesia in alumina and /or silicate-based materials. Two scenarios will be studied in this thesis. The one is to introduce reactive magnesia and sodium carbonate, together with an early-age oven curing regime as a means of re-using kaolin excavation waste to produce more sustainable cementitious materials. The other is to investigate the influence of waste glass as a silica source alone and the feasibility of replacing silica source in MgO-SiO_2 binders to provide a comparison with corresponding samples containing microsilica. (Chapter 6)

2. Chapter 2 Literature Review

2.1. Sustainability of Cement

Portland cement (PC) is the most abundantly produced and commonly used material in the construction sector owing to its outstanding engineering performance and durability. For instance, in 2018, over 4.1 billion tonnes of cement were produced worldwide [12]. Developing countries such as China, India, and some regions such as Northern Africa and the Middle East contributed the major growth in the production of cement [13], which can be seen from **Fig. 2.1**. The cement industry contributes approximately 8% of the global anthropogenic greenhouse gas emissions, which is the second biggest CO_2 emissions source after the energy industry [14]. The environmental impact of the cement industry is presented in **Fig. 2.2**, which demonstrated that CO_2 was generated from raw material extraction through material processing, manufacturing, distribution, usage, repair and maintenance, and disposal or recycling.
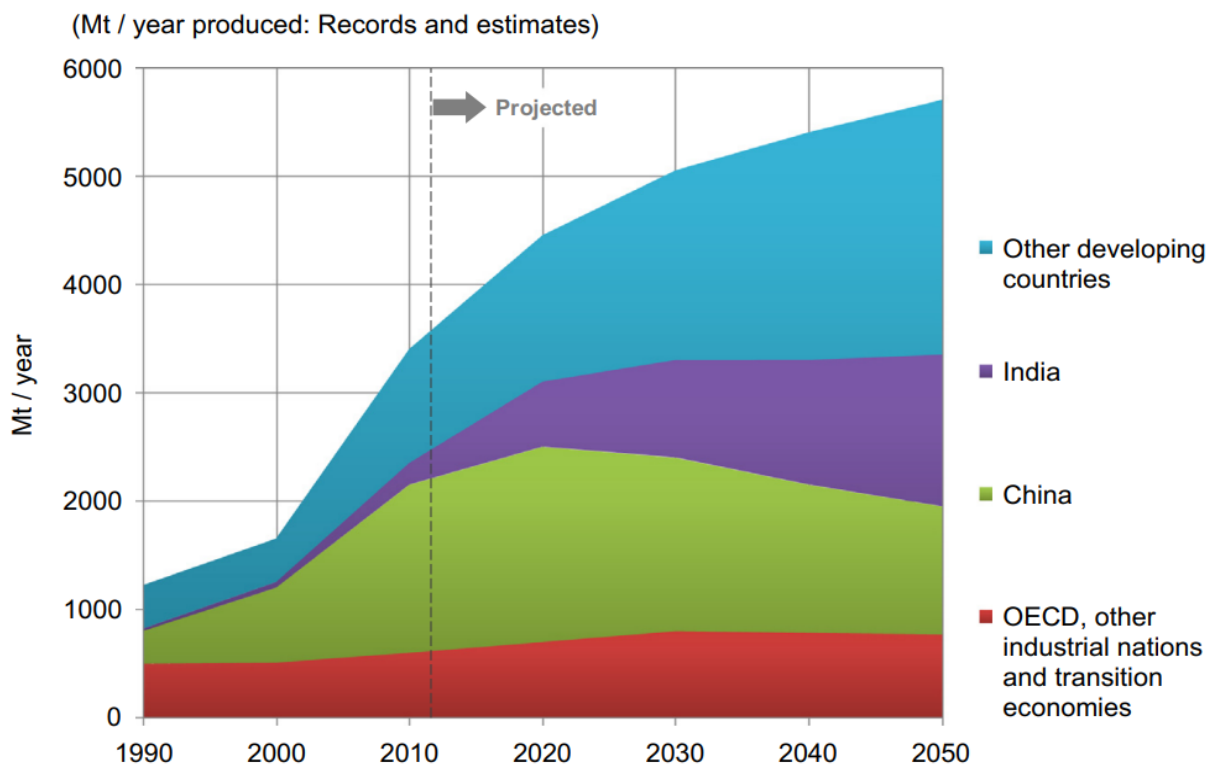
Fig. 2.1 Current and estimated global cement production [15]
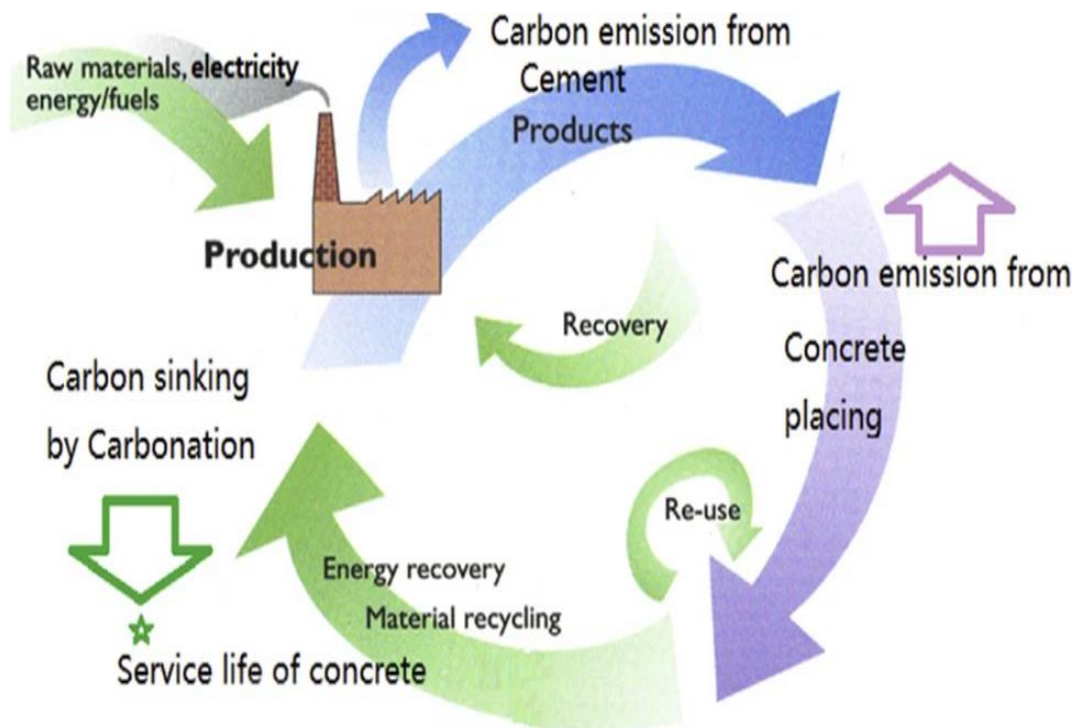
Fig. 2.2 Environmental impact of cement production and utilisation [16]

Fig. 2.3 illustrates the estimated CO_2 emissions up to 2050, which reveals the emissions of various stages in the cement industry contributes to the majority of CO_2 footprint, and as a result, CO_2 emissions in 2050 will be five times greater than that in 1990 if no improvements are made in the cement industry. The production of PC results in 10–11 EJ of energy annually, which contributes to 2–3% of global primary energy use [17]. Accordingly, the development of new types of binders and materials with lower carbon footprints, which are available in adequate amounts, has gained a burgeoning interest. Apart from key materials such as CaO, Al_2O_3 and SiO_2, MgO also seems to be widely available across the globe for producing low-carbon cements.
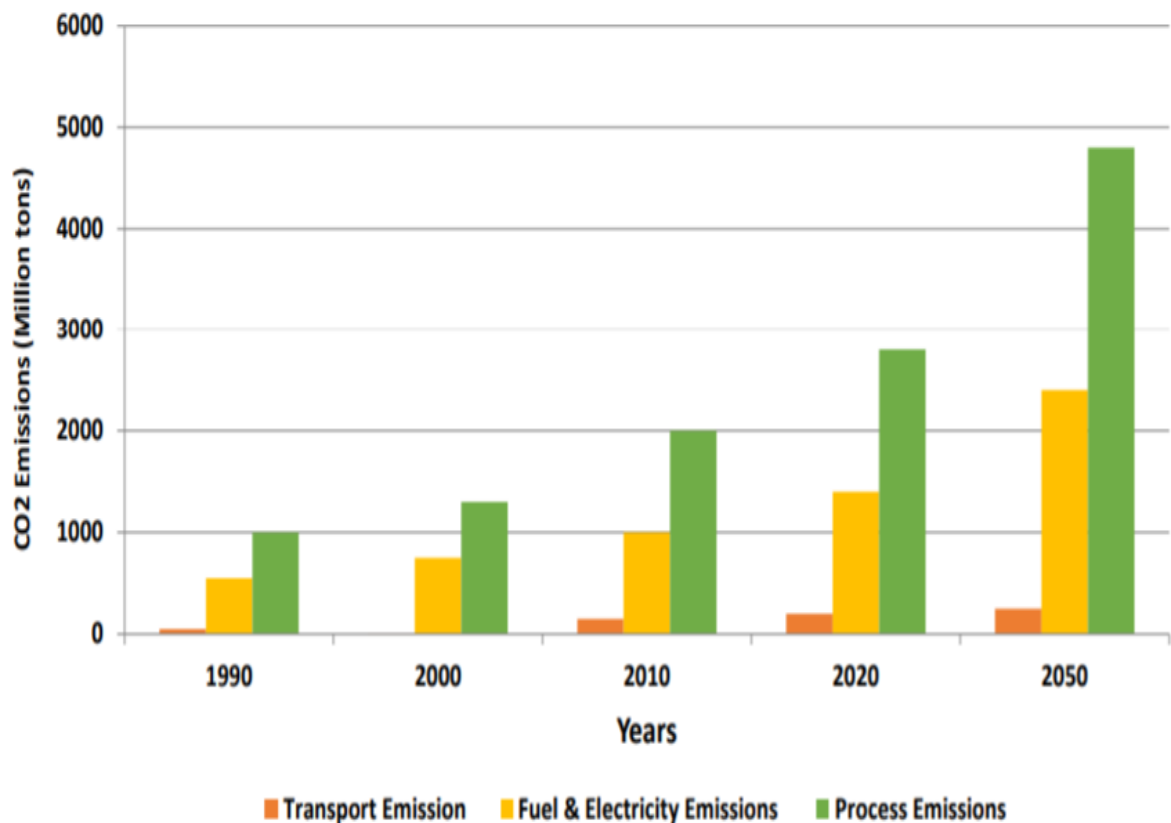
Fig. 2.3 Global CO_2 emissions in cement production [17]

Magnesium oxide is produced via calcining magnesite ($MgCO_3$) at approximately 700°C. The final reactive magnesium oxide (MgO) cement (RMC) can gain mechanical strength by sequestering CO_2 during setting and modifying the cement hydration chemistry [13]. Because of MgO's high resistance to aggressive environments (e.g. sulfate attack, chloride penetration and carbonation), the durability is improved, and it is also possible to reuse waste and industrial by-products in synthesizing RMC binders, because of its low sensitivity to impurities [18]. Moreover, when RMC is used as the only binder, it has the potential to be fully recycled [19].

2.2. Introduction of Magnesia in Concrete

Since the production of Portland cement causes 5-10% of the global anthropogenic CO_2 emissions and ~2–3% of global primary energy use [17], researchers introduced the reactive magnesium oxide cement as a new

cement formulation with potentially lower carbon footprints to face this problem.

Magnesia is an important mineral and 70% of the world's magnesia is produced from magnesium-rich minerals such as magnesite ($MgCO_3$) and dolomite ($Ca(MgCO_3)_2$). Apart from these minerals, salt deposits, bitterns and brines from seawater are also the sources of magnesia.

Magnesite, which contains 47.7 wt.% MgO, is a main source of magnesia. It normally exists in two physical forms - crystalline (i.e. a crystallite size in the range of 50-200 μm) and cryptocrystalline (a crystallite size $\leqslant$ 20 μm). Most crystalline magnesites, which are associated with dolomite, contain a small amount of ferrous iron. Most cryptocrystalline magnesites coexist with serpentinites. In seawater, magnesium content is approximately 1.3 grams per litre. Salt beds are an important source of magnesia-rich brines. Compared to the calcination of $MgCO_3$ and dolomite, the synthetic process of producing MgO from seawater or magnesia-rich brines is more expensive and requires higher energy consumption, however, it potentially emits less CO_2.

Besides being the more sustainable production process of MgO, the use of RMC as a binder has several advantages. First of all, it can carbonate and form a range of hydrated magnesium carbonates (HMCs), subsequently gaining strength during the carbonation [20]. The higher resistance of the hydration and carbonation products of RMC in aggressive environments can provide a great durability. Gonçalves observed that the shrinkage strain of cementitious materials decreases significantly with increasing MgO content in cement because of the expansion of the hydration product (i.e. brucite ($Mg(OH)_2$)) [10]. It severely depends on the reactivity of MgO and the content of hydrated phases in the binders. Meanwhile, the improvement of favourable fire resistance was due to the low thermal conductivity of MgO [21]. Since RMC is less sensitive to impurities, it can be used to process large amounts of waste and industrial by-products [18]. Moreover, when used as the sole binder, RMC decomposes into MgO upon heating, allowing for the complete recycling

of RMC at the end of its service life [19]. It is worth noting that the magnesium-based carbonate, including different types of HMCs and magnesites, can decompose back into MgO via calcination under elevated temperatures, as shown in the recycling within RMC-based systems (**Fig. 2.4**).
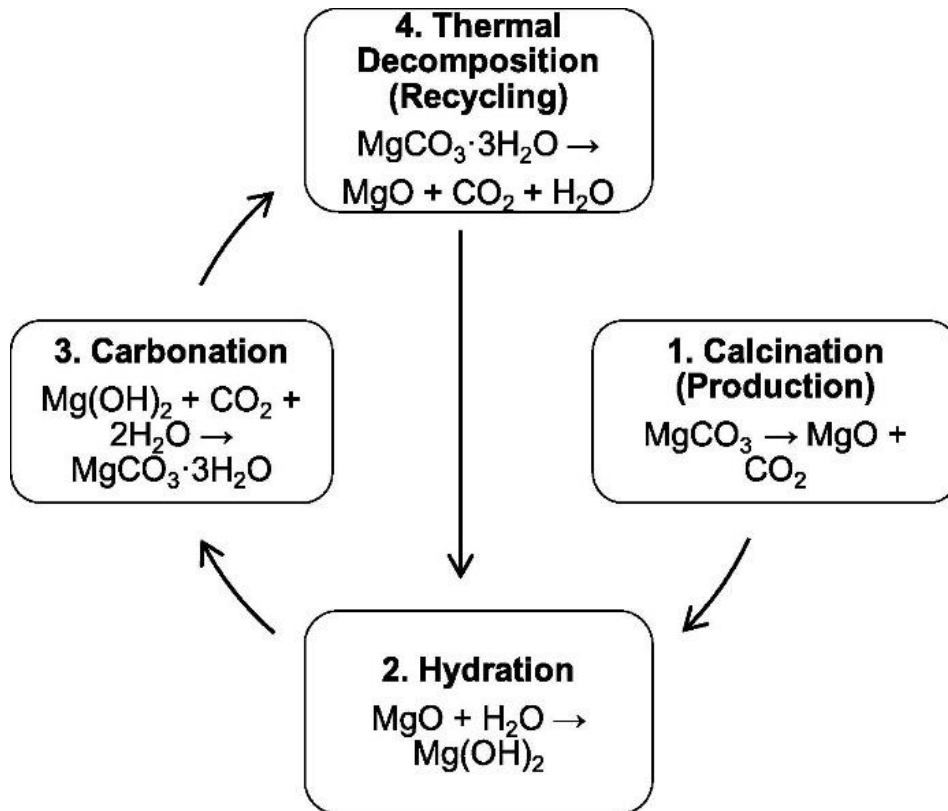
Fig. 2.4 Thermodynamic cycle in RMC-based systems [21]

2.3. Production of Magnesia

The calcination stage is an essential process in the production of MgO. The lower calcination temperature (700°C) leads RMC to have a better sustainability credential than PC, which is produced under calcination of raw material at 1450 °C; therefore, CO_2 emissions can be highly reduced during the production of MgO [22]. Besides the calcination of magnesite, seawater or brine can also be used to synthesize magnesium oxide, which has the potential to further reduce CO_2 emissions.

Four categories, i.e. Fused, Dead-burned, Hard-burned, and Light-burned,

according to the calcination temperature are used to classify MgO. With the growing calcination temperature, the reactivity of MgO decreases. Fused MgO at a calcination temperature of more than 2800 °C has the lowest reactivity. Dead-burned MgO is produced at a calcination temperature of 1400-2000 °C, it can result in significant volume expansions and cracks during its slow hydration process. Because of the high melting point, dead-burned MgO is widely used to form linings and bricks. Hard-burned MgO at a calcination temperature of 1000-1400 °C has moderate reactivity and crystallinity. Light-burned MgO with the highest reactivity and lowest crystallinity is produced at lower calcination temperatures of 700-1000 °C. RCM with light-burned MgO, whose hydration has a similar rate to PC, can avoid compatibility issues.

A majority of the MgO used in the construction today is light-burned MgO, which is produced from the calcination of $MgCO_3$ at temperatures between 700 – 1000 °C as shown in Equation 2.1. The dolomite ($CaMg(CO_3)_2$), calcite ($CaCO_3$) and siderite ($FeCO_3$) are often associated with magnesite, the thermal decomposition of these minerals also needs to be considered, as indicated in Equations 2.2, 2.3 and 2.4.

$$MgCO_3 \rightarrow CO_2 + MgO \tag{2.1}$$
$$CaMg(CO_3)_2 \rightarrow CaO + MgO + 2CO_2 \tag{2.2}$$
$$CaCO_3 \rightarrow CaO + CO_2 \tag{2.3}$$
$$4FeCO_3 + O_2 \rightarrow 2Fe_2O_3 + 4CO_2 \tag{2.4}$$
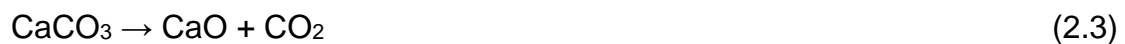
2.4. Properties of Magnesia

The source of magnesia (e.g. obtained from magnesite, seawater or brine) primarily dominates its physical and chemical properties [23]. Other factors that may affect the properties include the morphology of magnesia particles, temperature and time of calcination.

This thesis has collected a large amount of data regarding the physical and chemical properties of magnesia with come of the useful properties outlined

as follows.

2.4.1. Physical Properties of Magnesia

Magnesia normally has a grayish colour white with a density of 3.55–3.68 g/cm^3. It has a high melting point of 2800 °C, which is used as a critical temperature to classify MgO as fused MgO, the lowest reactivity MgO category. Magnesia has a cubic face-centered crystal lattice isomorphous with that of calcium oxide as shown in **Fig. 2.5**.
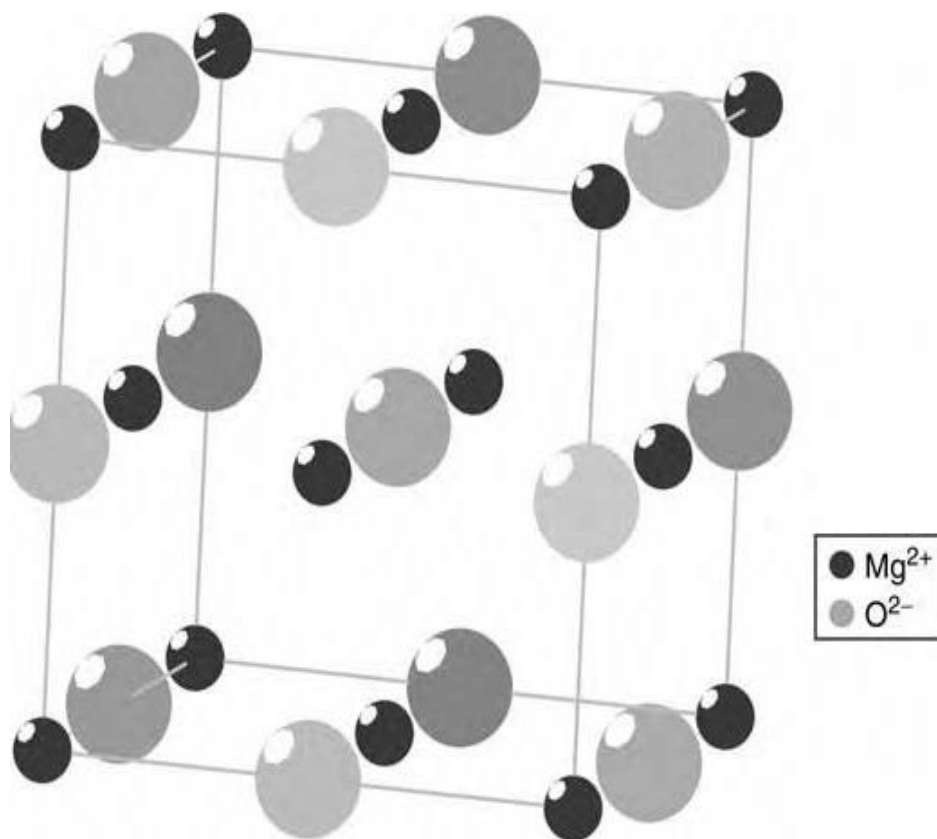
Fig. 2.5 Magnesium oxide crystal structure [24]

When considering the feasibility of magnesia as a construction material, the mechanical properties are essential. Some of the mechanical properties are listed in **Table. 2.1**.

Table. 2.1 Structural properties of magnesia [24]

Mechanical Properties	Value or value range (GPa)
Modulus of rupture	96.5–103.4
Shear modulus	75.8–131
Elastic modulus	210–317
Tensile strength	95.8
Flexural strength	89.6
Compressive strength	0.83–1.44

2.4.2. Chemical Properties of Magnesia

As the concentration of dissolved CO_2 varies in water, it may not be possible to make an accurate determination, especially if there is lime present as an impurity in the sample. Overall, the solubility of magnesia in water is very limited. Numerous measurements of solubility have been conducted, resulting in a wide range of results. Until now, the most accurate measurement has produced a result of 8.6 mg/L at 30 °C [24]. According to Segall et al. [25], the initial dissolution rate of magnesia is influenced by the rate at which water molecules are transported out of the Helmholtz layer when they are formed from the surface hydroxyl ions and protons. The Helmholtz layer is an electrical double layer which appears on the surface of an object (e.g. solid particles, porous bodies, or liquid droplets) when it is exposed to a fluid. The limited solubility of magnesia is the main reason for its limited hydration, while another factor is that the hydration product forms on the surface of the magnesia particles, resulting in the reduced reactive area of particles.

Fruhwirth et al. [26] studied the dissolution of MgO powders regarding H^+ and Mg^{2+} concentrations and found that there were various pH-dependent rate-controlling processes observed at room temperature. **Fig. 2.6** summarises the dissolution mechanism of MgO.

1. When pH is lower than 5.0, H^+ attack is the rate-controlling step, which is followed by desorption of Mg^{2+} and OH^-. These processes are part of the overall neutralization reaction (Equation 2.5)

$$MgO + 2H^+ \rightarrow Mg^{2+} + H_2O \tag{2.5}$$

2. When pH ≈ 5, proton diffusion is the rate-determining step and a proportional relationship exists between pH and the diffusion rate.

3. When pH > 7, OH^- adsorption is the rate-controlling step, which is then followed by desorption of Mg^{2+} and OH^-. This reaction is the most common one in reactive magnesia cement hydration.
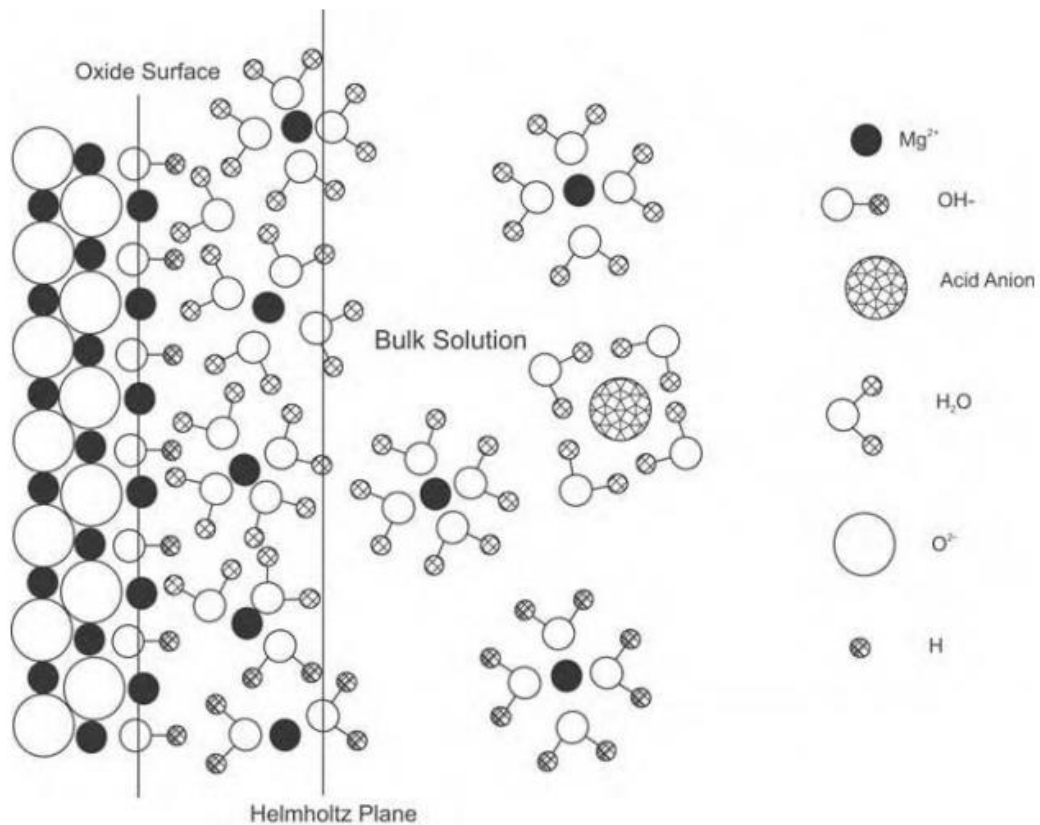
Fig. 2.6 Dissolution mechanism of MgO [24]

2.4.3. Chemisorption of Various Molecules on MgO

Acid-base interactions will dominate chemisorption on MgO surfaces. An interaction between cation sites and donor molecules, such as H_2O may result from an interaction between electrostatics (ion-dipole attraction) and orbital

overlap. The oxide ions can also serve as basic sites and can interact with acceptors (e.g. H^+). Deprotonating an adsorbate to produce surface hydroxyl groups is one of the most common dissociative reactions. Because of exposure to H_2O, the surface of MgO showed evidence of OH^-, which formed a monolayer of OH^- on the surface [24].

The dissociation of formic and acetic acids at room temperature and below results in surface hydroxide as well as the formation of formate ($HCOO_2$) and acetate (CH_3COO_2) species [24]. MgO can react with acetic acid (CH_3COOH) to form magnesium acetate ($Mg(CH_3COO)_2$) and water (H_2O), which is represented by Equation 2.6. The interaction between magnesium oxide and acetic acid is an acid-base reaction as discussed in the last subsection, with MgO functioning as a base, and acetic acid as an acid. In this process, MgO combines with the acidic hydrogen ions (H^+) present in acetic acid to produce water, while the magnesium ions (Mg^{2+}) from MgO react with acetate ions (CH_3COO^-) from acetic acid to yield magnesium acetate. This reaction happens regardless of the acetic acid concentration, although the reaction rate may fluctuate based on the concentration level.

$$MgO + 2CH_3COOH \rightarrow Mg(CH_3COO)_2 + H_2O \qquad (2.6)$$
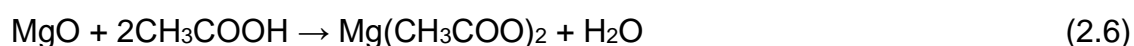
2.5. Carbonation of Magnesia

Three major steps can co-occur during the magnesia carbonation, which are hydration of magnesia, carbon dioxide dissolution, and carbonation of brucite. All these steps play important roles in the magnesia carbonation mechanism.

When MgO particles dissolve in water, consequently, the formation of brucite ($Mg(OH)_2$) will occur, which is described as the hydration of magnesia. As MgO produces a positively charged surface by contacting water, the releasing OH^- ions are absorbed by this surface. Afterward, Mg^{2+} and OH^- ions are released into the solution (Equations 2.7-2.9). When the concentration of Mg^{2+} and OH^- ions reaches the supersaturation level, the $Mg(OH)_2$ precipitation occurs on the surface of MgO particles (Equation 2.10), leading to a reduced

surface area for further hydration. As the hydration further progressed, the volume of brucite surrounding layer increased, leading to a breakup; thereby, the previously covered unhydrated MgO particles were exposed again for hydration. The hydration cycle repeats as follows.

$$MgO(s) + H_2O\ (l) \rightarrow Mg(OH)^+_{surface} + OH^-(aq) \qquad (2.7)$$

$$Mg(OH)^+_{surface} + OH^-(aq) \rightarrow Mg(OH)^+ \cdot OH^-_{surface} \qquad (2.8)$$

$$Mg(OH)^+ \cdot OH^-_{surface} \rightarrow Mg^{2+}(aq) + 2OH^-(aq) \qquad (2.9)$$

$$Mg^{2+}(aq) + 2OH^-(aq) \rightarrow Mg(OH)_2(s) \qquad (2.10)$$

CO_2 dissolution also plays a significant role in the carbonation process. Such a dissolution process starts with CO_2 dissolving into water (Equation 2.11), reacting with OH^- and H_2O molecules [27]. At a higher pH of binder (>10), a desolvation of CO_2 (Equation 2.12) predominates over the hydration of CO_2 (Equation 2.13). When the binder becomes more acidic, the hydration of CO_2 increases, then becomes the main reaction when the pH value of the binder becomes less than 7. As the pH value of the brucite slurry is around 10.5 and decreases through the whole reaction until it reaches stable, which is slightly higher than 7. The main reaction is the desolvation of CO_2 (Equation 2.12) until the end of the carbonation of MgO [27,28]. After these processes, CO_3^{2-} ions are released through the second dissociation (Equation 2.14).

$$CO_2\ (g) + H_2O\ (l) \rightleftharpoons CO_2\ (aq) \qquad (2.11)$$

$$CO_2\ (aq) + OH^- \rightleftharpoons HCO_3^- \qquad (2.12)$$

$$CO_2\ (aq) + H_2O \rightleftharpoons H^+ + HCO_3^- \qquad (2.13)$$

$$HCO_3^- + H^+ \rightleftharpoons CO_3^{2-} + 2H^+ \qquad (2.14)$$

As soon as CO_2 dissolves into water, the exposed brucite on the surface of the MgO particles reacts with the CO_2 (Equation 2.15) and the minor H^+ ions (Equation 2.16). Therefore, as shown in Equation 2.17, a series of hydrated magnesium carbonates (HMCs) are precipitated from the magnesium bicarbonate solution. The formed HMCs are shown in **Table. 2.2**.

$$Mg(OH)_2 \text{ (s)} + 2CO_2 \text{ (aq)} \rightleftharpoons Mg^{2+} + 2HCO_3^- \qquad (2.15)$$

$$Mg(OH)_2 \text{ (s)} + 2H^+ \rightleftharpoons Mg^{2+} + 2H_2O \qquad (2.16)$$

$$Mg^{2+} + 2HCO_3^- + xH_2O \rightleftharpoons MgCO_3 \cdot xH_2O + H^+ + HCO_3^- \qquad (2.17)$$
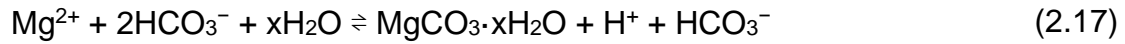
Table. 2.2 HMCs Identified in MgO Cements [29-33]

HMCs	Composition	Density (g/cm^3)
Nesquehonite	$MgCO_3 \cdot 3H_2O$	1.85
Lansfordite	$MgCO_3 \cdot 5H_2O$	1.70
Artinite	$Mg_2(CO_3)(OH)_2 \cdot 3H_2O$	2.03
Hydromagnesite	$Mg_5(CO_3)_4(OH)_2 \cdot 4H_2O$	2.25
Dypingite	$Mg_5(CO_3)_4(OH)_2 \cdot 5H_2O$	2.15

The carbonation of $Mg(OH)_2$ can be described as the subsequent carbonation to hydrated magnesium carbonate, as shown in Equations 2.18-2.21.

$$Mg(OH)_2 + CO_2 + 2H_2O \rightarrow MgCO_3 \cdot 3H_2O \text{ (Nesquehonite)} \qquad (2.18)$$

$$2Mg(OH)_2 + CO_2 + 2H_2O \rightarrow Mg_2(CO_3)(OH)_2 \cdot 3H_2O \text{ (Artinite)} \qquad (2.19)$$

$$5Mg(OH)_2 + 4CO_2 \rightarrow Mg_5(CO_3)_4(OH)_2 \cdot 4H_2O \text{ (Hydromagnesite)} \qquad (2.20)$$

$$5Mg(OH)_2 + 4CO_2 + H_2O \rightarrow Mg_5(CO_3)_4(OH)_2 \cdot 5H_2O \text{ (Dypingite)} \qquad (2.21)$$
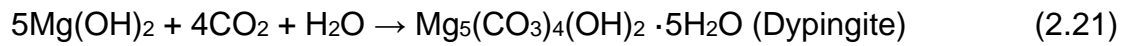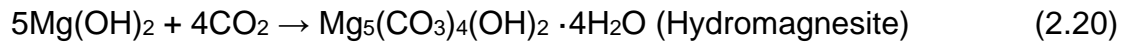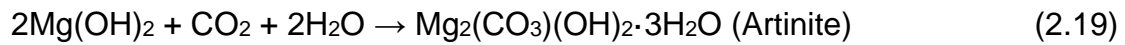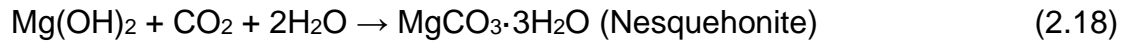
As three main processes (i.e. hydration of magnesia, carbon dioxide dissolution, and carbonation of brucite) can occur simultaneously during magnesia carbonation, all these factors can influence the carbonation of magnesia. The techniques to improve the carbonation of magnesia are mainly based on these three processes. For instance, some studies used the hydration agents (e.g. magnesium acetate ($(CH_3COO)_2Mg$), sodium bicarbonate ($NaHCO_3$), sodium chloride ($NaCl$)) to improve the hydration of magnesia, providing more reactants to involve in the reaction between CO_2 and reactants, consequently, increasing carbonation of magnesia [34]. Some studies utilize supercritical CO_2 (i.e. $scCO_2$) to accelerate carbonation. A solvent in a supercritical state has transport characteristics that fall between those of a gas and a liquid, resulting in significantly increased diffusivity, reduced viscosity, and decreased surface tension compared to regular liquids.

This promising technique aims to increase the dissolution in the binder. Moreover, hydrated magnesium carbonates (HMCs) are used as seed crystals to provide nucleation sites for carbonation, which can directly contribute to the carbonation of magnesia. These techniques or additives will be discussed in the later section.

On the one hand, carbonation is an undesirable reaction to mechanical strength and durability of PC mixes. It was reported by some studies that the carbonation of $Ca(OH)_2$ and C-S-H begin simultaneously, and the rate of carbonation in both cases is similar initially [35]. The carbonation process of C-S-H, however, continues, while $Ca(OH)_2$ becomes less accessible to carbonation, so its carbonation rate decreases. With the carbonation of PC mixes, strength can decrease as the C-S-H transforms into $CaCO_3$ and a highly porous and hydrous form of silica [36]. With the progression of carbonation, microcracks begin to form in the carbonated areas, increasing the permeability of concrete and reducing its strength [37,38].

On the other hand, magnesium-based carbonates show a higher compressive strength, compared with calcium-based binders, which are the main binder in PC mixes [39]. The conversion from brucite to HMCs is an expansion process (i.e. volume is increased by the formation of HMCs by a factor of 1.8-3.1), which reduces the porosity and overall pore volume. Additionally, the binding strength and the morphology of the HMC crystals positively contribute to the network structure of the binder, which can improve the microstructure. Therefore, the optimized microstructure of magnesium-based binder helps to improve mechanical properties including compressive strength, toughness, stiffness, and elastic modulus [40,41]. The morphologies of these HMCs, which are the main factor dictating strength, are depicted in **Fig. 2.7**.
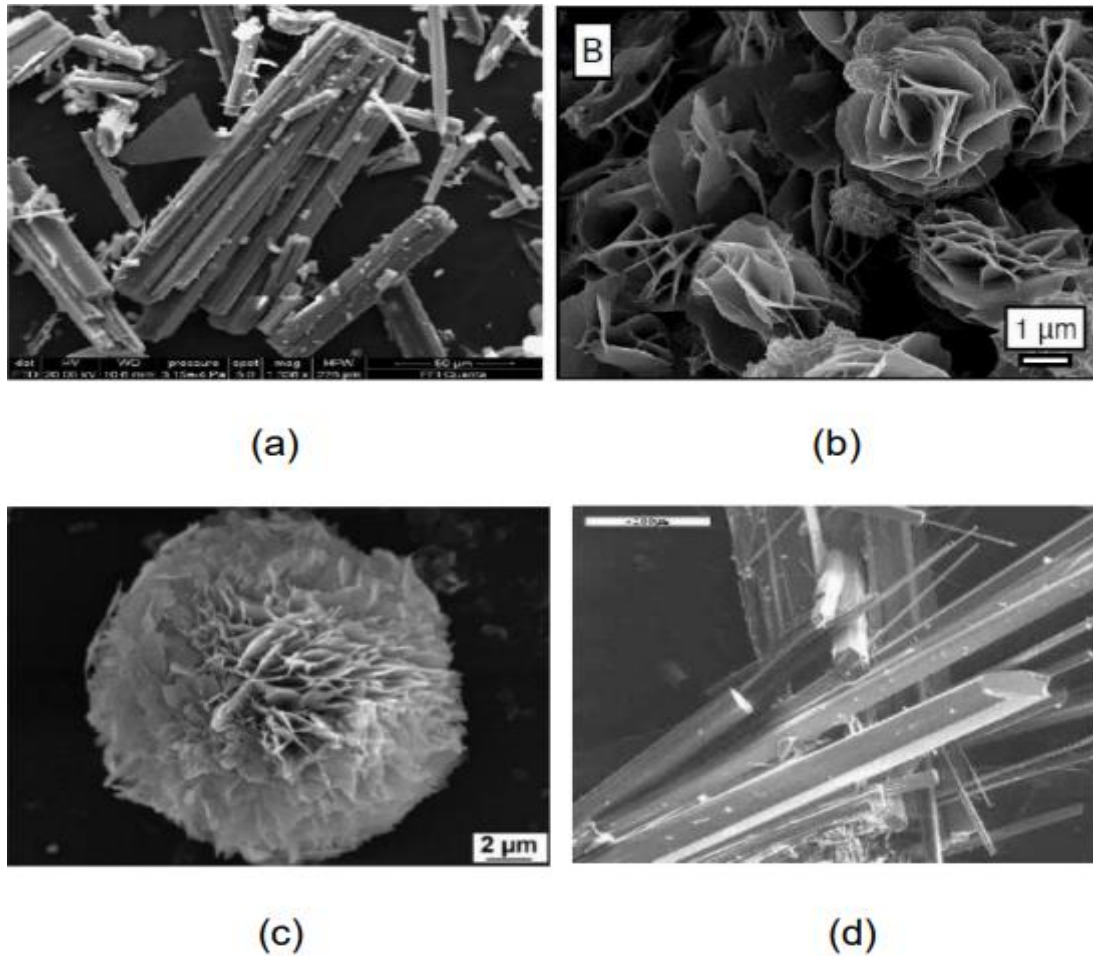
Fig. 2.7 Microstructure of typical HMCs: (a) nesquehonite [42], (b) dypingite [43], (c) hydromagnesite [44] (d) artinite [45]

2.6. Factors Influencing Carbonation of Magnesia

The hydration and carbonation of MgO are considered being synergetic, according to the mechanisms of these two processes. Since brucite precipitates on the surface of MgO particles, the unreacted MgO particles are covered by the hydration products, thus, hydration is hindered. When subjected to CO_2 curing, brucite further reacts with CO_2 on the MgO grain surface to produce HMCs, which in turn surround brucite, as illustrated in **Fig. 2.8** [19,21,34,46]. Because of the insolation of the available reactive surfaces, the formed HMCs and brucite result in a coating on MgO particles, slowing or inhibiting subsequent hydration and carbonation of those particles [47]. Because of this characteristic of the magnesia carbonation process,

unreacted periclase was always founded even after 196 days of hydration [48]. When available brucite has been fully carbonated, unreactive periclase is coated by HMCs, consequently, the carbonation of magnesia stops. As the hydration process continues over time, the brucite layer tends to rupture due to its expanding volume. This break can be advantageous for the hydration process as it exposes unhydrated MgO for hydration. Consequently, this phenomenon reveals fresh MgO surfaces, which, in turn, become accessible for the ongoing hydration of magnesia, effectively repeating the hydration cycle [49,50]. Obviously, the properties of the raw material (MgO) affect the process of carbonation. Apart from MgO characteristics, the formation of HMCs is highly related to the carbonation curing conditions [51]. As HMCs are the major contributor to strength and the densified microstructure, understanding the influencing factor on the carbonation of magnesia is crucial. According to Pu and Unluer, factors affecting carbonation are categorized into two groups: (i) CO_2 diffusivity and (ii) CO_2 reactivity [51]. Based on these distinctions, the factors affecting carbonation can be divided into three primary categories: (i) curing condition; (ii) material properties; and (iii) mix design (e.g. additives). As this thesis mainly utilizes high-purity magnesia as the main binders, therefore, this literature review specifically concentrates on the curing parameters and additives.
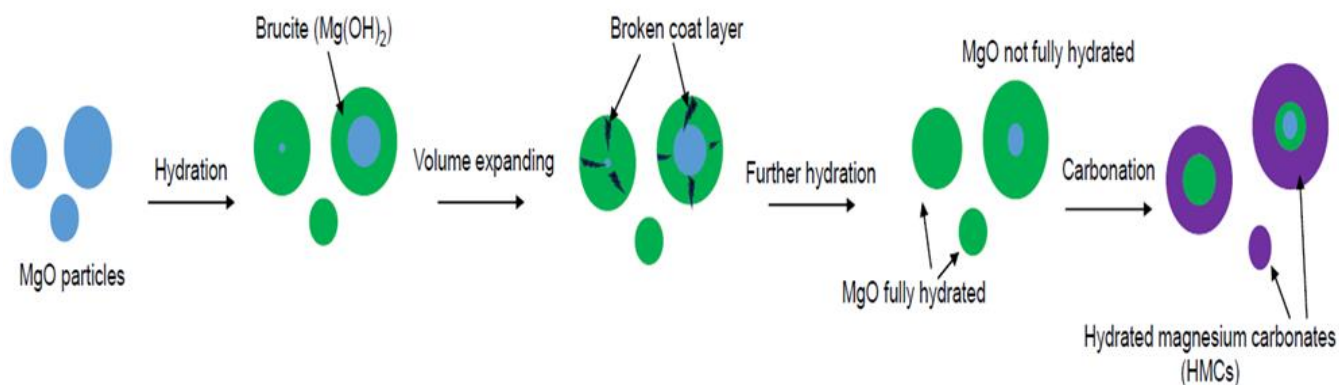
Fig. 2.8 Schematic illustration of magnesia carbonation process

2.6.1. Curing Parameters

2.6.1.1. CO_2 Concentration

Overall, carbonation is accelerated by increasing CO_2 concentration up to 99.9% [18,52]. Pu et al. and Liska et al. [41,51]. found that full-strength development of magnesium-based composites can be achieved within 14 days subjected to CO_2 curing with concentrations of 5–20%. According to Liska et al. [48], RMC-based masonry elements gained a compressive strength of 10-18 MPa at 28 days under CO_2 curing (20% CO_2 concentration), which was 6 times of that of ambient environment cured units, which only gained a compressive strength of 1.3–2.8 MPa at the same age. Besides that, Unluer and Al-Tabbaa [19] found that the 7-day compressive strength was 17.41, 23.53 and 24.00 MPa when under CO_2 curing with concentrations at 5%, 10%, and 20%, respectively. Although the compressive strength under 20% CO_2 concentration was higher than that under 10% CO_2 concentration, the difference was quite small, which suggests that 10% may be the optimum concentration of CO_2 for the development of strength. A similar scenario was reported by Dung et al. [53], comparable 28-day compressive strengths were observed (58, 63 and 60 MPa) when samples were cured under CO_2 with a concentration of 5%, 10%, and 20%, respectively. Although carbonation occurred at a slower rate when exposed to a 10% CO_2 concentration, the extent of carbonation and the compressive strength achieved after 7 days of CO_2 curing with a concentration of 10% were similar to those observed in samples cured for only 1 day under 100% CO_2. Hence, it can be concluded that subjecting RMC samples to a relatively low CO_2 concentration (e.g. 10%) remains effective in expediting carbonation. Moreover, prolonged exposure to CO_2 curing significantly augments the extent of carbonation. **Fig. 2.9** provides a comprehensive representation of the influence of carbon dioxide (CO_2) concentration on the compressive strength of RMC specimens, as reported in relevant studies [48,54-56] where the normalized strength is calculated as the compressive strength divided by the strength achieved during curing under the lowest CO_2 concentration in the particular study.
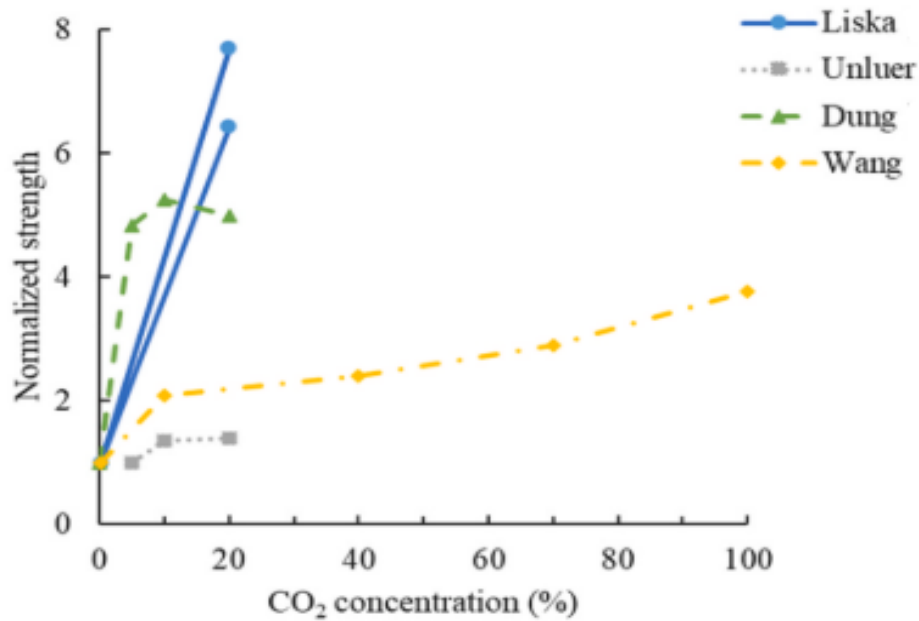
Fig. 2.9 The effect of CO_2 concentration on normalized strength of RMC samples [57]

2.6.1.2. CO_2 Pressure

The impact of CO_2 pressure on carbonation was also investigated by several studies [58-60]. The effect of CO_2 pressures on carbonation of magnesium-based samples was studied by Rausis et al. [60]. As the applied pressure increased (i.e. from 0.1, 0.4, 0.7, to 1.0 MPa), there was an increase in the amount of sequestered CO_2. However, the rate of the increase of sequestered CO_2 reduced beyond 0.4 MPa according to Mo et al. [59], who cured the samples at 0.1 MPa for 1 day and at 0.55 and 1.0 MPa for only 3 h, and found that the sample cured at 0.55 MPa and 3 h exhibited the highest compressive strength. In the presence of CO_2 with a high partial pressure, rapid diffusion of CO_2 occurred within the samples. Consequently, carbonation took place expeditiously, in the pore solution and on the surfaces of Mg phases, resulting in the formation of a substantial quantity of carbonate products. As carbonation progresses, the pores gradually become blocked, primarily because of the carbonate product layers formed on Mg phases. These layers effectively passivate the surfaces of those phases, impeding further diffusion of CO_2 or CO_3^{2-} to reach the reaction sites. Therefore, it is not a linear

relationship between the increase in CO_2 pressure and the increase in compressive strength. Between 0.1 and 0.55 MPa, higher pressures would be more effective in achieving comparable mechanical performance. However, when CO_2 pressure is higher than 0.55 MPa, the effectiveness is reduced. High CO_2 pressure only shows little effect on the increase of mixture strength.

2.6.1.3. Relative Humidity and Temperature

Under low relative humidity (RH) environments (i.e. lower than 30%), the conversion between MgO and $Mg(OH)_2$ is negligible, irrespective of temperature or CO_2 concentration to which magnesium-based materials are exposed. This is because of the dry curing environment not facilitating the hydration of magnesia and its subsequent carbonation [19]. Therefore, low RH is not recommended for curing magnesia because it does not support the transformation of magnesia into brucite, nor does it promote the formation of HMCs. As mentioned earlier, a high hydration degree is beneficial to carbonation, thereby, the presence of high relative humidity conditions contributes to carbonation [19], since high hydration is usually favored in a high relative humidity environment. Although hydration and carbonation require high relative humidity (RH), the diffusion of CO_2 slows down in a wet environment. Thus, increasing RH does not necessarily result in a linear increase in carbonation. According to Wang et al. [61], a relative humidity of 98% was beneficial for RMC samples, while Unluer and Al-Tabbaa [19] found that the optimal RH for carbonation was 78%. As the water content in the binder is also considered a factor that affects the carbonation, it should be noticed that different findings from the two studies may be related to the difference in water/binder (w/b) ratios, where Unluer and Al-Tabbaa adopted a w/b ratio of 0.7, which is higher than that of Wang et al. (i.e. w/b ratio of 0.25). Therefore, the optimum RH should be selected according to w/b ratio, which varies from 78% to 98%.

Moreover, because of the low RH curing environment, hydromagnesite and dypingite are more likely to form than nesquehonite. A high RH curing

environment, however, favours the formation of nesquehonite over dypingite [19,61]. The increasing amount of nesquehonite with the increasing RH is shown in **Fig. 2.10**. It is therefore important to take into consideration the relative humidity level of the environment when magnesia undergoes carbonation, since it may control the formation of HMCs.
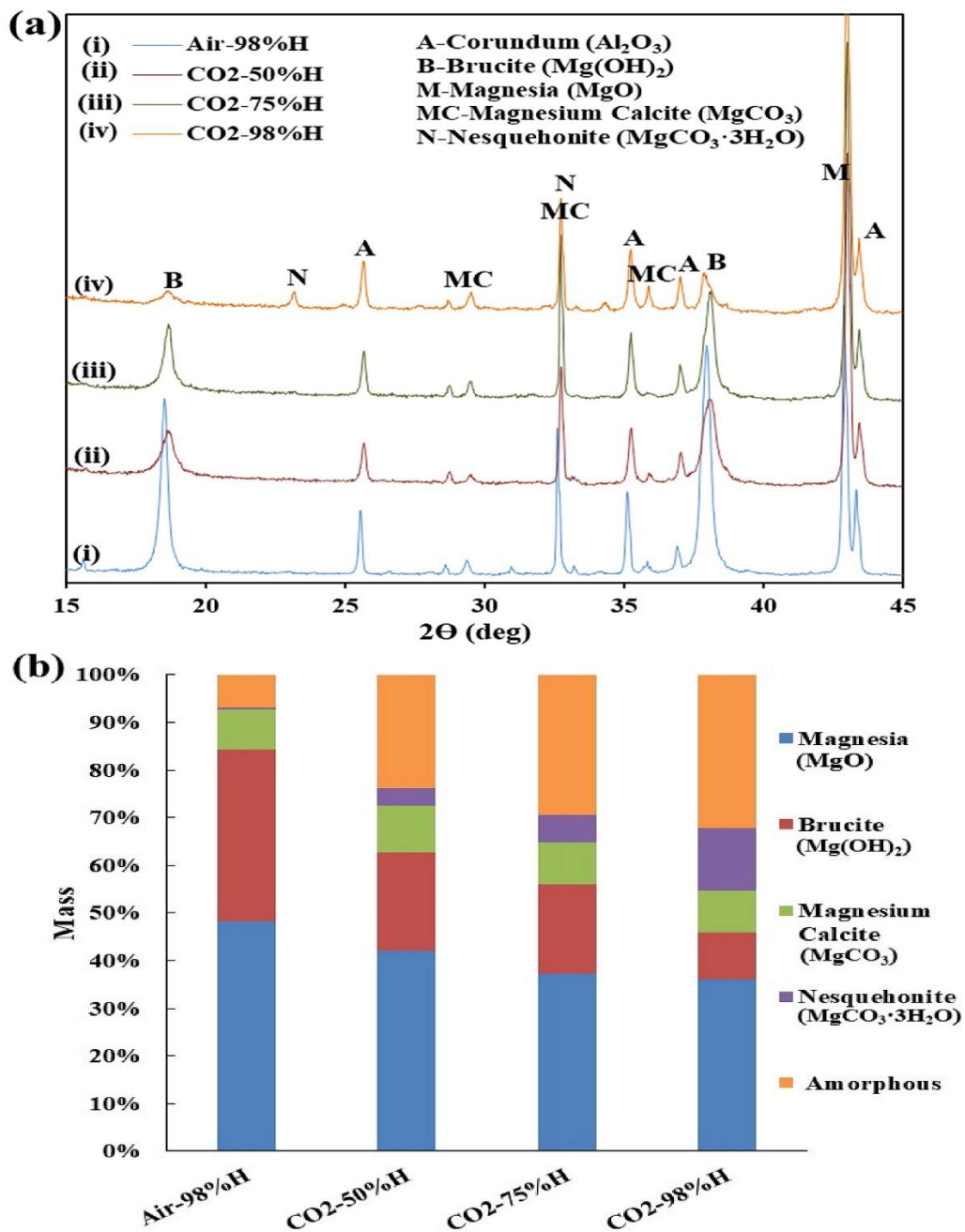
Fig. 2.10 XRD of reactive magnesia cement pastes after 1-day of CO_2 and air

curing with several relative humidities: (a) XRD patterns and (b) Q-XRD

analysis [61]

Apart from RH, temperature is considered another important factor that can affect carbonation and control the type of formed HMCs. More nesquehonite is formed than other magnesium carbonates under a curing temperature $\leqslant$ 20 °C. When subjected to a curing temperature of 40 °C, the amount of nesquehonite and other HMCs (e.g. hydromagnesite) generated is comparable [62]. Two studies have investigated the effects of pre-cured temperature on hydration and strength development of RMCs, which found that pre-curing RMC at 50 °C and 60 °C for 1-2 days before CO_2 curing can improve carbonation degree and early-age hydration [63,64]. The 56-day compressive strength of RMC samples subjected to 50 °C pre-curing was about 18% higher than that of the control samples without pre-curing [64]. Similarly, pre-cured at 60 °C, the compressive strength of the sample was increased by 35% at 28 days, compared to the control group without pre-curing [63]. Pu and Unluer [65] found that when high temperatures (150–550 °C) were adopted, the carbonation of RMC samples deteriorated because of the decomposition of HMCs and brucite. RMC samples retained their stability up to 80 °C. However, at elevated temperatures ranging from 150 °C to 550 °C, the decomposition of HMCs and brucite significantly compromises the strength of RMC, as these compounds are key contributors to its strength. In conclusion, the high temperature (>150 °C) should be avoided since it could negatively affect the mechanical performance of the RMC samples, while the carbonation degree and development of compressive strength of samples can be promoted by pre-curing at a moderate temperature (50–60 °C) for 1-2 days.

2.6.1.4. Duration

Achieving high carbonation as much as possible in a relatively short curing duration is the key to reduce the time and cost. According to Ruan and Unluer [66], compressive strengths of RMC samples showed a continuous increase

until 28 days, however, there was only a 9.3% of increment from 14 to 28 days. Similar results were also reported by Dung et al. [46] that only minor strength gain was found from 14 to 28 days (58 and 60 MPa). However, Liska and Al-Tabbaa [41] studied RMC masonry blocks cured under 20% CO_2, 21 °C, and 98% RH, and found that the 14-day compressive strength of the samples was slightly lower than their 7-day counterpart. Some studies [51,67] indicated that compressive strength increased until 14 days, and then decreased at 28 days. Moreover, it has been found that the carbon sequestration ratio increased by a negligible amount between 14 and 28 days. The explanation is that carbonation caused volume expansion, which led to cracks and internal stress [51,67]. Overall, long-term curing seems to have a minor or even harmful effect on the compressive strength of RMC binders. The optimum carbonation curing duration is between 7 and 14 days, which can achieve satisfactory mechanical performance and carbonation sequestration.

2.6.2. Additives

Using additives is an efficient way to improve hydration and carbonation of RMC systems, which is widely studied in recent years. The additives used in RMC-based material are divided into three categories: hydration agents, carbonation agents and nucleation seeding.

2.6.2.1. Hydration Agents

As discussed in **Section 2.6**, hydration and carbonation of MgO are synergetic under normal conditions (pH≈7), since hydration products (i.e. brucite ($Mg(OH)_2$)) are the reactant for carbonation. Therefore, to some extent, hydration agents can also improve carbonation by accelerating hydration to form more brucite, consequently, contributing to the subsequent carbonation. Some hydration agents such as magnesium acetate (($CH_3COO)_2Mg$) [46,63,68-70], hydrochloric acid (HCl) [56], sodium bicarbonate ($NaHCO_3$), sodium chloride (NaCl) [71,72], and magnesium chloride ($MgCl_2$) [73] have been studied and reported to be able to enhance the hydration of RMC-based

materials. Among these additives, magnesium acetate is the most widely studied additive and is regarded the most effective hydration agent.

The presence of $(CH_3COO)_2Mg$ allows the precipitation of brucite to occur in the bulk solution rather than on the surface of MgO, increasing the availability of surface area for further hydration [63]. The migration of complex magnesium acetate ions (CH_3COOMg^+) as shown in Equation 2.22 facilitates their movement away from their initial particles, allowing for the formation of $Mg(OH)_2$ within the pore spaces. Additionally, extra Mg^{2+} is provided by $(CH_3COO)_2Mg$, accelerating the formation of brucite, while the CH_3COO^- ions help in dissolving unreacted MgO. It has been reported that the addition of 0.5M $Mg(CH_3COO)_2·4H_2O)$ accompanied by pre-curing at 60 °C for 2 days results in an enhancement in the hydration degree (up to 52%) of magnesia in RMC-based concrete blends that were subjected to CO_2 curing for 28 days. Increased hydration degree led to the building of denser and well-connected HMC microstructure, resulting in strength gains of up to 40% compared to the control group [63]. Three types of hydration agents (i.e. HCl, $MgCl_2$, and $(CH_3COO)_2Mg$) were compared by Dung and Unluer [73]. It reported that the mechanical strength and carbonation degree of samples containing $(CH_3COO)_2Mg$ surpassed all other mixtures. In terms of their compressive strengths, mixes with $(CH_3COO)_2Mg$ achieve 273% and 107% higher strengths than the control group without additives at 14 and 28 days. In terms of hydration degree, $(CH_3COO)_2Mg$ demonstrated the highest hydration degree (i.e. 89%) at 14 days, which was 54% higher than that of the control group [73].

Dissolution of magnesia in the presence of acetate ions:

$$MgO + 2CH_3COO^- + H_2O \leftrightarrow CH_3COOMg^+ + 2HO^- \tag{2.22}$$

2.6.2.2. Carbonation Agents

By increasing the pH value and the dissolution of CO_2, $NaHCO_3$ is applied as

a carbonation agent in the RMC binder. Furthermore, additional HCO_3^- ions are provided by $NaHCO_3$, contributing to carbonation. A work conducted by Dung and Unluer [71] showed that a 28-day compressive strength of 50 MPa can be achieved by the addition of NaCl and $NaHCO_3$ into the solution, which was 110% higher than that of the control group. Ma et al. [72] compared the impact of Na_2CO_3, $NaHCO_3$ and $Na_3H(CO_3)_2·2H_2O$ on the hydration and carbonation of reactive MgO cement, which showed that the addition of $NaHCO_3$ and $Na_3H(CO_3)_2·2H_2O$ led to a higher compressive strength, while the use of Na_2CO_3 decreased the compressive strength, attributed to a decrease in the formation of hydration products that could undergo carbonation. In terms of the products of magnesium-based cement, nesquehonite formed as the primary product of carbonation in sodium bicarbonate and sodium sesquicarbonate containing samples, which can explain their higher mechanical performance. Moreover, an amorphous phase was detected in MgO cement containing $NaHCO_3$ and $Na_3H(CO_3)_2·2H_2O$, which made the main contribution to the enhancement of compressive strength.

2.6.2.3. Nucleation Seeding

HMCs are normally used as the seed crystals of RMC mixes, which can provide nucleation sites for carbonation [68,74-76]. The reactive surface area of MgO can be extended, as the HMCs can give nucleation sites for the formation of brucite, diverting them away from the magnesium oxide particles, which is shown in **Fig. 2.11**. The increased reactive surface area of MgO is beneficial for continuous hydration and subsequent carbonation. The carbonation degree and compressive strength of the concrete were increased by 96% and 33%, respectively, by adding 1% by weight hydromagnesite seeds ($Mg_5(CO_3)_4(OH)_2·4H_2O$) [74]. Moreover, hydromagnesite is not only an effective seeding agent but also accelerates the hydration of reactive magnesium oxide [77,78]. The combination of hydromagnesite and other additives was also investigated by several studies. The compressive strength of RMC-based samples with the addition of hydromagnesite and magnesium

acetate was 46% higher than that of the control batch without the seeds at 28 days, due to the increased CO_2 sequestration [68]. The high carbonation degree and densification of microstructures were achieved by the addition of hydromagnesite and sodium bicarbonate, resulting in a 142% increase in 28-day compressive strength, compared with that of the control samples [79].

(a)   (b)   (c)
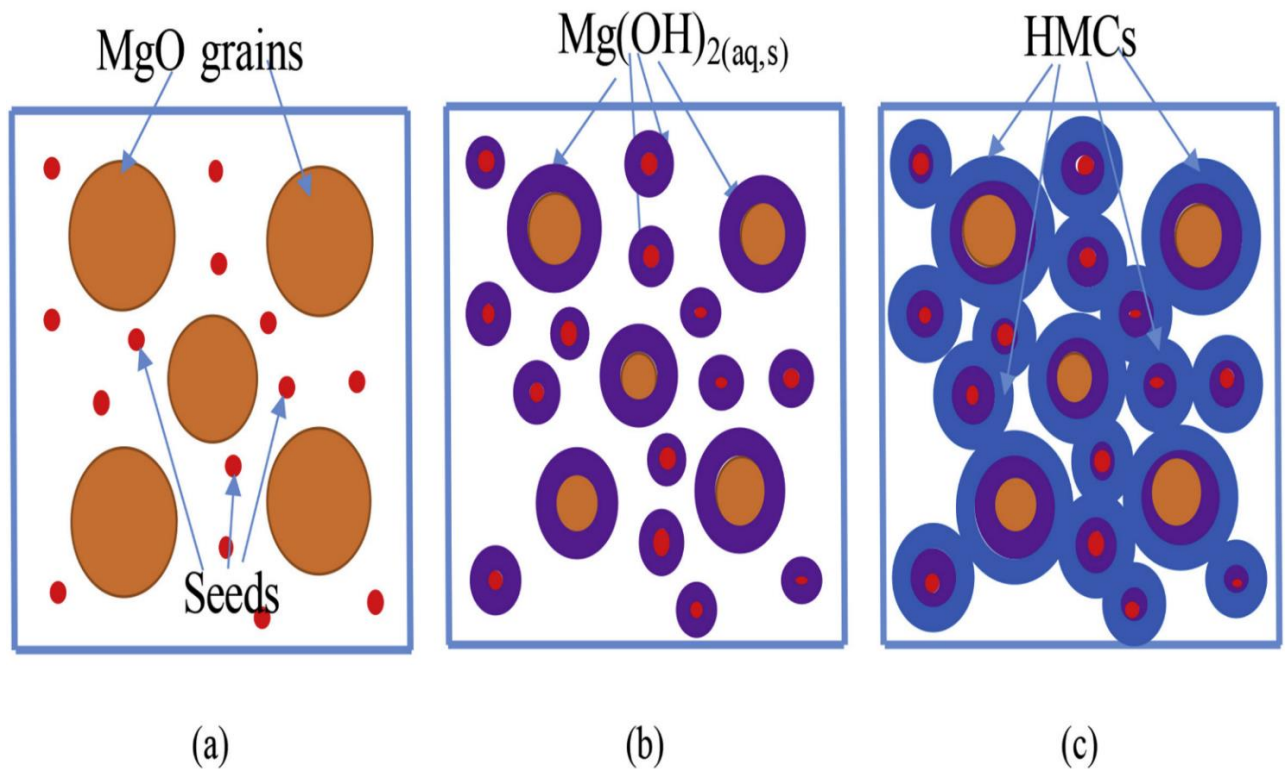
Fig. 2.11 Illustrations of how hydration and carbonation occur in seeded pastes: (a) seeds are introduced within pore spaces for nucleation on their surfaces; (b) $Mg(OH)_2$ nucleates on both MgO and seed surfaces to enhance carbonation; and (c) HMCs are formed on both $Mg(OH)_2$ and seed surfaces, thereby filling up pore spaces and densifying the microstructure [74]

2.7. Limestone Calcined Clay Cement (LC3)

This thesis innovatively proposes a new concept, i.e. modified magnesium-based carbonates calcined clay cement (MC3), where magnesium-based carbonates are used to replace the limestone in LC3. Therefore, the mechanism and mechanical properties of LC3 are reviewed in this chapter.

The carbon emissions and virgin resources consumed in cement production could be significantly reduced by utilizing supplementary cementitious materials (SCMs), particularly in developing countries. Fly ash (FA), limestone, and slag are the main SCMs to reduce the clinker content in cement. However, the availability of SCMs is a challenge in recent years. For instance, there is a threat to the supply chain of some widely used SCMs, such as fly ash, which contains a variety of glassy phases. Throughout the UK and the Netherlands, it is planned to retire all coal-fired power plants by 2025 and 2030 [80]. Also, steel demand is expected to grow less rapidly than cement demand, and more steel is being recycled because of environmental pressures. This indicates that the availability of slag is unlikely to increase in the future. The availability of commonly used SCMs is shown in **Fig. 2.12**.
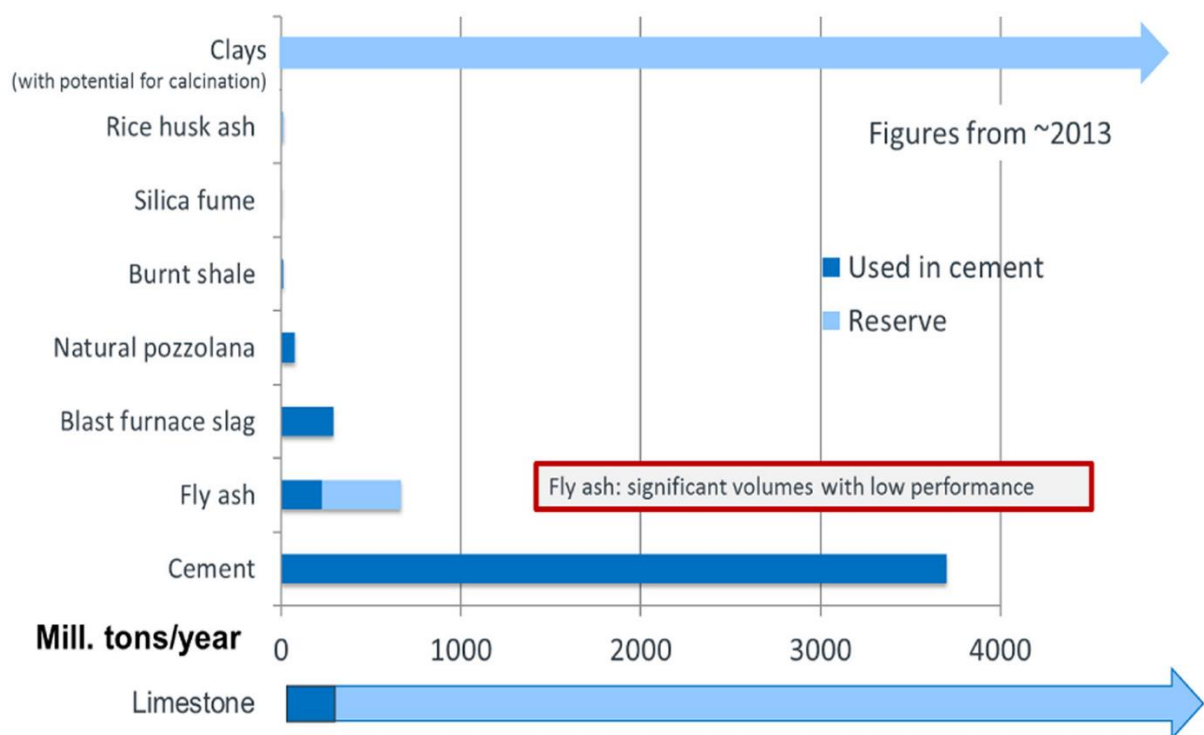
Fig. 2.12 SCMs' availability [81]

From **Fig. 2.12**, the large amount of limestone and clay are not well used in the cement sector, which indicates their high potential to be applied to the cement binder systems. To well-utilise limestone and clay, limestone calcined clay cement (LC3) was introduced. Clinker, calcined clay, limestone, and gypsum are the main ingredients of LC3 blends. The compositions of LC3 and

its CO_2 emission are shown in **Fig. 2.13**, compared with their counterparts of PC. It is worth noting that the productions of gypsum and limestone also require calcination, mining and milling, which may emit CO_2. It is not 'no CO_2' for using gypsum and limestone as shown in **Fig. 2.13**, however, the CO_2 emissions are still lower than that of PC binders. In the process of calcining clay containing kaolin, metakaolin is produced, which contains aluminosilicate. $Ca(OH)_2$, as a hydration product of cement, can react with aluminosilicate to form calcium aluminosilicate hydrate (C–A–S–H) [82-84]. Furthermore, carboalumination hydrates (i.e. mono-carbo aluminate (Mc) and hemi-carbo aluminate (Hc)) can be formed when alumina reacts with limestone. Therefore, this idea is based on that calcined clay is used as pozzolan, which can react with cement to produce the carboaluminate phase, because of its highest pozzolanic reactivity when compared with other SCMs.
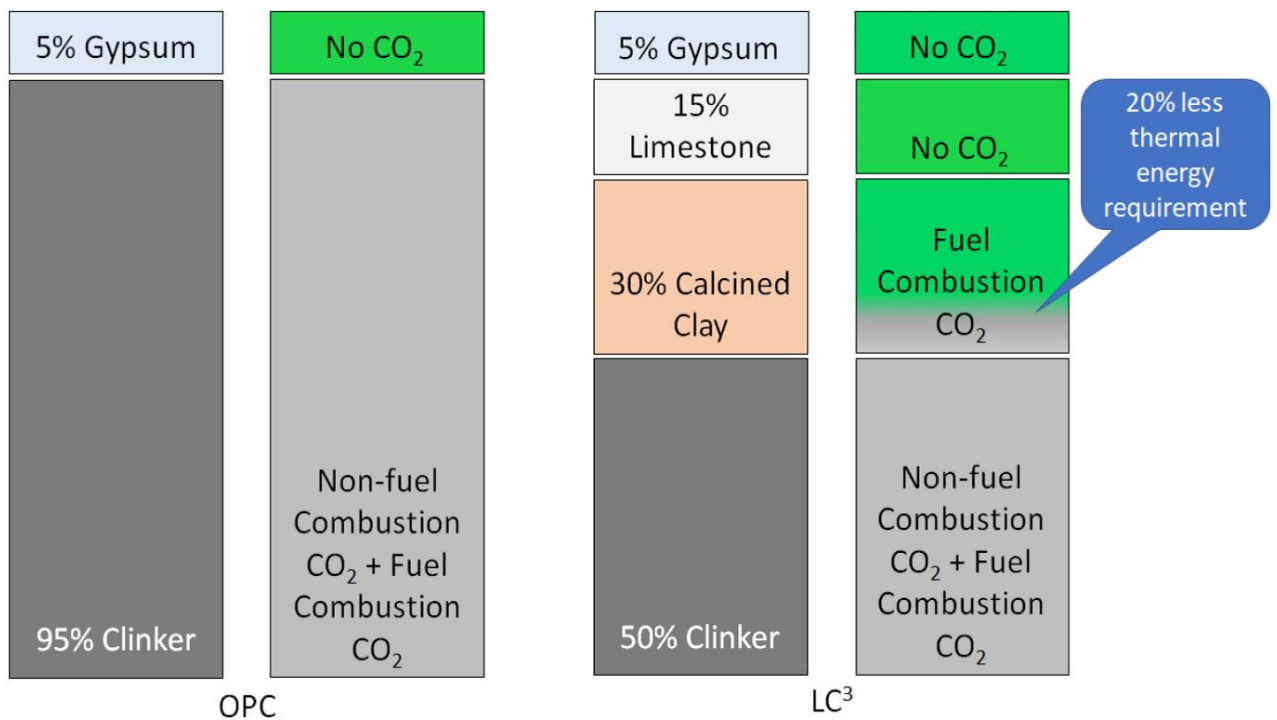
Fig. 2.13 Composition of OPC and LC3 and their CO_2 emissions [85]

Because of the addition of calcined clays to Portland cement, it has been found that hydration products are changed and thereby affect the durability of LC3 [86-88]. Portlandite ($Ca(OH)_2$) is consumed significantly by involving the reaction with clay, and this reaction also forms an additional calcium

aluminosilicate hydrate (C–A–S–H) [89,90]. Calcined clays provide additional aluminates for alumina uptake in C–A–S–H gels and the formation of hydration products such as ettringite and mono-sulphoaluminate (AFm) [91-94]. Alumina from clinker combines with limestone (Cc) powders to produce CO_3-AFm phases, besides the pozzolanic reaction of metakaolin (AS_2) with portlandite (CH) that produces C_2ASH_8 (strätlingite) and C-A-S-H. When carbonates and calcined clays are added simultaneously, ettringite is prevented from converting to AFm, resulting instead in mono-carbo aluminate (Mc) and hemi-carbo aluminate (Hc) phases [95,96]. These reactions are shown in Equations 2.23-25.

$$AS_2 +3CH +6H \rightarrow C\text{-}A\text{-}S\text{-}H +C_2ASH_8 \text{ (strätlingite)} \qquad (2.23)$$

$$AS_2 +0.5Cc+3.5CH +8.5H \rightarrow C_4Ac_{0.5}H_{12} \text{ (Hc)} \qquad (2.24)$$

$$AS_2 +Cc+3CH +9H \rightarrow C_4AcH_{12} \text{ (Mc)} \qquad (2.25)$$
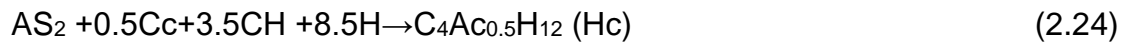
Although montmorillonite and illite have been trailed in some studies [97,98], kaolinite, whose reactivity is higher than that of montmorillonite and illite, is considered the main mineral in LC3. Because of the high aluminum content in kaolinite, the calcination process produces high-activity aluminum, making metakaolin highly reactive. The removal of structural water from clay is achieved through thermal activation. 60% by weight has been reported as the optimum kaolinite dosage, as the amount of reacted metakaolin in the LC3 binders is very close to that in calcined clays, which usualy has more than 50% by weight kaolinite [97]. This finding agrees well with that of another study, which shows that when the content of kaolinite is over 60% by weight, there is little to no additional improvement in compressive strength [99]. As only a small amount of limestone in LC3 can react with alumina phases in the binder, the majority of limestone acts as unreacted fillers. In addition, there is very little influence of the purity of limestone on the performance of LC3 binders [100]. Therefore, the feasibility of using alternative carbonates in LC3 binders is justified. The use of other carbonates (e.g. dolomite) in LC3 binders has been reported in other studies [101,102], indicating the potential to investigate alternative carbonates or other waste materials. The importance of

carbonates in this ternary binder system will be further discussed in **Chapter 5**.

According to Dhandapani et al. [103], the setting time of LC3 is shorter than that of OPC and cement-FA binders. The quicker setting is attributed to the faster hydration and the higher alumina content in LC3 [104]. In terms of workability, there are no significant changes that need to be made to achieve a workable LC3 concrete, compared with traditional concrete [105]. The higher negative surface charge on the surface of calcined clay particles results in the flocculation of particles, which dominates the thixotropic nature of LC3 pastes [106,107]. Therefore, the higher the metakaolin content, the lower the fluidity of the concrete mixtures [108]. Gypsum is also reported to affect the workability of LC3, because of its high water demand [109]. In contrast, the introduction of limestone can increase the workability of LC3, as it can reduce flow resistance [105].

It is well known that concrete's compressive strength is the key material property used in structural design, and it is crucial for the assessment of the performance of a binder. Factors including temperature, the composition of the clinker, alkali content and the particle sizes of the individual components all play an important role in strength development [110-112].

Most studies have found that LC3 has a comparable compressive strength to PC at 28 days, although some studies have different findings. It can be inferred that the pozzolanic reaction leads to the comparable strength, in which $Ca(OH)_2$ is reacted by silica in calcined clay, resulting in the formation of carboaluminates. Yuvaraj et al. [103] found that LC3 mix with similar mixture proportion showed comparable strength development with OPC at all ages up to 1 year. While Mishra et al. [110] also demonstrated that the limestone-calcined clay-cement combination can substantially improve the substitute level of clinker with desirable mechanical properties, the water demand is higher than that for ordinary mortars, thus casting is performed following the consistency of cement mortars, resulting in a reduction in strength at an early

age. Meanwhile, Lin et al. [113] found that the 28-day compressive strength was comparable to that of OPC pastes at a replacement rate of 30% by weight, while at a replacement rate of 45% by weight, the strength was significantly reduced, due to different reactivities from different types of calcined clay. The fineness of the individual components plays a more important role in influencing strength development than the overall fineness of the cement. The fineness of the limestone and clay fails to dynamically affect the strength, which is related to the limited availability of portlandite for the hydration of the calcined clay and limestone. While it has been reported that finer clinker particles can contribute to the strength development, because of their faster hydration, providing enough calcium ions to react with the other two components. The early hydration rate of clinker is accelerated by the rapid consumption of calcium ions in the secondary hydration stage, reducing the amount of unhydrated clinker phases [99,105]. As discussed earlier, LC3 has a shorter setting time than OPC, however, LC3 is disadvantageous because it contains many mineral admixtures which lead to an inferior early strength, especially after one day of curing. The development of strength is significantly affected by alkali degree in the cement. The early strength can be increased under a higher alkali environment, while long-term strength tends to decrease [111]. So far, there is a limited amount of research on the improvement of LC3's early strength. One study investigated the use of steam curing to improve early-age properties and found an early strength of LC3 mixture subjected to the steam-curing at 40 °C was comparable to that of concrete incorporated with a combination of ground granulated blast furnace slag (GGBS) and FA. This is because C-S-H precipitates at a higher rate at a higher temperature. The higher amount of the C-S-H increases the early-age compressive strength, although the continuous hydration reaction was retarded by the reduced reactive surface area of cement particles, which were covered by a dense C-S-H shell [114]. Another study [115]highlights the importance of the fineness of limestone, indicating that it can influence strength during an early age due to the impact on the sulphate balance of aluminate hydration and the filler effect.

There are many conflicting factors dictating the long-term durability of LC3, depending on the environment in which it is exposed to. During the pozzolanic reaction, controlled by the reactivity of clay, the ability of concrete to absorb CO_2 is reduced because of the decrease in the CH content [116]. Other than the CH content, a significant difference can also be seen in the amount of C–A–S–H phase that is formed, with the Ca/Si ratio decreasing as the amount of calcined clay increases [93]. Hemi-carboaluminate (Hc) could act as a CO_2 sink, which could alter the carbonation resistance of the LC3 binders [117]. It is expected that the conversion of carboaluminate phases to ettringite will be led by the presence of sulfate, but there is not a significant increase in the volume of solids. However, there is also evidence that these phases are susceptible to carbonation, which increases porosity significantly [117].

2.8. Magnesium Silicate Hydrate (M−S−H) Cement

The rationale for combining magnesia with Portland metakaolin cement is that Mg^{2+} can react with alumina and/or silica phases. One well-known binder system is magnesium silicate hydrate (M-S-H) based binders, in which M-S-H formation is enabled by the reaction between a magnesium (e.g. magnesium oxide (MgO)) and silica (e.g. silica fume or microsilica) source within a MgO-SiO_2-H_2O system. According to Zhang et al. [118], the MgO-SiO_2-H_2O system forms brucite ($Mg(OH)_2$) and M-S-H gel as hydration products. In these systems, M-S-H can be formed from the reaction between Mg^{2+} and dissolved silica complexes. When the Mg/Si ratio (i.e. molar mass) of the reactants is between 0.75 and 1.0, M-S-H has the crystalline structure of talc ($Mg_3Si_4O_{10}(OH)_2$); while at a higher Mg/Si ratio, M-S-H structure is related to serpentine ($Mg_3Si_2O_5(OH)_4$), as shown in Equations 2.26-27 [119-121]. Along with M-S-H gel, brucite ($Mg(OH)_2$) is also reported as a hydrate phase in MgO-SiO_2 mixtures, albeit resulting in lower strength [122]. In several studies [118,123,124], it has been demonstrated that the strength development of M-S-H binders is slow. Because of its cementitious properties and low pH values, M-S-H can be favourable in different applications such as castables and waste encapsulation, as well as combining the use of fibres to develop strain-

hardening composites. It can also be used for the replacement of cement in concrete blocks and building partitions that do not require high strength.

$$3Mg^{2+} + 6OH^- + 4SiO_2 \rightarrow Mg_3Si_4O_{10}(OH)_2 + 2H_2O \qquad (2.26)$$

$$3Mg^{2+} + 6OH^- + 2SiO_2 \rightarrow Mg_3Si2O5(OH)_4 + H_2O \qquad (2.27)$$
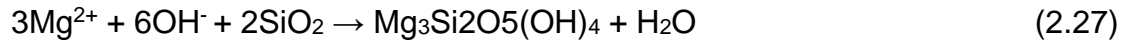
The properties of raw materials (e.g. MgO and SiO_2) are the key factors controlling the hydration process [125]. The characteristics of commercially available MgO affect the formation of M-S-H significantly, which can be enhanced via the use of highly reactive MgO sources [124,126]. In contrast, while the chemical composition and physical properties of the silica source also play a key role in the formation and properties of M-S-H, the effect of different silica sources on the performance of M-S-H-based mixes is limited. The chemical composition and physical properties of the silica source are controlled by the manufacturing process. Specifically, crystalline silica reacted only limitedly with MgO, resulting in low strength in MgO-SiO_2 mixes, whereas amorphous silica reacted more vigorously and developed greater strength. This limited strength development is because of a pure interaction between MgO and crystalline silica [123].

2.9. Effects of Magnesia on Soft Clay Stabilisation

Clay solidification should be employed in the construction of road pavements because of the considerable environmental and economic benefits [127], and Portland cement is one of the additives that is widely used in the clay (e.g. kaolinite) solidification. As a result, the strength of clay is greatly improved through some hydration phases (e.g. C-S-H) produced within samples [128-131]. The hydration of PC, which produces calcium silicate hydrates (C–S–H), calcium aluminate hydrates (C–A–H) and calcium aluminium silicate hydrates (C–A–S–H) is the primary mechanism of soil stabilisation by PC. However, the introduction of PC in clay solidification raises an environmental concern as PC is produced at a very high temperature (i.e. 1450 °C) and emits a large amount of CO_2 during this calcination. Some other strong alkalis were also

been chosen for clay solidification such as NaOH at a Na/Si ratio of 0.8-1, and this technique has been widely investigated and applied to road solidification in some developing countries [132-134]. Nevertheless, the production of strong alkali also accounts for heavy environmental burdens owing to its high energy consumption, even though it is introduced in clay solidification at a low dosage [135]. Moreover, lime has been widely adopted as well for clay solidification [129,136-138], and the process of clay solidification may sometimes be coupled with the incorporation of ground granulated blast-furnace slag (GGBS) into clay. For instance, Consoli et al. [139] indicated that the lowest level of lime concerning clay solidification was 3 wt.%, which led to a great improvement in both strength and stiffness of samples. In terms of the durability of clay samples, Consoli et al. also insisted that a minimum amount of 5 wt.% lime was required to ensure effective clay solidification in the long term.

Recently, another promising mineral additive, reactive magnesia has also been proposed for soil solidification [130,140-145], which is normally derived from the calcination of magnesite (i.e. $MgCO_3$) at a lower calcination temperature ranging from 700 to 1000 °C, thus its production process is more sustainable than that for PC (i.e. 1450 °C). Since soil contains a similar composition to clay, which is all alumina-silicate-rich phase, the confidence in using magnesium-based carbonates in Portland metakaolin cement is further enhanced. In addition, the involvement of magnesia in soil solidification has proved to be effective. For instance, Yi et al. [143] investigated the influence of magnesia with different reactivity on GGBS-clay samples, and they reported that the efficiency of clay solidification was greatly enhanced in the samples containing more reactive MgO, and their strength was greatly enhanced over time. Meanwhile, several studies also used CaO and MgO in soil solidification simultaneously, and Gu et al. [140] demonstrated that with an increasing MgO/CaO ratio, there was also an increment in the residual strength of clay samples subjected to various soaking regimes.

Instead of the usage of additives, some curing regimes such as high-temperature curing have also been widely accepted in soil solidification, which

has proven to be effective [134,146]. In the meantime, accelerated CO_2 curing was also adopted to solidify the contaminated soil facilitated by the use of magnesia, and the strength of contaminated soil was greatly improved with an effective stabilization of heavy metals consequently [147,148]. The steady strength development of samples through accelerated carbonation can be assigned to the formation of hydrated magnesium carbonates (HMCs) [61,149,150]. However, the carbonation process only occurs on the surface of samples, and the dense layer formed on the surface then inhibits the further procession of carbonation and the corresponding strength development of samples [61,149-152].

2.9.1. Influence of Magnesia on GGBS-Clay Systems

Yi et al. [143] investigated three types of MgO to activate GGBS. In that study, the weight ratio of MgO over GGBS (i.e. MgO/GGBS) was defined as activator content, while the GGBS content, in terms of the weight ratio of GGBS over dry clay, of 20% was chosen for all formulations investigated. Activator content varied from 0.05, 0.10, 0.20 to 0.40. A PC content, in terms of weight ratio of PC over dry clay, of 20% was made constant for all formulations. It has been found that excessive MgO would result in a negative effect on its strength performance. The strength development rate of stabilised clay was accelerated by containing appropriate MgO with high reactivity. However, GGBS-clay samples with a higher MgO content had a better pore size distribution and lower total pore volume. No brucite was detected in any of MgO-GGBS-stabilised clays, while C-S-H was detected for all of them.

2.9.2. Incorporation of Reactive Magnesia and Quicklime in Sustainable Binders for Soil Stabilisation

Gu et al. [140] investigated two model soils, a clayey soil and a slightly clayey silty sand, with four binder compositions by varying the weight ratio of MgO to CaO. A CaO to GGBS weight ratio of 3:9, MgO:CaO:GGBS weight ratio of

1.5:1.5:9, MgO:CaO:GGBS weight ratio of 2.8:0.2:9, and MgO to GGBS weight ratio of 3:9 was set for all formulations in Gu et al. [140]. Gu et al. [140] found that compressive strength of clayey soil increased with the increasing MgO/CaO ratio up to 90 days. After 56 days, the slag-stabilised soil merely activated by MgO had significantly higher strength than the other three binders. However, the amount of cementitious C-S-H gel decreased with the increasing MgO/CaO ratio of the binder because of the decreased reaction rate, which led to a more homogeneous formation of the C-S-H gel. This can also be attributed to the amount of hydrotalcite-like phases, which compacted the structure of C-S-H gel, increased with the increasing MgO/CaO ratio, and the C-S-H gel has a lower Ca/Si ratio. Additionally, the decreasing Ca/Si ratio leads to a decrease in the cohesion and strength of C–S–H gel, hence the relatively lower Ca/Si ratio may give a higher strength to the stabilised soil [153].

The increasing MgO/CaO ratio in the binder under different soaking conditions can increase the mechanical performance of soil. However, exceeded reactive MgO used in soil stabilisation may reduce the long-term strength because of the delayed hydration which can produce hydrotalcite-like phases and expansive brucite. Because of a higher pH environment produced by CaO, the hydration of the binder proceeded faster by using CaO than only using MgO in the activation.

3. Chapter 3 Materials and Methodologies

This chapter presents properties of the raw materials used in this study and experimental procedures used for the experimental work (i.e. work in Chapters 4, 5 and 6) performed on RMC mixes. The materials used are categorised as binders, aggregate and admixtures, and their essential properties are summarized in this chapter. Mechanical properties, durability, microstructure and hydration/carbonation phases were examined and elaborated.

3.1. Materials

3.1.1. Binders

(1) Reactive MgO (RM)

The reactive MgO (light-burnt MgO) used in sample preparation was sourced from Magnesia GmBH, Germany, with a purity of > 95% by weight. The specific surface area (SSA) of RM is 0.3 m^2/gram according to its supplier.

(2) Portland Cement (PC)

Type I Portland Cement (i.e. Grade 52.5) conforming to BS EN 197-1 was used for all specimens (if it was required) in this study, which was obtained from CEMEX, United Kingdom. Chemical compositions of PC obtained from the wavelength dispersive X-ray fluorescence (WDXRF) are presented in **Table. 3.1**. The XRD peak assignment of the PC used in this study was conducted. The results are shown in **Fig. 3.1**, and it was revealed that the PC contained ferrite (C_4AF), which is responsible for its dark grey color. Alite (C_3A) and Belite (C_2S) were noted to be the main phases in OPC. Hemihydrate was also present in PC, while gypsum, possibly due to dehydration of gypsum during milling, existed in PC as part of sulfate regulation. Calcite was present as a filler in PC, however, only in a minor amount, which also agreed well with

LOI (i.e. 1.48). Therefore, in Chapter 5, the majority of calcite in the LC3 binder was from limestone.

Table. 3.1 Chemical compositions (wt.%) of PC

	Chemical compositions (wt.%)									
	CaO	SiO_2	Al_2O_3	Fe_2O_3	SO_3	MgO	K_2O	Na_2O	TiO_2	LOI
PC	62.71	17.68	4.24	3.08	4.78	1.07	0.86	0.37	0.23	1.48
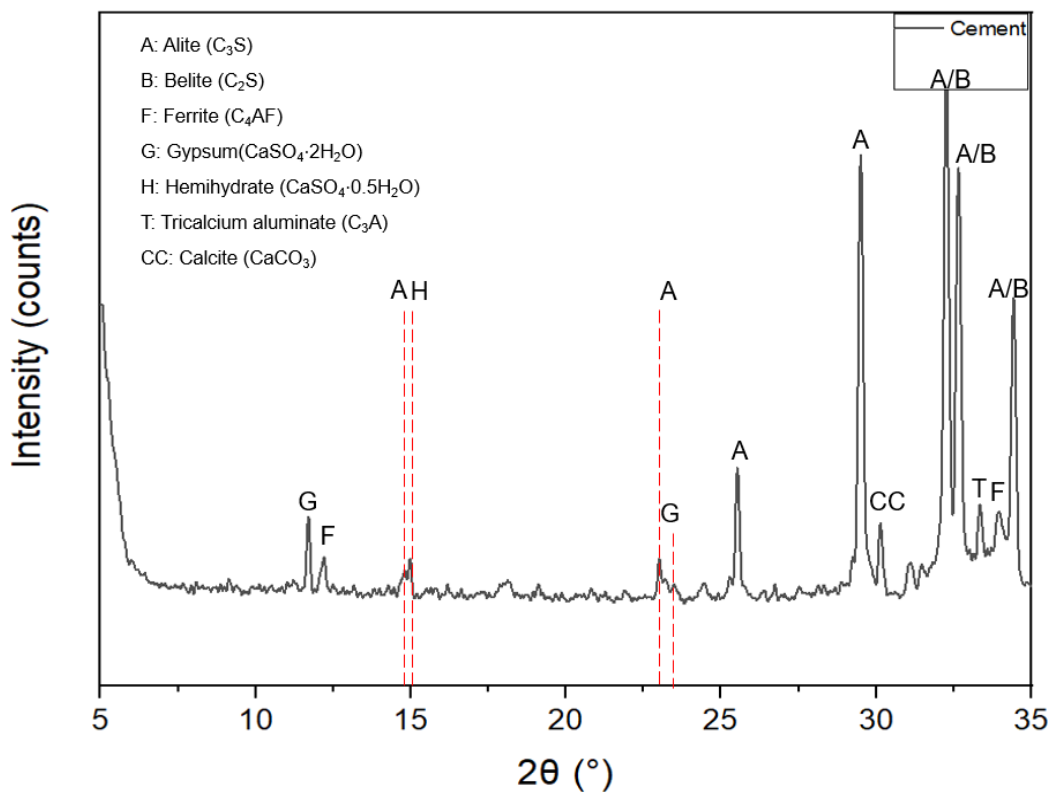
Fig. 3.1 XRD pattern of PC

(3) Quartz (Q)

A planetary ball milling machine (Retsch, PM 100, Germany) was used to grind river sand to produce quartz powders. The chemical compositions of Q acquired from the WDXRF are presented in **Table. 3.2**. Quartz was used as an inert material together with Portland metakaolin cement to simulate the ternary cement binder with non-carbonate fillers.

Table. 3.2 Chemical compositions (wt.%) of Q

	Chemical compositions (wt.%)									
	CaO	SiO$_2$	Al$_2$O$_3$	Fe$_2$O$_3$	SO$_3$	MgO	K$_2$O	Na$_2$O	TiO$_2$	LOI
Q	1.46	85.88	1.23	5.31	0.04	0.09	0.39	-	0.07	0.1

(4) Supplementary Cementitious Materials (SCMs) and Gypsum

Three types of SCMs, i.e. metakaolin (MK), and limestone (LS) and gypsum (Gyp), were acquired from BASF, Scientific Laboratory Supplies and Sigma-Aldrich, respectively, adopted for this study. The chemical compositions of MK, LS and Gyp, obtained from the WDXRF, are shown in **Table. 3.3**.

Table. 3.3 Chemical compositions (wt.%) of MK, LS, and Gyp

	Chemical compositions (wt.%)									
	CaO	SiO$_2$	Al$_2$O$_3$	Fe$_2$O$_3$	SO$_3$	MgO	K$_2$O	Na$_2$O	TiO$_2$	LOI
MK	0.03	47.89	50.24	0.27	0.04	-	0.09	0.32	1.03	1.21
LS	78.02	0.14	0.07	0.04	0.03	0.21	-	-	-	63.04
Gyp	37.68	0.08	-	-	47.07	-	-	-	-	20.91

The particle size distribution, which was obtained by laser diffraction after dispersing the powders in isopropanol, is presented in **Fig. 3.2**. Metakaolin had the finest particle size, indicating its high reactivity. Furthermore, there were no significant variations in the particle size of the ingredients used in this study.
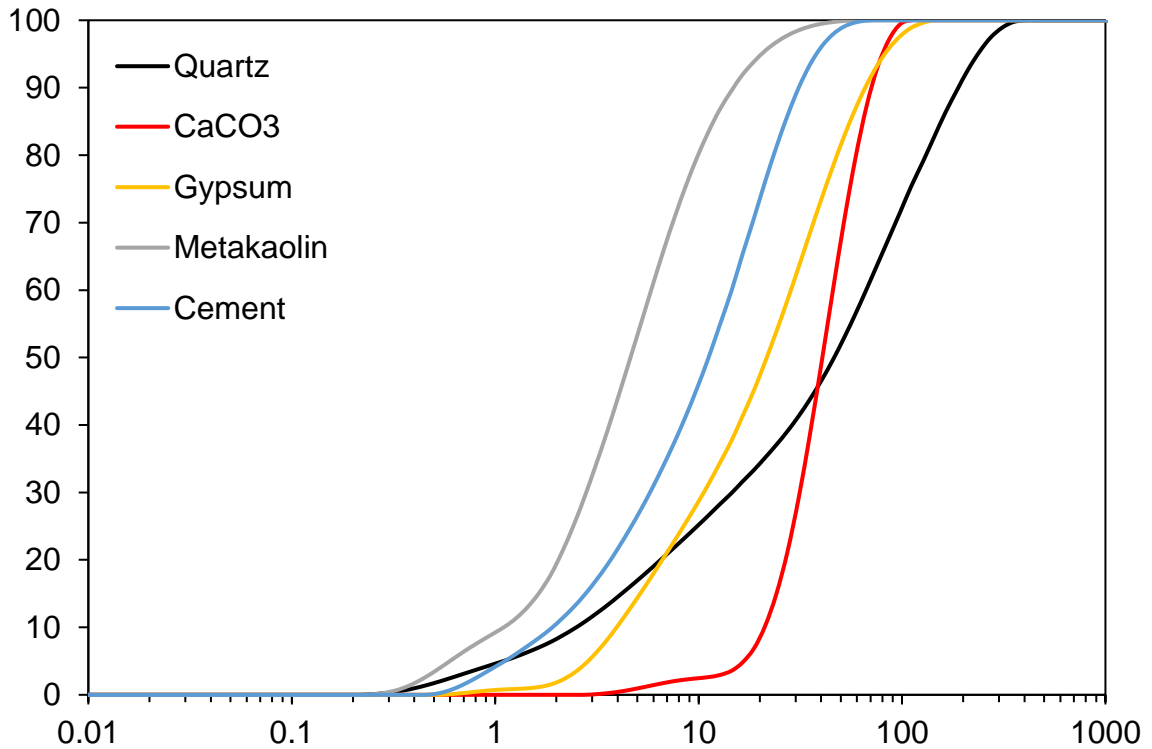
Fig. 3.2 Particle size distribution of PC, Q, K, LS, and Gyp

(5) Waste Kaolinitic Excavation Clay

The waste kaolinitic excavation clay used in this study was sourced from Poland, and its chemical formulation obtained from XRF spectrometry is shown in **Table. 3.4**. **Chapter 6** compares the effects of different additives (quicklime and magnesia) on clay solidification.

Table. 3.4 Chemical compositions (wt.%) of clay

	Chemical compositions (wt.%)								
	CaO	SiO_2	Al_2O_3	Fe_2O_3	MgO	K_2O	Na_2O	SO_3	TiO_2
Clay	1.73	61.02	18.85	7.87	3.03	3.40	1.27	0.05	1.43

(6) Quicklime (CaO)

The type and brand of quicklime for this study were Limelite NHL 3.5 acquired from Tarmac, United Kingdom. Its SSA is 0.9 cm^2/gram. Quicklime was used as a mineral additive in clay solidification.

(7) Microsilica (MS)

In construction materials, dry MS powders are used as fillers and reactive pozzolan to improve fire performance and durability. MS was supplied by Elkem, Netherland, whose chemical compositions are shown in **Table. 3.5**. In this study, MS was used to produce magnesium silicate hydrate (M−S−H) binders.

Table. 3.5 Chemical compositions (wt.%) of MS

	Chemical compositions (wt.%)								
	CaO	SiO_2	Al_2O_3	Fe_2O_3	MgO	K_2O	Na_2O	SO_3	TiO_2
MS	0.24	97.85	0.11	0.04	0.36	0.31	0.11	-	0.01

(8) Waste Glass (WG)

WG was sourced from the local municipality of Covilhã, Portugal. The exact chemical formulation, obtained from the WDXRF, is shown in **Table. 3.6**. The micro-morphology of the waste glass was examined using scanning electron microscopy (SEM) (Supra 35VP, Carl Zeiss, Germany), as shown in **Fig. 3.3**. Unlike the spherical morphology of MS, WG powders have a granulated rod-like shape.

Table. 3.6 Chemical formulations (wt.%) of WG

	Chemical compositions (wt.%)							
	CaO	SiO_2	Al_2O_3	Fe_2O_3	MgO	K_2O	Na_2O	SO_3
WG	10.04	68.71	2.12	1.48	1.76	0.77	12.44	0.33
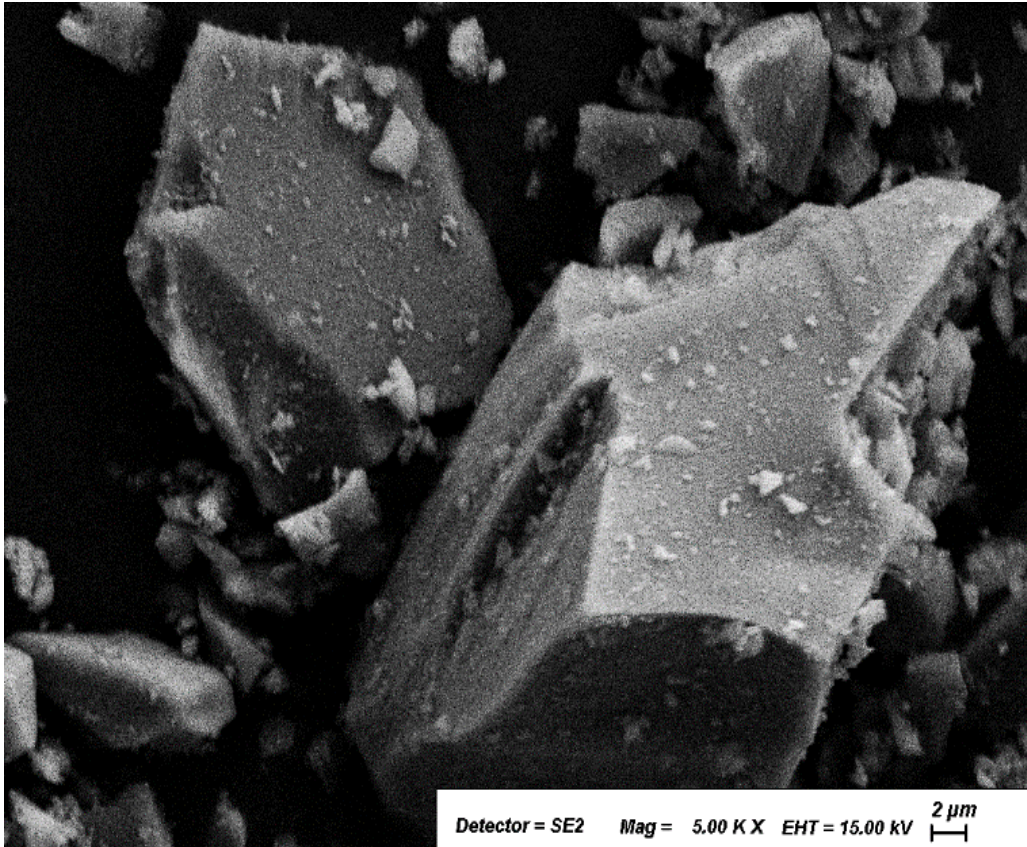
Fig. 3.3 Morphology of waste glass powders

(9) Commercial HMCs

Two different types of high-purity (i.e. ≥95%) commercial HMCs obtained from different sources (Fisher Scientific and Acros Organics) and characterized as "light" (LHMC) and "heavy" (HHMC) were included within the mixes, where light (LHMC), with the empirical formula $4MgCO_3 \cdot Mg(OH)_2 \cdot 4H_2O$, corresponds to hydromagnesite and heavy (HHMC), with the empirical formula $4MgCO_3 \cdot Mg(OH)_2 \cdot 5H_2O$, corresponds to dypingite [76].

3.1.2. Aggregate

Saturated surface dry (SSD) river sand used for making the mortars in this study was graded at a 4 mm nominal maximum aggregate size. To achieve SSD, sand was immersed in water for 24 hours, then a cotton towel was used to wipe sand until no free water on the surface.

3.1.3. Admixtures

(1) Amino Acids

To investigate the effectiveness of amino acids to control the polymorphy of hydrated magnesium carbonates (HMCs), the negatively charged L-aspartic (L-Asp) ($C_4H_7NO_4$) and positively charged L-arginine (L-Arg) ($C_6H_{14}N_4O_2$) were used in this study. They were obtained from Sigma Aldrich, United Kingdom.

(2) Superplasticizer

Polycarboxylate ether (PCE) superplasticizer is a widely used water-reducing agent in modern concrete. To achieve the same fluidity for all mortars, a commercial PCE provided by Flowaid Scc (United Kingdom) was used. The mass of PCE quoted in this study is the mass in liquid form as acquired from the supplier.

(3) Sodium Hexametaphosphate (NaHMP) ($Na(PO_3)_6$)

A specific water reducer for magnesium-based binder, namely NaHMP, obtained from Sigma-Aldrich, United Kingdom, was used to improve the rheology and reduce the water content of the fresh mix. Its molecule structure is shown in **Fig. 3.4**.
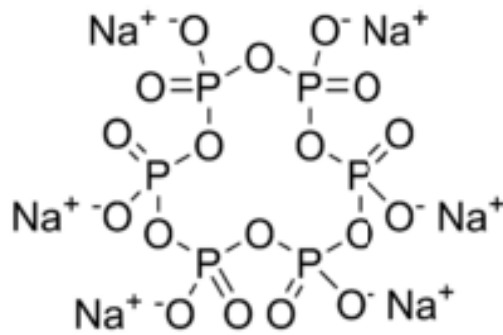
Fig. 3.4 Chemical structure of sodium hexametaphosphate

(4) Sodium Carbonate (Na$_2$CO$_3$)

Sodium carbonate and sodium bicarbonate with purity of > 99% by weight were used as a CO$_3^{2-}$ provider, supplied by Sigma-Aldrich, United Kingdom.

3.2. Methodology

3.2.1. Flowability Test

Flowability of the samples was measured conforming to BS EN 1015-3:1999 [154]. In this test, a mini slump cone is filled with fresh mortar and then removed, allowing the mortar to flow outwards. As soon as the mortar has reached a steady state, the flow table is dropped 20 times within approximately 20 seconds. Once the mortar mass has settled, the average diameter of the spread area is measured in two directions at right angles to one another using a calliper as the representative of the fluidity of the sample.

3.2.2. Compressive Strength

Compressive strength of the prepared samples was measured by Instron 5960 universal testing machine at a loading rate of 0.4 MPa/s in line with ASTM C109/C109M-13 [155]. In **Chapter 4**, compacted paste cubic samples with the dimensions of 20 x 20 x 20 mm^3 were tested at 1, 3, 7 and 14 days. In **Chapter 5**, mortar samples of 40 × 40 × 40 mm^3 were cast and their

compressive strengths were measured at 3, 7, 28 and 90 days. In **Chapter 6**, the paste was cast into cubic molds with the dimensions of 50 x 50 x 50 mm^3, compacted via a vibrating table, and trowel finished. The soil-based samples (**Section 6.2**) were subjected to compression testing at 7, 14 and 28 days, while the M-S-H samples (**Section 6.3**) were tested at 3, 7, 14, and 28 days. In all studies, the representative compressive strength was the average of the results obtained from three samples.

3.2.3. Setting Time

Setting test was conducted in **Section 6.3** to assess the engineering properties of M-S-H samples. Setting time of pastes was measured by a Vicat apparatus conforming to ASTM C191 [156]. A standard Vicat Needle was used in this study, which has a diameter of 1.0 ± 0.05 mm and a length of at least 50 mm.

3.2.4. Bulk Density

The measurement of bulk density is according to BS EN 12390-7:2019 [157]. The mass of samples was measured by a balance with a readability of 10 mg. To determine volume, the water displacement method is the most accurate and was therefore adopted in this study. The samples were put into a volumetric cylinder with water inside, and the water displacement caused by the sample was recorded, followed by calculations using actual dimensions and lastly calculations using verified dimensions. As a result, samples were weighed in triplicate at various stages of curing, and the density was calculated at each stage.

3.2.5. Porosity

The porosity of selected clay samples was obtained via Equation 3.1, which is derived from ASTM C642 [158], in which the void volume is the difference between M_{sat} and M_{dry}.

$$P = \text{Void volume/Total volume} = (M_{sat} - M_{dry})/V*100\% \qquad (3.1)$$

Where, M_{sat} is the mass of the sample saturated in water; M_{dry} is the mass of the sample dried at a temperature of 70 °C to constant mass; and V is the volume of the sample measured by an Vernier scale.

3.2.6. Carbonation

Weerdt et al. [159] used thermodynamic model to simulate the phase transition of PC under varying CO_2 concentrations. Upon CO_2 exposure, portlandite is initially identified as the first phase to carbonate, followed by the decalcification of hydration products, which corresponds to a silicate system with a pH of around 13. As carbonization continues, monocarbonate and siliceous hydrogarnet react with CO_2, leading to further decalcification of C-S-H. Ultimately, the carbonate phase stabilizes as calcite, aragonite, or zeolite, leading to the pH to drop to 10 or even lower. Therefore, phenolphthalein has often been used as a pH indicator for characterizing the carbonation depth with a sharp color demarcation at pH 8.2–8.5. To conduct carbonation, the samples cured for 28 days were split from the middle. Immediately after that, the fracture surfaces were sprayed with a layer of phenolphthalein as a carbonation indicator. The carbonation degree was determined by the ratio of the unchanged color area to the total cross-sectional area of the samples. This method was also adopted in other studies [113,160,161].

3.2.7. Particle Size Distribution

A Malvern Mastersizer 2000 Laser Diffraction Particle Size Analyzer was used to determine the particle size distribution (PSD) of the materials used in this study. Dispersion of the materials in distilled water was used in this study for characterisation. Before measuring particle size, all minerals were ultrasonically agitated for five minutes.

3.2.8. pH Value

The pH values of the sample (in **Chapter 4** and **6**) suspensions were determined at different time intervals by dispersing the powders in water under the room temperature (20 °C). After compression, the broken samples were ground to fine powders and passed a 125 μm sieve, then measured with a Mettler Toledo pH meter with an accuracy of ±0.01 according to ASTM C25-19 [162]. Before the measurement, the pH meter was calibrated by dipping the clean electrode into the pH buffer solution (Neutral pH 7.00) and waiting for the meter to stabilize. Then, rinse the electrode with distilled water and repeat the calibration process with the second buffer (pH 10.01). A solution of 5 grams of sample powders mixed with 100 grams of distilled water was prepared and mixed for 30 minutes before each pH measurement. All the measurements were conducted in six times and the average values were recorded as the representative quoted in the analysis. In **Chapter 4**, OH^- concentration was calculated according to the Equations 3.2-3.3. Regarding the ICP-OES results which can only show the concentration of cation, OH^- concentration was used as a supplementary result to demonstrate the whole ion condition in the binder.

$$pH = -\log [H^+] \tag{3.2}$$

$$[OH^-] = \frac{10^{-14}}{[H^+]} \tag{3.3}$$

3.2.9. Isothermal Calorimetry

To study the hydration behavior of the mixtures, an isothermal calorimeter (TAM Air, Thermometric AB, Sweden) was used at 25 °C to measure the heat flow and cumulative heat in each mixture, which was in line with ASTM C1702-17 [163]. 10 g of sample paste was poured into a glass ampoule, which was then sealed and placed in the calorimeter. To fully observe the heat evolution of each of the mixtures, it was necessary to minimize the time spent on the mixing and loading processes to less than a minute.

3.2.10. Ion Concentration

In **Chapter 4**, MgO was mixed with water, 0.1M and 0.2M of L-Asp solution, at a w/b ratio of 0.8 and then loaded into centrifuge tubes. Three centrifuge tubes were left to stand for 1, 3, 5, 7, 9 and 11 hours, respectively. The supernatant was taken and filtered through a 0.22 μm filter nozzle to obtain the original solution. To ensure that the ion concentration was distributed as far as possible in the standard curve range, the original solution was diluted 100 times and the concentration of Mg^{2+} in the diluted solution was determined by inductively coupled plasma emission spectrometry (ICP-OES, Perkin Elmer Optima 2100 DV).

3.2.11. Spectroscopic Analysis (XRD, FTIR)

All samples were immersed in pure isopropanol for 3 hours, then moved to new isopropanol for another 24 hours immersion and followed by being dried in a vacuum oven at 40 °C for 3 days. Before spectroscopic analysis, dried samples were crushed to pass through a 125 μm sieve. The XRD patterns of all samples were obtained using a Bruker D8-Advance X-ray diffractometer with Cu Kα radiation (λ=1.5418 Å), an operational voltage of 40 kV, a current of 40 mA, and a scanning rate of 0.02° 2θ /step from 5 to 50° 2θ in **Chapter 4**, 5 to 70° 2θ in **Chapter 5**, 10 to 90° 2θ, and 5 to 80° 2θ in **Chapter 6**, respectively.

Fourier transform infrared (FTIR) analysis with spectral subtraction was performed in a Perkin Elmer fitted with a Specac Quest attenuated total reflectance (ATR) accessory. The curves were recorded from 800 to 1350 cm^{-1} with a 2 cm^{-1} resolution, and a scan count of 32 at a scanning rate of 5 kHz. The spectra are used to identify the specific bonds that correspond to phases present in the samples.

3.2.12. Thermogravimetric Analysis

Thermogravimetric analysis/derivative thermogravimetry (TG/DTG) was conducted on a TA instrument TGA 4000 equipment from 20 to 1000 °C with 10 °C /min under nitrogen flow. The DTG curves were deconvoluted using the Gaussian area deconvolution method to quantify the number of products during thermal decomposition at each step of the process.

3.2.13. SEM

Scanning electron microscopes (SEMs) are used to analyze morphology and composition in this study. A Zeiss Supra 35VP SEM was used to obtain Secondary electron (SE) images, and then the images were further assessed by using an energy-dispersive X-ray (EDX) analyzer (EDAX). Before the SEM analysis, samples were broken into smaller pieces and then dried for a few days to make sure all the moisture was removed. Once ready, a double-sided adhesive carbon disk was used to mount small pieces from each mix onto aluminum stubs, and were sputter-coated with gold before being placed into the microscope. In Chapter 6, the backscattered secondary electron (BSE) images were acquired using a Zeiss Supra 35VP SEM, facilitated by the use of an energy-dispersive X-ray (EDX) analyzer. The sample slices of 5 mm were impregnated with ultralow-viscosity resin and polished by a series of graded polishing papers and diamond paste, and the grinder used in this study was PlanarMet 300 from Buehler Esslingen, Germany.

4. Chapter 4 Performance-Controlling Additives in Magnesium-Based Binder: Hydration and Carbonation

4.1. Introduction

Under appropriate curing conditions, MgO can react with CO_2 and water to produce a range of hydrated magnesium carbonates (HMCs), mainly nesquehonite ($MgCO_3 \cdot 3H_2O$), hydromagnesite ($4MgCO_3 \cdot Mg(OH)_2 \cdot 4H_2O$), artinite ($Mg_2(CO_3)(OH)_2 \cdot 3H_2O$), and dypingite ($4MgCO_3 \cdot Mg(OH)_2 \cdot 5H_2O$), which can act as the main binding phases to enable the matrix to gain strength. The magnesium-based carbonates show higher compressive strength, compared with the calcium-based binder. The morphologies of magnesium-based carbonates and calcium carbonate are different (needle-like v.s. plate-like morphology), which may affect the strength development [39]. Additionally, the magnesium-based carbonates also exhibit better cementing properties [61], and stronger resistance to acid and sulphate attacks [173] than the calcium-based carbonates, which are the main binder in PC mixes. Thereby, a recent rise of interest in the carbonation of magnesia is led by these advantages.

Nesquehonite normally can be found in alkaline soils, caves and weathering products of ultramafic rocks as a low-temperature carbonate. A problem with this formation is its instability at temperatures above 50 °C, as a result, nesquehonite is converted into more thermodynamically stable forms of HMC, such as dypingite or hydromagnesite [76,174].

According to previous studies, the hydration of reactive magnesia cement (RMC) can be improved by the addition of hydration agents (e.g. HCl, $MgCl_2$ and $(CH_3COO)_2Mg$) [46,56,63,73]. In terms of $MgCl_2$ and $(CH_3COO)_2Mg$, Cl^- and CH_3COO^- can migrate Mg^{2+} ions in binders away from their original particles and precipitate in the bulk solution to form brucite without covering the unhydrated particles [73]. Alternatively, introducing HCl decreased the pH value of the solution, creating a weak alkalinity environment, which improved

the solubility of $Mg(OH)_2$ on the surface layer of MgO, thereby allowing the formed brucite to move away from the original particles [73]. However, few studies reported the additives that can control the polymorphs or modify the morphologies of RMC. It is a novel concept to control the phase polymorphs of hydrated and carbonated magnesia composites with organic matrices, while this method has been widely applied to control the properties and polymorphs of $CaCO_3$, specifically, to stabilize typically metastable calcium carbonate polymorphs including aragonite, vaterite, and amorphous calcium carbonate (ACC) [175].

Amino acids are hypothesized to enable the enhancement of the performance of these composites. Amino acids could be used as an agent because of their ability to enhance the concentrations of Mg^{2+} and CO_3^{2-}, which leads to the formation of HMCs at early ages and facilitate carbonation to continue during later ages. A major advantage of amino acids as hydration agents lies in their ability to lead to the formation of HMCs at an early age and then facilitate the continuation of carbonation at late ages.

4.2. Impact of Amino Acids as Performance-Controlling Additives on Hydration of Reactive MgO

4.2.1. Introduction

This section only aims to investigate the impact of amino acids on the hydration of MgO before the investigation of the carbonation of MgO. The mechanical performance of samples up to 14 days was investigated, and the results were further interpreted by pH measurement and characterization analysis including X-ray Diffraction (XRD), scanning electron microscopy (SEM)-Energy-dispersive X-ray spectroscopy (EDX), thermogravimetry (TG) - differential thermogravimetry (DTG) and inductively coupled plasma optical emission spectrometry (ICP-OES).

4.2.2. Mix Compositions, Sample Preparation and Curing Conditions

Two types of samples were cast for the study of carbonation and hydration of MgO. (1) The thin sheet paste samples (thickness less than 2 mm) were prepared and used to investigate the HMC polymorph formation and evolution over time during carbonation. (2) The compacted paste cubic samples (20*20*20 mm^3) were used for measuring compressive strength.

Two L-Asp-containing solutions (0.1M and 0.2M) were prepared by mixing dry L-Asp with deionized water. MgO powders were then hand-mixed with the solutions for 5 min at a liquid (water or solution)/solid ratio (l/s) of 0.8. A control group was selected by mixing MgO with deionized water without L-Asp. These pastes were spread on a plastic film with a thickness of less than 2 mm and then subjected to ambient curing.

In ambient curing regime, the samples were placed in the environmental chamber to investigate the effects of L-Arg and L-Asp on the hydration of MgO with an ambient temperature of 25 °C) and ambient CO_2 concentration of 0.041 *vol.*% CO_2). The relative humidity (RH) was maintained at 95% to accelerate the hydration of MgO. The mix formulations of all groups studied and their curing regimes are shown in **Table. 4.1**. Hydrated thin pastes were removed from the chamber at intervals of 1, 3, 7, and 14 days. Then the samples were placed in isopropanol for another 7 days to arrest the hydration. Subsequently, the samples were dried at 30 °C to remove the solvent and then milled into powder using a mortar pestle. RM paste with an l/b ratio of 0.8 by weight was prepared and then poured into 20×20×20 mm^3 cubic moulds. Immediately after casting, the cubic samples in moulds were placed for 1 day in the same environmental chamber employed for curing thin paste samples. Then the cubic samples were demoulded and continued to cure in the environmental chamber up to the designated testing ages.

Table. 4.1 Mix formulations of MgO samples (wt.%) and curing regimes used in this study

Group	MgO	L-Asp	l/b ratio	Curing regimes
C-A	100 %	0	0.8	Ambient curing
0.1M-A	100 %	0.1 M	0.8	Ambient curing
0.2M-A	100 %	0.2 M	0.8	Ambient curing

4.2.3. Results and Discussion

4.2.3.1. XRD

Fig. 4.1 and **Fig. 4.2** show the MgO matrixes hydrated for up to 14 days with and without amino acids. Despite the involvement of amino acids, the observed phases are brucite ($Mg(OH)_2$) and unreacted MgO (Periclase) in all samples. It should be noted that even without carbonation curing, there is still a small amount of HMCs (i.e. 29.5° 2θ) in the samples, which can be attributed to the reaction between MgO and the CO_2 in the air. In terms of L-Arg samples, the intensity of brucite peaks decreased with the increasing concentration of L-Arg before 7 days, demonstrating that the addition of L-Arg hinders the hydration of MgO at the first 7 days. As there was no new product formed, amino acid only works as an inhibitor in the binders. However, this inhibiting effect began to weaken after 7 days and disappeared completely by 14 days. The amount of brucite was very close to that in all other batches at 14 days, which demonstrates the futility of L-Arg as an inhibitor.

Different from L-Arg samples, the intensity of brucite peaks decreased with the increasing concentration of L-Asp at all ages, showing that the addition of L-Asp obstructs the hydration of MgO during all ages. There was little MgO phase present in all batches after 14 days, which is the evidence that the samples were mostly hydrated. Another interesting finding is that the intensity of brucite peaks was still low in L-Asp samples, while the periclase (MgO) peaks were negligible in all groups after 7 days, which indicates the limited formation of brucite in the samples containing L-Asp though the MgO was

highly dissolved. Moreover, the amorphousness of brucite increased with the increasing concentration of L-Asp, as determined by the observation in all curing regimes where the peaks became broader as the concentration of L-Asp additive increased. Compared to control samples, L-Asp-containing samples have lower amounts brucite with the lower crystalline, which could be attributed to the combination of the negatively charged L-Asp and Mg^{2+}. Contrary to L-Asp-containing samples, L-Arg-containing samples show no differences in shape, compared to the control group, which shows that the hydration products are crystalline. Therefore, because of the outstanding impact of L-Asp on the hydration of MgO, L-Asp was selected as the benchmark amino acid in a later investigation.
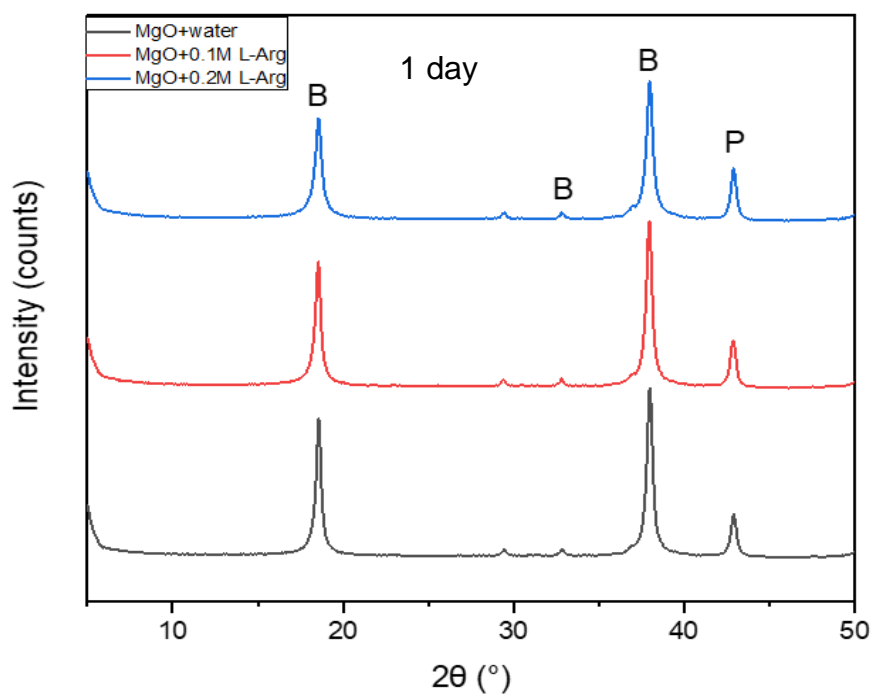
(a)
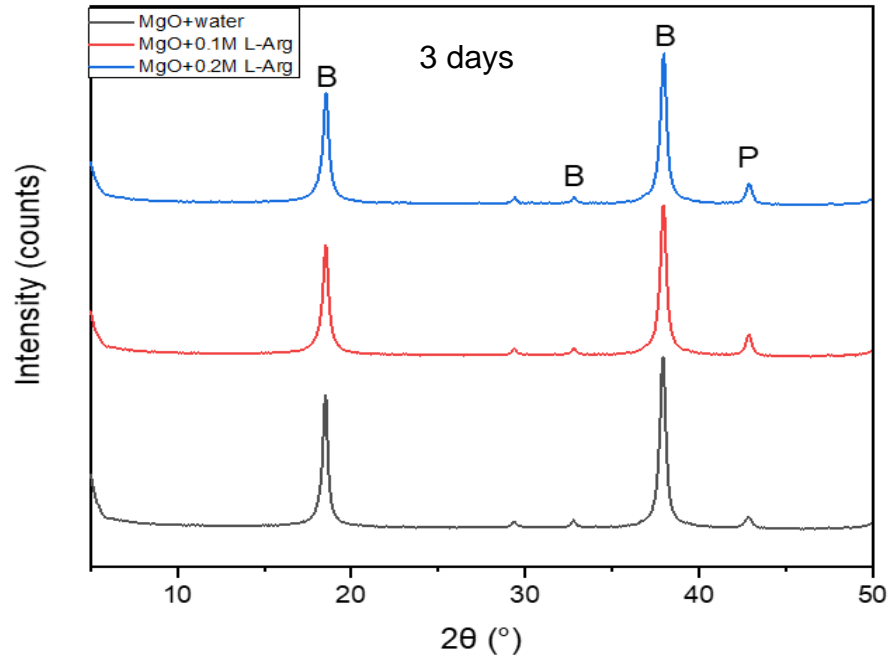
(b)
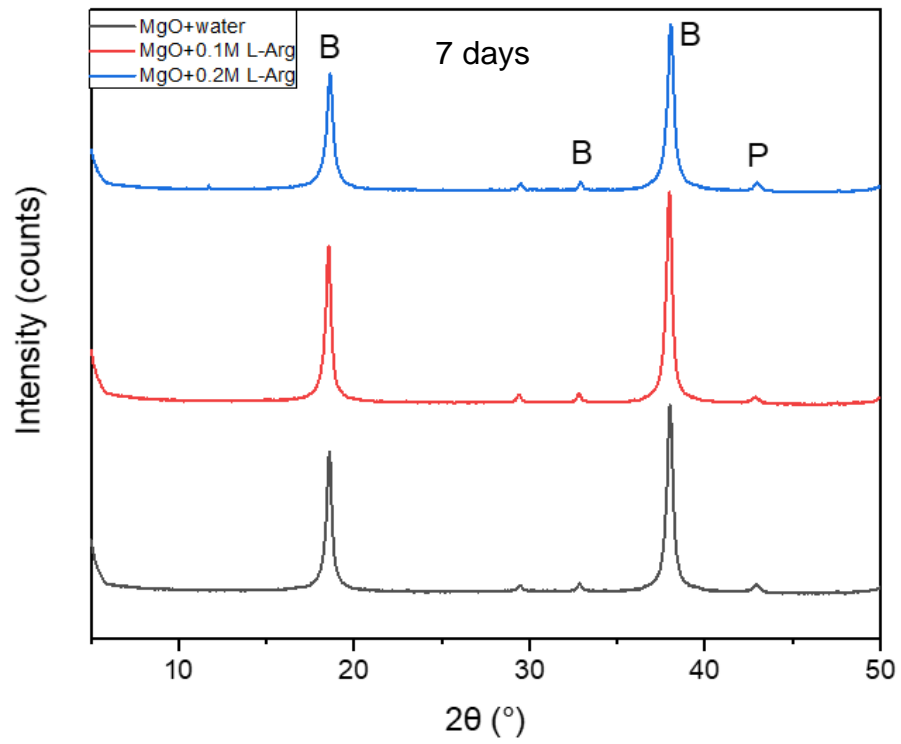
(c)
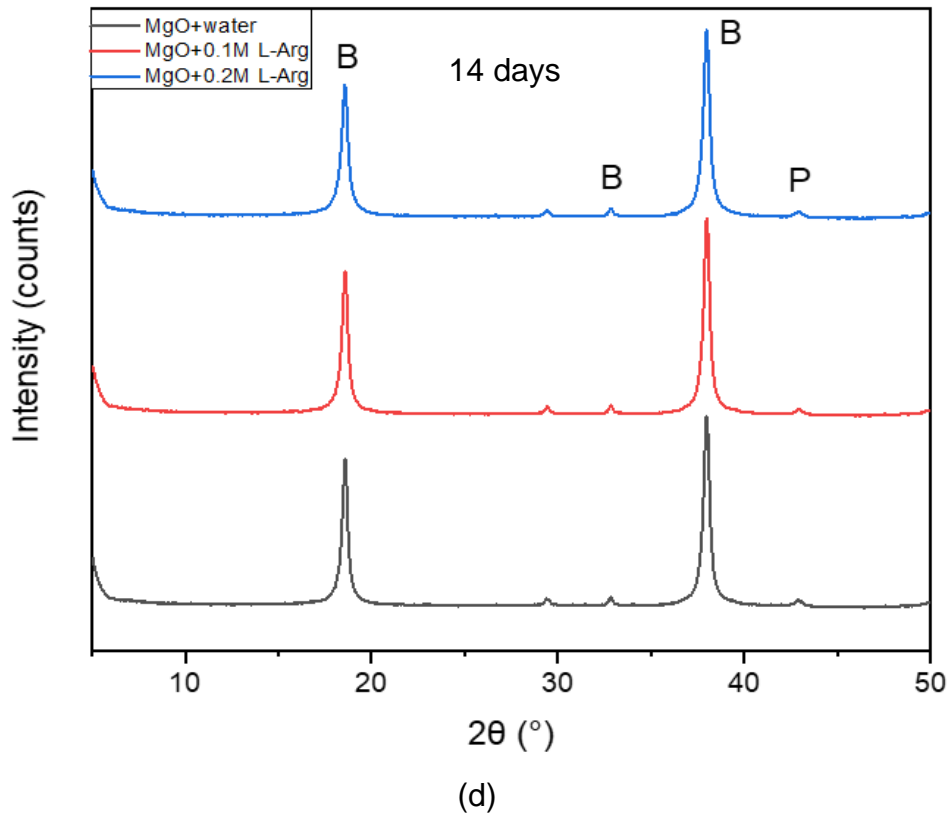
Fig. 4.1 X-ray Diffraction patterns showing the effects of L-Arg on the hydration of MgO after (a) 1; (b) 3; (c) 7; and (d) 14 days of ambient curing (B: Brucite ($Mg(OH)_2$)); P: Periclase (MgO))
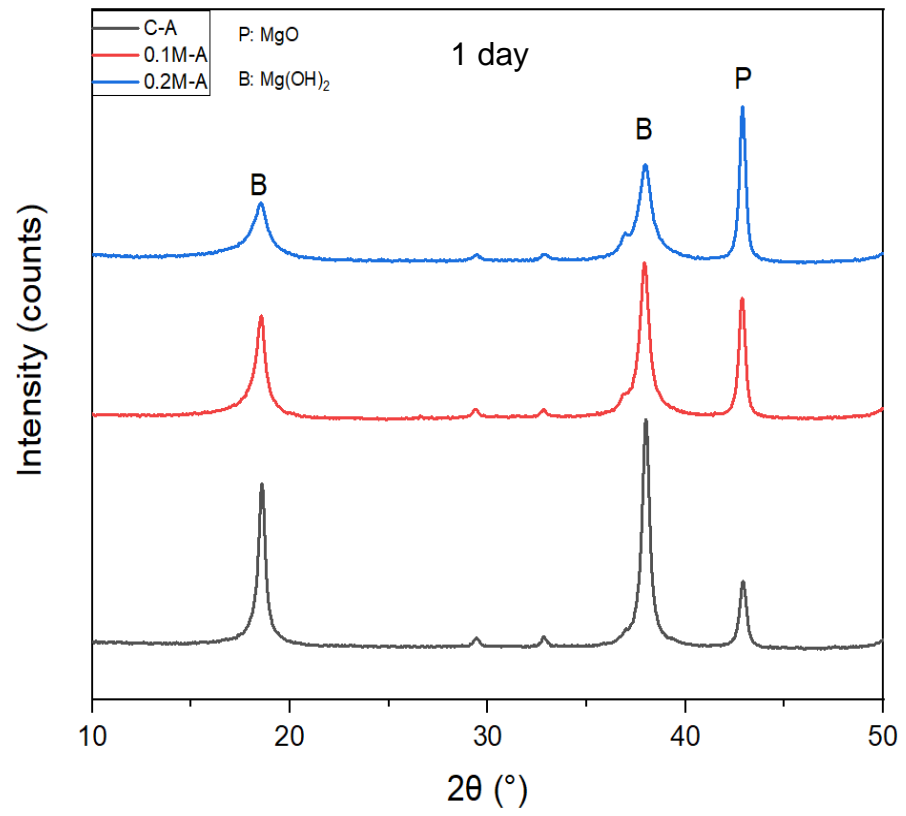
(a)
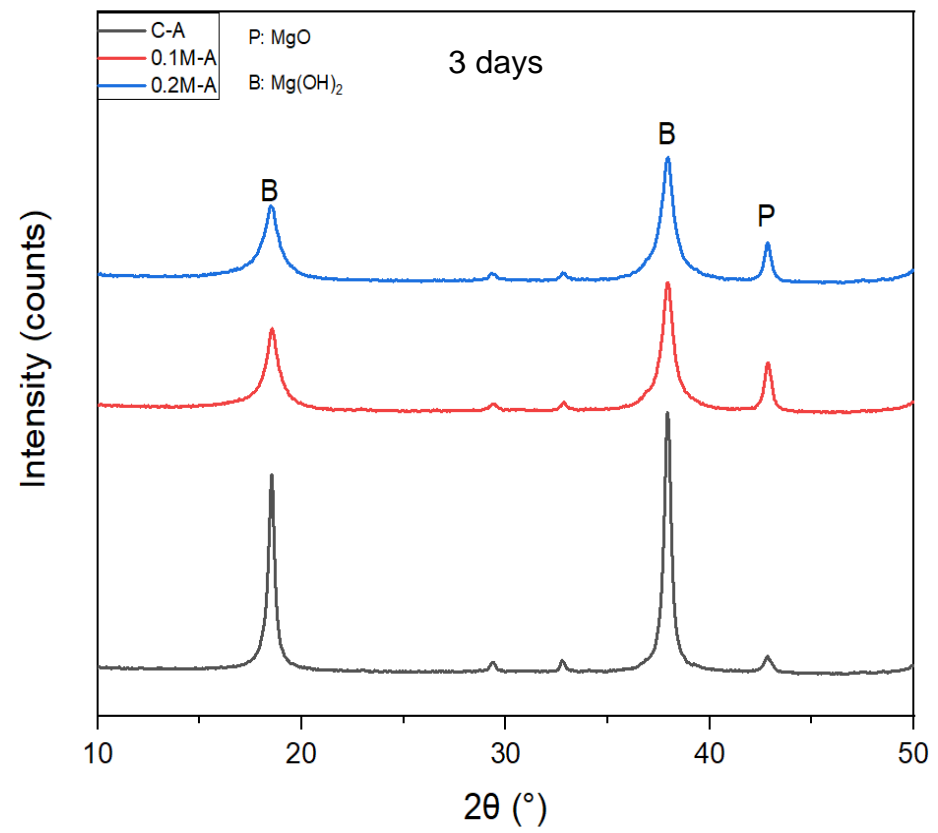
(b)
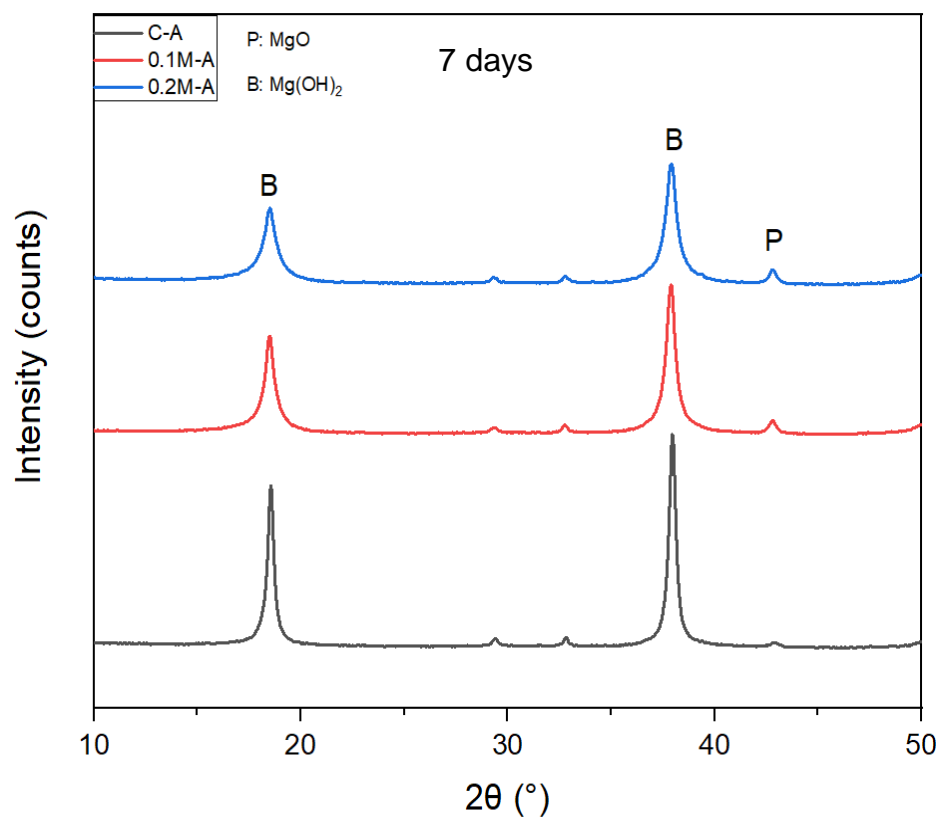
(c)
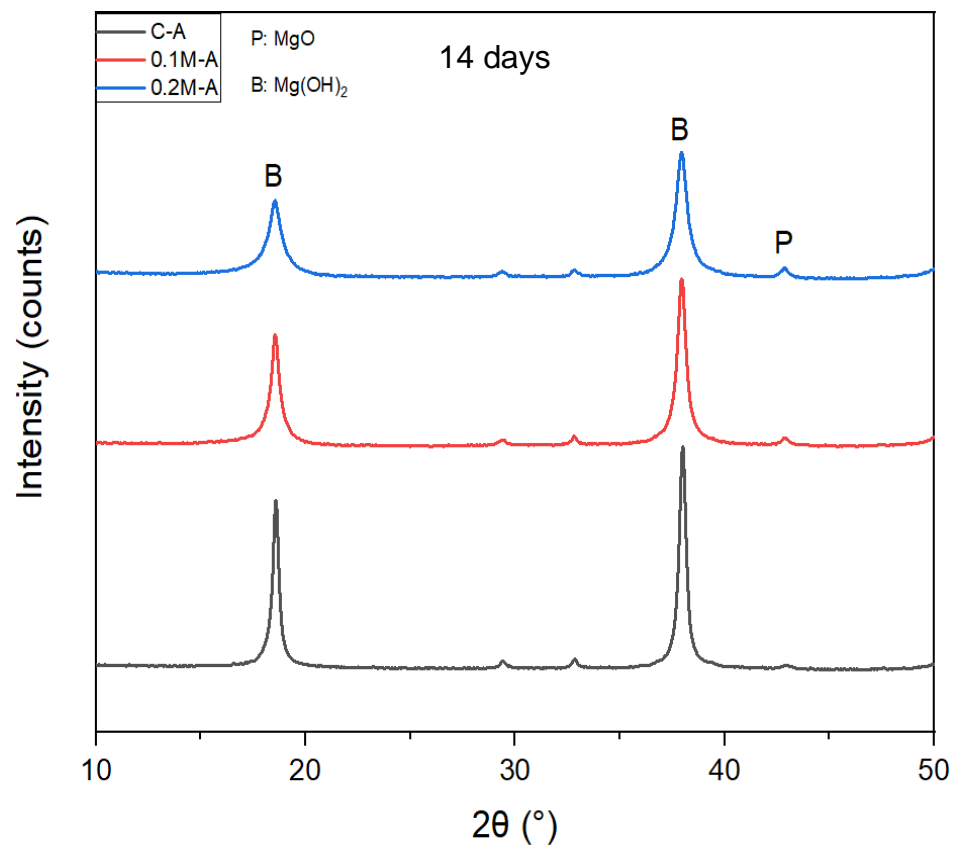
(d)

Fig. 4.2 X-ray Diffraction patterns showing the effects of L-Asp on the hydration of MgO after (a) 1; (b) 3; (c) 7; and (d) 14 days of ambient curing (B: Brucite (Mg(OH)$_2$); P: Periclase (MgO))

4.2.3.2. pH Value

The pH values and OH$^-$ concentration of sample suspensions are presented in **Fig. 4.3**. While a pure MgO suspension usually stabilizes at a pH of around 10.5, the original pH value of the control batch is 10.6, which indicates the high purity of the raw material (i.e. MgO). L-Asp retarded the precipitation of OH$^-$ ions (also shown in **Fig. 4.5**), consequently, increasing the hydroxide ions concentration, creating a weak alkaline environment, and a higher pH value was observed in the L-Asp-containing samples compared to the C-A samples. It should be noted that the most distinction was found on the first day, as the pH value of 0.2M-A is 0.21 higher than that of the C-A sample, which exhibited the most effective period of L-Asp should be before 3 days, suggesting the best opportunity to carbonate the L-Asp containing MgO binder is the first day of curing. However, at 14 days, 0.1M-A and 0.2M-A samples demonstrated lower pH values than that of the C-A sample, which could be attributed to the depletion of L-Asp.
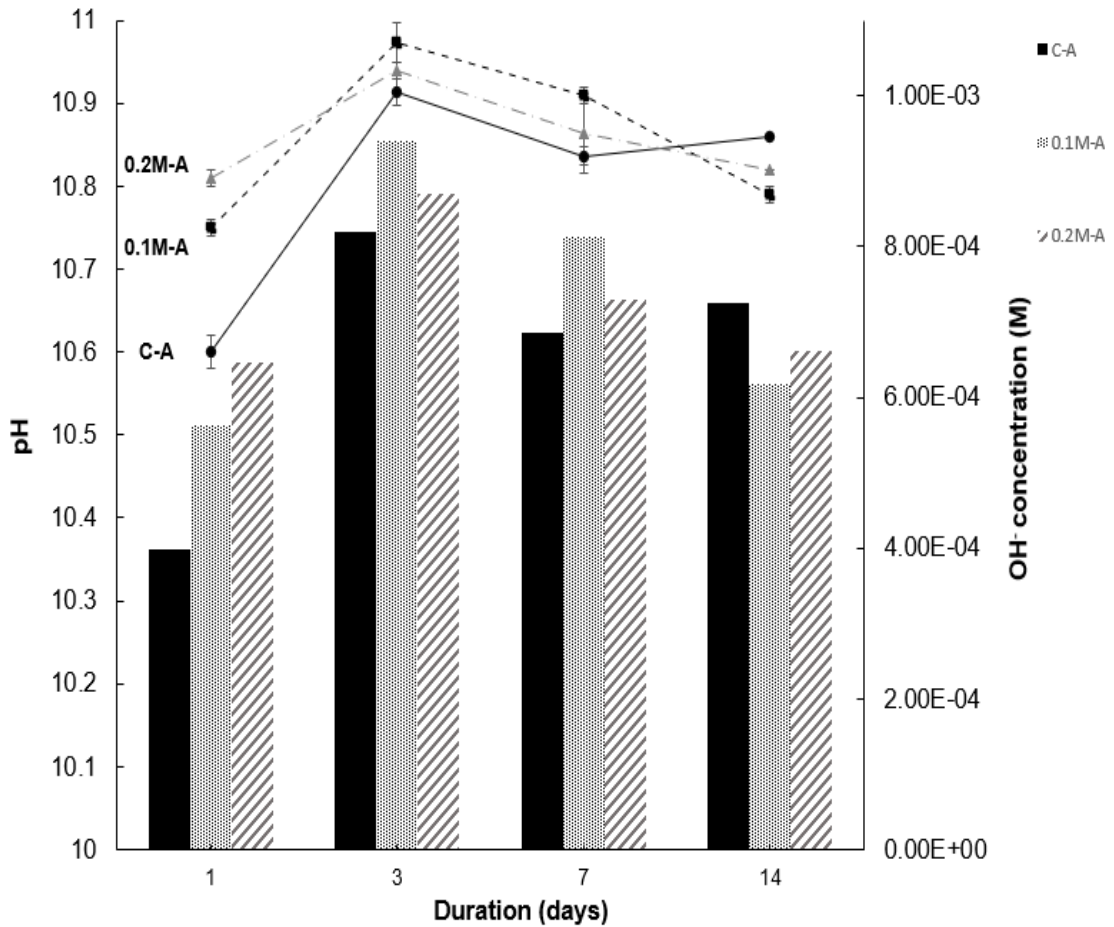
Fig. 4.3 pH values and OH⁻ concentration of all sample suspensions at 1, 3, 7, and 14 days (Lines correspond to pH values; Columns correspond to OH⁻ concentration)

4.2.3.3. Isothermal Calorimetry

Fig. 4.4 shows the heat flow released during the first 72 h of hydration in all samples. **Fig. 4.4 (a)** illustrates that the cumulative heat curve of the MgO sample slowed down approaching 36 hours of hydration, while that of two other groups of samples still kept increasing, suggesting the retardation of the hydration when L-Asp was added. According to XRD results (presented in **Section 4.2.3.1**), $Mg(OH)_2$ was the only hydration product formed in the pastes under ambient curing, therefore, the heat release of the sample is ascribed to the hydration of MgO, despite the presence of L-Asp. Using L-Asp led to two stages of hydration in samples with 0.1–0.2 M L-Asp. The first

stage of hydration displayed pre-induction peaks associated with the dissolution of RM and subsequent precipitation of brucite, which occurred during the first ~10 h of hydration. These pre-induction peaks, partially attributed to the endothermic reactions of the hydrolysis of L-Asp, were lower than the peaks of C-A samples. The low level of pre-induction peaks also indicated that the dissolution of RM in samples using the L-Asp mixture was low because of their higher initial pH when compared to the C-A samples. Between the two stages, an induction period occurred, during which the dissolved ions reached the critical concentration to form the hydration products. The second stage was the acceleration and deceleration phase which was associated with the increase in heat released from the nucleation, growth, and precipitation processes in hydration products. The higher L-Asp concentration was associated with the higher endothermic reactions in the MgO-L-Asp solution, thereby causing a delay in the appearance of peaks in the acceleration-deceleration process.

Samples C-A exhibited the most pronounced acceleration in the hydration of mixtures. Overall, the inclusion of 0.1M or 0.2M L-Asp in MgO blends increased the dormant period and enabled the appearance of the main peak at a later age (i.e. ~30 h in sample 0.1M-A and ~47 h in sample 0.2 M-A vs. ~12 h in sample C-A), resulting in an obvious retard of the hydration reaction, which is line with the XRD results (**Fig. 4.2**). However, the wider hydration peaks of the samples containing L-Asp demonstrated the enhancement of the dissolution of MgO by introducing amino acids. Nevertheless, the use of amino acids also delayed hydration by the combination of Mg^{2+} and OH^-, which will be discussed in **Section 4.2.3.8**.

(a)

(b)
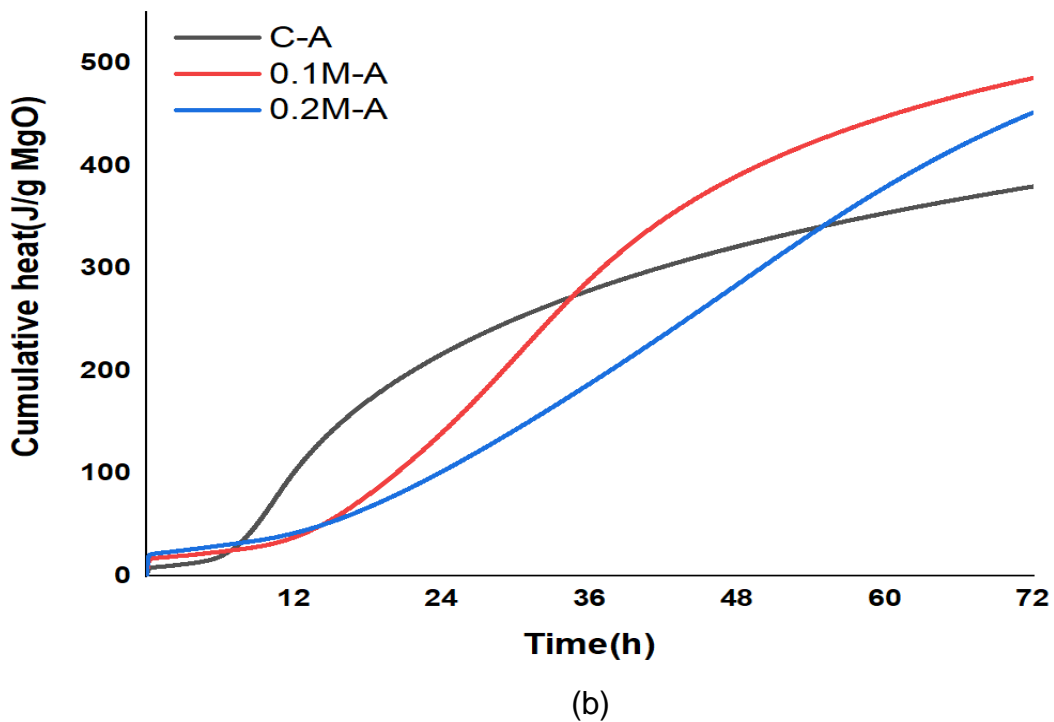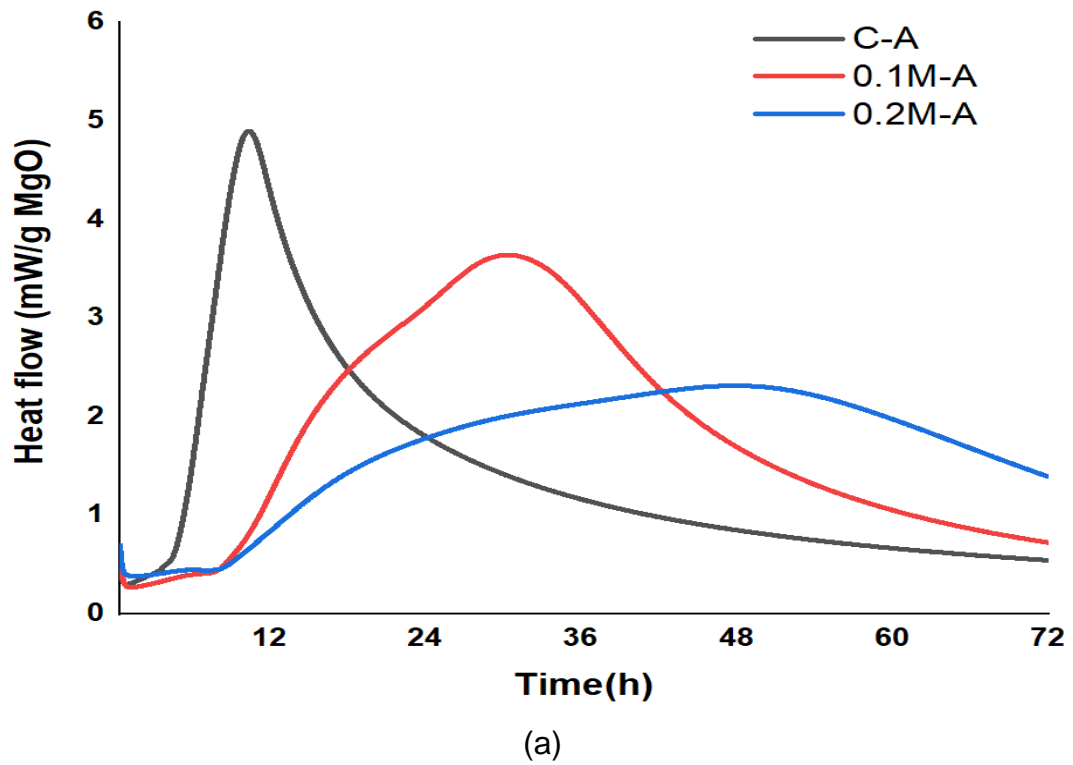
Fig. 4.4 (a) Heat flow and (b) cumulative heat of MgO paste samples with the addition of L-Asp under ambient curing

4.2.3.4. Ion Concentration

Fig. 4.5 shows the variation in Mg^{2+} concentration in the solution over the period of 1 to 11 hours of hydration. As demonstrated in **Fig. 4.2**, both 0.1M-A and 0.2M-A samples contained more unreacted MgO than the control samples, indicating the low dissolution of MgO (i.e. low Mg^{2+} in the solution theoretically). However, higher Mg^{2+} concentrations were observed in 0.1M-A and 0.2M-A samples, compared to C-A samples.The presence of L-Asp significantly increases the concentration of Mg^{2+} in solution by disturbing the precipitation of brucite. The MgO hydration process started with MgO playing an electron donator role in water, releasing OH^- anions adsorbed by the surface, which is positively charged, releasing Mg^{2+} and OH^- ions into the solution (Equations 4.1-4.3), therefore, the Mg^{2+} concentration rose. Then the precipitation of magnesium hydroxide ($Mg(OH)_2$) occurs on the surface of MgO particles, where the Mg^{2+} concentration decreased. The negatively charged carboxyl surface sites of L-Asp acid bind with Mg^{2+} sites by sharing an electron. Such a bond then inhibited further reaction between Mg^{2+} and OH^-, and the formation of brucite, which could explain the increased concentration of Mg^{2+} in the mixtures. The initial Mg^{2+} concentration of the 0.1M-A sample is 7.7 times that of the C-A sample, while the 0.2M-A sample is 14 times that of the C-A sample. The Mg^{2+} concentration in all samples deceased only after 1 hour of hydration because of the formation of brucite. However, the exhaustion of Mg^{2+} concentration occurred after approximately 4 hours of hydration in the C-A sample, while the 0.1M-A and 0.2M-A samples still contained high Mg^{2+} concentrations, suggesting that the formation of brucite was delayed by L-Asp, which agrees well with XRD and hydration heat results.

$$MgO(s) + H_2O\ (l) \rightarrow Mg(OH)^+_{surface} + OH^-(aq) \tag{4.1}$$

$$Mg(OH)^+_{surface} + OH^-(aq) \rightarrow Mg(OH)^+ \cdot OH^-_{surface} \tag{4.2}$$

$$Mg(OH)^+ \cdot OH^-_{surface} \rightarrow Mg^{2+}(aq) + 2OH^-(aq) \tag{4.3}$$
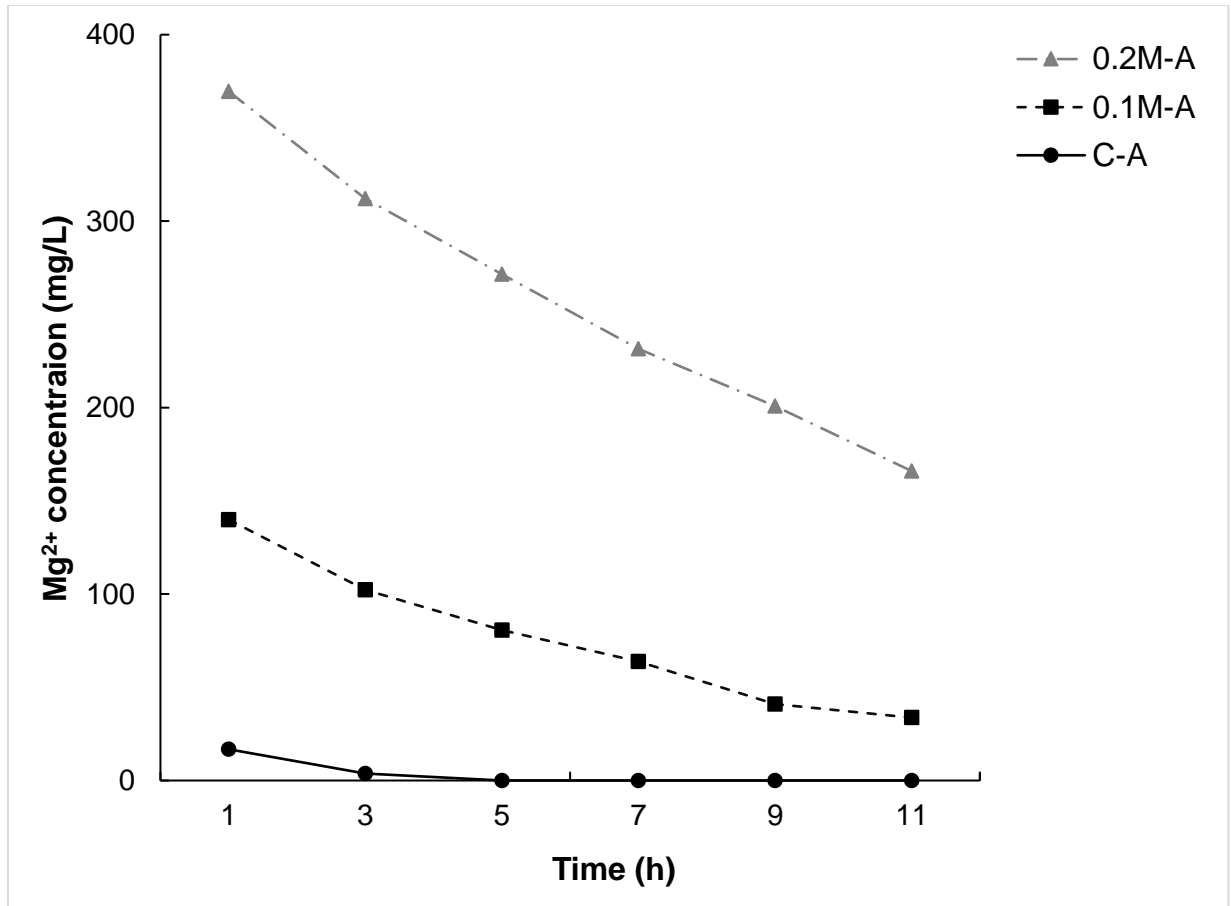
Fig. 4.5 Changes in the total Mg^{2+} concentration in suspension with hydration time for MgO in distilled water with/without L-Asp

4.2.3.5. Compressive Strength

Fig. 4.6 reveals the strength gain of paste samples versus duration during 14 days of curing. Because of limited hydration, the control sample only reached a strength of ~1.9 MPa at 1 day. This sample gained its strength with the further hydration of MgO from 1 to 14 days, reaching ~3.8 MPa at 14 days. The large error bars of 14-day strengths may be because of the small sample size, leading to greater variability in the data. However, the error bars of strengths before 14 days were minor, which indicates the reliability of the results. Samples containing 0.1 M L-Asp showed the worst strength development, reaching only around 3.2 MPa at 14 days. This poor strength could be attributed to the less hydration products compared to the control

group. Contrary to the 0.1 M L-Asp samples, compressive strengths of the 0.2M L-Asp samples were ~1.9 MPa at 1 day and increased to ~2.3 MPa at 3 days, which are similar to those of the C-A samples. Afterwards, the compressive strength of the 0.2 M L-Asp sample remained constant as the highest among all samples until 14 days, despite its limited hydration products. It should be noted that the samples were prepared with a high l/s ratio of 0.8 to accelerate the hydration of MgO, therefore, MgO-based binders do not exhibit comparable strength to PC when cured at the ambient environment. However, in the presence of desirable l/s ratio and accelerated carbonation conditions (CO_2 concentration was only 5%), brucite reacted with CO_2, resulting in blocks with a 1-day strength higher than 7 MPa [19], which meets the strength requirement of commercial concrete blocks [176]. Also, because of the low-strength nature of the brucite, the distinction of the compressive strength of all samples was not so obvious. However, more distinct differences can be seen when samples were subjected to accelerated CO_2 curing, which was depicted in **Section 4.3.3.2**. Several key factors influence the mechanical performance of brittle samples, such as the quantity of hydration phase formation, leading to reduced pores and more compacted structures. However, given the XRD patterns of the 0.2M-A and C-A samples, a higher amount of hydration phases was observed in the C-A samples compared to the 0.2M-A samples, whereas an opposite scenario was found regarding the compressive strength of the control and the 0.2 M L-Asp groups, which could be interpreted by the various morphology (i.e. amorphousness) of the hydration products formed within these two groups. However, the improved compressive strength was not observed in 0.1M-A samples, indicating that the morphology-modified effect may only act when amino acid has a higher concentration (e.g. 0.2M). Hence, for the strength of the samples investigated, it is possible that the morphology of the hydration phases in the magnesium-based binders may play a greater role than their content, and previous studies also reached a similar conclusion [39,177]. When MgO-based binders absorb CO_2, apart from HMCs, some unreacted brucite also maintains in the binders. The crystalline degree of brucite could be modified by L-Asp, contributing more to strength gain than the quantity of

brucite. Therefore, a much higher strength of the sample containing L-Asp can be expected when it is under accelerated carbonation curing.
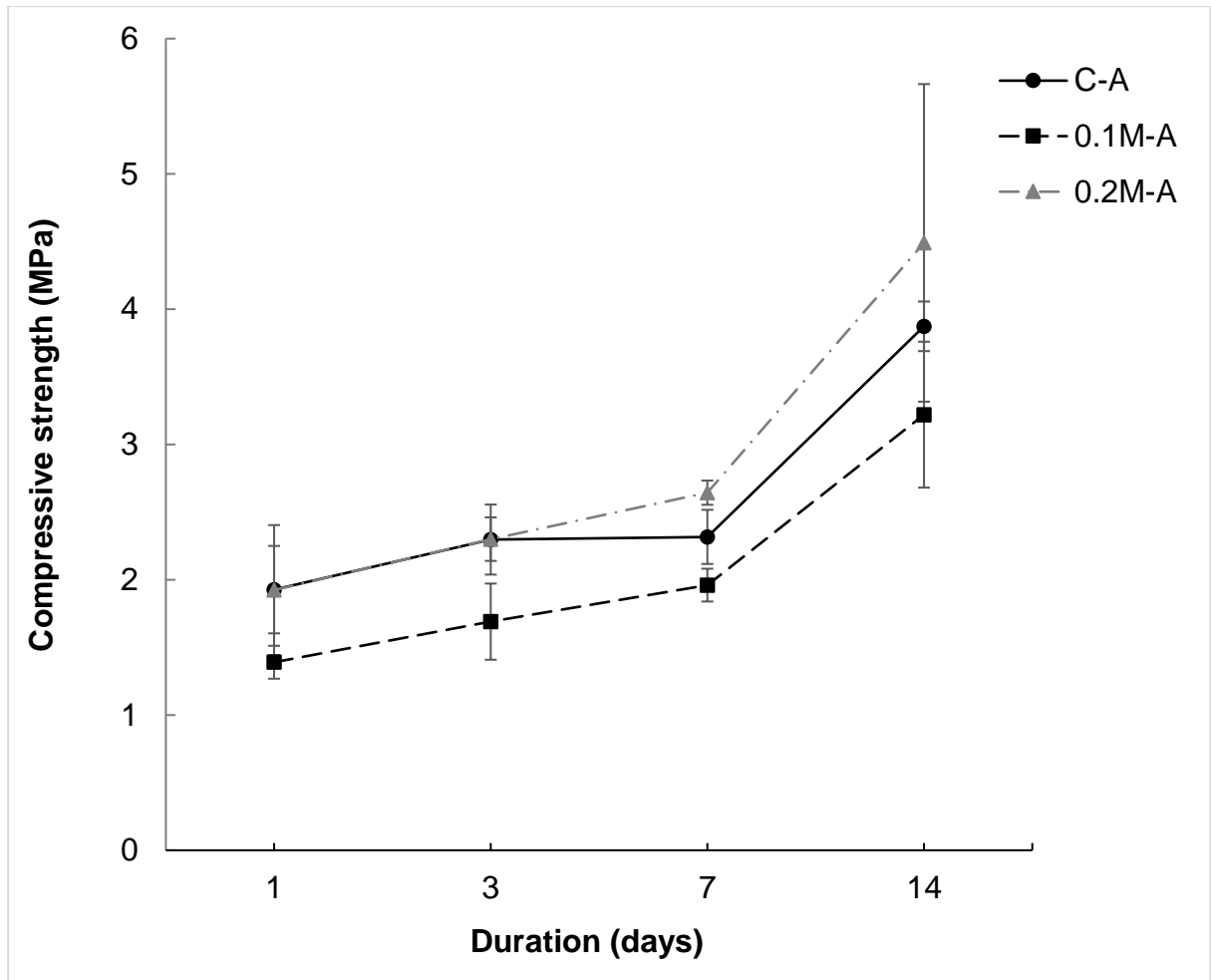
Fig. 4.6 Compressive strength of paste samples with and without L-Asp up to 14 days

4.2.3.6. TG/DTG

Fig. 4.7 shows the thermogravimetric results of all samples after 1 day of hydration. C-A samples maintained the lowest amount of residue (i.e. unhydrated MgO), suggesting they had the highest hydration degree, which agrees well with XRD results shown in **Fig. 4.2**. The TG data of all samples show multi-step weight loss for the hydration phases up to 1000 °C. To determine the decomposition temperatures of each phase, the endothermic peaks on the DTG curves were studied (**Fig. 4.8**). A strong endothermic peak

responsible for the decomposition of formed brucite was observed at around ~200–550 °C, indicating the high amount of hydration phase in the blend. According to DTG curves, the three stages of mass loss involved during thermal decomposition can be summarized as follows:

50-200 °C: Mass loss due to the loss of bonding water in the mixture.

200-550 °C: Mass loss due to the decomposition of uncarbonated brucite.

550-1000 °C: Mass loss due to decarbonation of HMCs.

As shown in **Table. 4.2**, the areas obtained by the deconvolution of DTG curves were used to calculate mass loss, which was related to the decomposition of all hydrate/carbonate phases. According to a study [78], it is hypothesised that the poorly crystalline phases in magnesia blends can be represented by the additional bonding water. The mass loss at ~ 90 °C in samples 0.1M-A and 0.2M-A were higher than that of the C-A sample, which further proves this hypothesis. Also, poorly crystalline phases in samples containing L-Asp could be observed from the XRD results (**Fig. 4.2**) and SEM images (**Fig. 4.10**). Compared to 0.1M-A and 0.2M-A samples, the C-A sample showed the highest mass loss (26% and 23.4% vs. 28.8%) at 200-550 °C, suggesting the largest amount of hydration phase (i.e. brucite), which is in line with the XRD results. Even though the C-A sample contained the most hydration products, it showed an undesirable mechanical performance, which proves that the amount of hydration phase is not the only reason to affect strength. The weight loss between 550 to 1000 °C was because of the decarbonation of HMCs, as discussed in **Section 4.2.3.1,** there was a minor amount of HMCs (i.e. indicated by the peak at 29.5° 2θ) formed in the samples, which can be attributed to the reaction between MgO and the CO_2 present in the air. The mass loss of the 0.2M-A sample (3.9%) is higher than that of the samples 0.1M-A (2.6%) and C-A (2.4%), possibly showing substantially higher carbonation degree of magnesia, which exhibits the

potential of L-Asp to improve the carbonation degree of the magnesia-based binders.
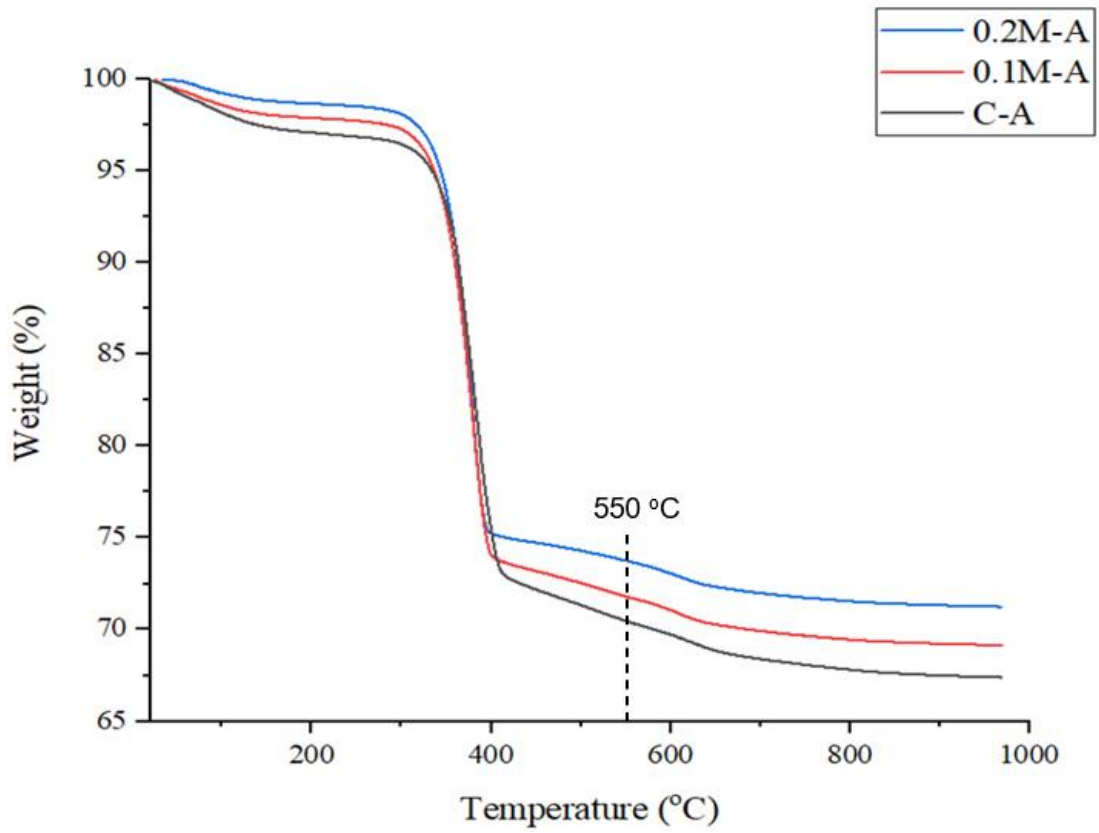
Fig. 4.7 TG results of all samples after 1 day of curing
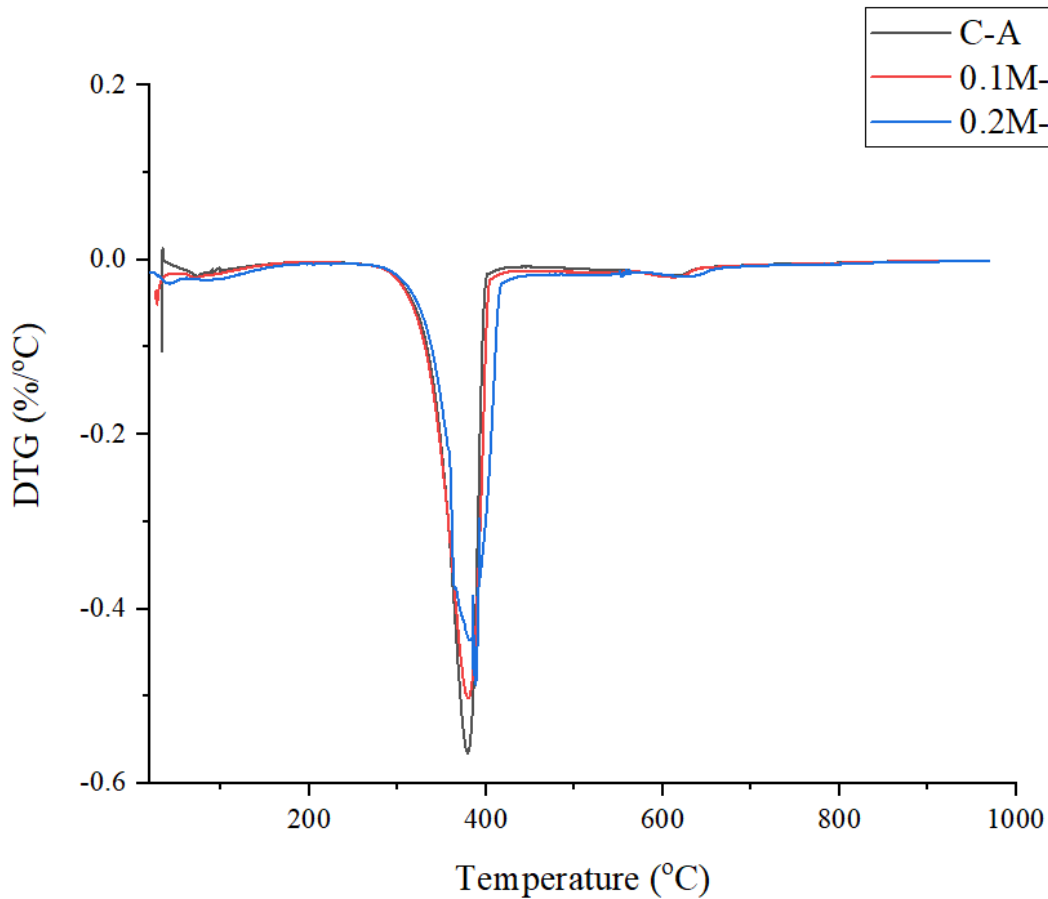
Fig. 4.8 DTG results of all samples after 1 day of curing

Table. 4.2 Mass loss (wt.%) of samples analyzed at 1 day by thermogravimetric analysis

Mixture	50-200ºC	200-550ºC	550-1000ºC
C-A	1.3	28.8	2.4
0.1M-A	2.1	26	2.6
0.2M-A	1.4	23.4	3.9

4.2.3.7. SEM

Considering the elemental spectra in **Fig. 4.9 (a)** and **(b)**, the only hydration product is brucite, which reveals the reaction of MgO under an ambient environment, and the formed hydration phases (i.e. brucite) account for its strength improvement, and the results are also in line with XRD patterns and mechanical performance. The morphologies of the hydration products of C-A and 0.2M-A samples after 14 days are shown in **Fig. 4.10 (a) (b)** and **(c) (d)**.

The morphology of brucite in 0.2M-A samples was significantly changed by L-Asp. The SEM images show different morphologies, and the hydration of the control sample formed brucite with a hexagonal crystal structure. C-A sample exhibited the lowest compressive strength because of the weak connection observed in the hexagonal brucite crystals. Interestingly, with the involvement of L-Asp, the brucite particles turned to spherical, suggesting their higher amorphousness. The noticeable improvement in compressive strength of 0.2M-A samples could be attributed to the densification of the microstructure, which is composed of hydration phases with improved morphologies.

(a)   (b)
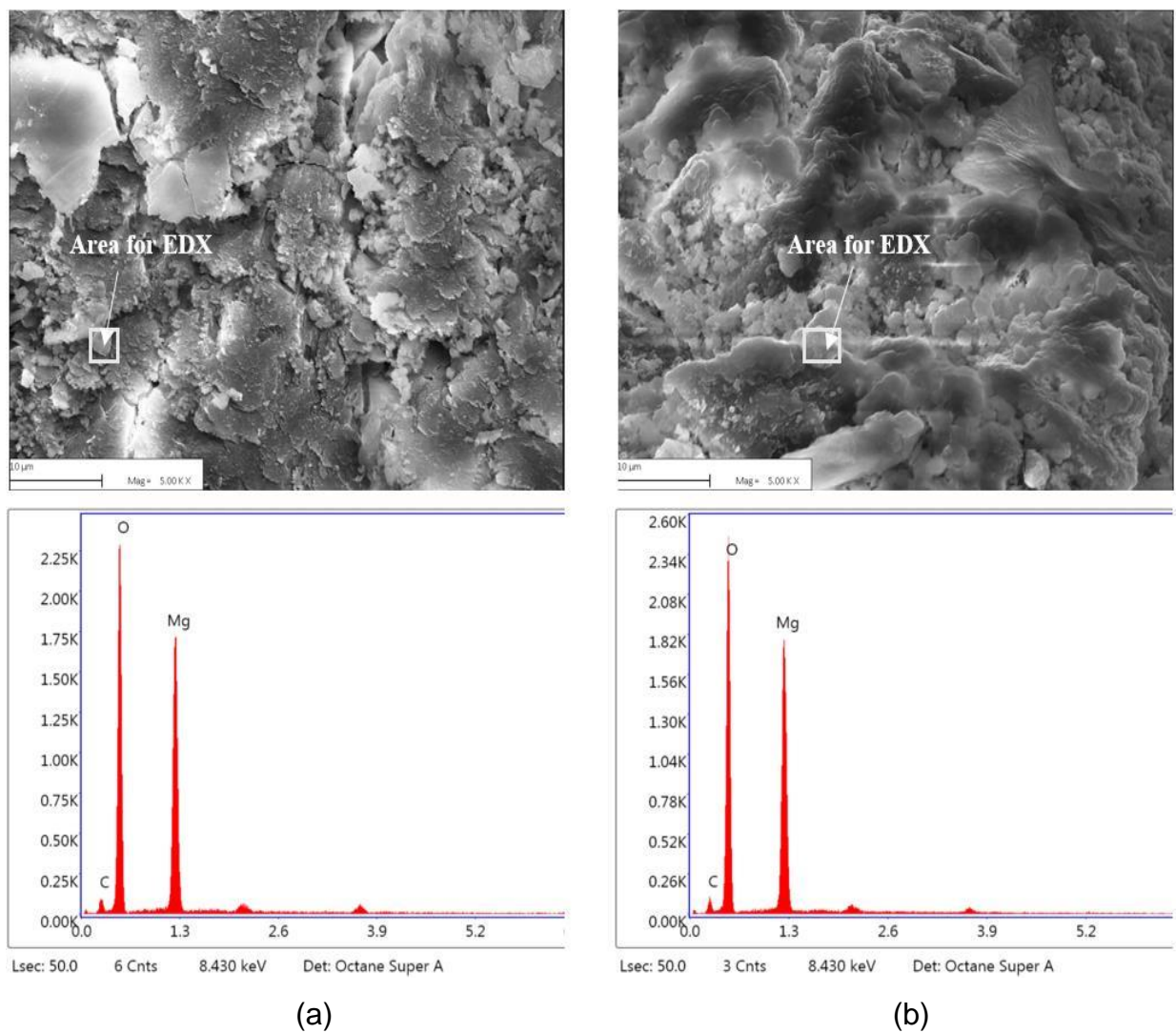
Fig. 4.9 Elemental spectra of selected areas in sample (a) C-A (magnification: x5000); and (b) 0.2M-A (magnification: x5000)

(a)

(b)

86
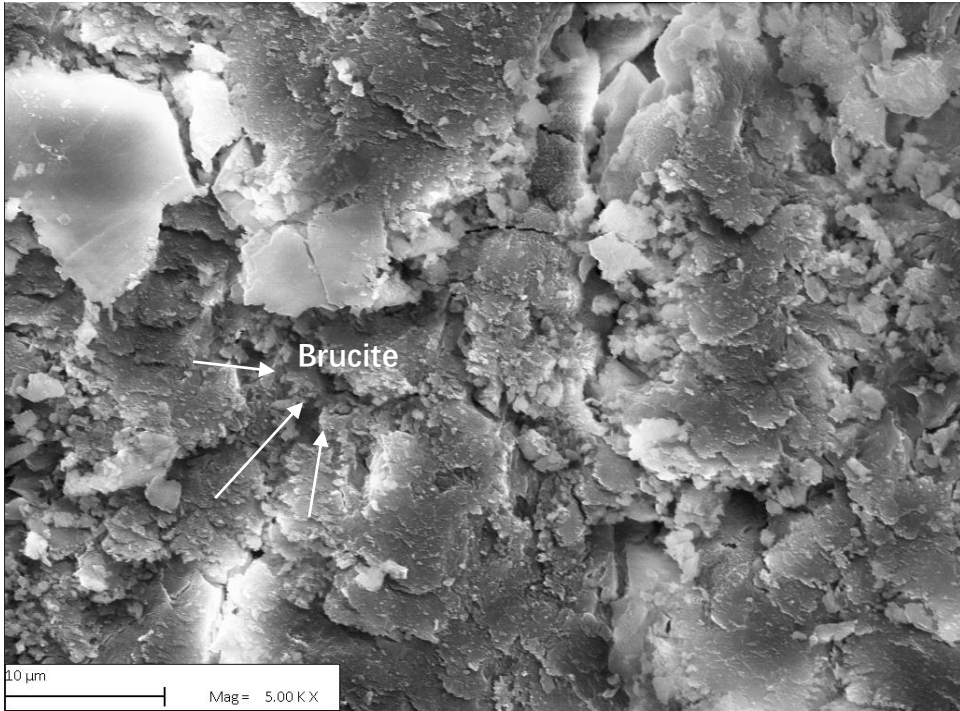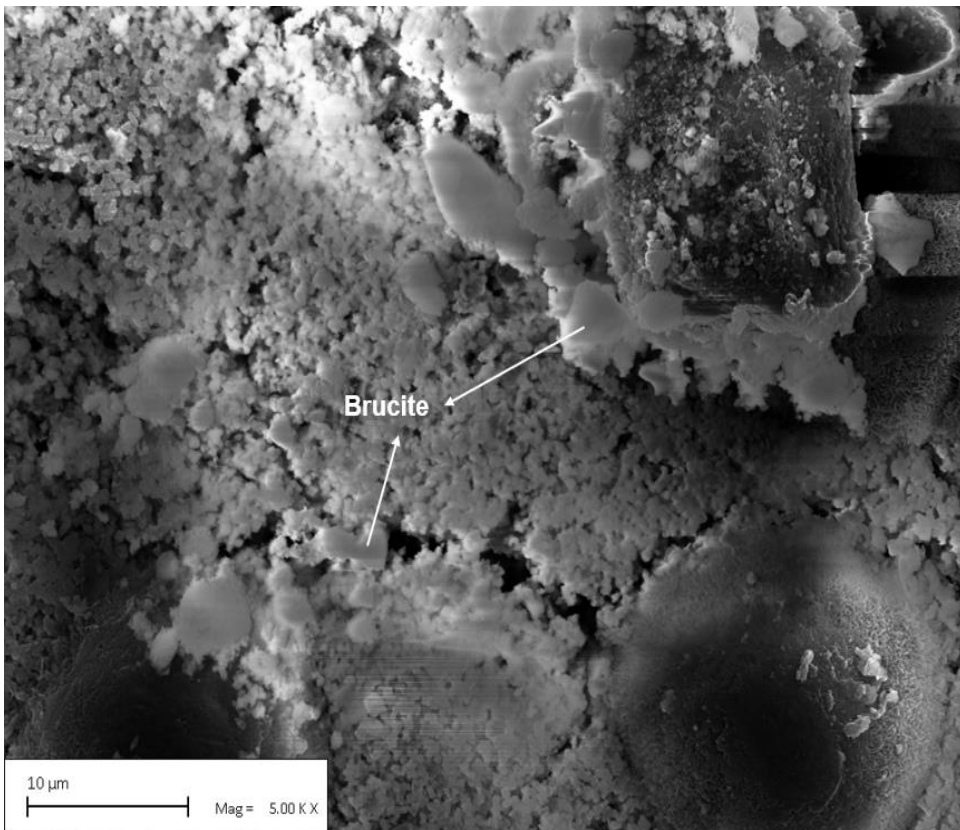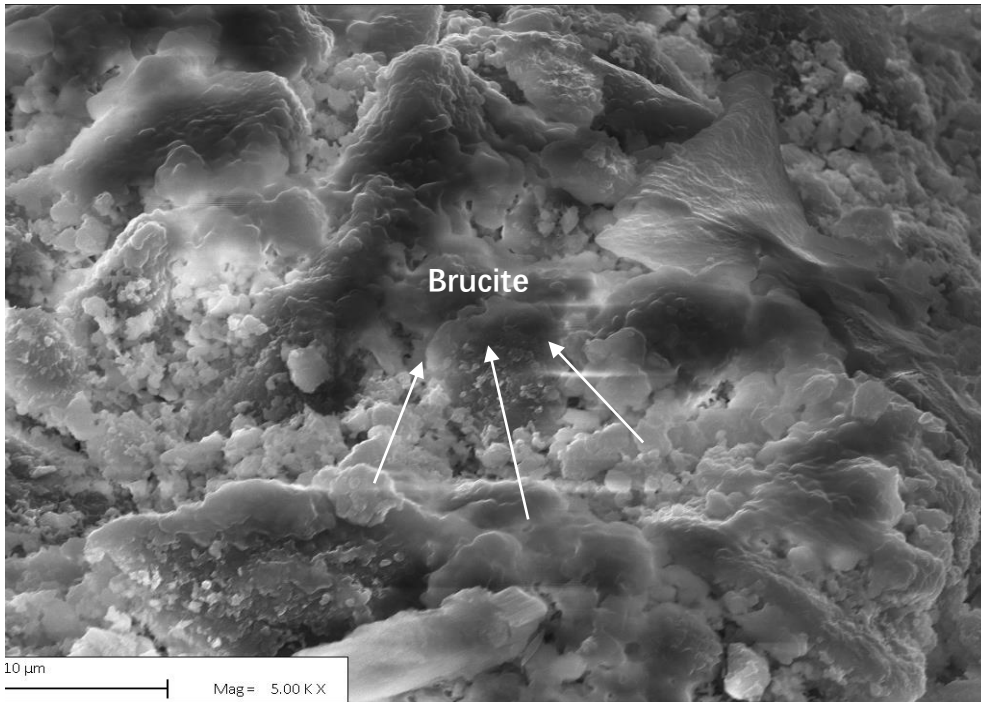
(c)
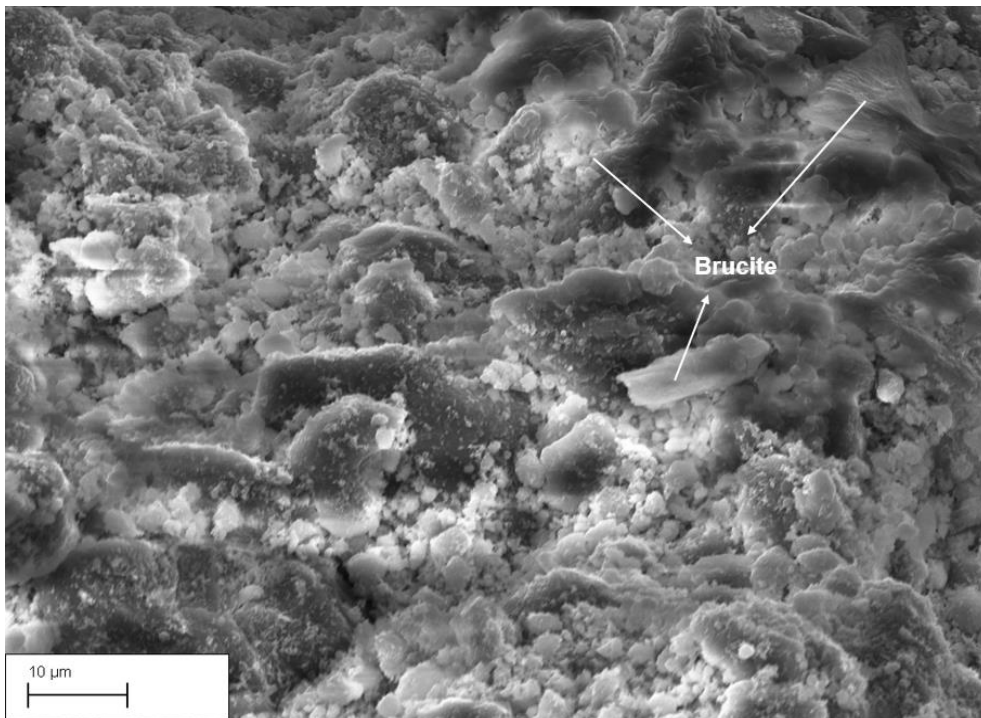
(d)

Fig. 4.10 SEM images of sample (a) (b) C-A (magnification: x5000); and (c) (d)

0.2M-A (magnification: x5000) after 14 days of curing

4.2.3.8. Discussion

The continuous hydration of MgO led to the formation of brucite, which connected the unhydrated MgO particles, explaining the strength development. With L-Asp, the types of hydration phase remain unchanged, but only the amount of hydration phase changes. Normally, the higher the hydration product content, the higher the strength. However, a contrary scenario was observed in this study, i.e. with L-Asp, a high-amorphousness brucite was formed, together with hexagonal brucite, leading to a greater strength improvement in the 0.2M-A samples compared with that in the C-A group. One explanation is that the hydration phases in the 0.2M-A samples provide a better microstructure which is related to their strong and dense nature. Even though, according to the XRD patterns, the formed brucite in the 0.2M-A samples was still crystalline and its amorphousness was much higher than that of C-A samples. In addition, it is reported that amorphous gel-like growths are more useful than hexagonal or tabular crystals in terms of strength improvement because of the structures of amorphous phases [178], suggesting that the morphology, rather than the amount, of hydration phases, plays a more important role in the determination of strength development in samples investigated.

Moreover, the ion concentration in the paste has also been modified by L-Asp. With L-Asp, a large amount of free Mg^{2+} and OH^- ions were maintained in the paste without precipitation, which is highly desirable for the carbonation of MgO. The high concentration of OH^- in the paste leads to an environment with a high pH value, which is helpful to dissolve CO_2, and for producing HCO_3^- and CO_3^{2-}. Afterwards, the exorbitant amount of Mg^{2+} ions can react with HCO_3^- and CO_3^{2-} to form the HMCs, further increasing the mechanical strength and improving the microstructure of the magnesia-based samples.

4.2.4. Conclusions

Based on the investigation of this chapter, the following conclusions can be

drawn:

1. L-Arg only reduced the amount of hydration phase (i.e. brucite) prominently at the early ages (before 3 days of curing), then the effectiveness of L-Arg was exhausted in 14 days. Also, L-Arg failed to alter the polymorphs of the hydration products.

2. Because L-Asp reduced the amount of hydration phase, it led to the formation of crystalline brucite with high amorphousness, which has a positive contribution to strength. The MgO-H_2O composites containing 0.2M L-Asp exhibited a 16% increase in compressive strength at 14 days, compared to the control batch. L-Asp highly changed the product's morphology and densified the magnesia-based samples' microstructure. The morphology of hydration products may affect the strength of the samples more than their amount.

3. Introducing L-Asp can retard the precipitation of Mg^{2+} and OH^-, consequently, the higher concentrations of Mg^{2+} and OH- were observed in the L-Asp-containing samples compared to the control sample, which provides the potential to improve the carbonation of MgO.

Overall, L-Asp not only decelerated the hydration of MgO but also reduced the number of hydration products (i.e. brucite). Accordingly, samples without L-Asp presented the highest brucite contents. L-Asp also led to the formation of brucite with poor crystallinity. However, L-Asp led to an increase in Mg^{2+} concentration, which subsequently resulted in a higher carbonation degree.

4.3. Impact of Amino Acids as Performance-Controlling Additives on Carbonation of Reactive MgO

4.3.1. Introduction

Very few studies have investigated additives that can control the polymorphs

or modify the morphologies of RMC. This section aims to explore a more practical approach that can control the polymorphs of HMCs in carbonated MgO, which is achieved via amino acids, representing a novel method that can facilitate the accelerated carbonation for RM under carbon dioxide curing. The experimental findings presented in this study were verified the above-stated hypothesis. The mechanical properties and mechanism of carbonation were also investigated. Then, the sustainability credential of the MgO-L-Asp mixtures and their potential applications in practice was discussed.

4.3.2. Mix Compositions, Sample Preparation and Curing Conditions

The mix design and sample preparation in this section are the same as that of the last section, which has been elaborated in **Section 4.2.2**. The only difference between the two studies is the curing regimes. In this section, CO_2 curing was utilized instead.

The laboratory CO_2 curing schematics utilized in this study are illustrated in **Fig. 4.11**. An industrial-grade CO_2 gas with a purity of 95% was used for curing the samples. The CO_2 pressure in the curing chamber was controlled by a regulator and kept at 1 bar for the specified carbonation duration. The carbonation chamber was placed in a temperature-controlled environment room at ~20 °C. During the curing process, the CO_2 concentration, temperature, and relative humidity were maintained at $(15 \pm 0.5)\%$, (30 ± 1) °C, and $(80 \pm 5)\%$, respectively.
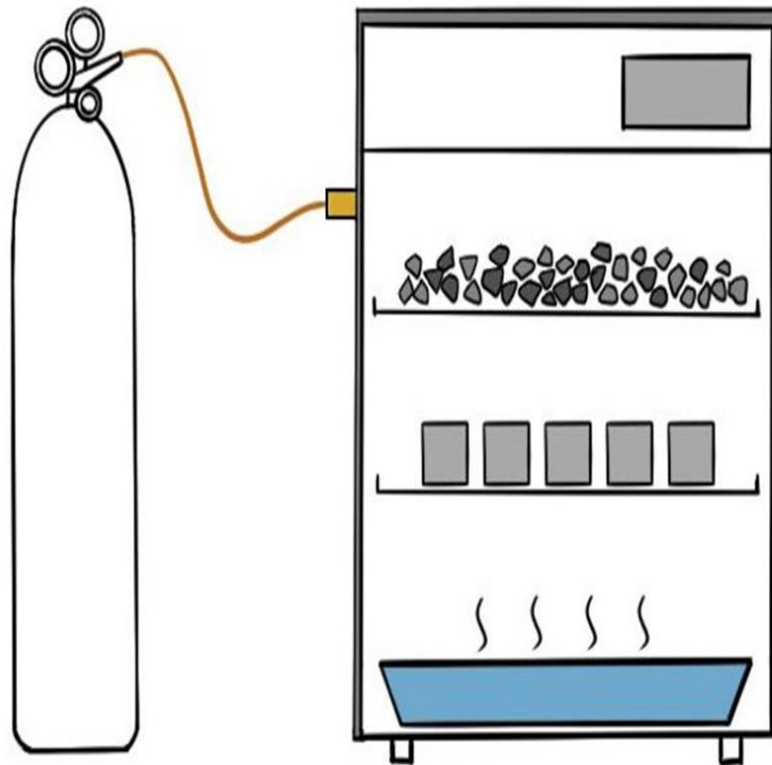
Fig. 4.11 Experimental setup of CO_2 curing

The mix formulations of all groups studied and their curing regimes are shown in **Table. 4.3**. Carbonated thin pastes were removed from the chamber at intervals of 1, 3, 7, and 14 days. Then the samples were placed in isopropanol for another 7 days to arrest the hydration. Subsequently, the samples were dried at 30 °C to remove the solvent and then milled into powder using a mortar pestle. RM paste with an l/b ratio of 0.8 by weight was prepared and then poured into 20×20×20 mm^3 cubic moulds. Immediately after casting, the cubic samples in moulds were placed for 1 day in the same carbonation chamber employed for curing thin paste samples. Then the cubic samples were demoulded and continued to cure in the carbon chamber up to the designated testing ages.

Table. 4.3 Mix formulations of MgO samples (wt.%) and curing regimes used in this study

Group	MgO	L-Asp	l/b ratio	Curing regimes
C-C	100 %	0	0.8	CO_2 curing
0.1M-C	100 %	0.1 M	0.8	CO_2 curing
0.2M-C	100 %	0.2 M	0.8	CO_2 curing

4.3.3. Results and Discussion

4.3.3.1. Bulk Density

The bulk density of the sample subjected to ambient and CO_2 curing is shown in **Fig. 4.12**. In the hydrated samples (**Fig. 4.12 (a)**), the decrease in density was noticed in the C-A sample during all ages, while the other samples did not. The results show that the C-A sample evaporated more water than the other samples, as the mass of the C-A sample was reduced by 5.3% at 14 days than other samples. The contrary scenario was observed in the 0.1M-A and 0.2M-A samples after 3 days of curing, where their densities increased, which may be related to the favourable interactions between water and salt ions. Water in salt has a lower vapour pressure (i.e. tends to evaporate slower), and this effect can be very apparent at high solute concentrations (i.e. 0.2M of L-Asp) [72]. Therefore, 0.2M-A samples had the highest density from 1 to 14 days, as L-Asp increased the viscosity of the aqueous solution, resulting in a slower movement of water.

Concerning the samples subjected to CO_2 curing (**Fig. 4.12 (b)**), their overall density was higher than that of the hydrated samples, which almost stabilised after the 3 days of CO_2 curing. The density of the C-C samples remained constant over time because of the formation of carbonate products that offset the decrease in density that occurred at ambient temperatures (i.e. as seen in the C-A samples). The rapid increase of the density from 1 to 3 days of CO_2 curing was exhibited in the 0.1M-C and 0.2M-C samples, corresponding to increases of 10.1% and 5.6%, respectively. This is probably because of the formation of a higher amount of HMCs which comprised CO_2 and water in

their chemical compositions. However, even though all samples were under CO_2 curing, their densities still decreased after 3 days, which may be related to the evaporation of water [179].

Apart from the water content in the samples, bulk density can also indirectly reflect the porosity of the samples. When the bulk density is lower, it often suggests higher porosity, as more of the volume is occupied by air or pore solution rather than solid phase. Conversely, a higher bulk density indicates lower porosity because a greater proportion of the volume is taken up by solid components rather than voids. In this term, L-Asp can reduce the porosity of magnesia-based samples regardless of curing methods. This may explain the increased compressive strength of 0.2M-A and 0.2M-C samples, shown in **Fig 4.6** and **Fig 4.13**.
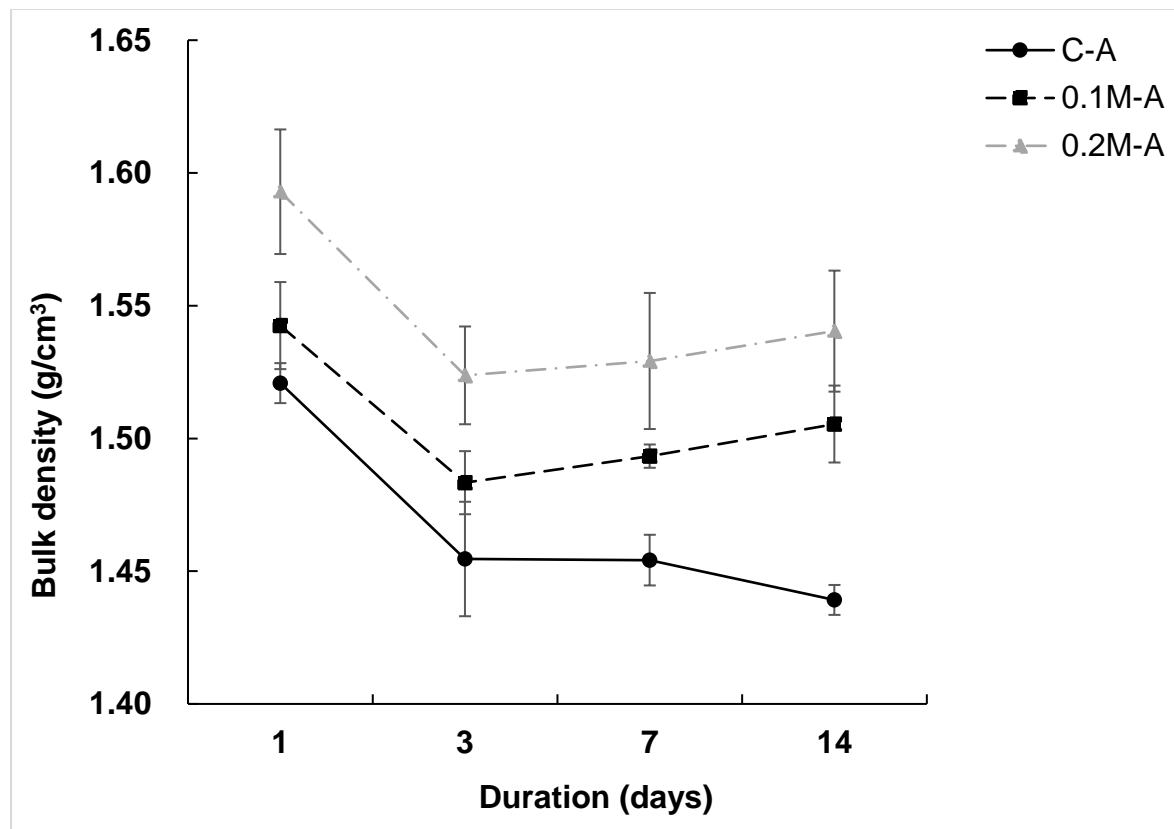
(a)
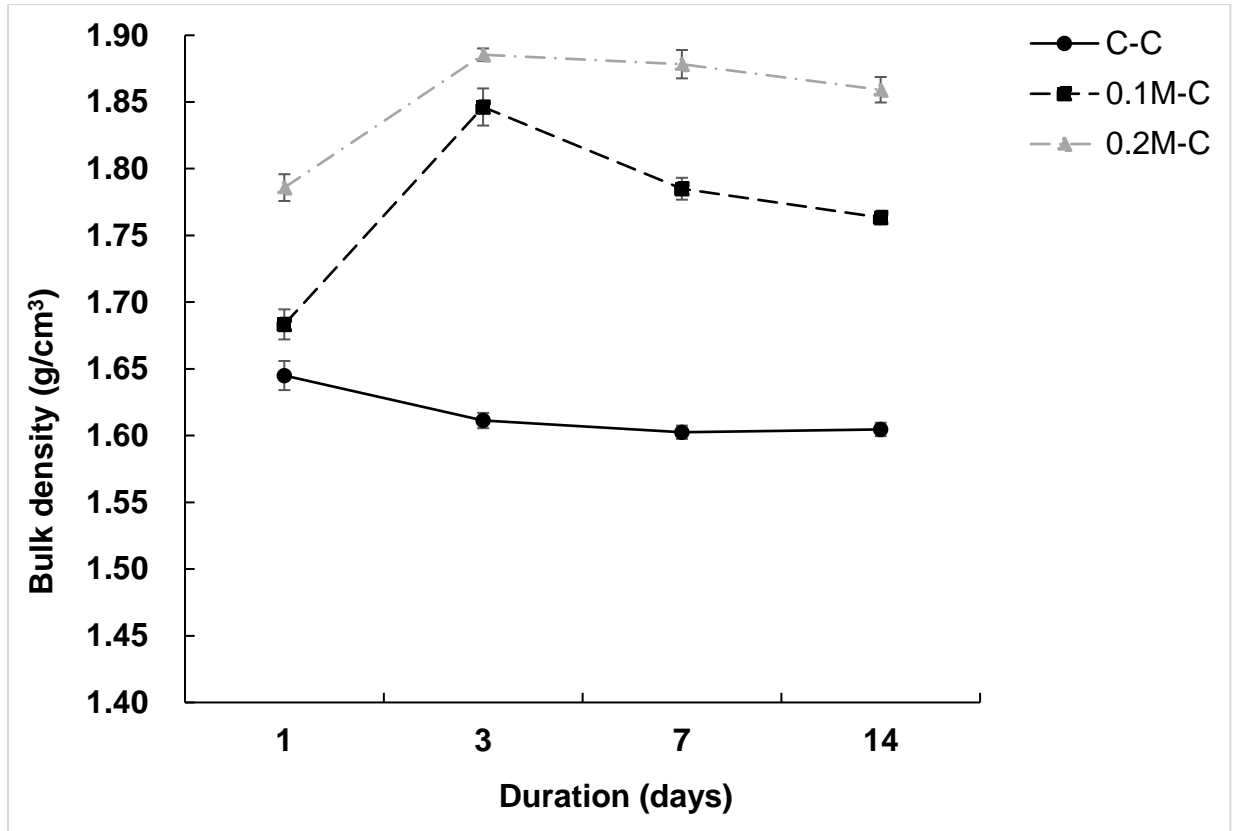
(b)

Fig. 4.12 Bulk density evolution: (a) Ambient curing and (b) CO_2 curing

4.3.3.2. Compressive strength

Fig. 4.13 shows the strength gain of all samples after 14 days of CO_2 curing. The C-C sample reached the highest strength of ~ 7.4 MPa in 1 day. Even though a higher amount of HMCs were observed in the 0.1M-C and 0.2 M-C samples at 1 day, which are revealed in XRD and TG/DTG results, they both had lower strengths compared to the C-C sample. It indicates that the mechanical strength of magnesium-based binder is contributed by the combination of hydration products and carbonation products, which agrees well with the findings from other studies [52,63]. Consequently, because of limited hydration, 0.1M-C and 0.2M-C samples only had strengths of ~4.5 MPa and ~6.6 MPa at 1 day, respectively. It is also worth noting that the samples were kept in the moulds during the first day of curing, where carbonation can only occur on the top surface exposed to CO_2. After 3 days of curing, the strength of both the 0.1M-C sample and 0.2M-C sample exceeded

94

that of the C-C sample, reaching a comparable strength of ~10 MPa. The similar mechanical strengths of the 0.1M-C and 0.2M-C samples are ascribed to the comparable content of hydration and carbonation products (i.e. brucite and nesquehonite), which agrees well with the XRD patterns (**Fig. 4.14**). The rapid development of compressive strength for 3 days could also be attributed to the efficiency of L-Asp, which can be seen in **Fig. 4.3**, the highest pH value was achieved, which was desirable for the dissolution of CO_2 within the binder. Afterwards, the strengths of the 0.1M-C and 0.2M-C samples were at least ~52.3% and up to ~104.5% higher than that of the C-C samples, suggesting that the content and polymorphs of HMCs played important roles in the strength development of magnesium-based binders.

The most desirable strength development was observed in the 0.2 M L-Asp-containing samples, which increased by 177% after 14 days of curing and eventually achieved the highest strength (i.e. ~18.3 MPa) among all samples. Despite the compressive strength of the 0.1M-C sample was increased by 302% after 14 days of curing, its 1-day strength was much lower than that of the 0.2M-C samples, only reaching ~4.5 MPa on 1 day. Afterwards, the compressive strength of the 0.1M-C samples remained constant as the highest value among all samples until 7 days, despite they did not contain the highest amount of HMCs, as shown in **Fig. 4.14**. This phenomenon further reinforces the conclusion that with a comparable amount of carbonation products, the mechanical strength of the magnesium-based sample was controlled by a synergistic effect of hydration and carbonation products. However, the highest strength was still achieved by the 0.2M-C sample, which was 18.3 MPa at 14 days, because of the enormous amount of HMCs. It should be noted that the samples were prepared with a high l/s ratio at 0.8 to ensure a good flowability, therefore, MgO-based binders do not exhibit the optimum mechanical properties. However, in the presence of the desirable l/s ratio and other additives, a much higher strength of the sample containing L-Asp can be expected.

The mechanical performance of samples is determined by various factors, for instance, the quantity of formed products that leads to reduced pores and more compacted microstructures. However, given the XRD patterns, a similar amount of carbonation phases was observed in the C-C samples compared to the 0.1M-C samples at 14 days (**Fig. 4.14**), while the strength of the 0.1M-C samples was much higher than that of the C-C sample (i.e. 18.1 vs. 13.6 MPa), which could be interpreted by the various morphology of the carbonation products formed within these two groups. Hence, for the strength of the samples investigated, the morphology of the HMCs in the magnesium-based binders may play a greater role than their content. Fibrous and needle-like crystallizations are more beneficial for the development of strength than rounded or tabular crystals [151]. Thus, the fibrous nesquehonite and its interlocking effect resulted in a higher compressive strength than other HMCs mixtures because of its 3D structure, therefore, the L-Asp-containing samples had a higher compressive strength than the C-C samples.
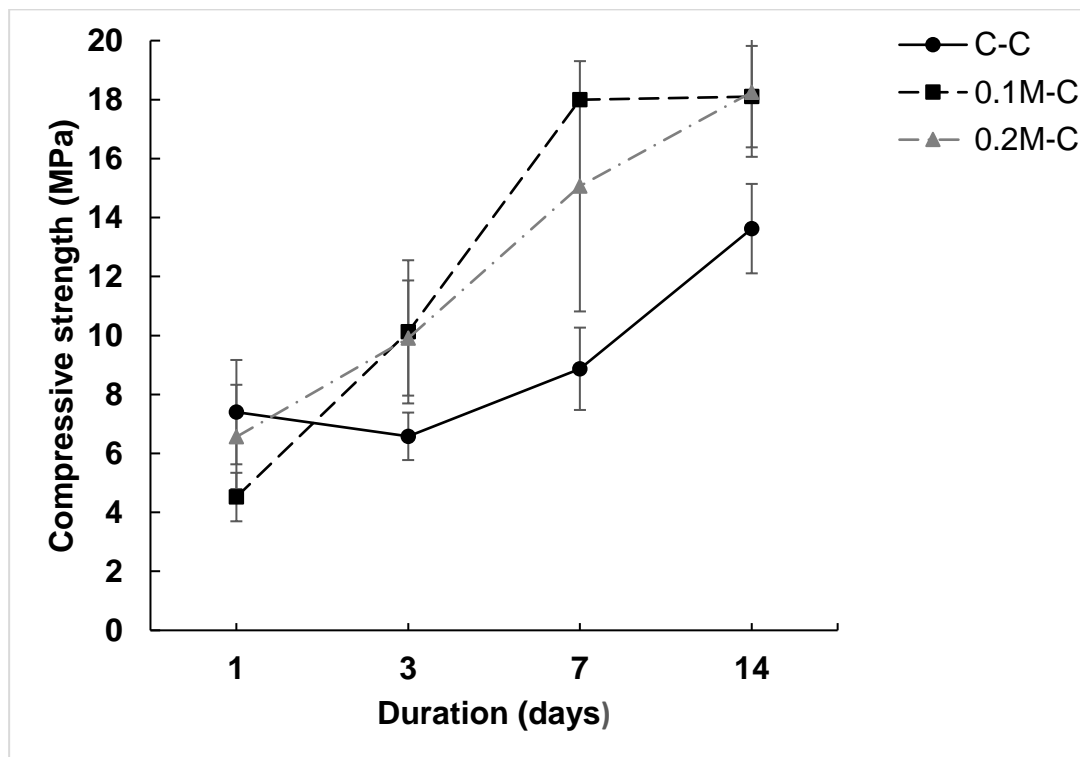
Fig. 4.13 Compressive strength of all samples under CO_2 curing up to 14 days

4.3.3.3. XRD

All samples showed the formation of HMCs, which could be ascribed to the carbonation of samples. Aside from the HMCs, unhydrated MgO (indicated by the main peak at 42.9° 2θ in **Fig. 4.14**) was also detected in all samples, irrespective of the presence of L-Asp, suggesting that MgO was not fully carbonated after 14 days. A different scenario was founded in the samples subjected to ambient curing, where the periclase (i.e. unhydrated MgO) peak was very minor, suggesting that MgO was mostly reacted. The main reason for this phenomenon is that the unreacted MgO particles were covered by the formed hydration and carbonation products, therefore, the availability of the surface that can react with CO_2 and H_2O was largely reduced, i.e. the carbonation of MgO harmed its further reaction.

The peak detected at 29.5° 2θ can be associated with HMCs, nesquehonite ($MgCO_3 \cdot 3H_2O$) and dypingite ($4MgCO_3 \cdot Mg(OH)_2 \cdot 5H_2O$), which can be found in all samples across all curing ages. It is not discernible whether one carbonate or both carbonates have been detected; however, in C-C samples, other peaks of nesquehonite detected at 13.5°, 23°, 34.5°, and 36° 2θ are negligible. Therefore, it is safe to assume that this peak was the dypingite peak for the control sample only, suggesting that the primary carbonate of the control sample was dypingite, a more stable form of magnesium carbonate. As aforementioned, nesquehonite tends to be converted into more thermodynamically stable forms of HMC, such as dypingite or hydromagnesite under a high temperature. In the C-C sample, almost all the nesquehonite had been transformed into dypingite, which is a more stable carbonate. Also, this peak (i.e. 29.5° 2θ) was most prominent after 14 days of curing for the control sample (C-C), which indicates the highest amount of HMCs was still dypingite.

On the other hand, nesquehonite peaks for all samples containing amino acids (L-Asp) were present at every curing age but with different intensities. For curing ages 1, 7 and 14 days (see **Fig. 4.14 (a), (c) and (d)**, respectively), the peaks had the highest intensity in the 0.2M-C samples, followed by the 0.1M-C samples, and as mentioned with negligible intensity in the C-C sample.

The observation is that increasing the concentration of amino acid (L-Asp) in the MgO system increased the amount of nesquehonite formed. During the decomposition of nesquehonite to hydromagnesite, dypingite was formed as an intermediate phase. The transition caused the loss of CO_2 and water [180]. Therefore, this particular hydrated magnesium carbonate (i.e. nesquehonite) sequestered more CO_2 than the other carbonates such as dypingite found in the control sample. The biomimetic interaction between negatively charged amino acids with calcium carbonate solutions stabilised the unstable carbonates [181-184]. This is comparable to the stabilisation of nesquehonite, a relatively unstable magnesium carbonate. Moreover, the impact of L-Asp occurred immediately after one day of curing and continued for 14 days without signs of decomposing of nesquehonite into other more stable carbonates, such as the primary carbonate (i.e. dypingite) found in the control sample. This immediate impact of L-Asp will be discussed in **Section 4.2.3.8**.

However, a deviation from this behaviour can be observed on 3 day (see **Fig. 4.14 (b)**), where the 0.1M-C sample had a more intense peak of nesquehonite than the 0.2M-C sample. This might also explain a spike in brucite on the same curing day, in contrast to the curing days 1, 7 and 14, where the brucite peaks were negligible at 19° and 38° 2θ. Similarly, the 0.1M-C sample could experience the same process; the intensity can be interpreted to be decreasing in the nesquehonite peak relative to the 0.1M-C sample after 14 days of curing (**Fig. 4.14 (d)**) since it can be observed that the intensity of the nesquehonite peak in the 0.2M-C sample was significantly higher. Also, the brucite peak of the 0.1M-C sample was higher than that of the control sample, which has the highest peak for brucite observed after 14 days of curing. Since this specific break-in pattern was not observed in the control sample on any of the curing days, suggesting that L-Asp led to this occurrence on the hydration of MgO and carbonation of brucite. Additionally, the concentration of the L-Asp affected the time at which it occurred during the curing process, i.e. the higher the concentration, the sooner the occurrence, which agrees well with **Fig. 4.5**.

It is worth noting here that, in the 0.2M-C sample, periclase peak at 37°, 43°

2θ had the highest intensity across all ages suggesting a higher amount of unreacted MgO, i.e. a higher concentration of L-Asp reduced the hydration, which agrees well with the findings in **Section 3.1**. This high amount of unreacted MgO also demonstrates the potential of the 0.2M-C sample to be further carbonated in the long term, which may gain strength continuously through the process of capturing CO_2. On the other hand, the control sample had the lowest amount of periclase after 1 day of curing but after 3 and 14 days of curing, 0.1M-C sample had the lowest amount of periclase; however, both samples were tied after 14 days of curing, suggesting that L-Asp only reduced hydration when it had a higher concentration (i.e. 0.2M). Alternatively, a sample at a lower concentration of 0.1M exhibited that its hydration was not too dissimilar to that of the C-C sample, which also agrees well with the XRD patterns of hydrated samples (**Fig. 4.2**). Moreover, there was still a significant amount of unreacted MgO in all samples, which is different from that of the samples subjected to the ambient curing, where MgO was almost entirely reacted after 14 days, suggesting that carbonation had an inhibitory impact on the hydration of MgO, as the carbonation products covered the surface of unreacted MgO particles [34,74,76].

(a)

(b)
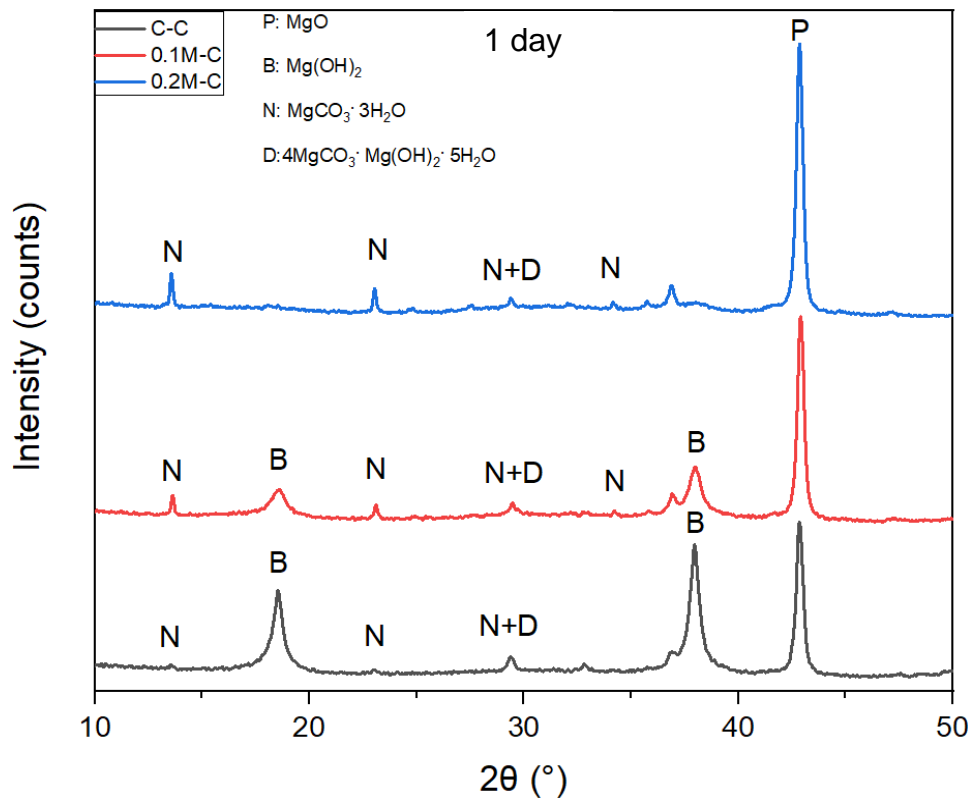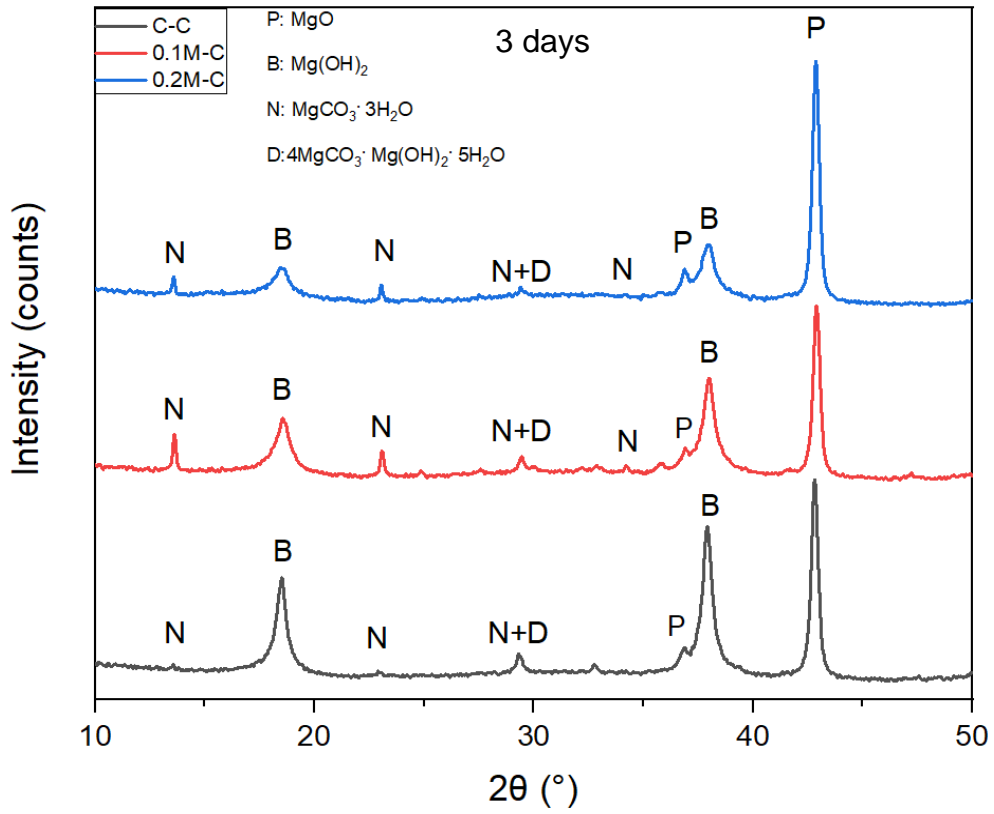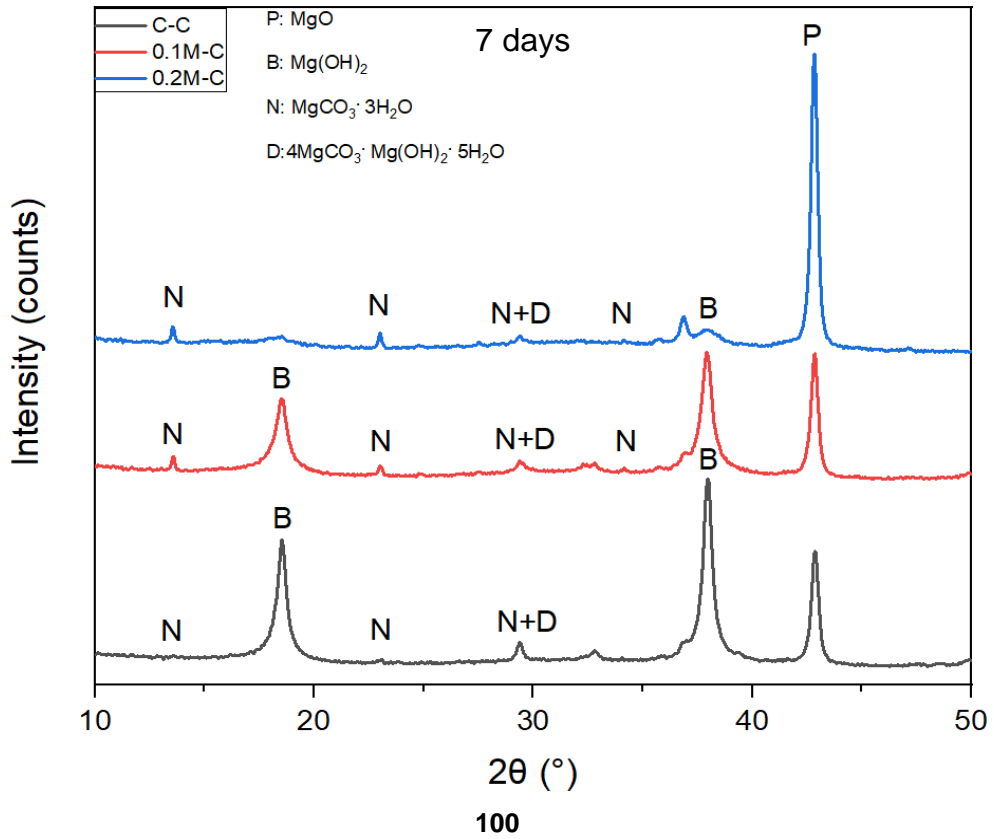
(c)
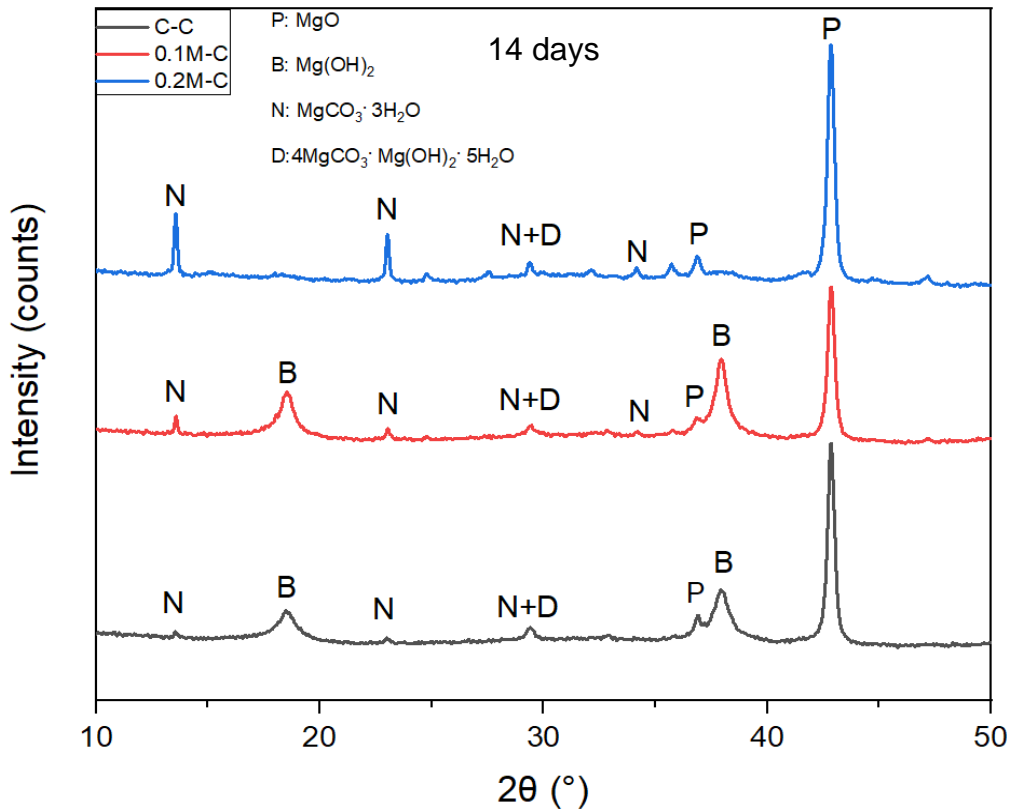
(d)

Fig. 4.14 XRD of all samples subjected to (a) 1; (b) 3; (c) 7; and (d) 14 days of carbonation curing (B: Brucite (Mg(OH)$_2$); N: Nesquehonite (MgCO$_3$·3H$_2$O); D: Dypingite (4MgCO$_3$·Mg(OH)$_2$·5H$_2$O); P: Periclase (MgO))

4.3.3.4. TG/DTG

In this study, TG was employed to calculate the amount of CO$_2$ absorbed, which was captured by the binders after 14 days of carbon curing, to quantify the sequestration abilities of MgO as a cementitious material under the influence of different concentrations of L-Asp and evaluate its viability. **Fig. 4.15** presents the TG and DTG curves of all samples after 14 days of carbonation. The highest total mass loss (i.e. 42.7%) of sample containing 0.2M L-Asp compared to other groups indicated its highest reaction degree. However, it was only slightly higher than that of the 0.1M-C samples (42.7% vs 38.4%), indicating that high amount unreacted MgO still existed even using

a high concentration of L-Asp. In 0.2M-C sample, the third stage (i.e. from 540 to 900 °C) of mass loss (as shown in **Table. 4.4**) was 7.6%, which was higher than that of 0.1M-C sample (6.0%), suggesting the highest amount of carbonate phases within the 0.2M-C sample. The results also present the mass loss over specific temperatures through the release of water from the HMCs, dehydroxylation from brucite, and the HMCs (the release of hydroxyl functional group through water); and decarbonation of the HMCs. These are shown as three slopes in the figure; however, the second slope (the largest drop in mass loss) was an amalgamation representing the dehydroxylation of brucite and HMCs and the parts of the decarbonation of the HMCs; these three processes are known for overlapping temperature ranges [76,185]. Therefore, the TGA curves were differentiated regarding temperature, resulting in three peaks, as shown in **Fig. 4.15** as a differentiated thermogravimetric (DTG) curve. The decomposition temperatures of each phase were determined based on the endothermic peaks on the DTG curves, and the area under those peaks represents the weight loss. In summary, the three main decomposition steps observed in all samples were listed below [46,76,185,186].

a) 60 to 240 °C: Dehydration of water bonded to HMCs (e.g. nesquehonite ($MgCO_3 \cdot 3H_2O$), dypingite ($4MgCO_3 \cdot Mg(OH)_2 \cdot 5H_2O$));

b) 240 to 540 °C: Decomposition of uncarbonated brucite, dehydroxylation of HMCs (e.g. dypingite ($4MgCO_3 \cdot Mg(OH)_2 \cdot 5H_2O$)) and decarbonation of HMCs (e.g. nesquehonite ($MgCO_3 \cdot 3H_2O$)); and

c) 540 to 900 °C: Decarbonation of HMCs.

As shown in **Fig. 4.15**, the 0.2M-C sample's peak at 400 °C was shifted to a higher temperature compared to its counterpart of the control and 0.1M-C samples (390 °C), suggesting that the hydroxyl functional group in both brucite and the HMCs had a higher bond strength and required more energy to break. The same shift was present in the water molecules associated with

the HMCs, such as nesquehonite and dypingite, present in the XRD results in **Fig. 4.14**. The same trend of a smaller shifting peaks was also found in the 0.1M-C sample, and the varying shift in peaks suggests that the higher the concentration, the stronger the bonds found in the carbonates, which can verify the shifting peaks in the FT-IR in the next section, where certain carbonates, possibly of higher instability, decompose into more stable carbonates and this trend delayed in the samples with L-Asp.
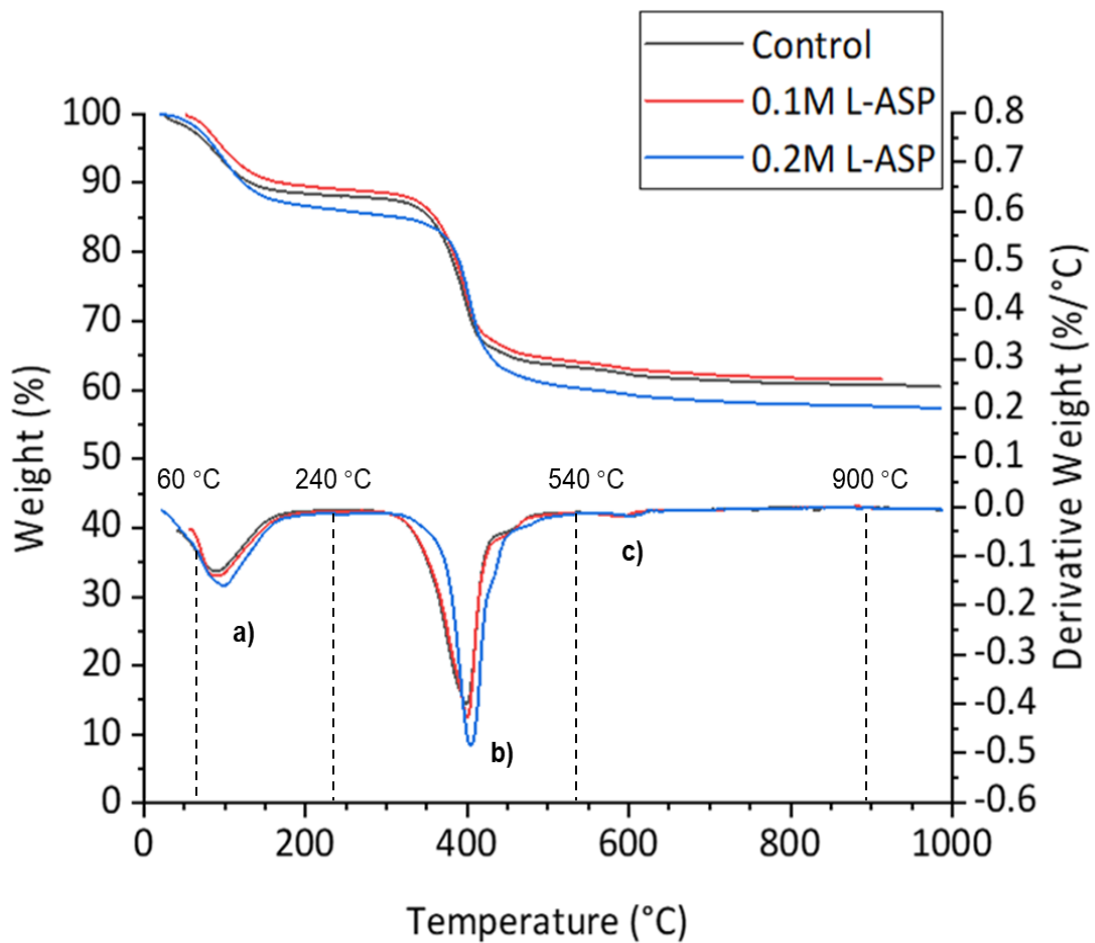
Fig. 4.15 Thermogravimetric analysis of all samples after 14 days of CO_2 curing

4.3.3.5. Phase Quantifications from DTG

The DTG curves were deconvoluted using the Gaussian area deconvolution method to quantify the amount of water and CO_2 produced during thermal decomposition at each step of the process. **Fig. 4.16** shows the deconvoluted

DTG curves for all samples cured for 14 days. For each sample, the original data was included in the plots with the cumulative fit (represented by the purple lines), formed by the combination of all deconvoluted curves. Different decomposition reactions can be represented by the corresponding deconvoluted curves. For instance, two curves (Fit Peak 1 and 2) were used to represent the dehydration of adsorbed water and loss of bonded water of HMCs within the C-C, 0.1M-C and 0.2M-C samples, as demonstrated in Equation 4.4. The light blue and pink curves (Fit Peak 4 and 5) centred at ~400 °C were used to characterize the dehydroxylation of brucite in all samples. Fit Peak 4 was attributed to the decomposition of brucite within the formed HMC (i.e. dypingite) to MgO, shown in Equation 4.5. While Fit Peak 5 was mainly related to the decomposition of the uncarbonated brucite to MgO (Equation 4.6). Finally, the decomposition of the magnesium carbonate to MgO is characterized by Fit Peak 6-8 (Equation 4.7) [76]. Compared to the C-C and 0.1M-C samples, which contained three curves to represent the dehydration of HMCs, the lower number of curves (i.e. two curves) for the 0.2M-C sample was observed because of the high HMCs formation within this sample, suggesting the main weight loss of 0.2M-C sample was dehydration of the formed HMCs.

$$4MgCO_3 \cdot Mg(OH)_2 \cdot 5H_2O \rightarrow 4MgCO_3 \cdot Mg(OH)_2 + 5H_2O \qquad (4.4)$$

$$4MgCO_3 \cdot Mg(OH)_2 \rightarrow 4MgCO_3 + MgO + H_2O \qquad (4.5)$$

$$Mg(OH)_2 \rightarrow MgO + H_2O \qquad (4.6)$$

$$4MgCO_3 \rightarrow 4MgO + 4CO_2 \qquad (4.7)$$

(a)

(b)
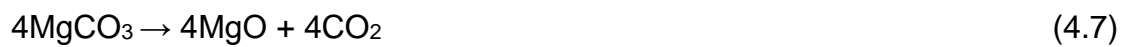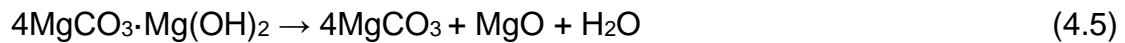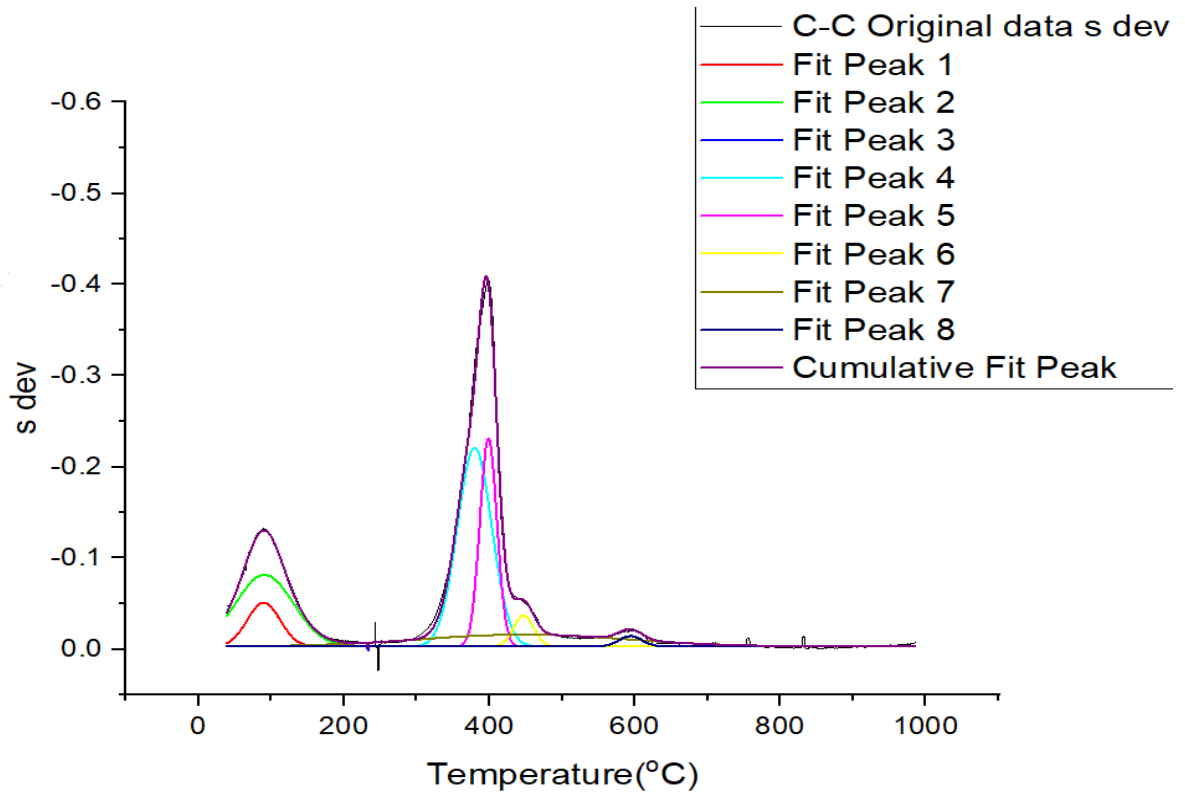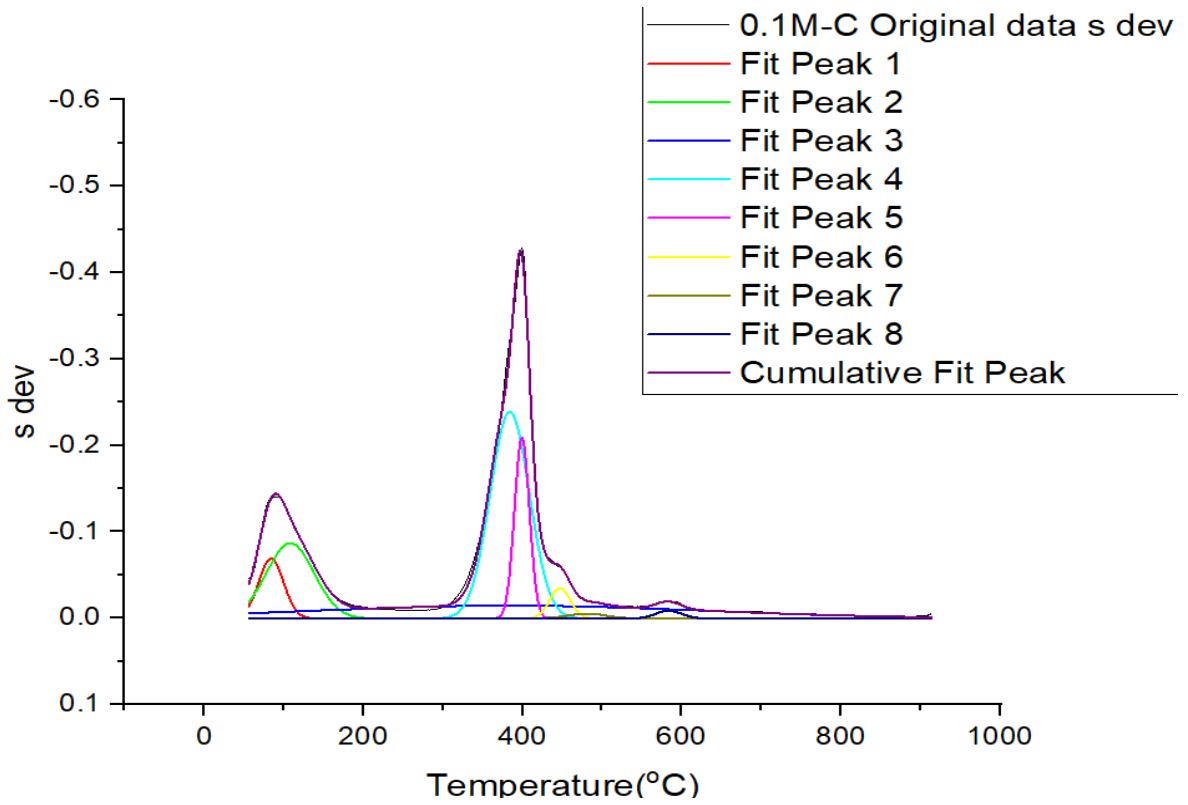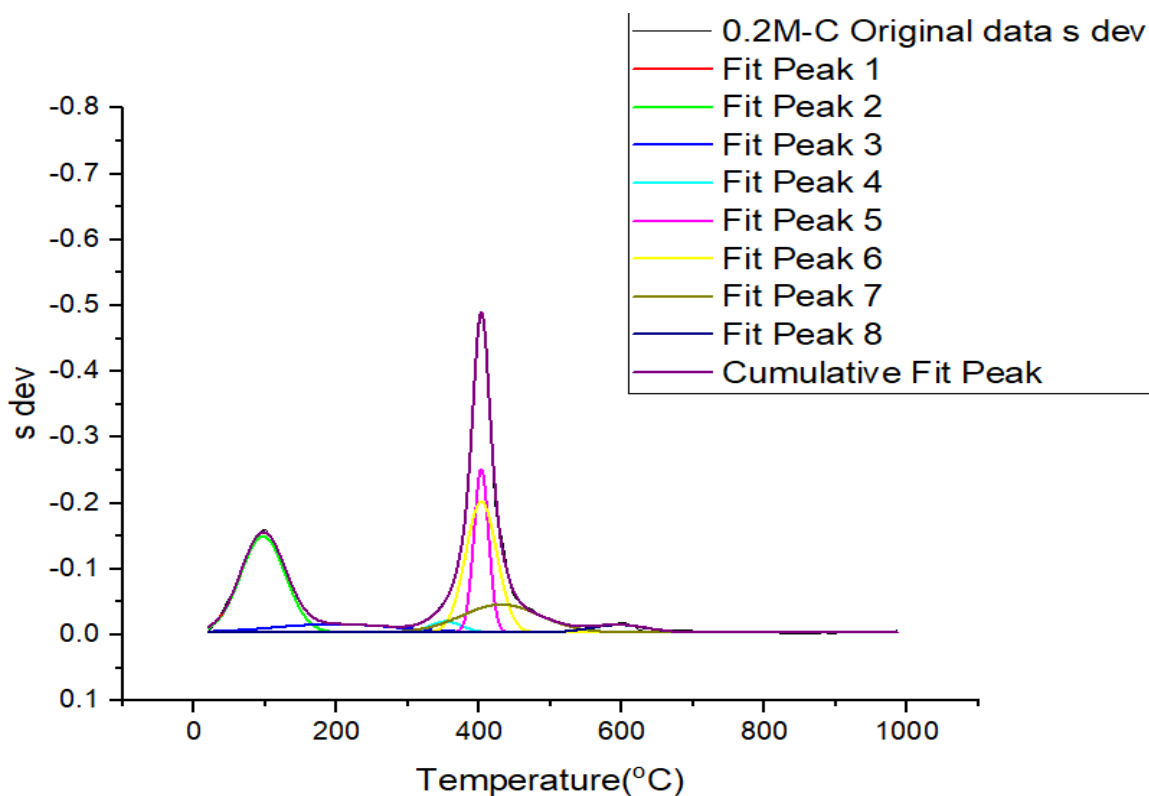
Fig. 4.16 Deconvoluted DTG curves of (a) C-C, (b) 0.1M-C, and (c) 0.2M-C samples at 14 days

Table. 4.4 presents the mass loss associated with each decomposition process obtained by calculating the area under the corresponding deconvoluted DTG curves (shown in **Fig. 4.16**). As the temperature of dehydroxylation of brucite and decarbonation/dehydroxylation of HMCs are largely overlapped between 240 to 540 °C, it is difficult to evaluate the influence of L-Asp on the amount of brucite and HMCs. However, this was obvious from the mass loss because of the decarbonation, which was up to 38% higher in the sample containing 0.2M L-Asp compared to the control batch (i.e. 7.6% vs 5.5%, see **Table 4.4**). The highest contents of dehydration (15.2%) and decarbonation (7.6%) in the 0.2M-C sample showed the highest formation of HMCs. The results suggested a different outcome, even though theoretically, if the main carbonate of the C-C samples were dypingite, it would be expected to have more bound water due to the high amount of crystalline water bonded with dypingite. The C-C sample exhibited the lowest

amounts of dehydration (11.4%) and decarbonation (5.5%), suggesting the low level of bound water, therefore, it was evident that the C-C sample had a low content of HMCs. In terms of dehydroxylation, the C-C sample exhibited the highest weight loss (22.6%) owing to the highest amount of brucite. However, the weight loss of the 0.1M-C sample (21%) was slightly lower than that of the C-C sample (22.6%) between 240 and 540 °C, though the 0.1M-C sample contained a higher content of brucite, shown in XRD patterns (**Fig. 4.14**). It suggests that the majority of HMCs in the C-C sample were dypingite, which contains oxhydryl, while nesquehonite comprises no oxhydryl, therefore, it can exhibit a higher weight loss due to the dihydroxylation. The capacity of the sample to absorb CO_2 can be demonstrated via the CO_2 sequestration ratio (R_{CO2}), which was calculated as shown in Equation 4.8, where P_{CO2} is the percentage of CO_2 sequestered and P_{MgO} is the percentage of final mass at 900 °C (i.e. residual MgO). The percentage of CO_2 sequestered is shown in **Table. 4.4**, from which it can be seen that CO_2 capture was increased by L-Asp.

$$R_{CO2}=P_{CO2}/P_{MgO} \tag{4.8}$$

Table. 4.4 Mass loss of carbonated samples obtained by TG-DTG after 14 days of carbonation

Sample	Dehydration (%)	Dehydroxylation (%)	Decarbonation (%)	R_{CO2} (%)
C-C	11.4	22.6	5.5	9.1
0.1M-C	11.4	21.0	6.0	9.7
0.2M-C	15.2	19.9	7.6	13.2

4.3.3.6. FTIR

The FTIR spectra of the MgO samples with different concentrations of L-Asp under accelerated carbonation are shown in **Fig. 4.17**, after 1, 3, 7 and 14 days of curing, respectively. The spectra are used to identify the specific bonds that correspond to phases such as HMCs present in the samples, as shown in **Table. 4.5** with references. It is also to be noted that the higher

intensity of the band (i.e. higher transmittance), the higher the bond strength, therefore higher amounts of that specific phase.

The bands 3700 cm^{-1}, 1650 cm^{-1}, 1420-1480 cm^{-1}, 1094 cm^{-1}, 850 cm^{-1} and 2750-3500 cm^{-1} were always visible in all curing stages and amino acid concentrations but with different intensities. The magnesium atom in the brucite was positioned in an octahedral configuration with its hydroxyl ligands. In this configuration, the hydroxyl ions occupied the C_{3v} sites, which generated a strong IR band at 3700 cm^{-1} because of the antisymmetric O–H stretching vibrations. Also, the bands at 1420 cm^{-1} found in all samples at all curing ages investigated were not a single symmetrical band, but an amalgamation of multiple phases of hydrated magnesium carbonate in an asymmetric band. These different carbonation products are verified in the XRD results in **Fig. 4.14 (a)** to **(d)**, where there are products of nesquehonite and dypingite at 29.5° 2θ for all samples and at all curing ages.

There are two bands at 1740 cm^{-1} and 1223 cm^{-1} that were not identifiable; both of which were present for all three samples after 1 day of curing, but there were no bands corresponding to 1740 cm^{-1} and 1223 cm^{-1} for the sample C-C onwards after 3 days of curing. Also, there were no corresponding bands to 1740 cm^{-1} and 1223 cm^{-1} for the 0.2M-C and 0.1M-C samples after 7 days of curing and onwards. Although references can be found for those peaks associated with a double bond between a carbon and oxygen atom (C=O) [187], it does not specify a specific origin or movement, since the bond was prevalent in many molecules. However, it is safe to assume that this peak was not associated with the L-Asp. Although it also has a double bond between carbon and oxygen in the carbonyl functional group, it was not present in the control sample (i.e. sample C-C). Therefore, the only alternative would be to associate this double bond between carbon and oxygen to the carbonate ions found in the hydrated magnesium carbonates, as shown in **Fig. 4.14 (a)** to **(d)** in the XRD patterns corresponding to their respective samples and curing ages.

Furthermore, the same pattern of disappearing bands was observed in the shoulder at 1380 cm^{-1} located on the right side of 1420 cm^{-1}. However, the difference is that these bands were identifiable, referenced in **Table. 4.5**, as carbonate ions associated with magnesium carbonates. Simultaneously, a shoulder appeared on the left side of the same band corresponding to 1480 cm^{-1}, another carbonate ion associated with magnesium carbonate. The overall observation suggests that all samples followed an orderly pattern; however, there was a delay in the occurrence of these bands shifting depending on the presence of amino acids. To summarise, L-Asp had a possible stabilising effect on the relatively unstable carbonates that are short-lived, which is in line with the XRD results. Additionally, the concentration effect cannot be discerned since both sample 0.2M-C and 0.1M-C shifted bands simultaneously. Perhaps testing samples cured for between 1 and 7 days would help prove if the concentration is variable. As mentioned in **Section 4.3.3.3**, there was a discrepancy in the pattern that results in diminished nesquehonite peaks and elevated brucite peaks dependent on the concentration of L-Asp, which may be linked to the shifting FTIR peaks as mentioned.

(a)

(b)

(c)

(d)
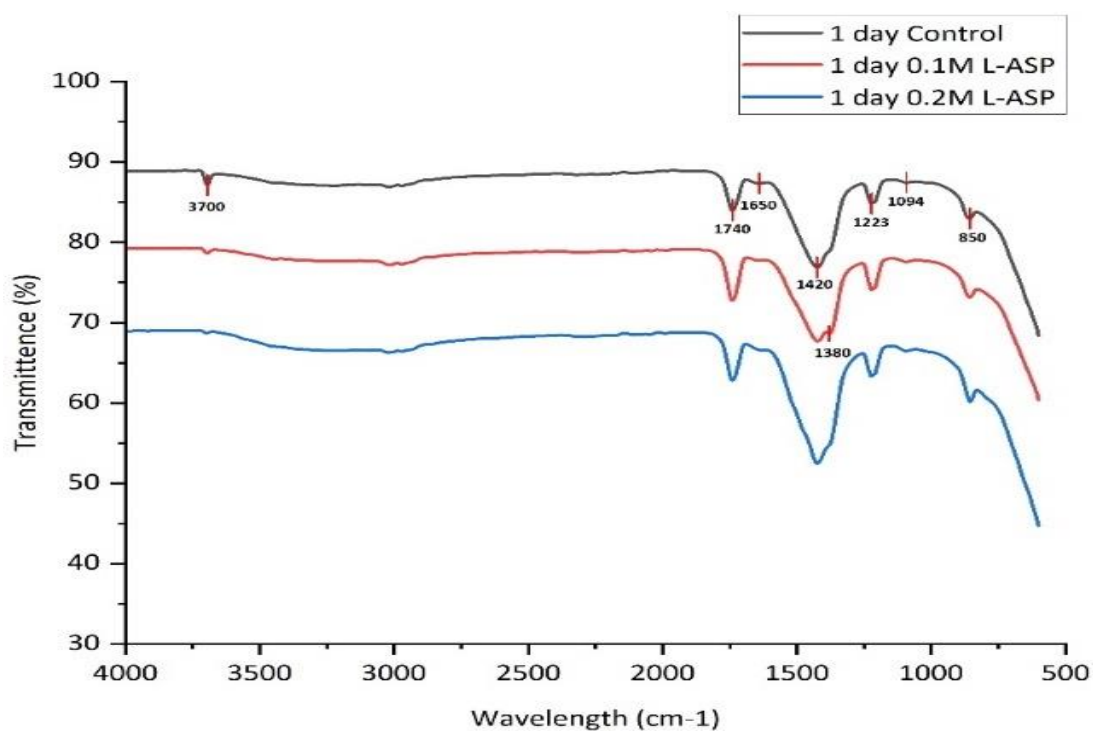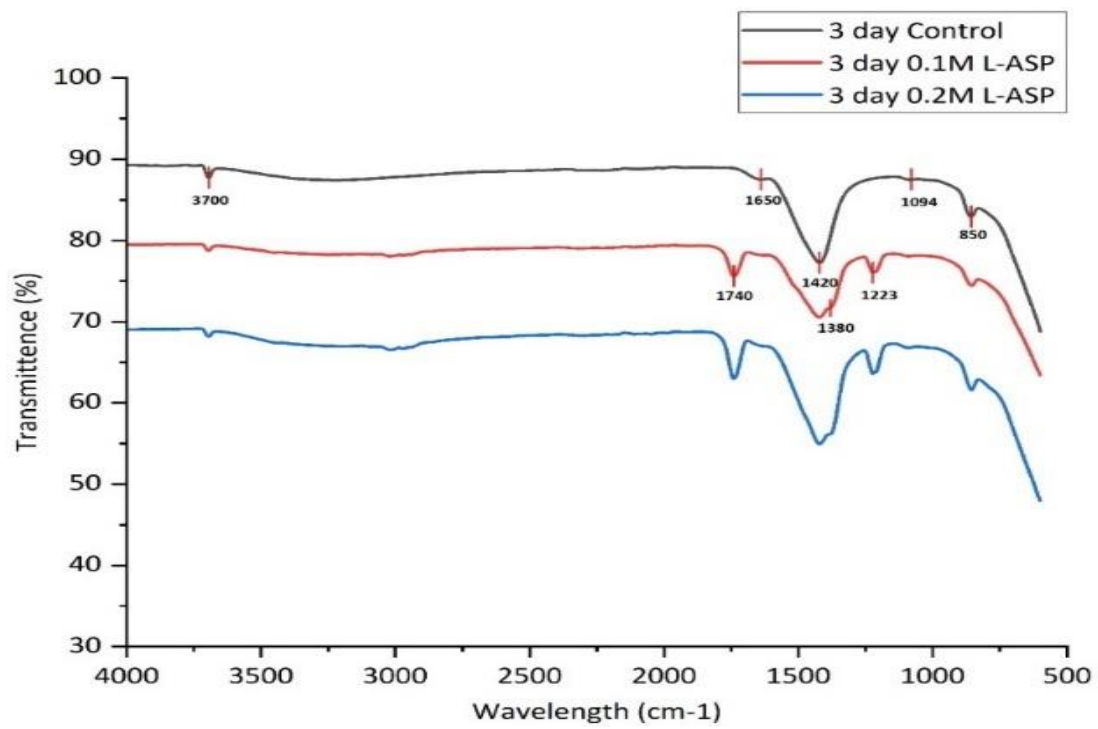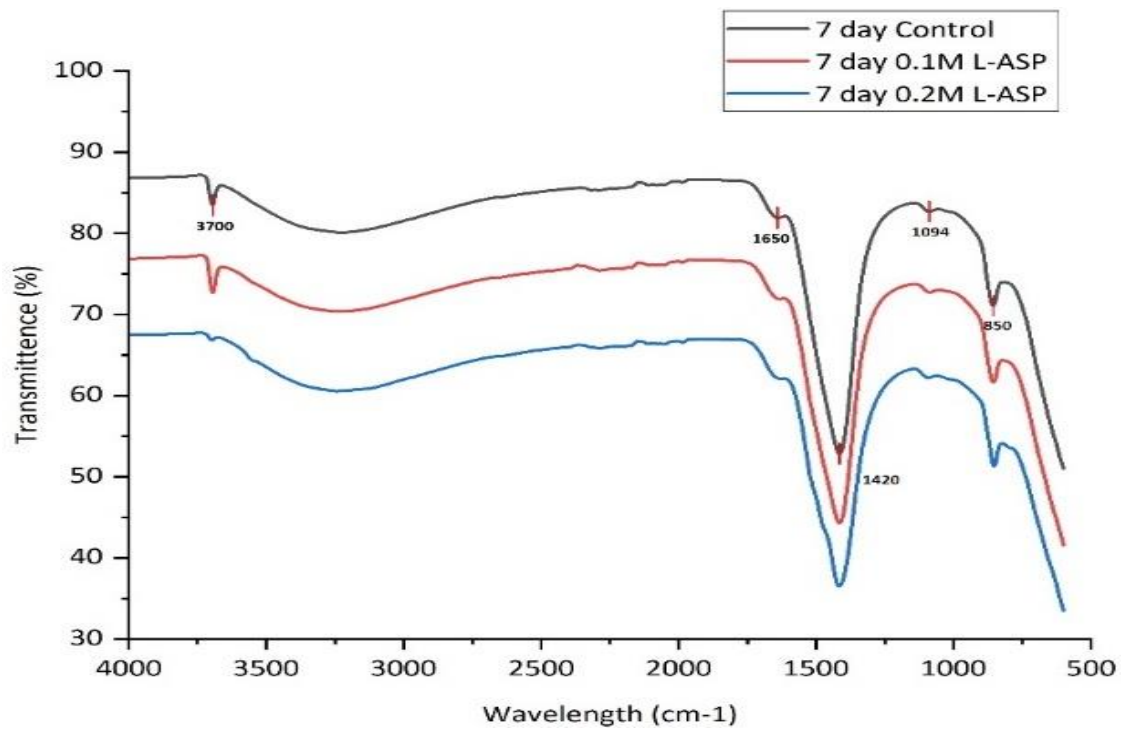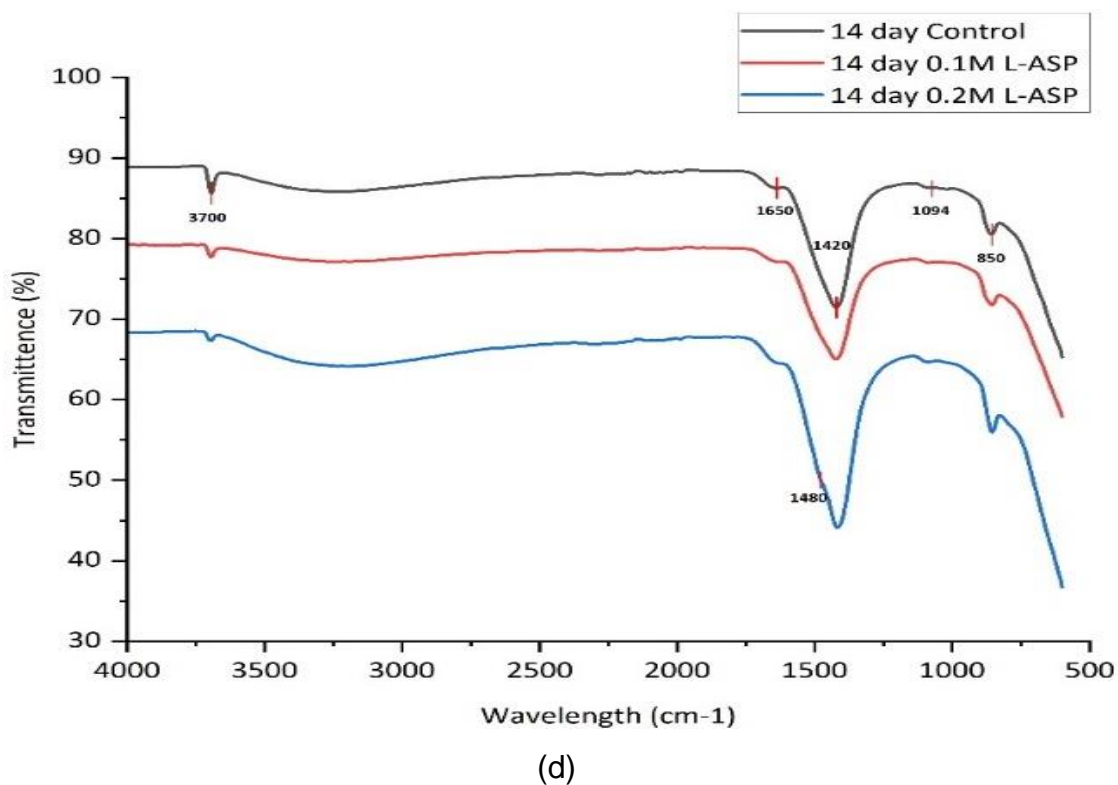
Fig. 4.17 FTIR spectra of all samples subjected to CO_2 curing for (a) 1, (b) 3, (c) 7, and (d) 14 days

Table. 4.5 Wavenumbers (cm^{-1}) of FTIR absorption peaks for different HMCs polymorphs

Band Position (cm^{-1})	Origin	Movement
3700	Brucite ($Mg(OH)_2$)	Asymmetrical stretching OH bond [77,188]
1740	C=O unknown	Unknown [187]
1650	H_2O from HMC	Bending vibration of H-O-H bonds [188,189]
1420 - 1480	CO_3^{2-} from HMC	v_3 asymmetric stretching vibration [63,77]
1380 (shoulder)	CO_3^{2-} from HMC	Vibration [77,190]
1223	C=O unknown	Unknown [187]
1094	CO_3^{2-} from nesquehonite	v_1 symmetric stretching mode [191,192]
850	CO_3^{2-} from HMC	Bending vibrations [77,193]
2750 – 3500 (broad)	Water of crystallisation	Bending vibration of H–O–H bonds [77,189]

4.3.3.7. SEM

Fig. 4.18 shows the microstructures of all samples after 14 days of carbonation, in which **Fig. 4.18 (a)** presents a sparse microstructure of the C-C sample observed by SEM, which reveals several unhydrated MgO grains and agree well with previous results (i.e. XRD and TG). The growth of large rosette-like crystals within a porous microstructure as shown in **Fig. 4.18 (a)**, demonstrated the morphology of the HMCs in the C-C samples. Compared with the C-C samples, it can be seen that L-Asp improved the morphology of hydration and carbonation products through the densification of the microstructure, as demonstrated in **Fig. 4.18 (b)** and **(c)**. The involvement of L-Asp also resulted in a remarkable transition in the polymorph of HMCs from a composition of rosette-like crystal agglomerates to microstructures involving the appearance of needle-like crystals (i.e. nesquehonite). The morphology of nesquehonite formed in 0.2M-C samples is shown in **Fig. 4.19**, where the well-formed needle-like shape was obvious. Moreover, unlike the products in C-C samples, which demonstrated a higher crystalline degree, the sample containing L-Asp had more amorphous phases, which proves the ability of L-Asp to control the polymorph.

Alternatively, the different concentrations of L-Asp show different effects on the microstructure (seen in **Fig. 4.18 (b)** and **(c)**). A denser structure was seen in the 0.2M-C samples than in the 0.1M-C samples, accounting for its higher nesquehonite content, which is also in line with the TG results. The needle-like nesquehonite was agglomerated and surrounded by various phases, which can densify the microstructure of the 0.2M-C samples. The agglomeration of needle-like nesquehonite may be ascribed to the nucleation effect provided by L-Asp.

Overall, the addition of L-Asp exhibited the desirable effect on the microstructure and morphology, which resulted in a denser microstructure and control of the polymorph of HMCs. The improved morphology of mixes contributed to the improvement in mechanical performance, which needs to be investigated in the future. Furthermore, the controlled polymorph of HMCs

can provide the potential to increase the reactivity of HMCs, which can be applied to other binder systems (e.g. high reactive aluminosilicates cementitious systems).
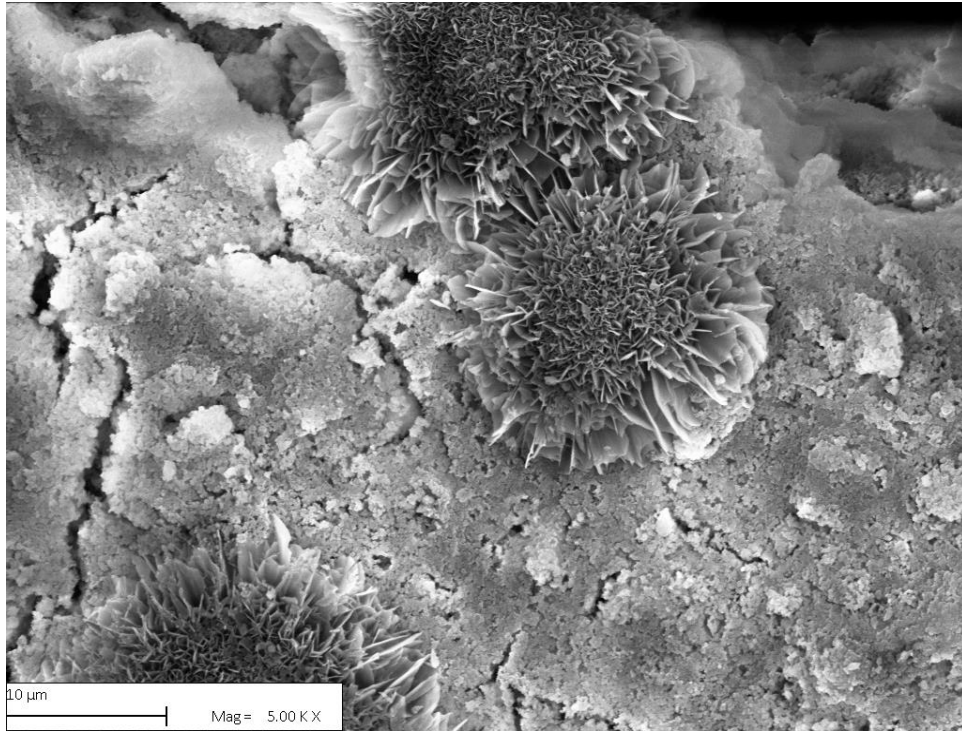
(a)
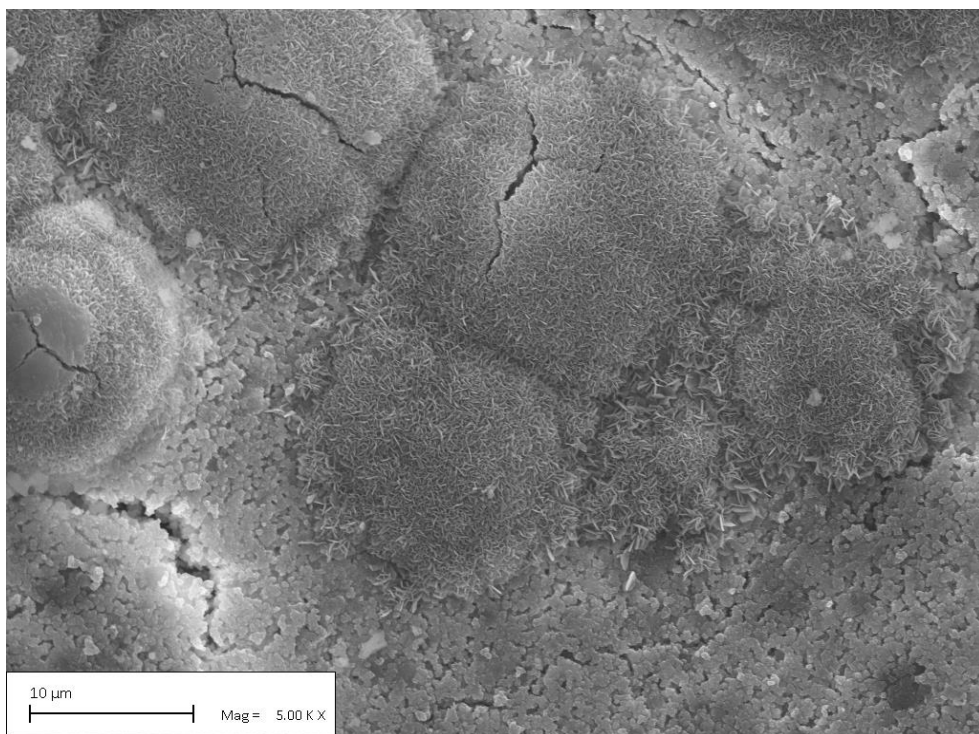
(b)
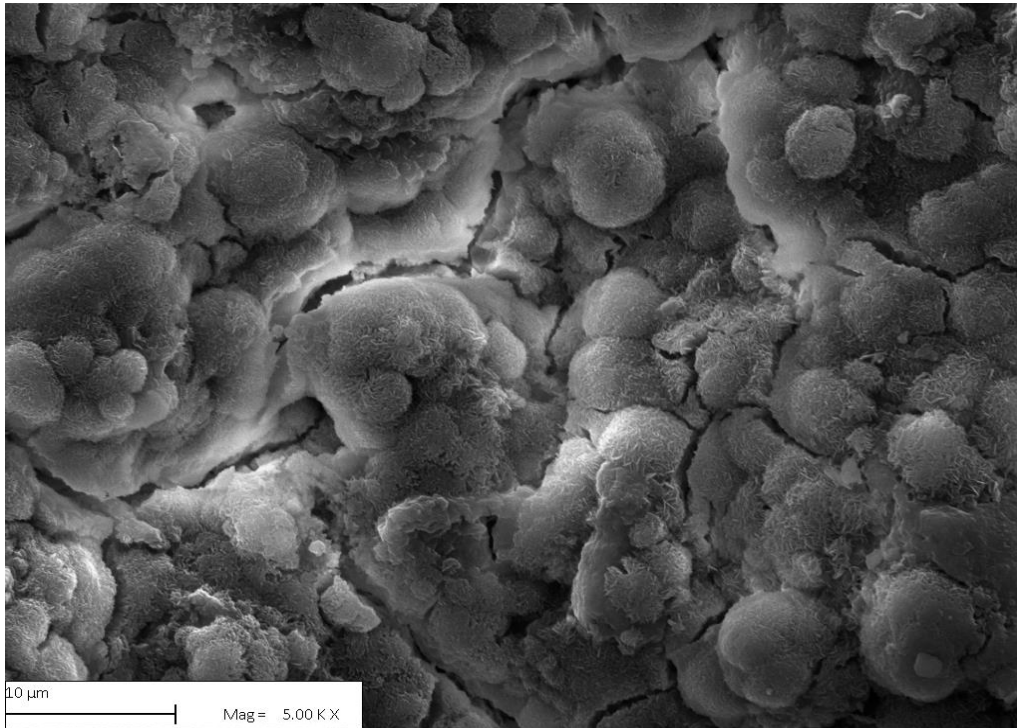
(c)

Fig. 4.18 SEM images of MgO with/without L-Asp after 14 days of accelerated carbonation curing: (a) C-C; (b) 0.1M-C; and (c) 0.2M-C
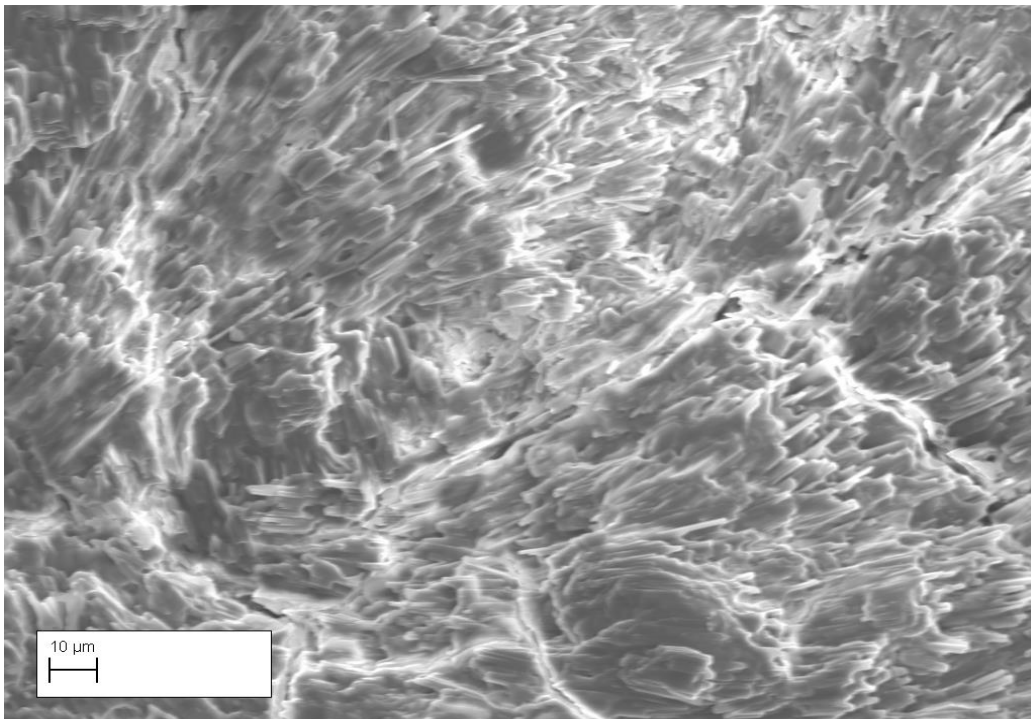
Fig. 4.19 Morphology of nesquehonite within 0.2M-C sample after 14 days of accelerated carbonation curing

4.3.3.8. Discussion

In general, the stability of Mg-carbonates increases from more to less hydrated phases, in the order of nesquehonite < dypingite < hydromagnesite < magnesite [194]. According to Ostwald's step rule, a polymorph with lower stability crystallizes first. Therefore, nesquehnotie is considered the primary carbonation product during the carbonation of MgO. The L-Asp in solution or adsorbed onto the surface of nesquehonite stabilises nesquehonite against the further thermal decomposition as in all cases crystallization was significantly delayed [184,195,196]. In this way, because of the stabilisation of a particular metastable polymorphic phase, the Ostwald step sequence was halted at one of its intermediate stages. The schematic diagram to demonstrate the formation of hydration and carbonation products in magnesia with and without amino acids is illustrated in **Fig. 4.20**. It has been explained that amino acids are amphoteric substances and that their isoelectric point (pI) is the pH of the solution when they are in an isoelectric state. Amino acids exist primarily as anions at pH > their pI, while at pH < their pI, they are predominantly cationic. The pI of L-Asp is 2.77, which is much lower than the pH value of MgO-binder (usually > 10.5), based on a theory of electrostatic interaction and charge matching [197], when L-Asp reaches supersaturation, a strong attraction exists between the excess negative charge of L-Asp and Mg^{2+}, increasing the ions concentration and promoting the precipitation of carbonate. This theory may also explain the outstanding performance-controlling effects led by the high concentration L-Asp. Moreover, because of its double negative carboxyl groups, L-Asp could bind to the specific crystal plane, inhibiting crystal growth [181,197], therefore, amorphous brucite was formed as a result (shown in **Fig. 4.14**). Because of the attraction from amino acids, the carbonation products are dispersed among the binder rather than covering the MgO particles. Therefore, more available unreactive MgO particles are exposed to H_2O and CO_2, leading to a higher carbonation degree. The well-dispersed HMCs within the binder are also considered contributing to a higher compressive strength and denser microstructure.Additionally, carbon

dioxide is another by-product which generates during oxidative deamination of amino acids, and it tends to dissolve and transform into either HCO_3^- or CO_3^{2-} at elevated pH [198], which can provide more reactant to produce HMCs. The proposed impact of amino acid on the carbonation of MgO composite is shown in **Fig. 4.20**. Based on the results presented above, the accelerated dissolution of MgO by amino acids enhances carbonation, which subsequently boosts strength development. Additionally, amino acids become highly negatively charged when pH > pI, attracting Mg^{2+} ions, resulting in ion concentration and promoting carbonate precipitation. This is ultimately reflected in the significant increase in compressive strength observed in the L-Asp-added samples.

The improved ability of carbon absorption was a highlighted advantage of the usage of L-Asp. In this study, the amount of absorbed CO_2 was also calculated, according to the thermogravimetric analysis (**Table. 4.4**). C-C sample captured 5.5 wt.% CO_2 of the total binder mass, where unreacted MgO is 60.5 wt.% of the total binder mass. Therefore, 1 tonne of plain MgO can capture 90 Kg of CO_2 after 14 days of CO_2 curing. When 0.2M L-Asp was added to the binder, the captured CO_2 was 7.6 wt.% of the total binder mass, consequently, 1 tonne of MgO with 0.2M L-Asp can absorb 132 Kg of CO_2 under 14 days of accelerated CO_2 curing, which is 46.7% higher than that of the C-A binder. As other studies [164,199] reported that the CO_2 sequestration capacity of RMC is 430 kg CO_2/t, the MgO-L-Asp composite can achieve approximately 31% of the maximum CO_2 absorption after 14 days of CO_2 curing, which is a satisfactory performance.

Apart from the polymorph controlling effects, L-Asp also demonstrated the impact on the amorphousness of the reaction products and their microstructure (shown in **Fig. 4.14** and **Fig. 4.18**). This study found that the amorphousness of the products can affect the mechanical properties of the MgO-based binders. Furthermore, higher amorphousness leads to the higher reactivity of the products, which provides a wider prospect of applications as studied in the following chapter.
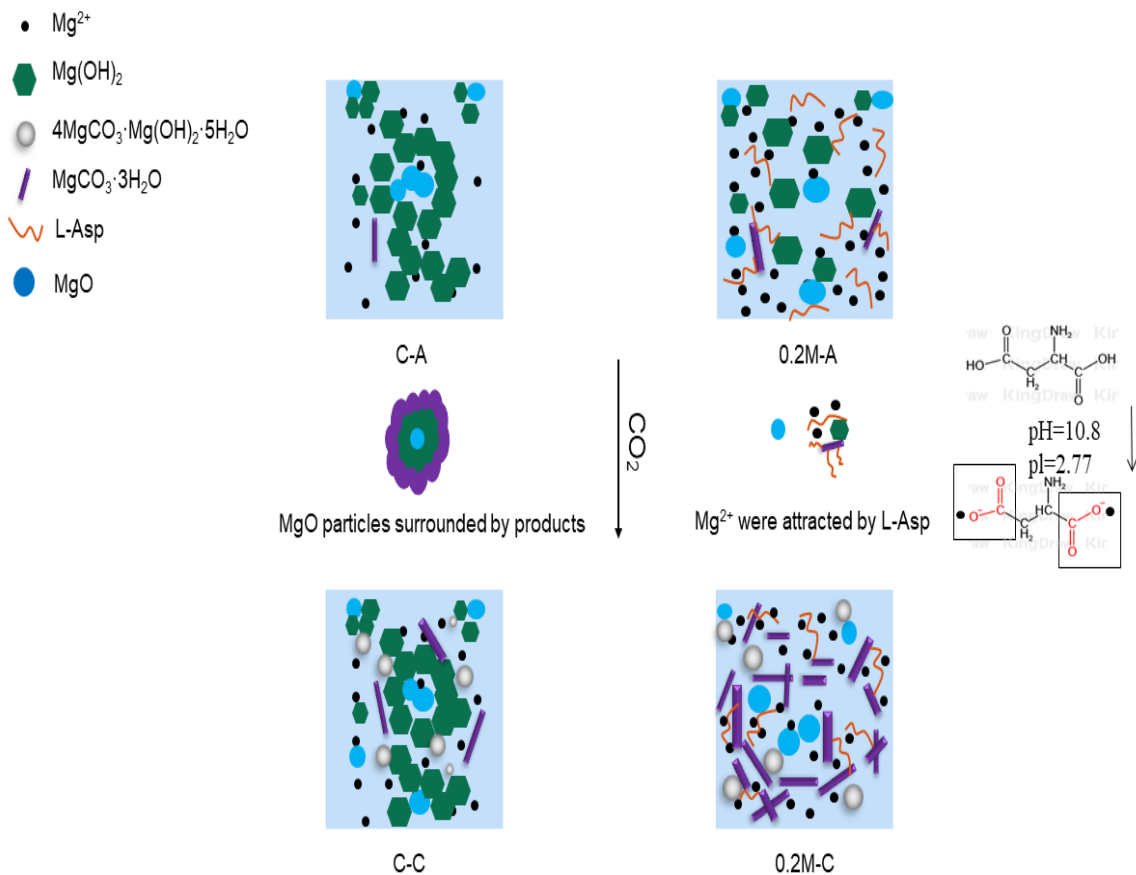
Fig. 4.20 Mechanism of synergetic hydration and carbonation in MgO composites with L-Asp

4.3.4. Conclusions

1. The addition of amino acids resulted in the stabilisation of the typical polymorph of HMCs, which is nesquehonite, in carbonated MgO composites. In terms of enhancing carbonation degree, the effectiveness of L-Asp increases with increasing concentration. With the addition of L-Asp, a higher amount of CO_2 can be absorbed by the MgO composites. The samples containing L-Asp showed up to a 34.2% increase in compressive strengths at 14 days, compared to the control batch.

2. Moreover, the 0.2M-C sample showed 46.7% higher CO_2 sequestration, compared to the C-C sample. As the higher compressive strength was achieved by the 0.2M-C sample, it also captured more CO_2, the MgO-L-Asp composite can be considered a high sustainability mixture, compared

to plain MgO mixtures. The amount of amorphous products increased by L-Asp, leading to higher reactivity of the products. This feature is able to apply to the Portland metakaolin cement to replace the calcium-based carbonate in the binder, which will be investigated in **Chapter 5**.

3. The observed difference in influencing hydration and carbonation among different amino acids-added samples can be attributed to its variations of the pH vs. isoelectric point gap, and a higher gap leads to a greater dissolution of Mg^{2+}, followed by higher carbonation degree, and then a higher strength.

5. Chapter 5 Use of Magnesium-Based Carbonates in Development of a Portland Metakaolin Cement with Enhanced Properties

5.1. Introduction

In the cement industry, the use of supplementary cementitious materials (SCMs) offers significant potential to reduce carbon emissions and conserve precious natural resources [200]. Ground granulated blast furnace slag (GGBS) and fly ash (FA) constitute over 80 wt.% of the SCMs that are adopted to reduce clinker in cement [3]. For instance, ternary blended cement offers a high clinker replacement rate of approximately 70 wt.% by SCMs, such as slag and FA. However, considering the increasing demand for cleaner fuels in power plants and steel manufacturing plants, the supply of traditional SCMs (i.e. FA) is expected to decrease significantly soon [201]. Thus, it is important to investigate alternative low-carbon SCMs such as limestone and calcined clay.

A blend of limestone, calcined clay, clinker and gypsum is introduced as a ternary blended cement called Limestone Calcined Clay Cement (LC3) [202]. The wide availability of kaolinitic clay and limestone in many regions around the world provides a bright future for LC3. Therefore, LC3 blends have gained significant scientific interest in the last decade. Even though the LC3 binder only contains 50 wt.% clinker content, it exhibits comparable mechanical and higher durability as PC [103,203]. Calcined clay, a pozzolanic material, reacts with portlandite, and sulfate during the hydration, producing C-A-S-H, ettringite (AFt), and monosulphate (AFm). In the presence of limestone, the hemi- and mono-carboaluminate phases (Hc, Mc) are formed through the reaction between calcite ($CaCO_3$) and C_3A in clinker and aluminate phase in calcined clay [92,96,204]. These reactions can be described by the simplified Equations 5.1-5.4.

$$Al_{cal} + Si_{cal} + CH + H_2O \rightarrow \text{C-A-S-H} \tag{5.1}$$

$$Al_{cal} + CaSO_4 + H_2O \rightarrow AFt \qquad\qquad (5.2)$$

$$AFt + Al_{cal} + H_2O \rightarrow AFm \qquad\qquad (5.3)$$

$$AFm + CaCO_3 + H_2O \rightarrow Hc/Mc \qquad\qquad (5.4)$$
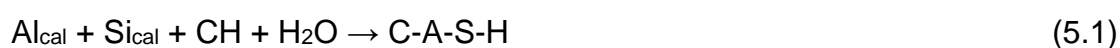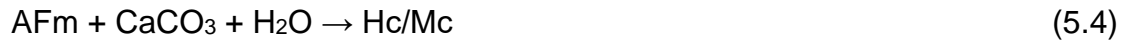
The importance of the purity of clay has been widely investigated by several studies, which suggested that the later stage hydration is limited by kaolinite clay [203]. This may be related to higher alumina incorporation, leading to the polymerization of C-S-H, or hindering the solubility of other phases, consequently, inhibiting the hydration of cement [87,205].

Because of the reaction between limestone and alumina, carboaluminates are formed, which contribute to reducing the volume of pores and refining the pore structure owing to its space-filling capacity [87,96]. The alumina is primarily from C_3A in PC, while the presence of calcined clay provides additional alumina for the CO_3^{2-} to react with and form the carboaluminate phases. Because of the formation of carboaluminate phase, ettringite is prevented from transforming to AFm. The well-refined pore structure is assured by the formation of additional C-(A)-S-H gel and carboaluminates in conjunction with the stabilized ettringite phases [101]. The carbonate sources, therefore, play an important role in the ternary cement systems. Nevertheless, only a few studies have explored the role of different sources of carbonates. The hydration mechanism and the role of carboaluminates formed during hydration on the strength development in LC3 are still unknown. Though Shah et al. [102] have discussed the importance of carbonates on the performance of Portland metakaolin cement and found that the addition of carbonate can enhance early-age compressive strength by the formation of carboaluminates, more types of carbonates, especially magnesium-based carbonates, but it still needs to be investigated. Moreover, when compared to Portland cement, LC3 exhibits a lower early strength and a slower strength gain [100]. Knowing that the reactive carbonate source can improve the early age properties of LC3, it is crucial to investigate the feasibility of other carbonate sources in the blend of Portland cement and metakaolin. With a similar mechanism of dissolution, magnesium-based carbonates (i.e. magnesite and HMCs) can be considered

as alternative carbonates. In the presence of water, magnesium carbonate ($MgCO_3$) and calcium carbonate ($CaCO_3$) partially dissolve their lattice ions, releasing Ca^{2+} and Mg^{2+}, respectively. For magnesium carbonate dissolution, $MgOH^+$ and $Mg(OH)_2$ are produced following the dissolution of the lattice ions, and for calcium carbonate dissolution, $CaOH^+$ and $Ca(OH)_2$ are produced following the dissolution of the cathode ions [206].

HMCs have various solubilities, so it can be expected that, when using different HMCs in Portland cement with the presence of metakaolin (Portland metakaolin cement), it will lead to different performances. As elaborated in **Chapter 4**, MgO is carbonated to produce HMCs such as nesquehonite ($MgCO_3 \cdot 3H_2O$), hydromagnesite ($4MgCO_3 \cdot Mg(OH)_2 \cdot 4H_2O$), and dypingite ($4MgCO_3 \cdot Mg(OH)_2 \cdot 5H_2O$). In **Section 5.2**, commercial hydromagnesite, dypingite, and magnesite were used as carbonate sources to investigate the effects of magnesium-based carbonates on the properties of Portland metakaolin cement. The compressive strength of samples up to 28 days was measured, and the strength results were later interpreted by density measurement, water absorption, x-ray Diffraction (XRD), scanning electron microscopy (SEM), and carbonation depth. In **Section 5.3**, the lab produced HMCs by using the method developed in **Chapter 4** used as carbonates in Portland metakaolin cement to improve the early age compressive strength. The mechanical property was tested for up to 90 days, and then the sample was characterized by XRD, TG/DTG, and SEM.

5.2. Feasibility of Using HMCs in Portland Metakaolin Cement

5.2.1. Introduction

Generally, with the more hydrated phases, magnesium-based carbonates show higher stability, compared with other carbonates, in the order: lansfordite < nesquehonite < dypingite < hydromagnesite < magnesite [194,207]. Higher reactivity is expected in the less stable magnesium-based carbonates, which can potentially improve the properties of Portland metakaolin cement. To

investigate the effects of HMCs on the performance of ternary cement systems, pure dypingite, hydromagnesite and magnesite were used as carbonate sources in this study. The limestone and quartz were also used in this study to produce Quartz calcined clay cement (QC3) and Limestone calcined clay cement (LC3), which subsequently are compared with magnesium-based carbonates calcined clay cement.

5.2.2. Mix Design and Sample Preparation

The mixes in the study are referred to as either QC3, LC3, MC3, LMC3, or HMC3 based on the variable component presented in them. The mix composition of all the blends investigated in the study is given in **Table. 5.1**. Quartz (Q) does not react with the other components in this cement mixture, therefore, QC3 can be used as a reference to reveal the role of carbonates in Portland metakaolin cement. Two different types of high-purity commercial HMCs obtained from different sources (Fisher Scientific and Acros Organics) and characterized as "light" (denoted as LHMC) and "heavy" (denoted as HHMC) were included within the mixes, where light (LHMC), with the empirical formula $4MgCO_3 \cdot Mg(OH)_2 \cdot 4H_2O$, corresponds to hydromagnesite; and heavy (HHMC), with the empirical formula $4MgCO_3 \cdot Mg(OH)_2 \cdot 5H_2O$, corresponds to dypingite [76]. Pure magnesite (M) was also used in this study to produce an MC3 blend.

To compare their compressive strength, all samples were prepared using the same water-to-binder (w/b) ratio of 0.55 with different dosages of polycarboxylate ether (PCE) superplasticizer. Each sample was mixed for 2 min at a mortar mixer and then cast into the $40 \times 40 \times 40$ mm^3 moulds. All samples were placed in an environmental chamber and demoulded after 1 day, then the samples continued to be cured at 20 °C temperature, and 95% relative humidity (RH) up to 3, 7, 14, and 28 days. Accordingly, sample QC3, which contained quartz as the non-carbonate filler, was selected as the control group. Samples LC3, MC3, LMC3 and HMC3 contained limestone, magnesite, light hydrated magnesium carbonate (i.e. hydromagnesite) and

heavy hydrated magnesium carbonate (i.e. dypingite) for their carbonate sources, respectively.

Table. 5.1 Compositions of mixtures investigated (wt.% except for w/b)

ID	w/b	PC	MK	Q	LS	M/LM/HM	Gyp	PCE
QC3	0.55	55	30	15			2	2
LC3	0.55	55	30		15		2	2
MC3	0.55	55	30			15	2	5
LMC3	0.55	55	30			15	2	7
HMC3	0.55	55	30			15	2	6.5

5.2.3. Results and Discussion

5.2.3.1. Density and Water Absorption

The density and water absorption of all samples were measured at 3, 7, 14, and 28 days, as shown in **Fig. 5.1** and **Fig. 5.2**, respectively. At 3 days, HMC3 formulations showed the highest density among all samples, while the lowest density obtained was 2.11 kg/cm^3 for the mixture containing hydromagnesite as the carbonates. The density can normally reflect the compactness of a sample, however, the 3-day water absorptions of LMC3 and HMC3 only demonstrated a minor difference, which indicates their similar porosity. Therefore, the great difference in density between HMC3 and LMC3 was possibly related to the bond water from HMCs ($4MgCO_3 \cdot Mg(OH)_2 \cdot 5H_2O$ vs $4MgCO_3 \cdot Mg(OH)_2 \cdot 4H_2O$). The density decreased from 3 to 7 days, due to the evaporation of water. After 14 days, the density of all samples tended to increase, due to the continuous formation of hydration products.
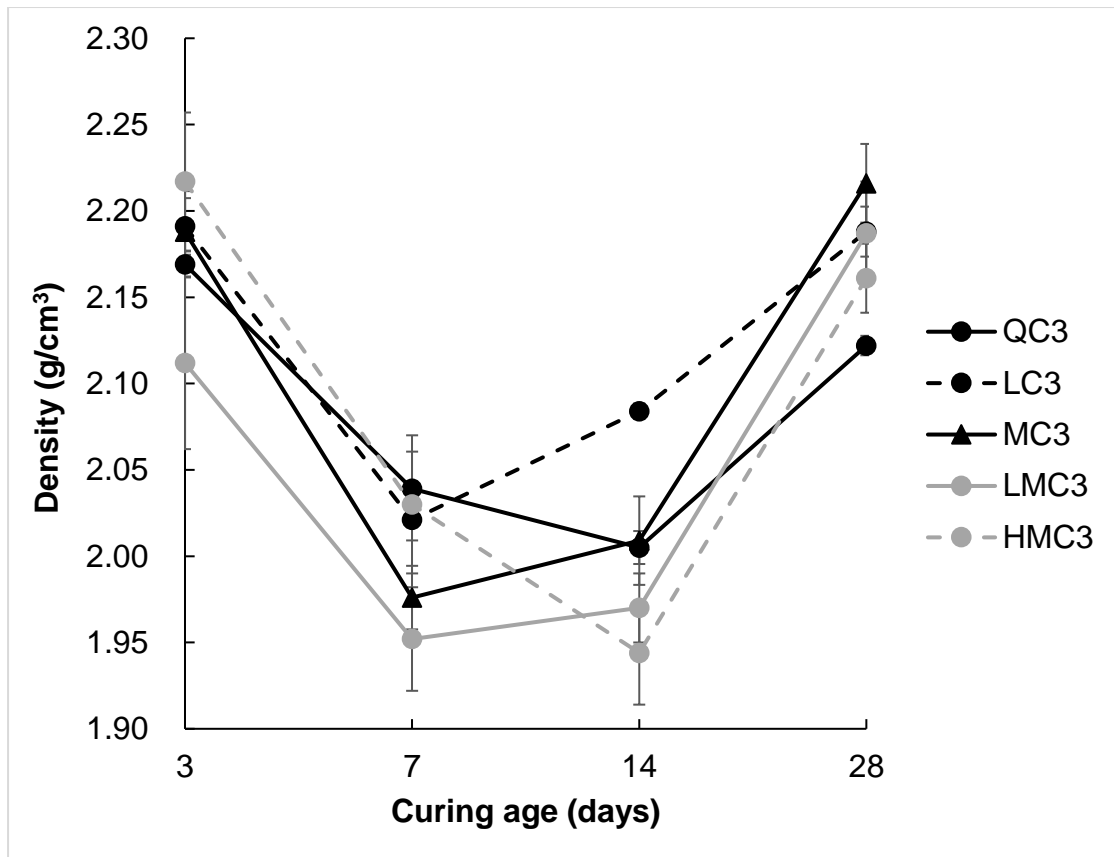
Fig. 5.1 Density at 3, 7, 14 and 28 days for: QC3, LC3, MC3, LMC3, and HMC3

Variations in water absorption can be ascribed to the differences in pore structure (e.g. pore size) of the samples. From **Fig. 5.2**, the LC3 sample revealed the lowest water absorption through all curing ages, indicating its densest microstructure. It was shown that the type of magnesium-based carbonate did not affect the pore refinement significantly, while the calcium carbonate showed a more critical effect on the refinement of pores. It should be noted that, except for QC3 samples, water absorptions of all samples were reduced after 14 days, which may be because of the refined effect provided by carboaluminates. Higher water absorptions were observed in samples containing magnesium-based carbonates (i.e. MC3, LMC3 and, HMC3), compared to LC3 samples, which suggests these samples have a better capability of maintaining free water, which can be seen in **Fig. 5.3**, where samples containing magnesium-based carbonates demonstrated more wet cross-sections, compared with LC3 samples.
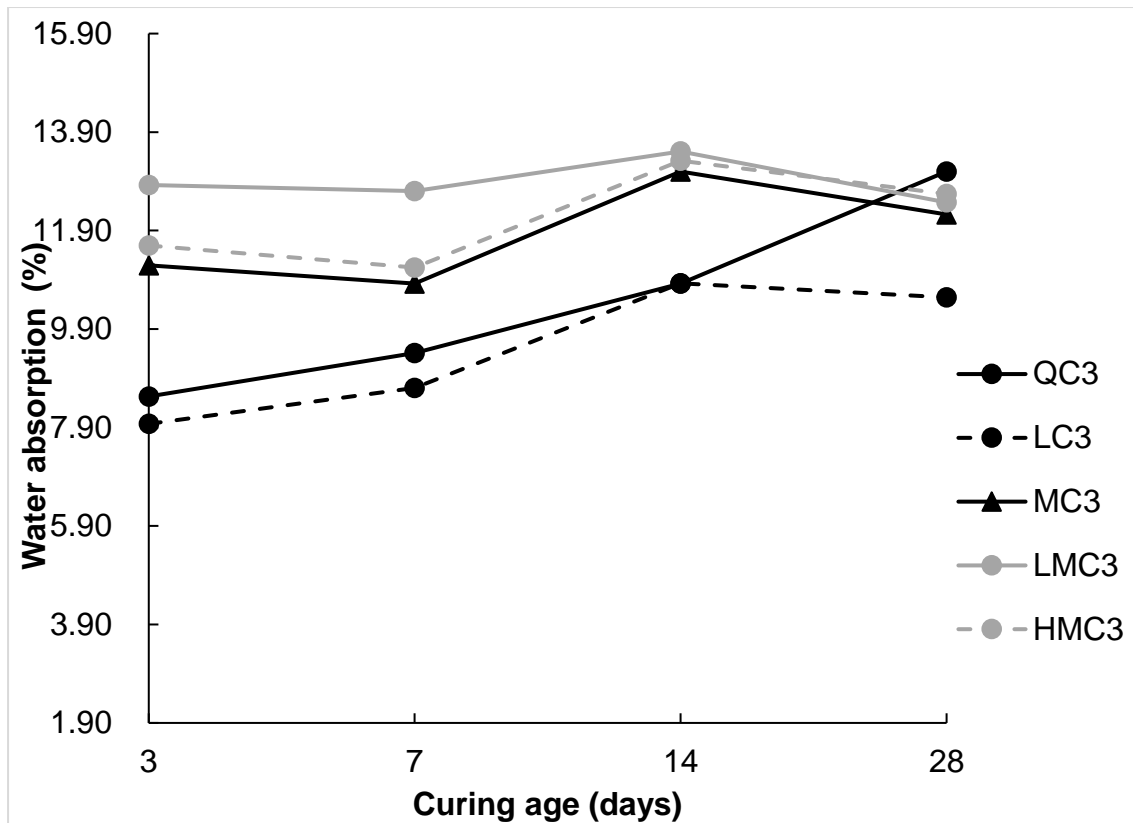
Fig. 5.2 Water absorption at 3, 7, 14 and 28 days for QC3, LC3, MC3, LMC3, and HMC3
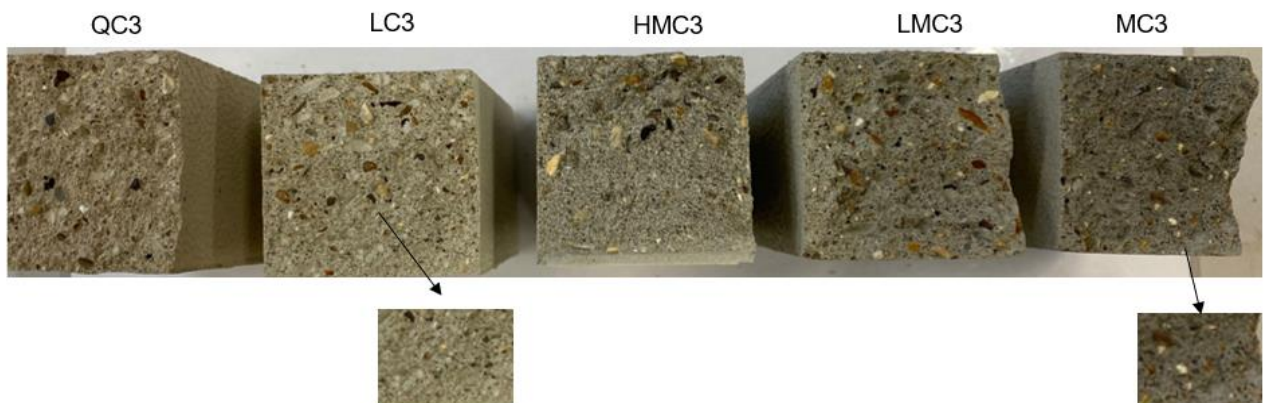
Fig. 5.3 Cross-sections of all samples at 14 days

5.2.3.2. Workability and Compressive Strength

The flowability of fresh mortars with different sources of carbonates is shown in **Table. 5.2**. Due to the high water demand of HMCs [56], with incorporating magnesium-based carbonates, the flowability of the mixture greatly decreased.

During the mixing of the mortar, it was noticed that magnesium-based carbonates tended to agglomerate and formed clusters, reducing the mobility of cement particles, and thereby resulting in a decrease in workability. In order to achieve constant workability for all Portland metakaolin mortars made from different carbonate sources, polycarboxylate ether (PCE) superplasticizer was used accordingly to achieve the acceptable flowability of samples, as shown in **Table. 5.1**. It should be noticed that LMC3 samples demonstrated the lowest flowability, even though they also contain hydrated magnesium carbonate as the carbonate source, which is similar to HMC3 samples. As the carbonate source in LMC3 is hydromagnesite ($4MgCO_3 \cdot Mg(OH)_2 \cdot 4H_2O$), whose crystalline water is less than that of dypingite ($4MgCO_3 \cdot Mg(OH)_2 \cdot 5H_2O$). This may explain the lower flowability of LMC3 samples.

Table. 5.2 Flowability of Portland metakaolin cement with different carbonates

ID	QC3	LC3	MC3	LMC3	HMC3
F (mm)	174	171	157	129	158

The compressive strength of all samples under curing up to 28 days is presented in **Fig. 5.4**. During all ages investigated, a distinct difference in strength is observed between the LC3 mix and magnesium-based carbonates mixes (i.e. MC3, LMC3, and HMC3), which highlights the importance of carbonate sources. Compared to other materials, the use of calcite along with metakaolin is found to have considerable advantages. A possible explanation for the increase in strength might be the formation of carboaluminates during the synergetic reaction of metakaolin with calcite, which also explains the fact that the highest strength always appears in LC3 samples at all ages. It is worth noting that, despite the presence of carboaluminates in the MC3 mix, the compressive strength was not significantly impacted by the formation of these compounds as it was with the LC3 mix. Unlike calcite, magnesite and HMCs did not release additional calcium ions that were required by some hydration reactions upon dissolution, which might lead to the low strength. This finding agrees well with another study [102], which only investigated

magnesite as the alternative carbonate in Portland metakaolin cement. In addition to this study, there is no other research reported the use of magnesite in Portland metakaolin cement.

Compared with magnesite ($MgCO_3$), HMCs (i.e. $4MgCO_3 \cdot Mg(OH)_2 \cdot 5H_2O$ and $4MgCO_3 \cdot Mg(OH)_2 \cdot 4H_2O$) used in this study have different molecular structures, which contain hydroxyl and crystalline waters. However, the different molecular structures of magnesium-based carbonates did not show a distinct effect on the mechanical property of samples. Therefore, the critical factor to affect the properties of Portland metakaolin cement is not only the reaction between the carbonates and other phases, but also falls in the filler effect of the carbonate source.
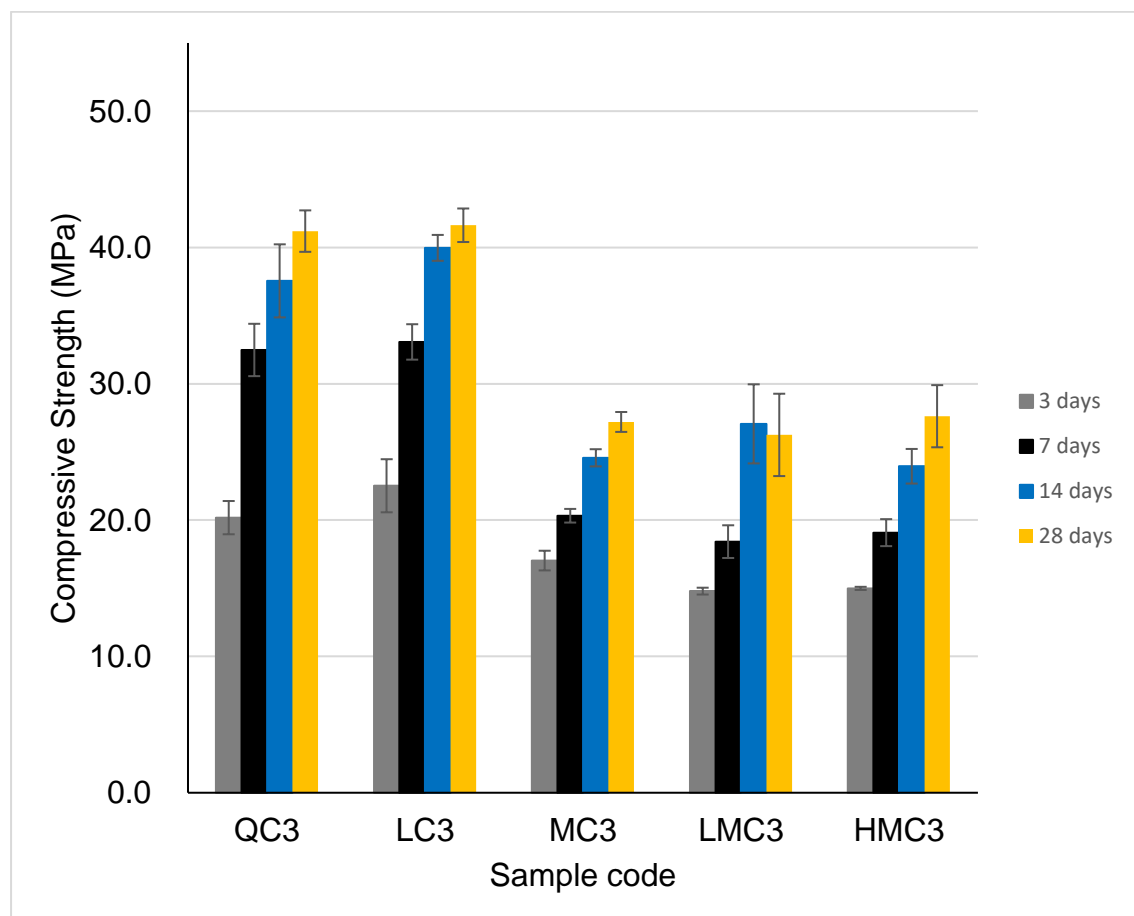
Fig. 5.4 Compressive strength of QC3, LC3, MC3, LMC3 and HMC3 at 3, 7, 14 and 28 days

5.2.3.3. XRD

XRD patterns of hydrated Portland metakaolin cement blends at 3 and 28 days with various carbonate sources are shown in **Fig. 5.5**. At 3 days, the higher amount of Hc was observed in QC3 and LC3 samples, which can explain their high compressive strengths, as carboaluminate can enhance strength by refining the pores [101,208]. This is also in line with the water absorption results, shown in **Fig. 5.2**. With the formation of carboaluminate, the reaction between portlandite ($Ca(OH)_2$) and excess alumina from metakaolin was inhibited, therefore, CH maintained in QC3 and LC3 samples (**Fig. 5.5 (a)**).
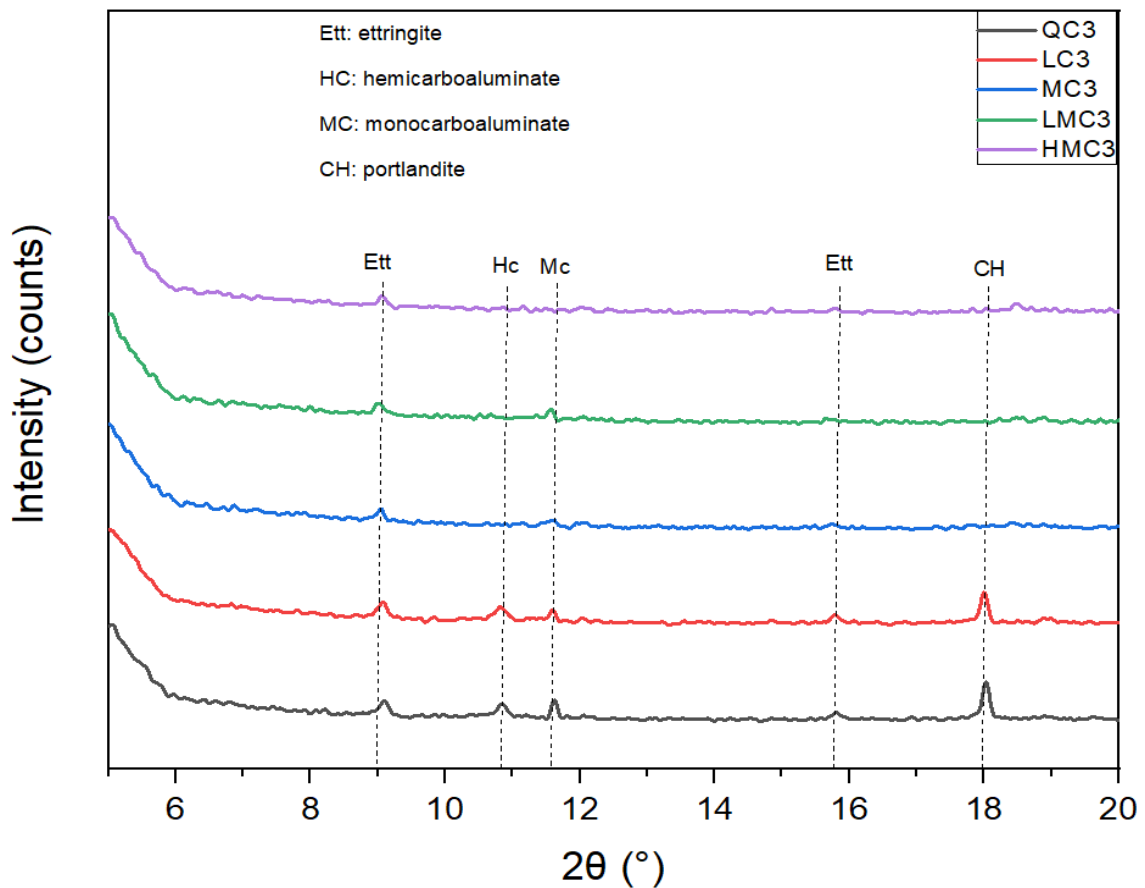
(a)
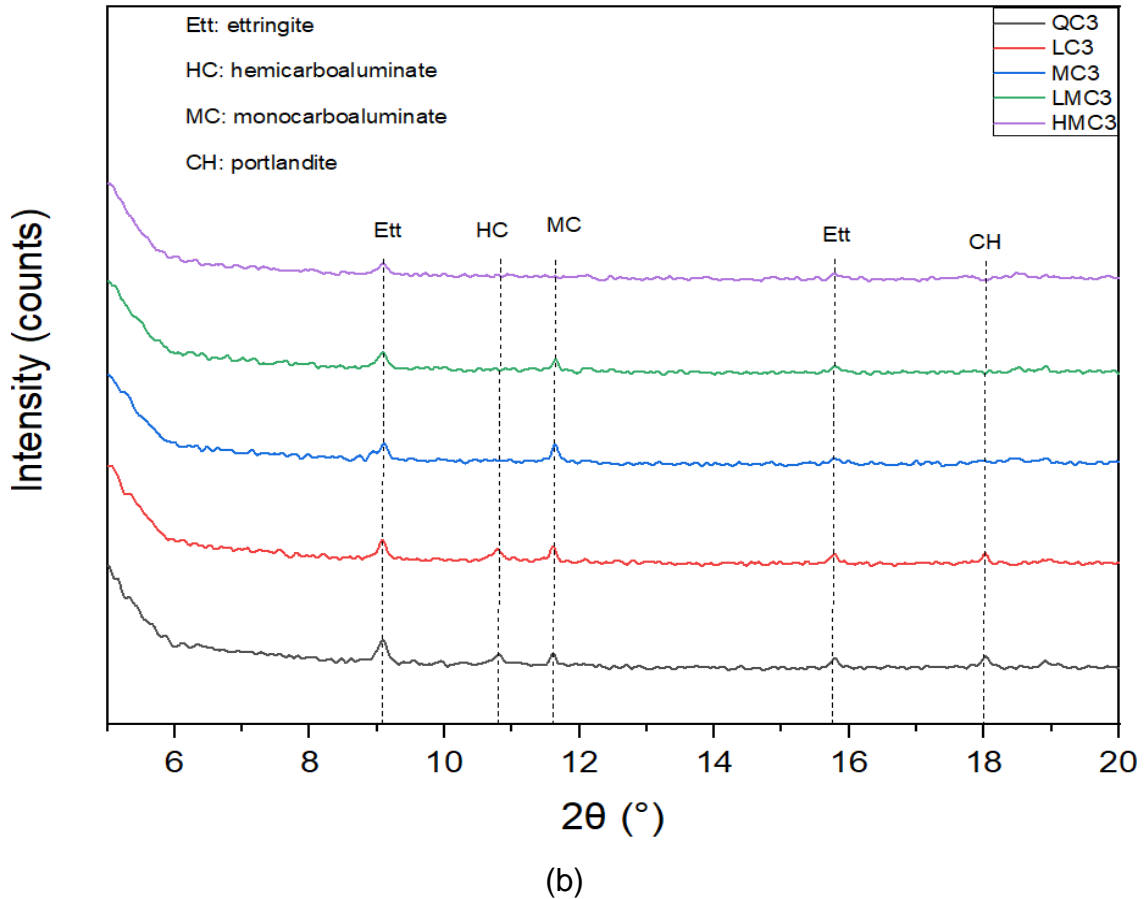
Fig. 5.5 XRD patterns of sample pastes at (a) 3 days and (b) 28 days (Ett: ettringite, Hc: hemicarboaluminate, Mc: monocarboaluminate, CH: portlandite)

At 28 days, portlandite was almost completely consumed as a result of hydration. In samples LC3 and QC3, the amounts of hydration products such as ettringite, Hc and Mc were similar, which agrees well with their comparable compressive strengths. In other words, mechanical properties were mainly dominated by these products. The CH content in the samples with magnesium-based carbonates was lower than that in other samples (i.e. QC3 and LC3), which suggests that metakaolin consumed CH to generate additional amorphous C-A-S-H gel.

Additionally, the reduced intensity of AFt peaks was found in samples containing magnesium-based carbonates, where the decreases were more pronounced in LMC3 and HMC3 samples. As the carbonate sources in LMC3 and HMC3 samples were dypingite and hydromagnesite, which both have hydroxyl, thereby, leading to a high alkali concentration, then decomposing

AFt. Intriguingly, Mg^{2+} released from magnesite/HMCs should precipitate as brucite ($Mg(OH)_2$), however, the brucite peak (at ~19° 2θ) was not observed in MC3, LMC3, and HMC3 at either 3 or 28 days. The magnesium ions may involve in the formation of hydrotalcite ($Mg_6Al_2CO_3(OH)_{16} \cdot 4H_2O$), whose peak highly overlapped with the peak of Mc [101].

5.2.3.4. SEM

All samples after 28 days of curing were examined by SEM, as depicted in **Fig. 5.6**. A large number of needle-like ettringite crystals can be found in all samples, which matches well with XRD results. In QC3 and LC3 samples, obvious honeycomb-like C-(A)-S-H was observed, which was formed through a pozzolanic reaction, leading to a denser and more compact microstructure. The densified microstructure can also explain the high compressive strengths and low water absorptions of QC3 and LC3 samples, as demonstrated in **Fig. 5.2** and **Fig. 5.4**. Different from QC3 and LC3 samples, magnesium-based carbonates series samples (i.e. MC3, LMC3, and HMC3) showed inferior mechanical properties, which could be related to their relatively loose structures with some pores, observed from the SEM images (**Fig. 5.6 (c)**, **(d)**, and **(e)**).

(a)

(b)

(c)

131
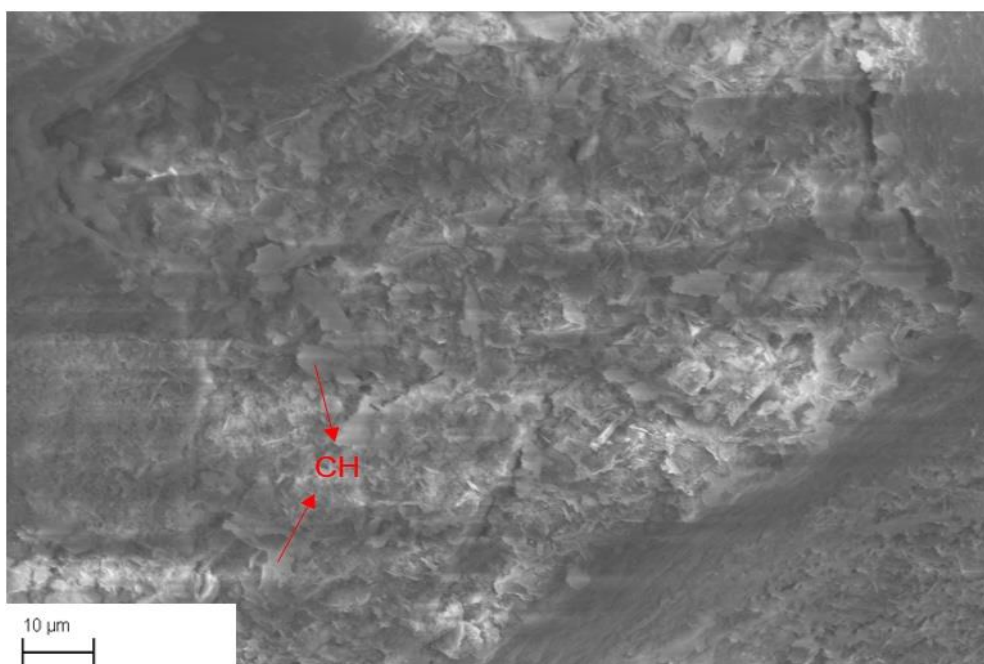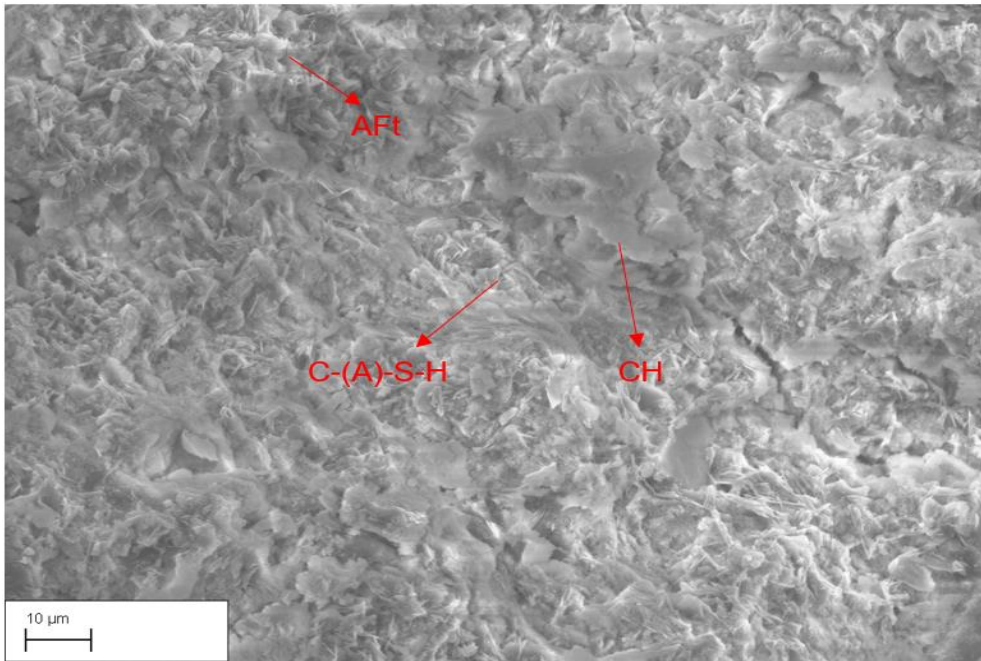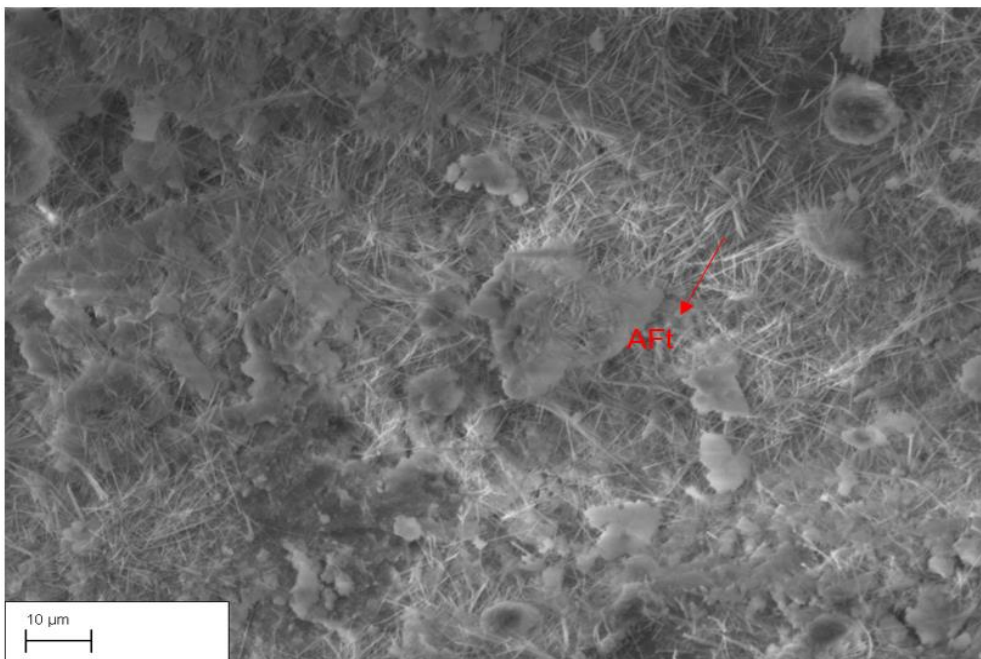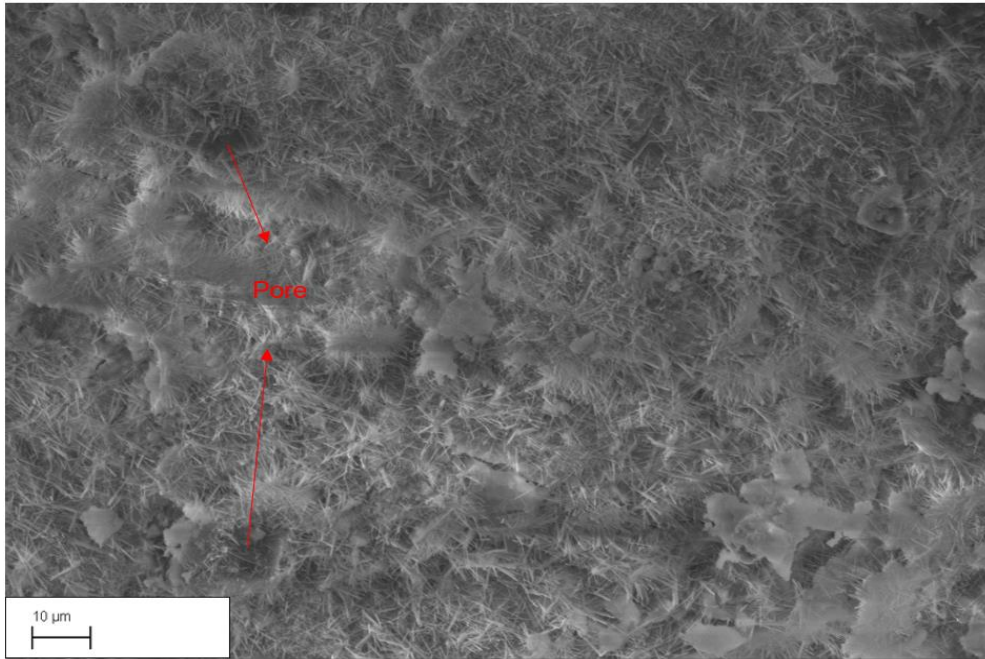
(d)
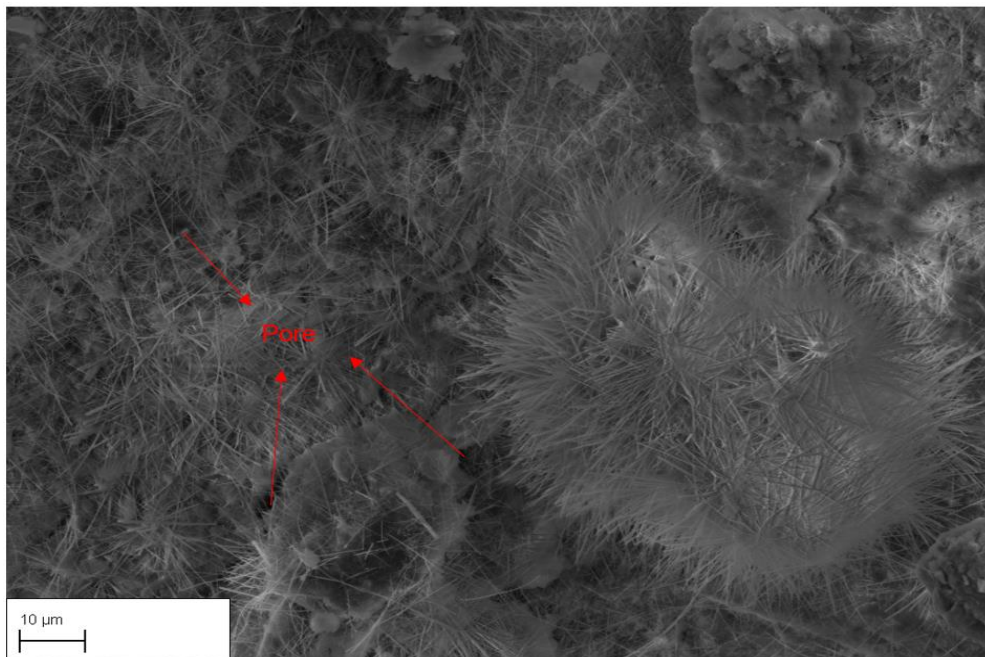
(e)

Fig. 5.6 SEM images of (a) QC3; (b) LC3; (c) MC3; (d) LMC3; (e) HMC3 with a magnification of 3000 after 28 days of curing

5.2.3.5. Carbonation

A phenolphthalein layer was sprayed on the surface of the fracture to investigate the depth of carbonation. As the carbonation of CH leads to a reduced pH value, the colour of the carbonated surface does not change, while the uncarbonated area becomes pink. The images of sample surfaces were then processed by the software, ImageJ, to calculate the carbonated area, which was characterized by the ratio of the uncarbonated area to the cross-sectional area of the sample. The original cross-sections of samples sprayed by phenolphthalein and the images processed by ImageJ are demonstrated in **Fig 5.7 (a)**. Visually, magnesium-based carbonates series samples showed bigger areas without colour change, which were indicators of a higher carbonation degree. The carbonation degree is shown in **Fig. 5.7 (b)**, where the area of a circle in the chart refers to the carbonated area. MC3 and LMC3 demonstrated the first and second-highest carbonation degrees, which could be attributed to their loose and porous microstructure. It was reported that CH content in the binder can affect carbonation [209]. The high content of CH can reduce the carbonation degree in the binders, which is also supported by this study, as a higher amount of CH was detected by XRD (**Fig. 5.5**).

QC3   LC3   MC3   LMC3   HMC3
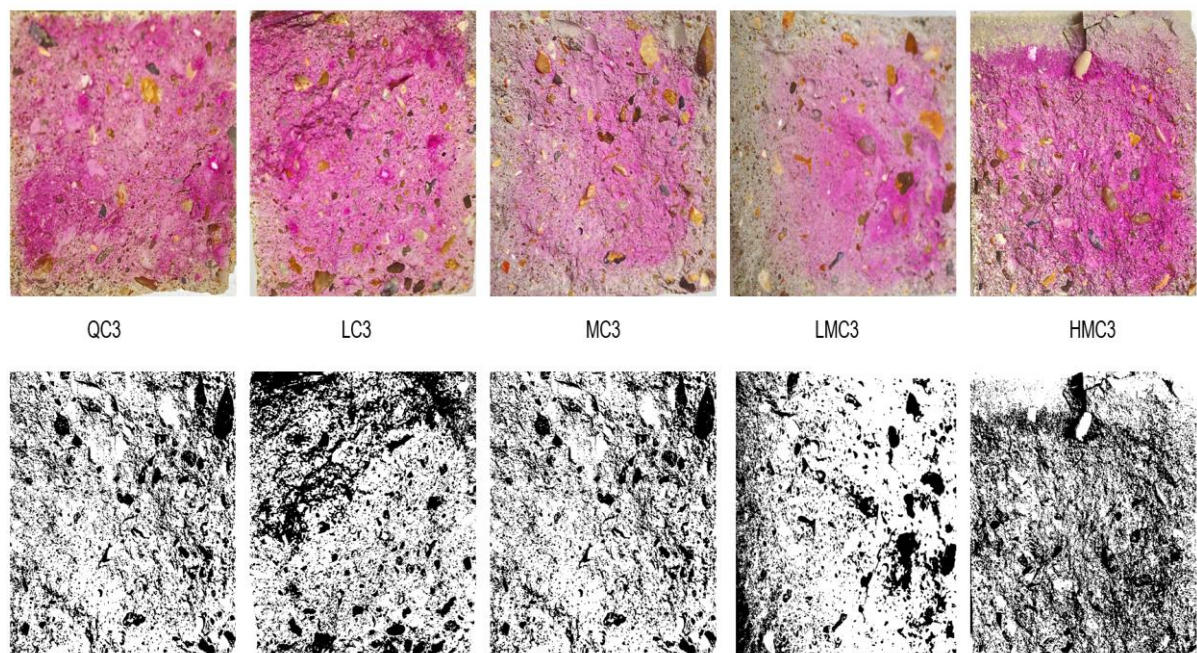
(a)
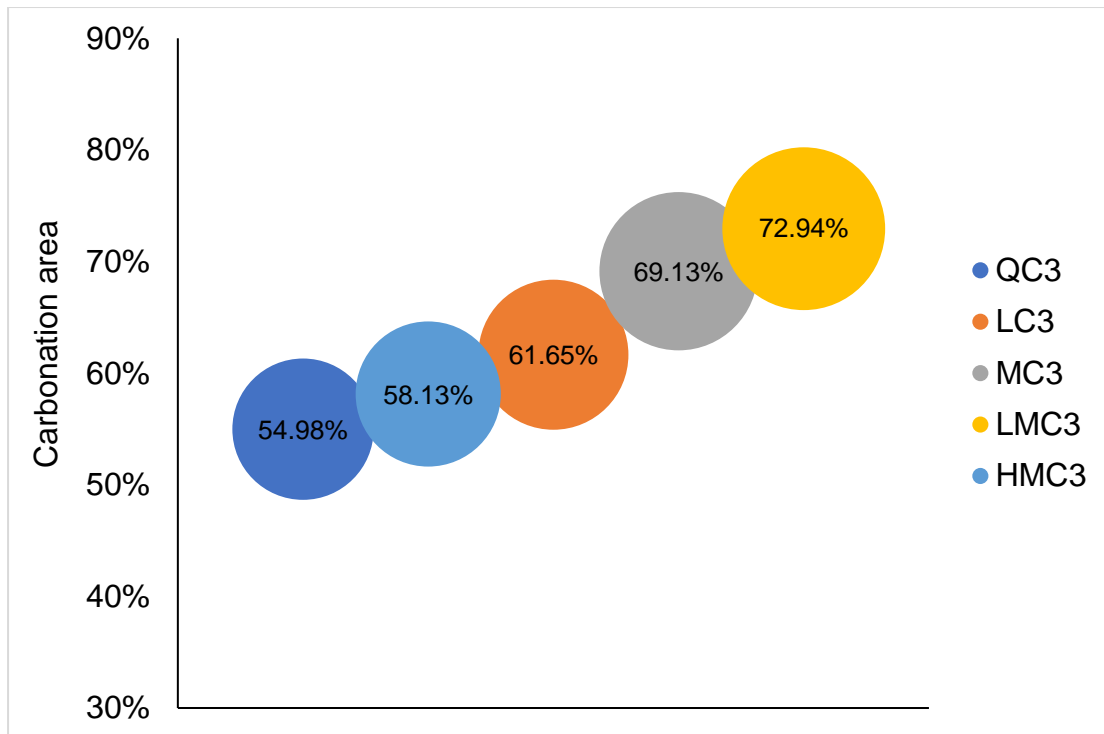
(b)

Fig. 5.7 Carbonation degree measured with a phenolphthalein indicator: (a) upper images: original image of carbonated cross-sections; lower images: ImageJ processed cross-section; (b) carbonated area calculated by ImageJ

As various carbonates were used in this study, the carbonation degrees of samples also varied. Consequently, the carbonate does not only affect the mechanical performance of the binders, but also influences their durability. This further emphasizes the importance of carbonate sources in Portland metakaolin cement.

5.2.4. Conclusions

This section investigated different carbonate sources and non-carbonate powders in Portland metakaolin cement binders by examining their mechanical properties, microstructure, and durability (carbonation depth). The main findings are listed below:

1. Except for HMC3 samples, the formation of carboaluminates was

observed in other samples, which indicates the reaction between the magnesium-based carbonates (i.e. $MgCO_3$ and $4MgCO_3 \cdot Mg(OH)_2 \cdot 4H_2O$) and AFm, proving the feasibility of using magnesium-based carbonates into the Portland cement with the presence of metakaolin.

2. The formation of carboaluminates proved a distinct advantage of carbonate addition in terms of compressive strength. LC3 exhibited the highest compressive strength as it formed the highest amount of carboaluminates. Additionally, the consumption of CH can be prevented by the formation of carboaluminates.

3. Carbonate sources affect the properties of Portland metakaolin cement, in terms of mechanical strength, microstructure, and durability. This is mainly through changing the hydration products in the binder. Magnesite ($MgCO_3$), hydromagnesite ($4MgCO_3 \cdot Mg(OH)_2 \cdot 4H_2O$), and dypingite ($4MgCO_3 \cdot Mg(OH)_2 \cdot 5H_2O$) are not considered as the desirable carbonates sources in this binder system. When using them as carbonate sources in Portland metakaolin cement, inferior mechanical strength, microstructure, and durability were observed.

5.3. Lab-made HMCs in Portland Metakaolin Cement

5.3.1. Introduction

As mentioned in **Section 5.2**, hydromagnesite ($4MgCO_3 \cdot Mg(OH)_2 \cdot 4H_2O$) and dypingite ($4MgCO_3 \cdot Mg(OH)_2 \cdot 5H_2O$) have been selected as the carbonate sources to replace the limestone in LC3 blends, however, the binders with these magnesium-based carbonates failed to demonstrate satisfactory performances. As nesquehonite ($MgCO_3 \cdot 3H_2O$) is considered the most reactive HMC, it is expected to perform better in the magnesium-based carbonates series blends than the magnesite and other HMCs. As per **Chapter 4**, the HMCs produced by carbonating MgO-L-Asp blend, which contains nesquehonite as the main phase, were used in this study to replace

the carbonate. The lab-made HMCs need to be in the powder format, however, crushing HMCs by ball milling machine released a lot of heat during the milling. One problem with nesquehonite is its instability at temperatures above 50 °C, making it unsuitable for some applications involving high temperatures. In such cases, nesquehonite transforms into thermodynamically more stable HMCs, such as dypingite or hydromagnesite. The high temperature could be a factor that affects the mechanical performance and the hydration reaction. Therefore, to avoid the high temperature, the hardened paste produced by carbonating MgO-LAsp blend was grounded into powders by using an agate mortar and pestle and then added to the blend.

5.3.2. Mix Design and Sample Preparation

The mixes in the study are referred to as either QC3, LC3, MC3, or AMC3 based on the variable component present in them. The mix compositions of all the blends investigated in the study are given in **Table. 5.3**. As discussed in **Chapter 4**, when magnesia paste was subjected to CO_2 curing, the addition of L-Asp was to control the polymorphy of HMCs. This lab-produced HMCs were labelled as Asp-magnesium-carbonates (AMCs). Therefore, the mixtures that contained AMCs were called AMC3 in this study. The XRD pattern of lab-produced HMCs is shown in **Fig. 4.14 (d)**, which contains the nesquehonite ($MgCO_3 \cdot 3H_2O$) and unreacted MgO as the main phases. Pure magnesite (M) was also used in this study to produce MC3 blend.

A water-to-binder (w/b) ratio of 0.55 was applied to all samples with different dosages of PCE. Each sample was mixed for 2 min at a mortar mixer, and then cast into $40 \times 40 \times 40$ mm^3 moulds. All samples were placed in an environmental chamber and demoulded after 1 day, then the samples continued to be cured at 20 °C, and 95% relative humidity (RH) up to 3, 7, 28, and 90 days.

Table. 5.3 Compositions of mixtures investigated in this section (wt.% except for w/b)

ID	w/b	PC	MK	Q	LS	M/AMCs	Gyp	PCE
QC3	0.55	55	30	15			2	2
LC3	0.55	55	30		15		2	2
MC3	0.55	55	30			15	2	5
AMC3	0.55	55	30			15	2	5

5.3.3. Results and Discussion

5.3.3.1. Hydration Heat

The rate of heat evolution per gram of cement measured using isothermal calorimetry for all mixes is shown in **Fig. 5.8**. The hydration peaks of silicate (i.e. at ~6 h) were obvious in QC3 and LC3 blends, and the age of reaching maximum peak heat was also enhanced with the involvement of limestone. The depression of silicate reaction in magnesium-based carbonates series samples was observed. As discussed in **Section 5.2.3.2**, magnesium-based carbonate particles have a very high specific surface area and tend to agglomerate, which can hinder the movement of water molecules, resulting in a decrease in the availability of water for hydration.

Another peak that occurs at ~8 h indicates the consumption of aluminum ions in the formation of C-(A)-S-H gel. This peak was obvious in AMC3 samples, which shows the high amount of carboaluminates formed during the hydration, as shown in XRD results (**(c)**
Fig. 5.12 (c)). The difference between the silicate and aluminate hydration peaks of all mixes suggests that the presence of a carbonate source can affect the initial stage of hydration (<24 h).

The sulfate peaks, which correlated with sulfate depletion, varied with

carbonates used [210]. The peak of AMC3 occurred at ~46 h, while those of QC3 and LC3 at ~35 h. The appearance of the sulfate peak is primarily attributed to the involvement of gypsum in the reaction. As shown in **Fig. 5.8**, Asp-HMCs can delay the reaction of the sulfate phase. This may be because of the sulfate in gypsum forming complexed with reactive Mg^{2+}, which adsorbed onto the positively charged C_3A surface, thus inhibiting hydration. However, this retarded effect did not occur in samples containing low-solubility magnesite (MC3), due to the more available surface of C_3A that was not covered by Mg^{2+}. It can be also seen in XRD pattern (**Fig. 5.12 (a)**), MC3 contained the smallest ettringite peak, which was because of the higher amount of C_3A, led to the conversion from ettringite to AFm.
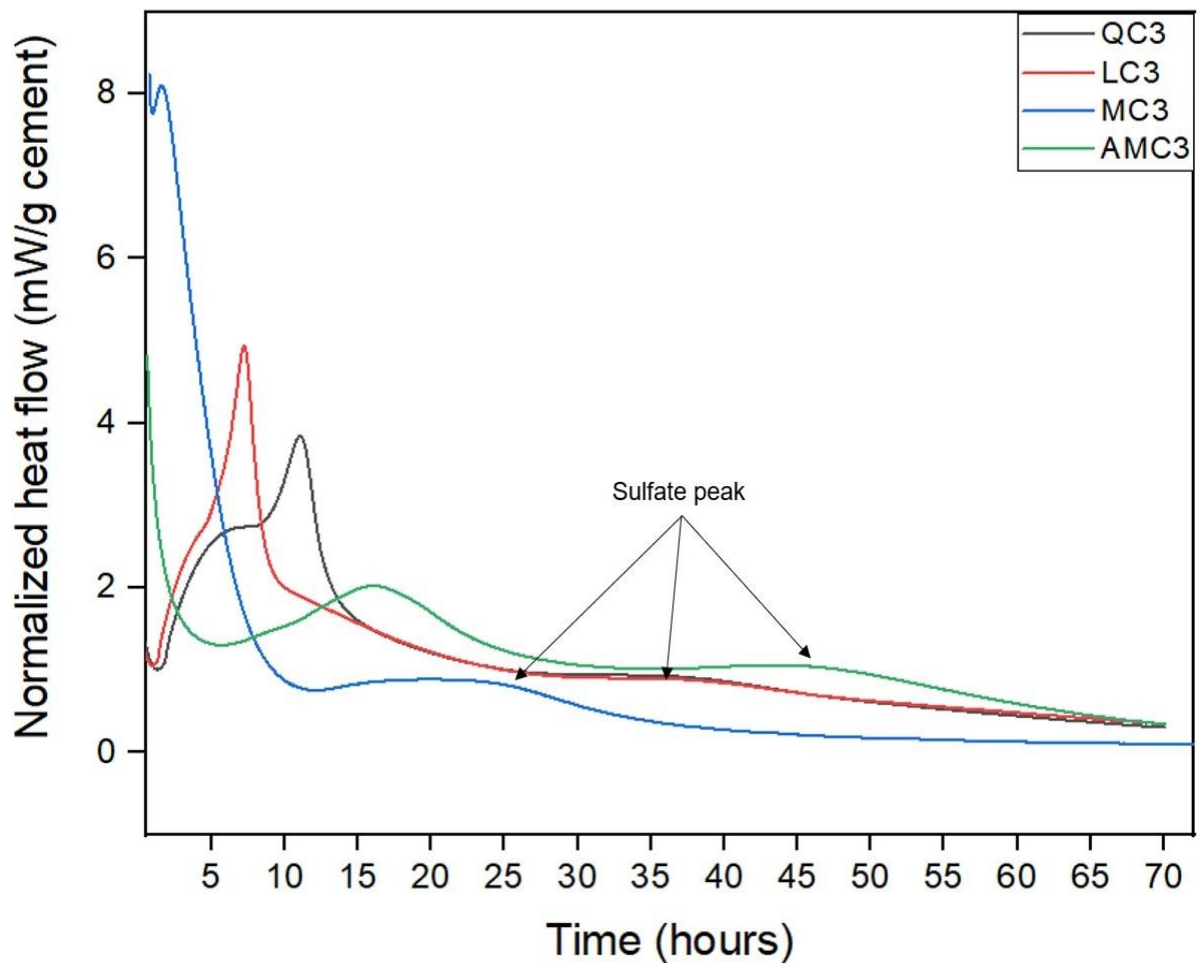
Fig. 5.8 Normalised heat release per gram of cement for QC3, LC3, MC3, and

The cumulative heat released per gram of cement for 3 days is shown in **Fig. 5.9**. Similar values were observed for QC3 and LC3 mixes during the first 72 h of curing even though there was no carbonate source in QC3, which could be because of the intensive pozzolanic reaction provided by the high metakaolin content in the mixes. The lower hydration heat of the MC3 sample was because of the low dissolution of the magnesite, inhibiting it from being involved in the reactions. It can be seen that the AMC3 mix exhibited the highest cumulative heat after around 52 h of curing, suggesting its superior hydration after 3 days.
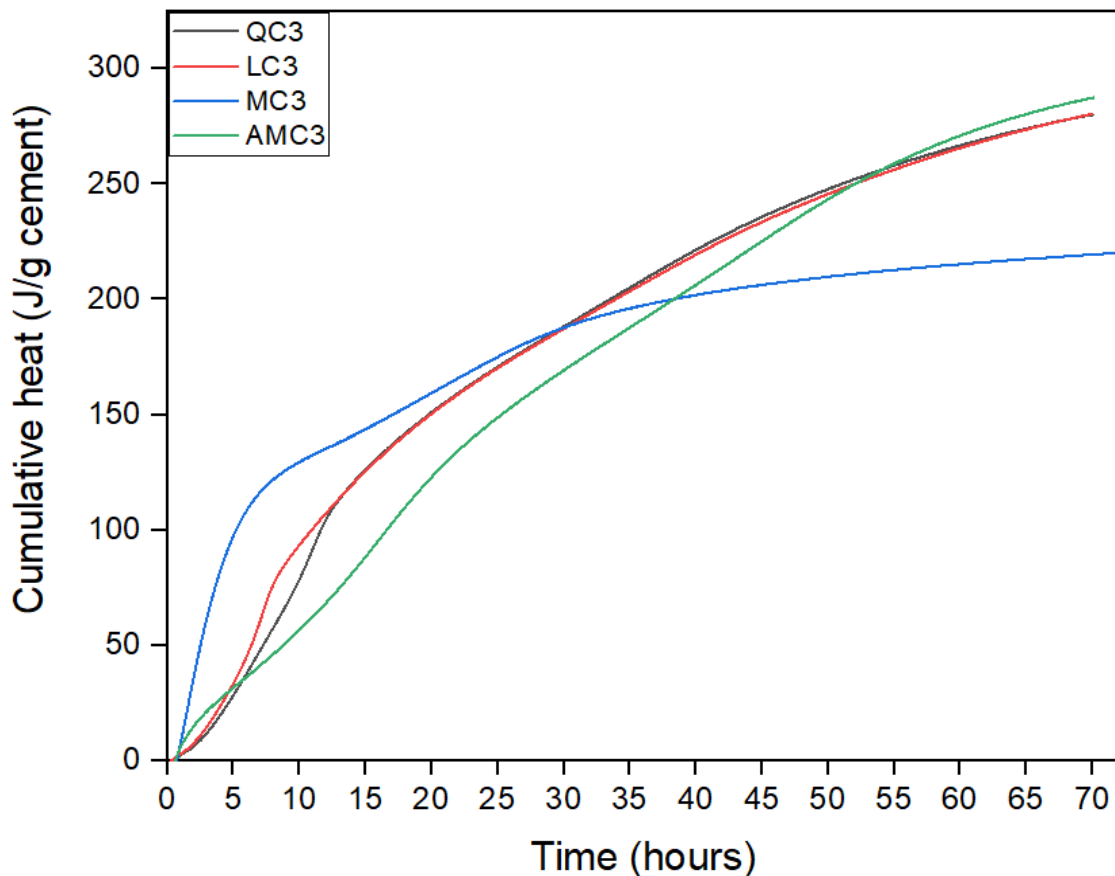
Fig. 5.9 Cumulative heat released per gram of cement for QC3, LC3, MC3, and AMC3 up to 72 hours

5.3.3.2. Compressive Strength

The compressive strength of all mixes up to 90 days is depicted in **Fig. 5.10**. Except for MC3 samples, all samples showed similar strength at 3 days, suggesting their similar hydration degree, which is in line with the results in **Fig. 5.9**. Compared to other mixes, the total heat release of MC3 mix was much lower until 3 days, leading an inferior strength.

From 3 to 7 days, a noticeable increase of strength was observed in all mixes, which was because of the rapid formation of carboaluminates. AMC3 showed the highest 7-day compressive strength, which was 8% higher than that of the LC3 mix, reaching 32.4 MPa. Using lab-made HMCs successfully improved the early-age strength of Portland metakaolin cement.
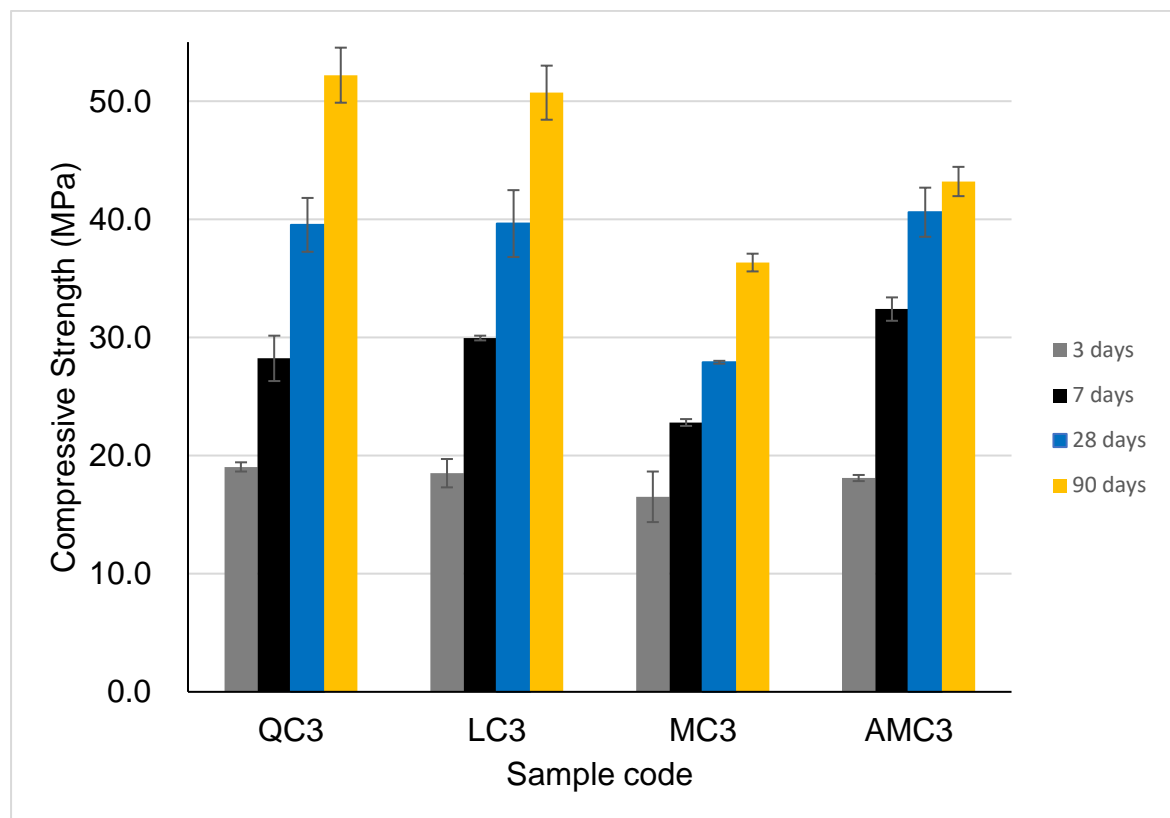
Fig. 5.10 Compressive strength of all mixes for up to 90 days

In this study, the compressive strength of all mixes was normalized against that of the LC3 mix, as shown in **Fig. 5.11**. At 3, 7, 28, and 90 days, the compressive strengths of LC3 blend were 18.5, 30, 39.6, and 50.7 MPa,

respectively. The AMC3 revealed the enhancement of 7- and 28-day compressive strength, compared with LC3 samples, although the increases were only 8% and 2%, respectively. The MC3 mix showed lowest strengths at all ages, which demonstrates that the type of magnesium-based carbonate is crucial in Portland metakaolin cement. In terms of mechanical strength, nesquehonite is an alternative carbonate source, while magnesite seems to be an undesirable carbonate for Portland metakaolin cement. However, after 90 days, the strength of the AMC3 mix was lower than that of the LC3 mix, but it still can achieve a satisfactory compressive strength of 43.2 MPa. Interstingly, the calcite or quartz had little impact on compressive strength in the long term, suggesting the filler effect provided by quartz [102,211].
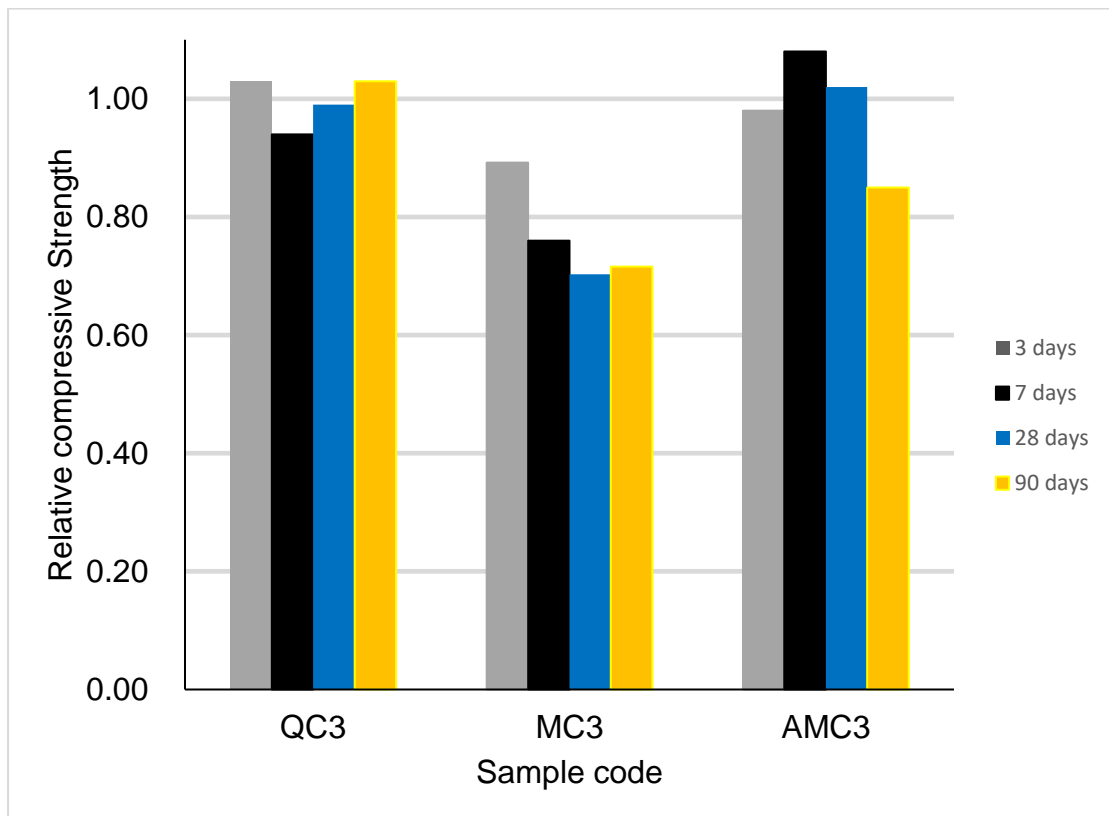
Fig. 5.11 Normalised compressive strength of QC3, MC3, and AMC3 normalized compressive strength of LC3 mix from 3 to 90 days

5.3.3.3. XRD

XRD patterns of QC3, LC3, MC3, and AMC3 samples at 7, 28 and 90 days

are shown in **Fig. 5.12**. Overall, the phase assemblage was similar to that in **Section 5.2**. As discussed in **Section 5.2.2.3** (i.e. XRD results), the formation of carboaluminates at the early ages leaded to superior mechanical properties. High intensity of Mc can be observed in the AMC3 mix at 7 and 28 days (**Fig. 5.12 (a)** and **(b)**), which supports the finding that carboaluminates contribute to the majority of strength at early ages. The CH peaks in MC3 and AMC3 were negligible for 3 days, indicating that CH was consumed by the formation of hydrotalcite ($Mg_6Al_2CO_3(OH)_{16} \cdot 4H_2O$), whose peak highly overlapped with the peak of Mc [101]. While CH was maintained in QC3 and LC3 samples at 3 days, the absence of CH in MC3 and AMC3 samples could be an evidence of the formation of hydrotalcite. Remarkably, no magnesite and HMCs peaks were detected in the XRD patterns of MC3 and AMC3 during all ages, instead, the calcite peaks were observed in these binders. As the calcite of QC3 samples was from PC, the calcite peaks of MC3 and AMC3 samples were higher than that of QC3 samples, suggesting the formation of calcite in MC3 and AMC3 samples. An explanation might be that magnesite ($MgCO_3$) can be converted to calcite ($CaCO_3$) when it reacts in an environment containing calcium hydroxide ($Ca(OH)_2$), this may also explain the low CH content in MC3 and AMC3 samples.

(a)

(b)

(c)
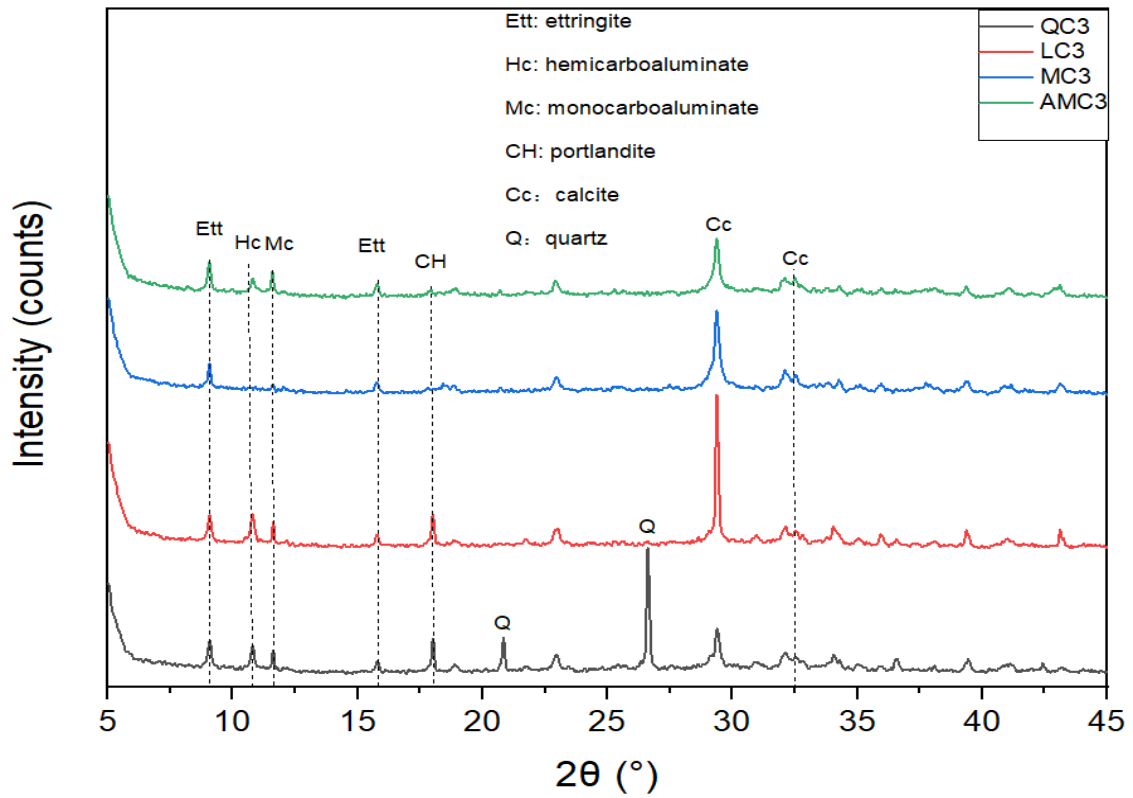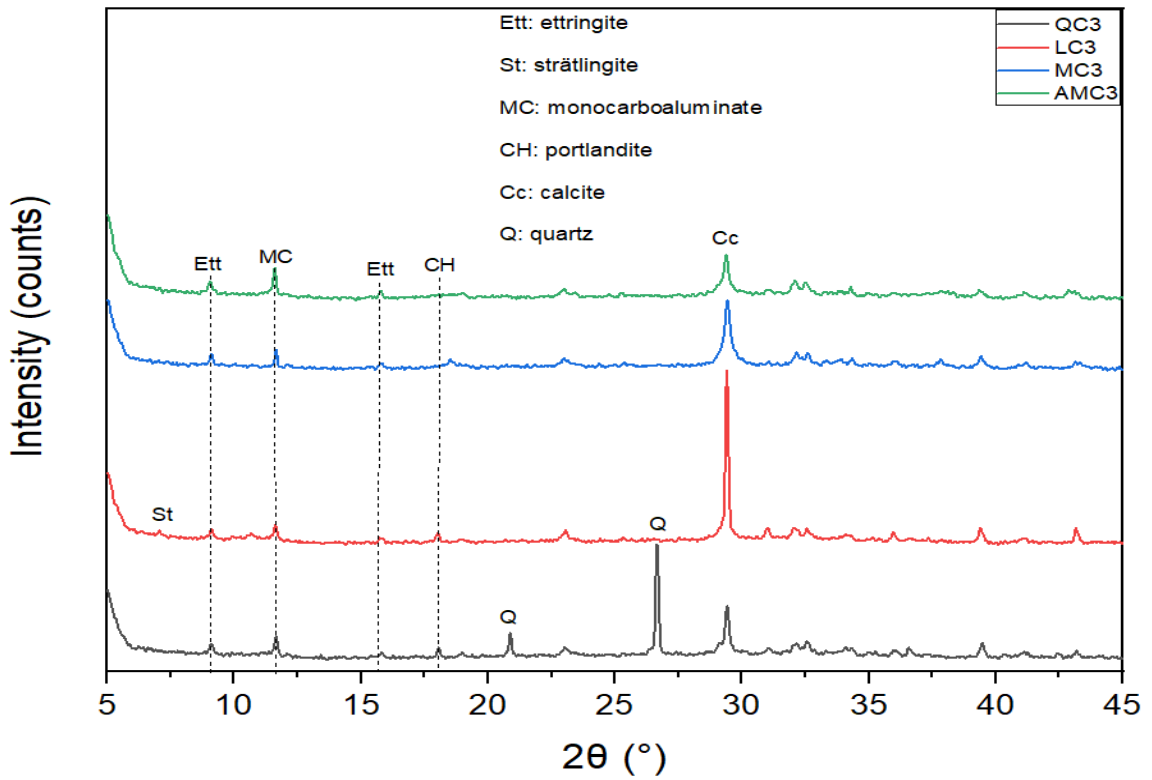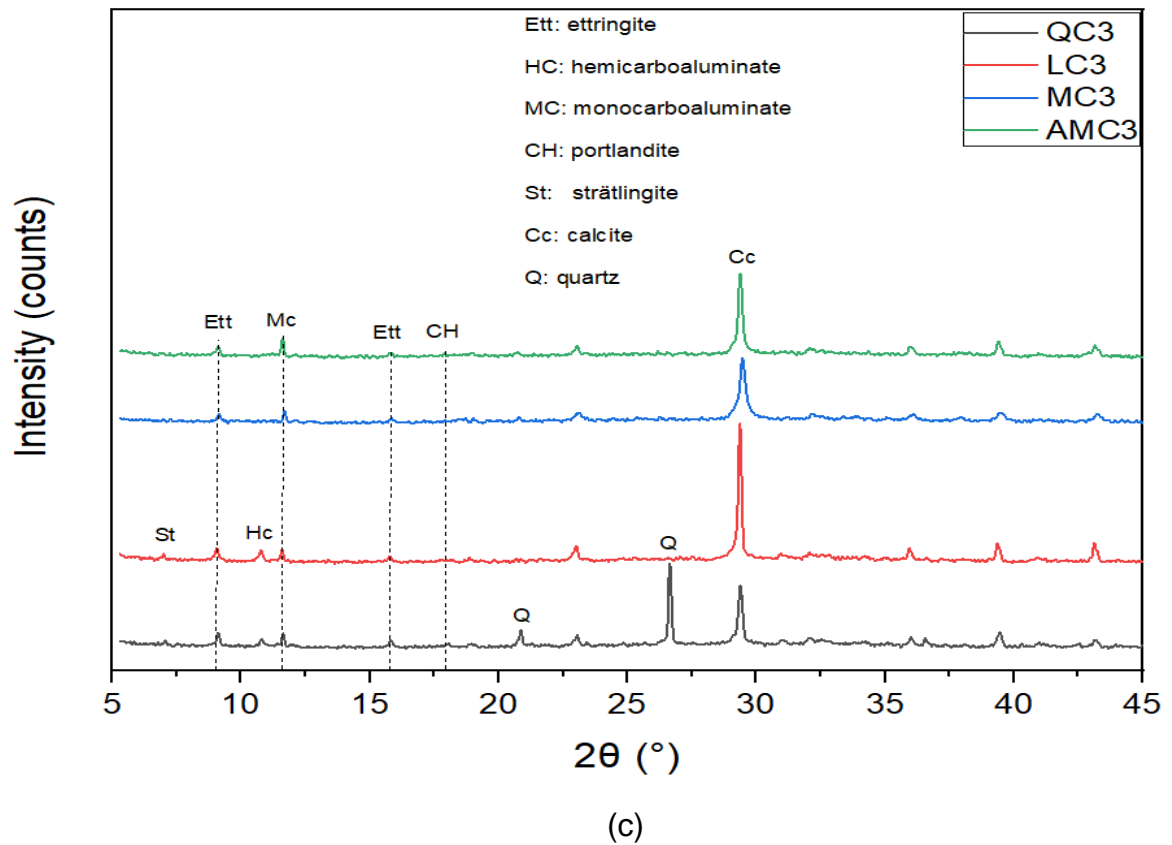
Fig. 5.12 XRD patterns of all sample pastes at (a) 7 days; (b) 28 days; (c) 90 days (Ett: ettringite, Hc: hemicarboaluminate, Mc: monocarboaluminate, CH: portlandite, St: strätlingite)

After 90 days, strätlingite can be detected in LC3 and QC3 samples, as shown in **Fig. 5.12 (c)**, while a small strätlingite peak was already observed in LC3 samples at 28 days. Strätlingite is formed through the reaction between the silica and the alumina from metakaolin, with the absence of CH and carbonate ions [88,101,102]. Therefore, the appearance of strätlingite is an indicator of the exhaustion of reactive carbonates in the blend. It should be noted that calcite still existed even after 90 days of curing, suggesting the carbonate source in Portland metakaolin cement binders not only worked as a CO_3^{2-} provider but also provided a filler effect. Although high-intensity Mc peak was observed in AMC3 samples, it did not show an outstanding strength at 90 days (**Fig. 5.10**), suggesting strätlingite can contribute more to the strength at the late age, compared to the carboaluminates. Additionally, the precipitation of $Mg(OH)_2$ (at ~19° 2θ) was still not observed in AMC3 samples, even though AMCs contain MgO as the ingredient. As previously mentioned, the

involvement of magnesium ions may contribute to the formation of hydrotalcite $(Mg_6Al_2CO_3(OH)_{16}\cdot 4H_2O)$.

5.3.3.4. TG/DTG

The thermogravimetric and derivative thermogravimetric curves of the samples at 28 days are shown in **Fig. 5.13 (a)** and **(b)**. The peaks at around 180 °C could be seen in all samples owing to the decomposition of carboaluminate [212], which is consistent with the XRD results (**Fig. 5.12 (c)**) demonstrating the various amounts of carboaluminate in samples. The decomposition of portlandite occured at ~450 °C, while only QC3 and LC3 had this peak. The absence of a peak at 450 °C in MC3 and AMC3 mixes indicates the consumption of portlandite in the pozzolanic reaction with metakaolin. The peak at ~ 750 °C was likely ascribed to the decomposition of carbonate. This peak in LC3, MC3, and AMC3 mixes is possibly due to the unreacted carbonate sources, providing the potential for further reaction. In terms of QC3, some carbonates were from the cement, as XRD showed there was only a minor amount of calcite in the cement. Other calcite was from the carbonation by CO_2 in the air, which is shown in **Fig. 5.7**. According to the intensity of this peak, LC3 samples showed the highest amount of unreacted carbonate, while AMC3 samples the lowest amount. This phenomenon may explain the LC3 mix had a higher increase in compressive strength than that of the AMC3 mix from 28 to 90 days, as there was still an amount of carbonate that existed and could be involved in the hydration, contributing to the development of strength.
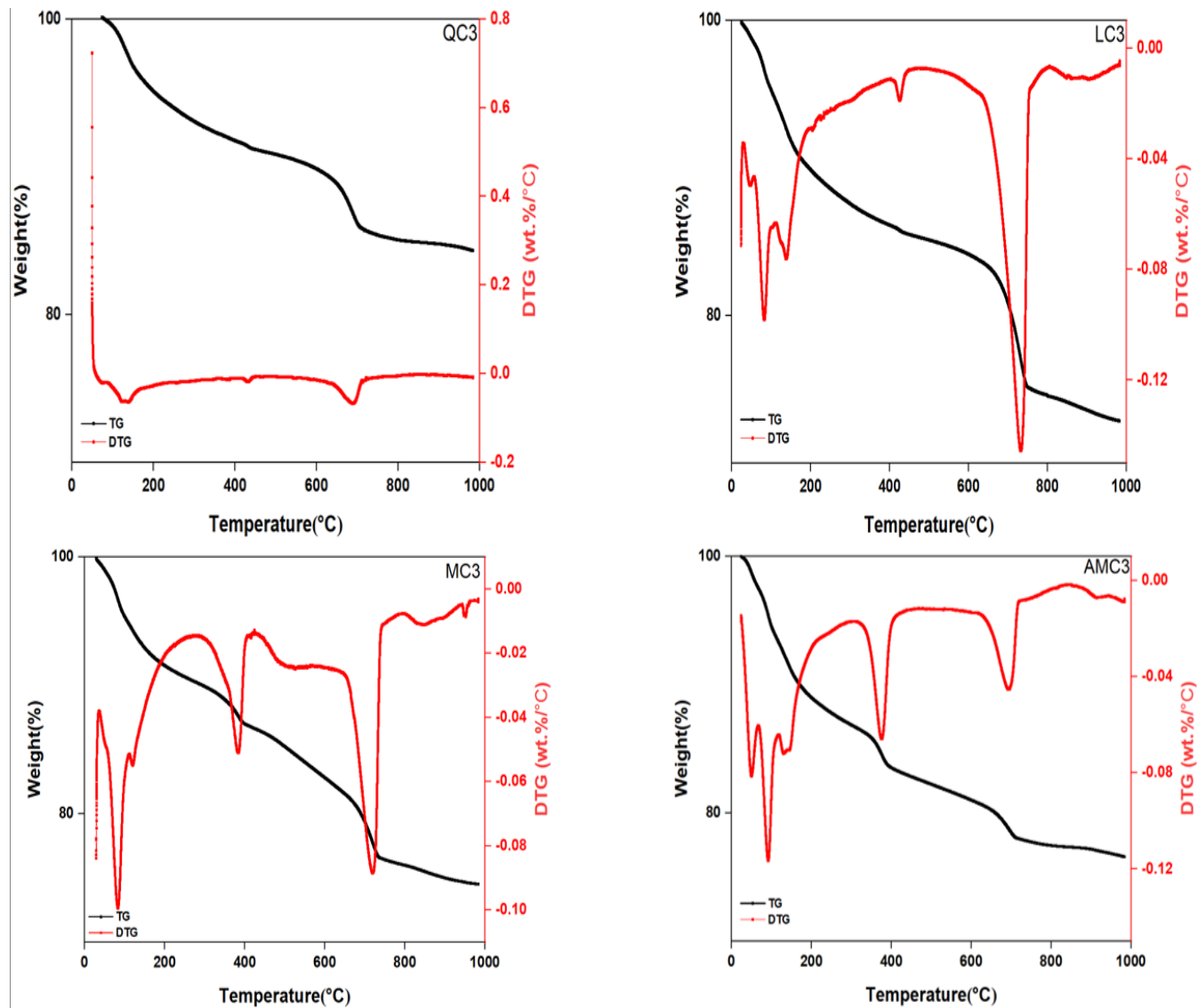
Fig. 5.13 Thermogravimetric analysis of all samples after 28 days of curing
(black line: TG curve; red line: DTG curve)

5.3.3.5. SEM

Since the microstructure of LC3 and QC3 have already been characterized in **Section 5.2.3.4**, this section only focuses on the microstructure of MC3 and AMC3 samples, as depicted in **Fig. 5.14 (a)** and **(b)**. Compared to the AMC3 sample, the MC3 sample primarily comprised a needle-like phase. Because of the separation of these needle-like phases, a spatial network structure with more pores was formed. Water cannot be prevented from entering such a structure, and as a result, the properties of the sample was greatly affected by

it. For instance, high water absorption was achieved in MC3, as shown in **Fig. 5.2**. From **Fig. 5.14 (b)**, compared with the MC3 sample, AMC3 specimens formed more gelatinous phases and the microstructure was relatively dense. Additionally, the size of the needle-like phase was also superior. Water can be prevented from entering such structure effectively, thereby the AMC3 may have better water resistance (i.e. low water absorption). The pozzolanic reaction between silicate and alumina phases in metakaolin resulted in amorphous C-(A)-S-H gel when metakaolin was added to the magnesium-based binder.

C-(A)-S-H gel networks protected the needle-like phases by surrounding them. Additionally, the incorporation of metakaolin into the magnesium-based binder also inhibited the growth of $Mg(OH)_2$, suggesting that metakaolin can prevent magnesium-phase hydrolysis [213]. This is a reason for the negligible $Mg(OH)_2$ in XRD patterns. Therefore, as $Mg(OH)_2$ is a well-known low-strength product, the enhanced mechanical properties of the AMC3 sample can also be attributed to the inhibition of the growth of $Mg(OH)_2$ by metakaolin.

(a)

147
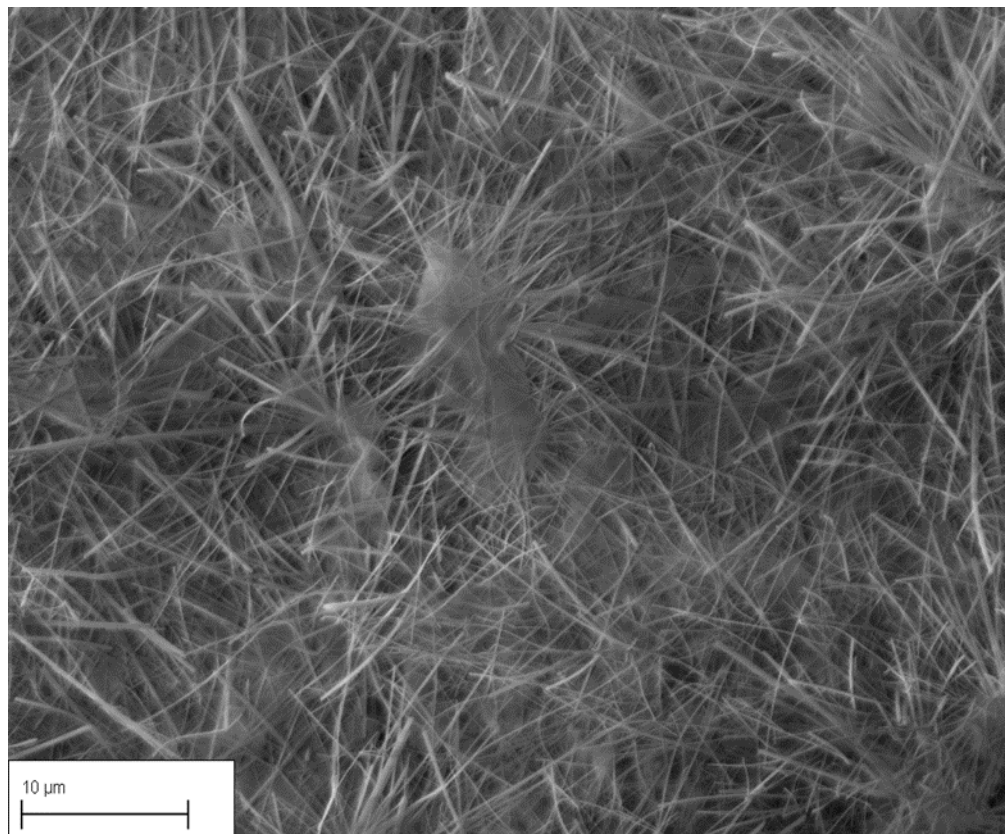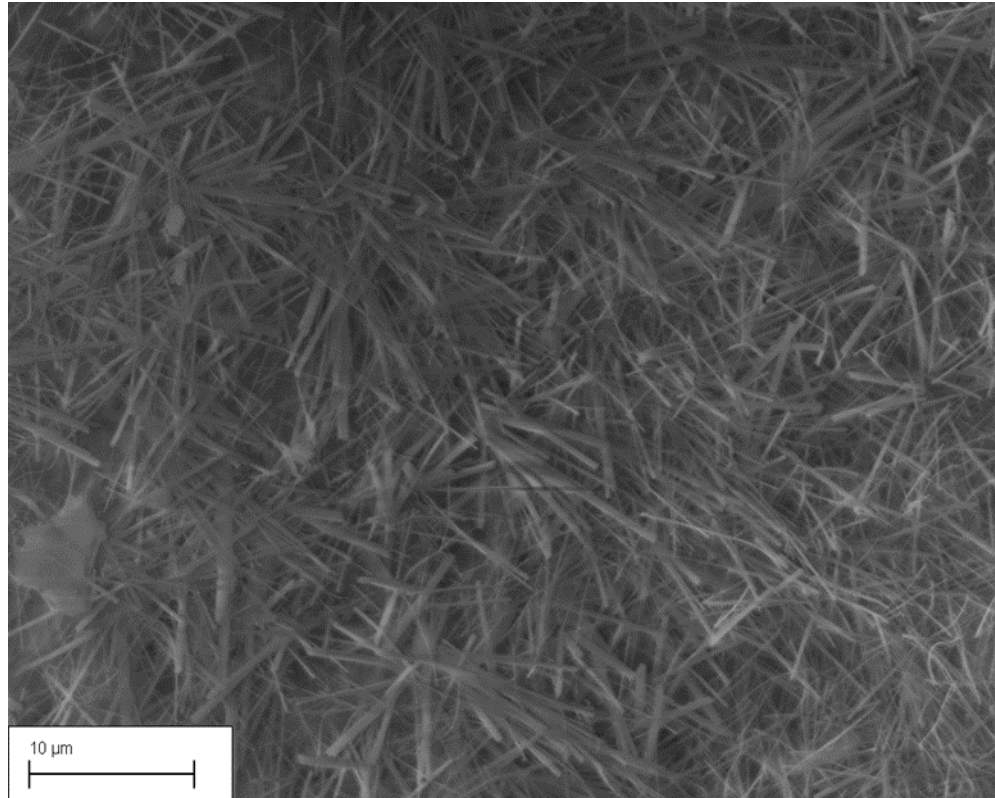
(b)

Fig. 5.14 SEM images of (a) MC3 and (b) AMC3 with a magnification of 5000 at the curing age of 28 days

5.3.4. Conclusions

This chapter investigated an alternative magnesium-based carbonate obtained in **Chapter 4** to replace limestone in Portland metakaolin cement. The feasibility of these lab-made HMCs was assessed via examing their compressive strength, phase assembly, and microstructure. The main findings are listed below:

1. The lab-made HMCs can improve the early-age strength of the binders. In comparison with the LC3 mix, AMC3 showed a 7-day compressive strength of 32.4 MPa, which was 8% higher than that of the LC3 mix.

2. Ettringite was observed in all samples at all curing ages, which is a major factor in the development of strength. The formation of strätlingite was only

detected after 28 days, while carboaluminates existed from the beginning of curing. In the Portland metakaolin carbonate binder systems, the carboaluminates contribute more to compressive strength before 28 days, while strätlingite plays a more important role in controlling the late-age strength gain.

3. The microstructure of the AMC3 sample was improved by metakaolin, which limited the formation of $Mg(OH)_2$, leading to an outstanding mechanical performance (i.e. high compressive strength).

6. Chapter 6 Magnesia in Alumina Silicate Hydrate Binder Systems

6.1. Introduction

Reactive magnesium oxide used as an alternative construction material has been considered as a technique to further reduce the composite's overall environmental impact and improve its performance from certain perspectives. Reactive magnesia can enhance the strength and hydration of cement and improve its carbon-capture capacity [10]. Light-burned MgO with relatively lower calcination temperatures of 700-1000 °C shows high reactivity and expansion feature. During the production and life cycle process, its net CO_2 emissions are reduced by 70% compared to those of ordinary Portland cement [151].

MgO differs significantly from CaO in chemstry, so changing the feedstock for Ca-based cements will not produce a directly comparable material. The chemistry and phase formations differ significantly between them when compared to the respective $(MgO, CaO)-Al_2O_3-SiO_2$ ternary phase diagrams (**Fig. 6.1**), as the raw materials mixed with MgO in this Chapter are clay (i.e. alumina-silicate) and waste glass (i.e. silicate). Specifically, no magnesium silicate phases are formed at elevated temperatures that have hydraulic properties akin to those formed in the calcium-rich region of the $CaO-SiO_2-Al_2O_3$ system: Ca_3SiO_5, Ca_2SiO_4, and $Ca_3Al_2O_6$ (shaded regions in **Fig. 6.1 (b)**) are key hydraulic phases in PC, but have no magnesian analogues in **Fig. 6.1 (a)**. Consequently, MgO cannot directly replace CaO in PC manufacture, and therefore, the development and use of MgO-based cements require different approaches. Several possible approaches have been showed, including combining carbonates or other oxysalts with MgO to form a cohesive mineral binder, using a magnesium-silicate bond, and the production of acid-base cements by reacting MgO with acid-phosphate compounds (e.g. magnesium phosphate cements (MPCs)). These methods provide numerous possibilities for using MgO in practice. For instance, **Chapter 5** investigated the application of magnesium-based carbonates in Portland metakaolin

cement, which shows the feasibility of HMCs in cementitious systems with aluminosilicates.
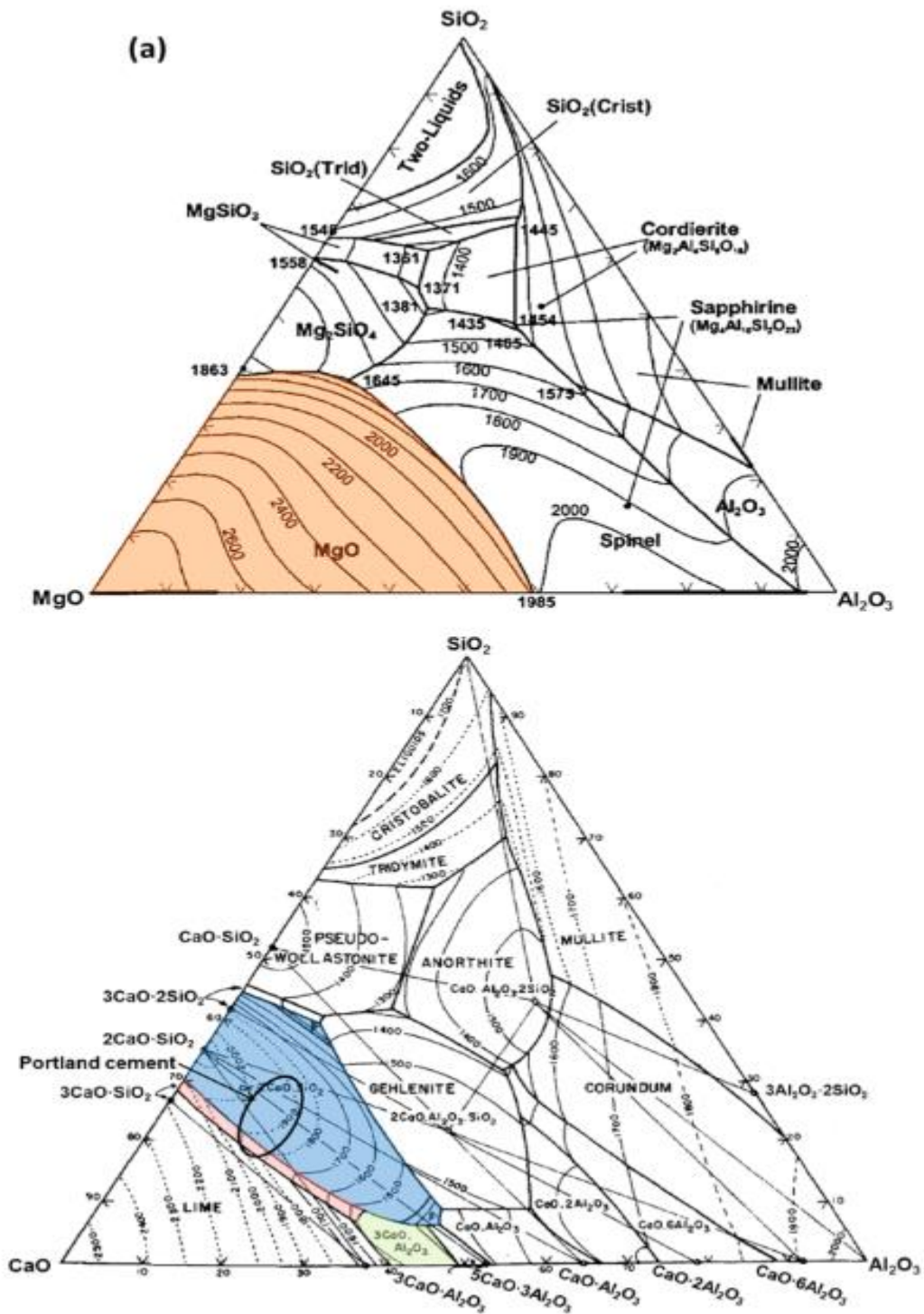
Fig. 6.1 Ternary phase diagrams, in units of weight per cent, for the systems (a) MgO−SiO₂−Al₂O₃ and (b) CaO−SiO₂−Al₂O₃ [214]

In this chapter, two applications of MgO were demonstrated and critically assessed. Although MgO cannot directly replace CaO in PC manufacture because of the lack of hydraulic magnesian analogues in a binder, MgO was considered being used in clay solidification, which does not require high strength as that for structural elements. Based on the above theory, **Section 6.2** assessed the performance of MgO- and CaO-based clay samples subjected to natural and oven curing.

Another approach, the magnesium−silicate bond, mentioned previously, provides a reuse opportunity for waste glass. **Section 6.3** investigated replacing microsilica (MS) with waste glass for preparing $MgO-SiO_2$ formulations to form magnesium-silicate-hydrate (M-S-H).

6.2. Solidification of Waste Excavation Clay via the Adoption of Reactive Magnesia, Sodium Carbonate and Early-Age Oven Curing

6.2.1. Introduction

Soil solidification should be employed in the construction of road pavements because of the considerable environmental and economic benefits [127], and Portland cement (PC) is one additive that is widely used in the clay (e.g. kaolinite) solidification. As a result, the strength of clay is greatly improved by hydration phases (e.g. C-S-H) [128,131].

Recently, to reduce the environmental impact, another promising mineral additive, i.e. reactive magnesia, has also been proposed in soil solidification [130,140-142]. Given the foregoing, instead of using a large quantity of strong alkali such as NaOH in clay solidification, this study adopted some mineral additives including quicklime (i.e. CaO) and reactive magnesia (i.e. MgO), which can provide an alkaline environment in clay solidification. Moreover, different from the previous studies, which introduced accelerated carbonation curing to promote the strength development of soil, this study took advantage of the formation of carbonates via the reactions between CO_3^{2-} ions and

Ca^{2+}/Mg^{2+} ions within the clay samples. The dissolution of Na_2CO_3 externally included in clay at a very low dosage derived the CO_3^{2-} ions. In addition, the Na_2CO_3 in this study can also provide some OH^- ions to promote the dissolution of clay particles, although its content in clay was very low. The Ca^{2+}/Mg^{2+} ions in this study were acquired from the hydration of additives included in clay. Besides, to accelerate the hydration process and strength development, some MgO- or CaO-based clay samples were then subjected to oven curing for up to 3 days. The compressive strength of samples up to 28 days was measured, and the strength results were later interpreted by pH measurement, porosity, x-ray Diffraction (XRD), Fourier-transform infrared (FTIR) and scanning electron microscopy (SEM)-Energy-dispersive x-ray spectroscopy (EDX).

6.2.2. Mix Design and Sample Preparation

To reduce the content of strong alkali used in clay solidification (e.g. NaOH), only 10 wt.% of Na_2CO_3 compared with total solids was mixed with water, which provides some CO_3^{2-} ions and an alkaline environment at the same time. A control group was selected which contained 100 wt.% of clay, whereas, for the other two groups, 20 wt.% of clay was replaced by the use of quicklime or magnesia, respectively. The w/b ratios of all three groups were chosen accordingly to ensure the same workability of fresh paste. After mixing, the pastes were cast into 50 × 50 × 50 mm^3 cubic molds, compacted via a vibrating table and trowel finished. All samples were demolded after 24 h, and two curing regimes were adopted: (1) The samples were cured in a natural environment (i.e. temperature: 25 ± 1 °C; Relative humidity: 60 ± 5%) up to 28 days; (2) The samples were cured in an oven (i.e. 80 °C) first for 3 days and then in a natural environment (i.e. temperature: 25 ±1 °C; Relative humidity: 60 ± 5%) for another 25 days. The mix formulations of all groups studied and their curing regimes are shown in **Table. 6.1**.

Table. 6.1 Mix formulations of clay samples (wt.%) and curing regimes

Group	Clay	Na$_2$CO$_3$	Quicklime	Magnesia	w/b ratio	Curing regimes
C-NC	100%	10% of total solids	0	0	0.34	Natural curing
L20-NC	80%	10% of total solids	20%	0	0.41	Natural curing
M20-NC	80%	10% of total solids	0	20%	0.41	Natural curing
C-OC	100%	10% of total solids	0	0	0.34	Mixed curing
L20-OC	80%	10% of total solids	20%	0	0.41	Mixed curing
M20-OC	80%	10% of total solids	0	20%	0.41	Mixed curing

6.2.3. Results and Discussion

6.2.3.1. pH Values

The 7-, 14- and 28-day pH values of all samples subjected to the natural and mixed curing regimes are presented in **Fig. 6.2**. Irrespective of curing ages, compared with the pH values (i.e. 12.3~13.0) shown in the control group, there is a distinct increase in pH values, ranging from 13.3 to 14.9, shown in the CaO- and MgO-based clay samples. In the meantime, it is clear that the CaO-based samples produced a stronger alkaline environment than the MgO-based counterparts, which could be explained by the following mechanisms: (1) Ca(OH)$_2$ formed due to the hydration of quicklime reveals a greater solubility (i.e. $K_{sp}=5.5\times10^{-6}$) than Mg(OH)$_2$ (i.e. $K_{sp}=1.5\times10^{-11}$) in room temperature, and the corresponding reactions are represented in Equations 6.1-6.2. Therefore, compared with Ca(OH)$_2$ in the L20-OC and L20-NC groups, the smaller quantity of OH$^-$ ions released by Mg(OH)$_2$ brought about the lower pH values within the clay samples; (2) Another possible explanation could be related with a higher content of hydration phases formed in the MgO-based samples (i.e. M20-OC and M20-NC), and these hydration phases could then consume or absorb more alkali within the clay samples, which led to smaller pH values presented in these groups than in the CaO-based

counterparts (**Fig. 6.2**), and the above findings were also supported in previous studies [123,215]. However, the first explanation seems to be a more reasonable interpretation considering the later results. From the figure, it is also interesting to note that, except for the control group, the mixed curing regime, which introduced oven curing at the beginning, also led to lower pH values shown in these samples than the natural curing groups, which could be ascribed to the higher content of hydration phases formed (i.e. more alkali consumed or absorbed) under this regime within the samples, facilitated by the faster hydration kinetics resulting from the elevated temperature, and the outcomes were also well explained by the subsequent experiments in this study. Besides, from **Fig. 6.2**, it is also obvious that the pH values of all samples fluctuated over time, and a possible interpretation could be related to the carbonation of samples, which resulted from the reaction between the hydration phases and atmospheric CO_2 in the clay samples, thus their pH equilibrium was influenced correspondingly.

$$CaO+H_2O\rightarrow Ca(OH)_2\leftrightarrow Ca^{2+}+2OH^- \tag{6.1}$$

$$MgO+H_2O\rightarrow Mg(OH)_2\leftrightarrow Mg^{2+}+2OH^- \tag{6.2}$$
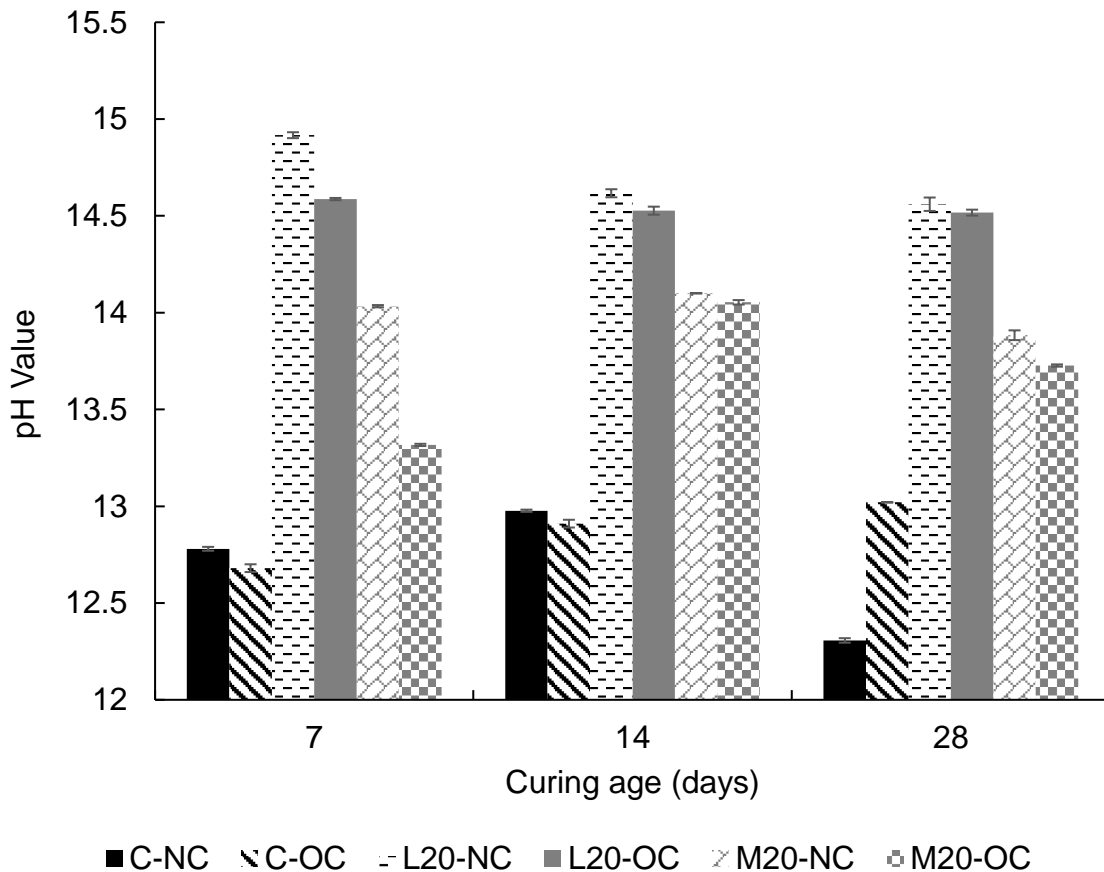
Fig. 6.2 pH values of the CaO- and MgO-based samples under the natural and mixed curing regimes up to 28 days

6.2.3.2. Compressive Strength and Porosity

Up to 28 days, the compressive strength of CaO- and MgO-based clay samples are shown in **Fig. 6.3**, where the natural and mixed curing regimes were adopted. The figure indicated that regardless of the curing regimes adopted, the strength of control groups without any mineral additives (i.e. the C-NC and C-OC groups) is relatively low (i.e. close to 0 MPa) even after 28 days of curing, while the C-OC group performed only slightly better than the C-NC group concerning the strength development, which is related to their relatively porous structures, as shown in **Fig. 6.4 (a)**. As indicated by a previous study [134], coupled with an elevated temperature curing, a strongly alkaline environment is required to dissolve the alumino-silicate in clay, and a Na/Si ratio of 0.8-1 is a necessity in clay solidification, whereas the Na/Si ratio

in this study was only about 0.2, which resulted in low efficiency of clay solidification due to the insufficient pH provided by the sole usage of 10 wt.% Na_2CO_3 in clay, as discussed in **Section 6.2.3.1**. When it comes to the strength results of samples subjected to the natural curing regime (i.e. L20-NC and M20-NC groups), given the 7- and 14-day compressive strength, the CaO-based clay samples outperformed the MgO-based counterparts. The higher pH values revealed in L20-NC group (see **Fig. 6.2**) may explain the variations, which resulted in a better hydration behaviour of clay particles and greater strength achieved in the L20-NC group. However, after 28 days of natural curing, both the CaO- and MgO-based samples demonstrated comparable compressive strength (i.e. 10 MPa), which could be interpreted by the improvement in the homogeneity of hydration phase distribution when a higher content of magnesia replacement was introduced in clay samples [140].
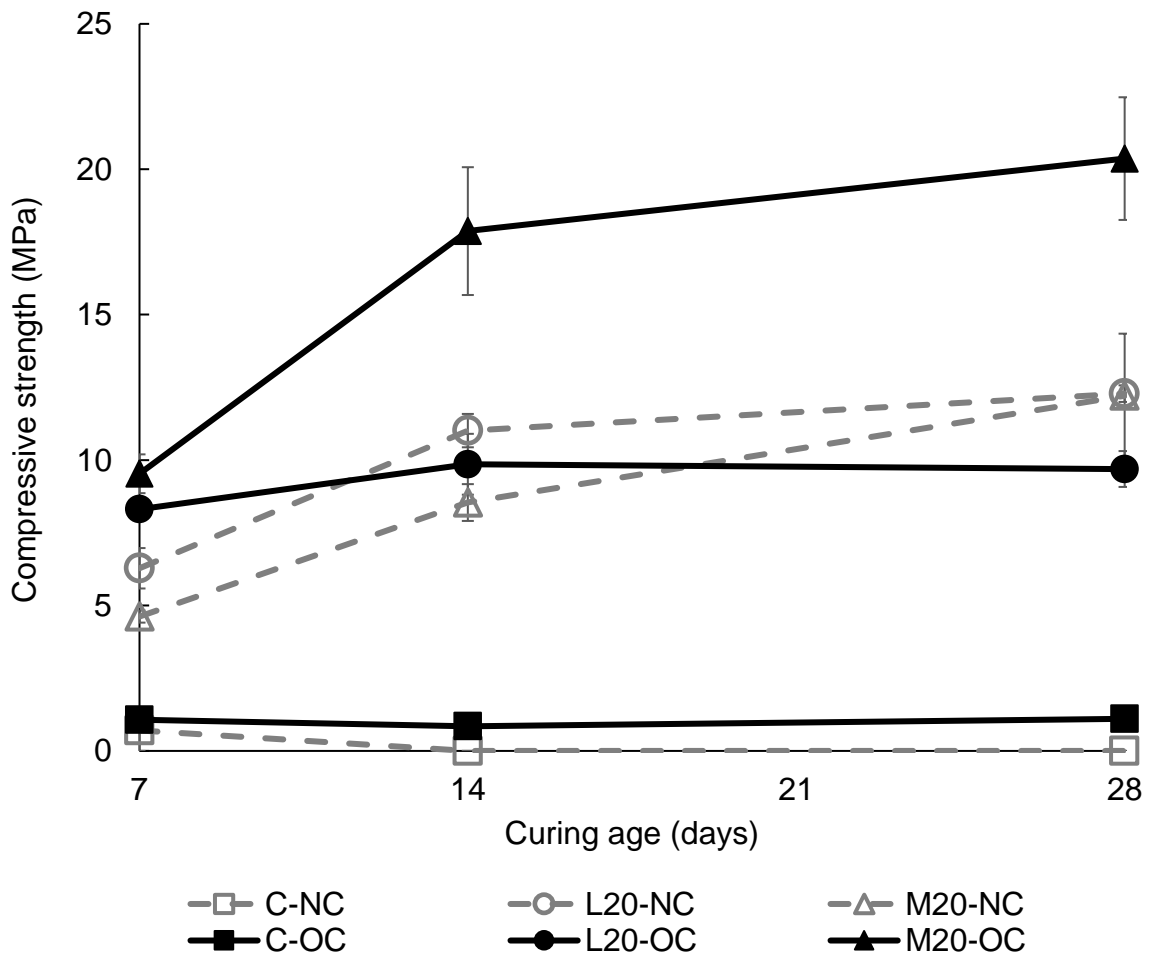
Fig. 6.3 Compressive strength of the control, CaO- and MgO-based groups under the natural and mixed curing regimes up to 28 days

For the mixed curing regime, **Fig. 6.3** also clearly reveals that the M20-OC group presents superior compressive strength than that of the L20-OC group. For instance, after 28 days of mixed curing, the average compressive strength revealed by the M20-OC group is 20.4 MPa, which is 110% higher than that of the L20-OC group. It is widely accepted that strength among samples is highly related to porosity, and the formed hydration phases would fill in the pores within the mixture, which led to a more compacted structure and therefore higher strength [216]. However, this theory may not be applicable in this study, as a quite similar sample porosity (i.e. around 27%) was observed in both the CaO- and MgO-based clay samples, as shown in **Table. 6.2**. Considering this, an the strength difference between the M20-OC and the L20-OC groups could be resulting from the varying morphology of hydration phases, which will be elaborated in later. Besides, another cause of inferior compressive strength observed in the L20-OC group can be assigned to the occurrence of micro-cracks in samples (**Fig. 6.4 (b)**) because of the oven curing (or drying). Although this curing regime may also promote the hydration of precursors [217], a different surface image was observed in the M20-OC group (**Fig. 6.4 (b)**). This difference could be associated with the volume expansion of samples owing to the magnesia hydration [218]. Additionally, the delayed hydration of magnesia, which was resulted from its low solubility, reduced the probability of micro-cracks formation as a consequence of thermal shrinkage at a later curing age [219-221]. For quicklime, although it was also used as an expansive additive, the rapid reaction of CaO with water, as well as its potential hydration during storage even in a natural environment, reduced its expansion capacity in concrete [222].

Table. 6.2 Porosity of CaO- and MgO-based clay samples

Mixture	Controlled clay samples	CaO-based clay samples	MgO-based clay samples
Porosity	-*	27.7% ± 0.3%	27.9%±2.1%

*The porosity of controlled clay samples cannot be measured as it broke into pieces in water due to their porous structure
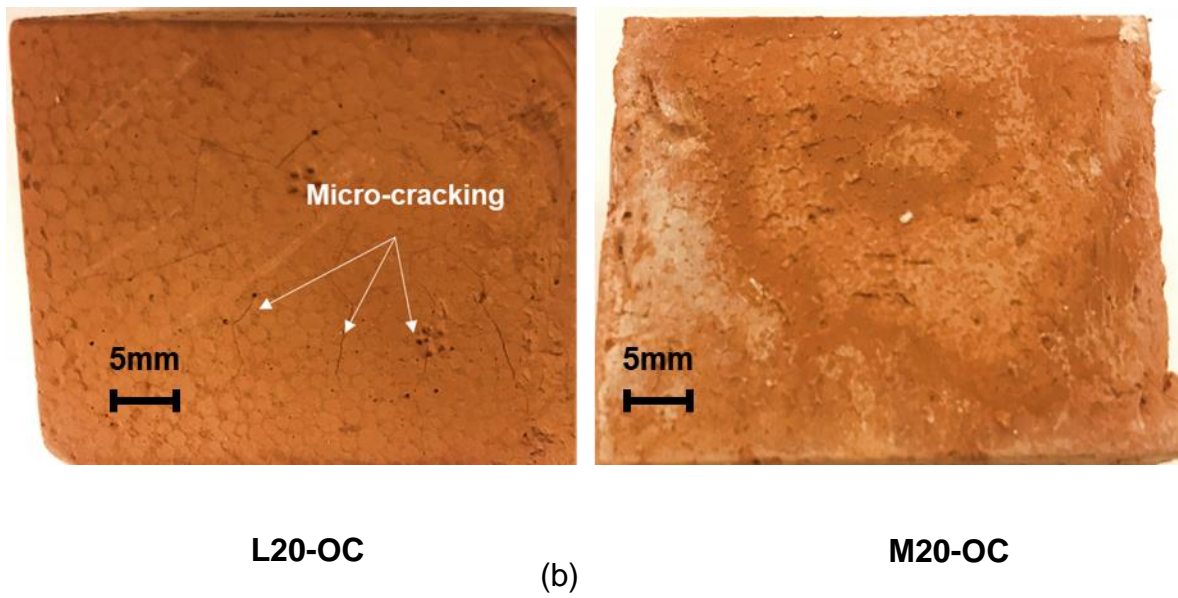
Fig. 6.4 (a) Images of the control groups after 7 days of natural and mixed curing; **(b)** Images of the L20-OC and M20-OC groups after 28 days of mixed curing regime

6.2.3.3. XRD

The XRD patterns of the C-OC, L20-OC, M20-OC and M20-NC groups subjected to the mixed curing regime are shown in **Fig. 6.5 (a)** and **(b)**. Within

all the groups investigated, the presence of quartz and kaolinite can be found after 28 days of mixed curing, and these phases are derived from the clay, as seen in **Table. 3.4**. The table also shows that the C-S-H together with the calcite ($CaCO_3$) is detected (28-29° 2θ) in the patterns of the L20-OC group, and this finding is also in line with a previous reference [143]. For the M20-OC group, the peak of 28-29° 2θ can be ascribed to the presence of nesquehonite ($MgCO_3 \cdot 3H_2O$), yet the presence of M-S-H in this mixture is still uncertain, which is because of its amorphous nature and broad hump shown in the XRD patterns [215,223]. Meanwhile, the clay used in this study is also almost free of CaO (**Table. 3.4**), thus the possibility of calcium-bearing phases in the M20-OC group could be eliminated, which is also confirmed by the XRD pattern of the C-OC group as show in **Fig. 6.5 (a)** since the peaks of C-S-H or calcite were both absent. Further, **Fig. 6.5 (a)** also indicated the absence of portlandite ($CaOH)_2$) or brucite ($Mg(OH)_2$) from the patterns, revealing that after 28 days of curing, the Ca^{2+} and Mg^{2+} ions may be completely involved in the formation of Ca- and Mg-containing phases within the clay samples under an alkaline environment, and the outcomes were also in accordance with several previous investigations [224-226]. In addition, the corresponding peaks of Na_2CO_3 cannot be identified from all the XRD patterns, showing its complete dissolution within the samples after 28 days of curing, and the resultant CO_3^{2-} ions in the pore solution were then involved in the formation of calcite or nesquehonite at a later stage.

The XRD patterns of the M20-OC and M20-NC groups are presented in **Fig. 6.5 (b)**. The patterns indicate that the oven curing at an early stage facilitated the formation of nesquehonite ($MgCO_3 \cdot 3H_2O$), which could also be ascribed to the better dissolution of magnesia facilitated by elevated temperature, whose solubility is quite low at room temperature [179]. Therefore, in comparison with the L20-OC group, the introduction of oven curing at an early age promoted the formation of more Mg^{2+} ions, which would readily react with CO_3^{2-} in the pore solution and a larger quantity of nesquehonite was produced as a result in the M20-OC group, which enhanced the strength of samples subjected to

the mixed curing, and the details of nesquehonite formation can be found in the **Section 6.2.3.6**.

(a)

(b)
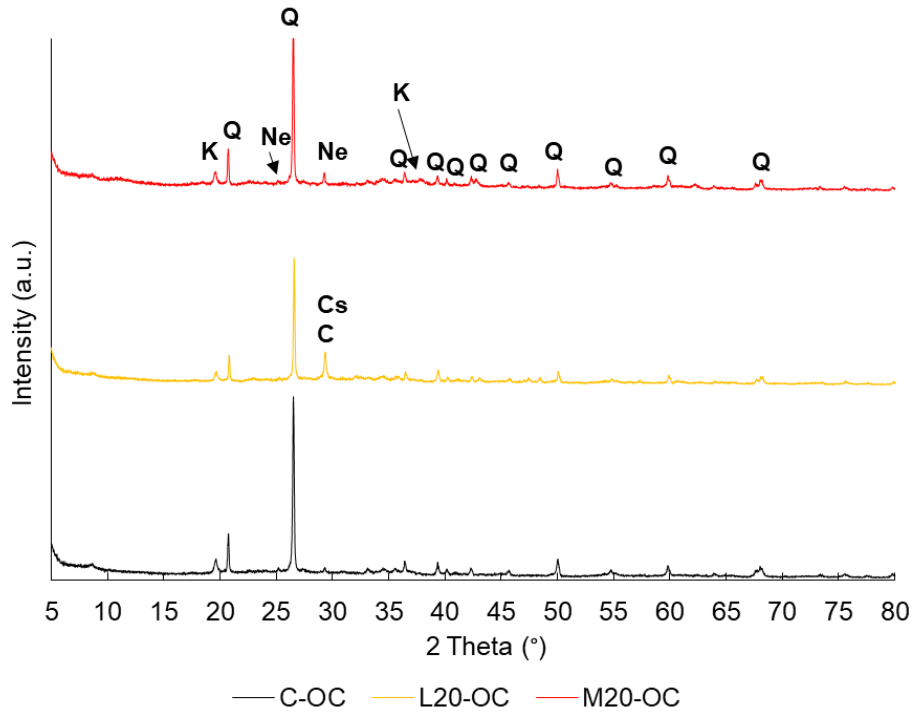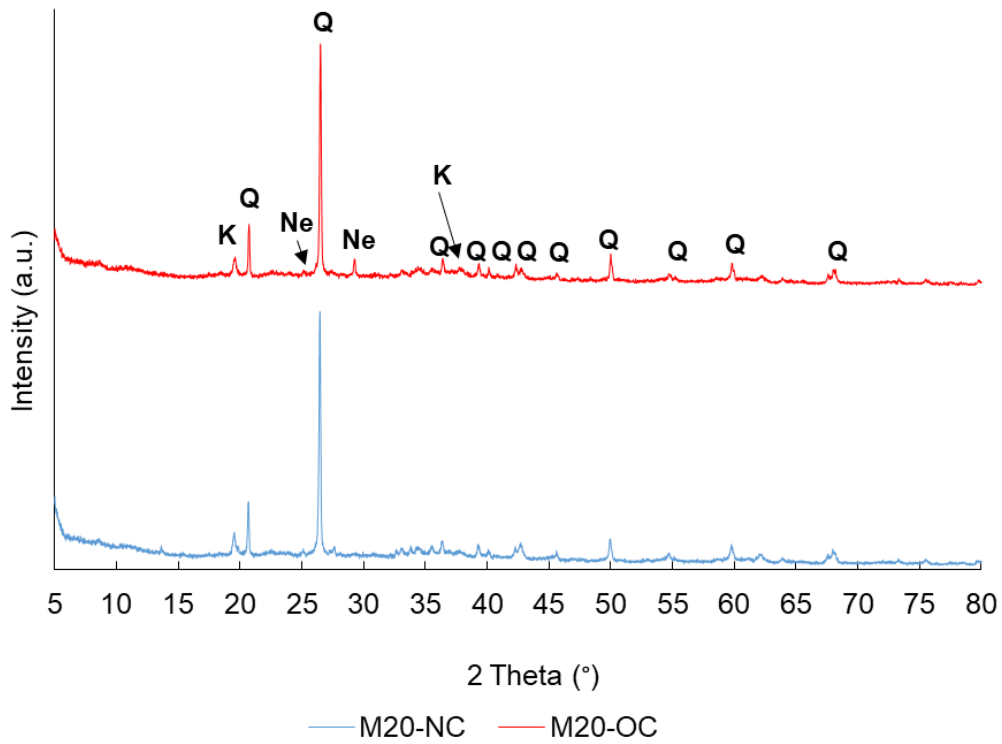
Fig. 6.5 XRD patterns of (a) selected samples after 28 days of mixed curing; (b) the MgO-based clay samples after 28 days of natural and mixed curing

6.2.3.4. FTIR

The FTIR spectra of clay, quicklime, magnesia and selected clay samples subjected to the mixed curing regime are presented in **Fig. 6.6 (a)**. The spectra of the L20-OC and M20-OC groups indicate a peak at the band of 800-1200 cm^{-1}, though they present different shapes and locations (i.e. peak centre) when compared with their counterparts of the C-OC group and precursor, which is mainly attributed to the Si-O bond [227]. Besides the stretching vibrations of Si-O, the 870 cm^{-1} bands in the L20-OC and M20-OC groups can be ascribed to the bending band of CO_3^{2-} ions, which was usually reported at around 875 cm^{-1} [228]. In view that the Na_2CO_3 was dissolved in these clay samples after 28 days of curing, the bending band of CO_3^{2-} ions also confirms the presence of calcite ($CaCO_3$) or nesquehonite ($MgCO_3 \cdot 3H_2O$), as shown in **Fig. 6.5**. In the C-OC, M20-OC and L20-OC groups, the circled portions between 1070 cm^{-1} and 1210 cm^{-1} are related to the presence of clay, but the remainders ranging from 800 cm^{-1} to 1070 cm^{-1} indicate the presence of some hydration phases produced within the C-OC, L2O-OC and M20-OC groups, which are different from that of the precursor. Therefore, for a clearer comparison, the produced phases were conservatively estimated by a spectral subtraction (with linear baseline correction applied), as indicated in **Fig. 6.6 (b)**. The figure shows that the produced phases reveal their main peaks between 960 cm^{-1} and 980 cm^{-1}, which can be assigned to the presence of some hydration products (i.e. C-S-H or M-S-H possibly), and the findings were also in line with the previous studies [124,145,229], although the evidence of M-S-H within the M20-OC group is not very strong because of its amorphous nature, which will be discussed later (**Section 6.2.3.6**). Further, the relatively low intensity of peaks within the range of 960 cm^{-1} and 980 cm^{-1} in the C-OC group reveals a

scarcity of hydration phases, explaining its porous structure and negligible compressive strength, which is also confirmed by the XRD patterns in this study. Besides, from **Fig. 6.6 (b)**, it can also be found that the L20-OC group may contain a greater quantity of hydration phases than the M20-OC group, reflected by its stronger peak intensity and larger peak area, yet the M20-OC group still outperformed the L20-OC group regarding the compressive strength, showing that the quantity of produced phase (or porosity) is not the only factor that dictates the strength of clay samples in this study, which will be elaborated later in **Section 6.2.3.6**. Finally, **Fig. 6.6 (b)** has a clear representation that the three peak centres of the C20-OC, L20-OC and M20-OC groups differ slightly, ranging from 960 cm^{-1} and 980 cm^{-1}, and Zhu et al. [230] suggested that this variation could probably be interpreted by the varying Ca/Si ratios, and a higher Ca/Si ratio in the samples was accompanied by a lower wavenumber in the FTIR curves.
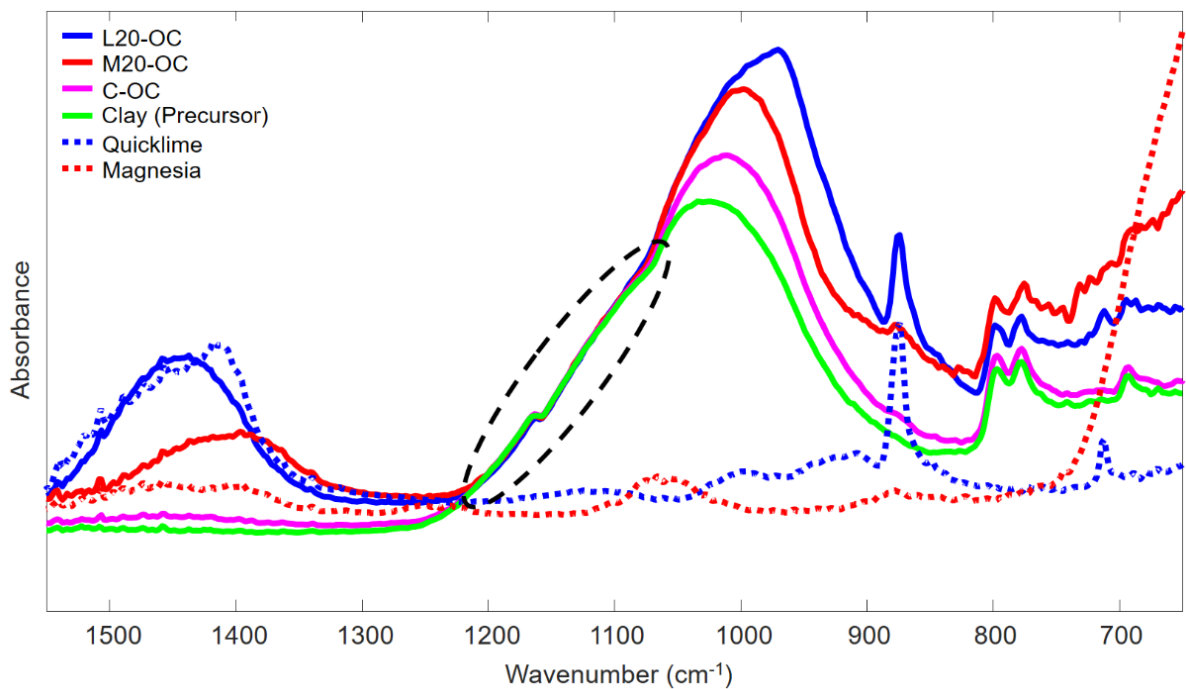
(a)
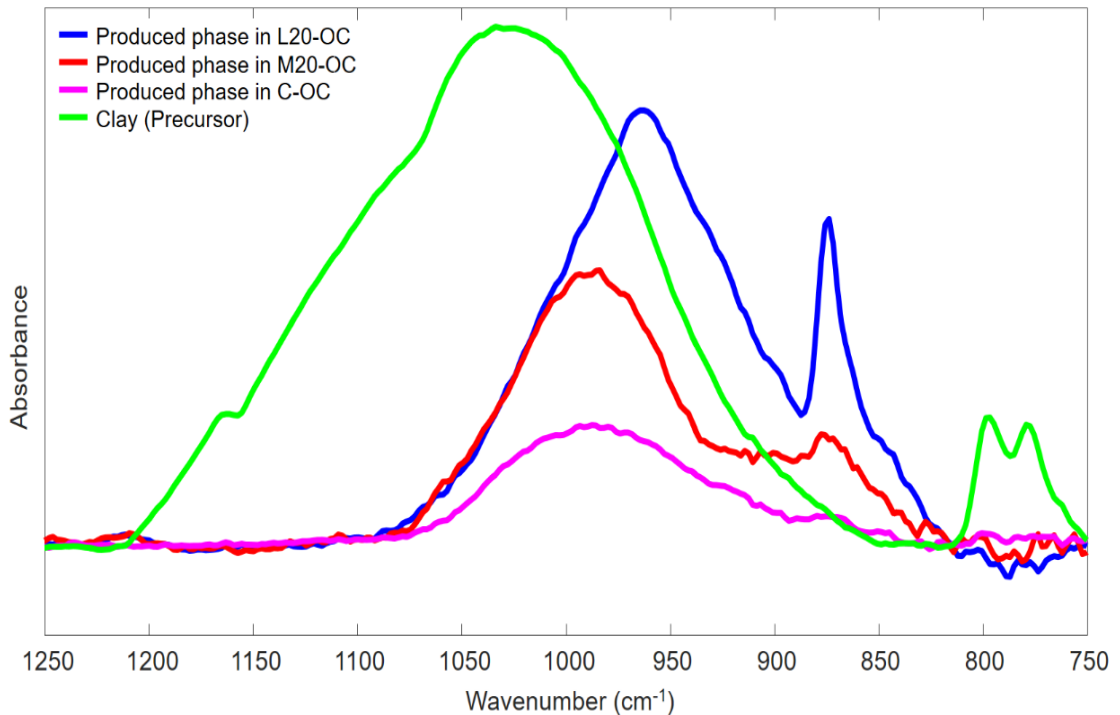
(b)

Fig. 6.6 (a) FTIR spectra of precursor, quicklime, magnesia and selected clay samples; (b) subtraction of the spectra (i.e., after baseline correction) of the selected samples after 28 days of mixed curing regime

6.2.3.5. SEM-EDX

Some BSE images of selected samples after 28 days of mixed curing are presented in **Fig. 6.7**. As expected, in the C-OC group, there is a large amount of unreacted quartz (i.e. SiO_2; spherical particles) left, and it is also reported that dark grey areas on BSE images refer to the presence of C-S-H in the samples [231], thus very little C-S-H is found from the BSE image in the C-OC group (**Fig. 6.7(a)**), which is also supported by the previous results. For the L20-OC group, the unreacted particles (i.e. kaolinite and quartz) are connected by some dark grey areas, which is C-S-H or possibly calcite in **Fig. 6.7 (b)**, and a denser structure was seen in the L20-OC group than that in the C-OC group, accounting for its greater strength achieved. Besides, through the elemental spectra in **Fig. 6.8 (a)**, owing to the presence of carbon in the dark area, the presence of calcite ($CaCO_3$) can also be confirmed, which is intermixed with the C-S-H in the L20-OC group. While the C-S-H results from

164

the reaction between the clay particles and the Ca^{2+} ions, the source of Ca^{2+} ions in the formation of calcite may vary, which will be discussed later.

Different from the L20-OC group, fibrous hydration products are prevailing in the M20-OC group (**Fig. 6.7 (c)**), and these crystals resemble the morphology of nesquehonite ($MgCO_3·3H_2O$) [232] or natrite (Na_2CO_3) [233], however, from the XRD patterns, the possibility of natrite (Na_2CO_3) is eliminated in the M20-OC group. In addition, the elemental spectra in **Fig. 6.8 (b)** also indicate the presence of carbon within the fibrous crystals, consequently, the dominant hydration phases in M20-OC can be attributed to the presence of nesquehonite ($MgCO_3·3H_2O$), which is also in line with the XRD results. As expected, it is still very difficult to confirm the existence of M-S-H in the M20-OC group from BSE images, which will also be discussed later (**Section 6.2.3.6**).

(a) (b)

(c)
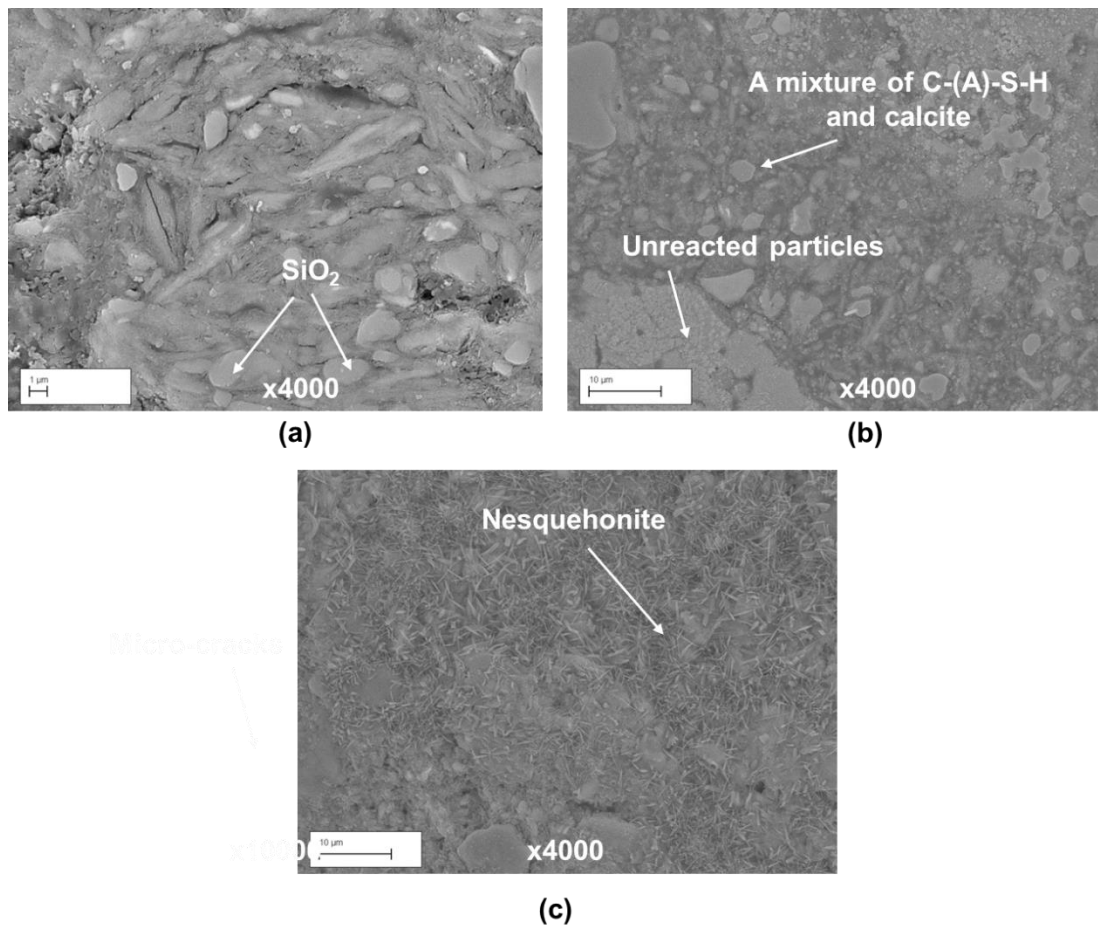
Fig. 6.7 BSE images of (a) C-OC (magnification: x4000); (b) L20-OC (magnification: x4000 and x10000); (c) M20-OC (magnification: x4000) after

165

28 days of mixed curing
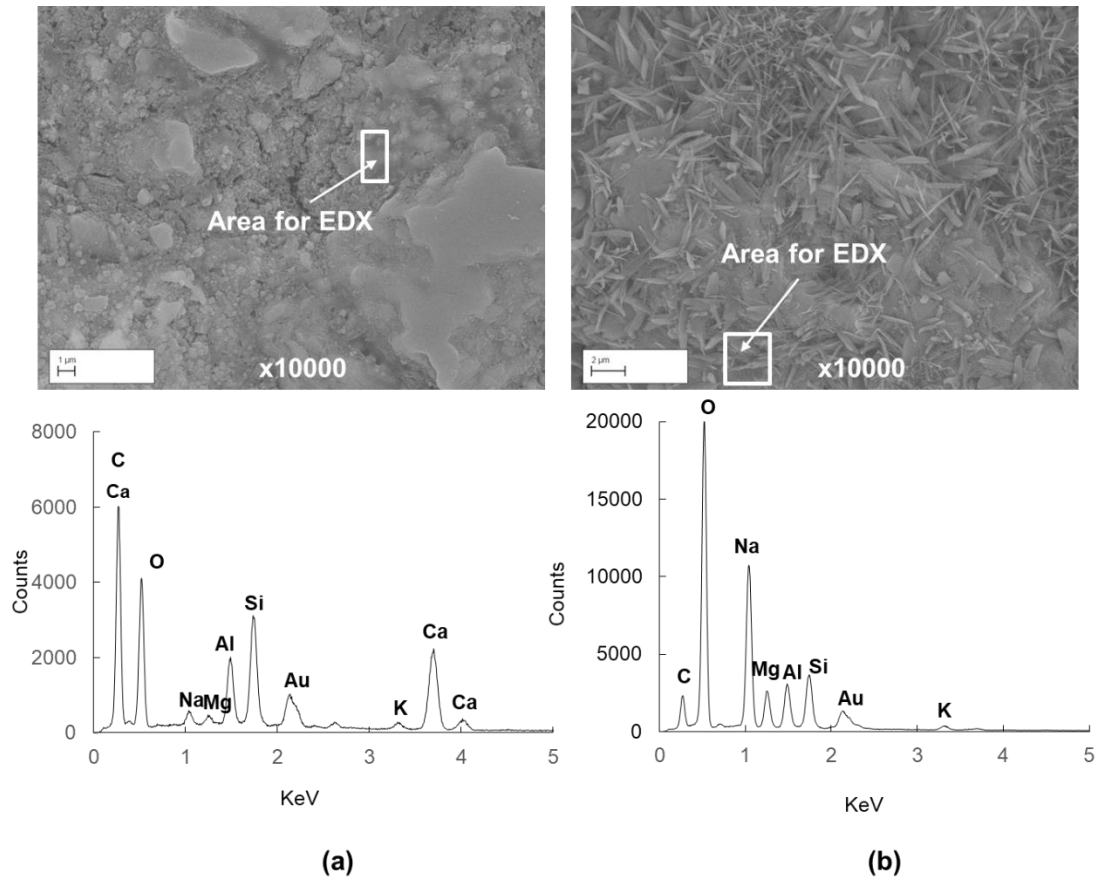
Fig. 6.8 Elemental spectra of selected areas in (a) L20-OC (magnification: x10000) and (b) M20-OC (magnification: x10000) after 28 days of mixed curing

6.2.3.6. Discussion

The effects of quicklime on clay solidification are pronounced. The continuous hydration of the L20-OC group led to the C-S-H produced that connected the clay particles, which resulted in a denser structure than that seen in the C-OC group. It was reported that amorphous C-S-H including C-S-H gel, C-S-H (I) and C-S-H (II) is a thermodynamic metastable phase, and the relatively low temperature led to the formation of amorphous C-S-H, whereas crystalline C-S-H can be formed including tobermorite and xonotlite at elevated-temperature [234]. Therefore, the 3-days oven curing at an early stage led to the formation of C-S-H with more crystallized structure in the clay samples.

From the previous sections, the calcite produced (Equation 6.3) is also intermixed with the C-S-H in the L20-OC group. There are two possible Ca^{2+} ion sources, i.e. the hydration of CaO or the leaching of C-(A)-S-H in the L20-OC group. However, it is also clear that the crystalline C-S-H, which is formed in this study, shows greater stability than the amorphous C-S-H gel, suggesting its relatively inferior capacity of Ca^{2+} ions release owing to its lower solubility [235]. Given this circumstance, it is believed that the Ca^{2+} ions in Equation 6.3 were mainly derived from the dissolution of mineral additive (i.e. CaO). Meanwhile, the dissolution of Na_2CO_3 is supposed to play a major role in the provision of CO_3^{2-} ions in Equation 6.3. Because of the low concentration of CO_2 in the air (~0.04%), only a small proportion of atmospheric CO_2 would be dissolved into the pore solution even after 28 days of curing, leading to a negligible CO_3^{2-} ions resulting from the carbonation in the L20-OC group. Another study [123] also reported that the solubility of crystalline silica (i.e. quartz) that is found in this study is several orders of magnitude lower than the amorphous silica, which greatly inhibits the dissolution of clay particles as well as the formation of the C-S-H correspondingly, reflected by the lower compressive strength in the C-OC and C-NC groups. Consequently, the calcite may play a more important role than the C-S-H in the determination of compressive strength in the L20-OC group.

$$Ca^{2+}+CO_3^{2-} \rightarrow CaCO_3 \tag{6.3}$$

The benefits of magnesia incorporation in clay solidification are also clear. Different from the formation of calcite, it is very difficult to produce magnesite (i.e. $MgCO_3$) within the samples [24], and inevitably, the Mg^{2+} ions would readily react with CO_3^{2-} ions as well as combine several molecules of H_2O to produce a series of hydrated magnesium carbonates (HMCs) with varying morphology within samples [232,236]. In this study, the HMC that was found within the M20-OC group is identified as nesquehonite through the XRD patterns and the SEM images, and its reaction can be represented by Equation 6.4:

$$Mg^{2+} + CO_3^{2-} + 3H_2O \rightarrow MgCO_3 \cdot 3H_2O \qquad (6.4)$$

In Equation 6.4, the Mg^{2+} ions could be either obtained from the dissolution of $Mg(OH)_2$ or possibly M-S-H, albeit the presence of M-S-H in the M20-OC group is still in doubt, which deserves further investigations. Besides, as aforementioned, considering the low solubility of quartz in clay, the amount of M-S-H should also be low as well, which is also confirmed by the low peak density and small peak area of produced phase than C-S-H through the FTIR curve in the M20-OC group, provided that the main peak of 960 cm^{-1} and 980 cm^{-1} was assigned to the presence of M-S-H. Further, Zhang et al. [215] also demonstrated that the amorphous M-S-H presents a higher solubility compared with the crystalline M-S-H such as sepiolite ($Mg_4Si_6O_{15}(OH)_2 \cdot 6H_2O$) or chrysotile ($Mg_3(Si_2O_5)(OH)_4$). Therefore, in terms of the foregoing, even though M-S-H indeed formed at an early stage within the pore solution in the M20-OC group, after 28 days of curing, the leaching of Mg^{2+} ions from the M-S-H because of its good solubility may then absorb CO_3^{2-} ions and H_2O molecules to produce the HMCs. As a result, nesqhehonite was formed in this study. Compared with the L20-OC group, the M20-OC group exhibited a greater strength owing to the presence of fibrous nesquehonite. The mechanical performance of brittle samples is determined by several key factors such as the quantity of hydration phases formed, which resulted in a reduction of pores and a more compacted structure within the samples. However, given the FTIR curves and the similar porosity results of the L20-OC and M20-OC groups, more hydration phases were observed in the L20-OC group than in the M20-OC group, whereas an opposite scenario was found concerning the compressive strength of the L20-OC and M20-OC groups, which could be interpreted by the different hydration products formed within these two groups, and the produced phases present various morphology, i.e. the morphology of hydration phases within the clay samples could play a more important role than their content as well as their porosity for the strength of samples investigated and a similar finding was also reported in a previous study [39], where the mechanical performance of samples was also greatly influenced by the morphology of hydration phases instead of their

quantity. In addition, Ruan and Unluer [151] proposed that fibrous and needle-like crystal growths are more useful than rounded or tabular crystals concerning the strength development of samples. Hence, owing to the 3D structures, the fibrous nesquehonite revealed better microstructural strength than the C-S-H/calcite mixture, and the compressive strength of the M20-OC group is much higher than that of the L20-OC group consequently. In the meantime, it is also speculated that the possible effects of interlocking resulting from the fibrous nesquehonite may further enhance the compression resistance of the MgO-based clay samples, which is also proposed in a previous reference [151]. Therefore, based on the above elaboration, it can be concluded that instead of the content, the morphology of hydration phases could be more crucial in controlling the compressive strength of clay samples investigated in this study.

For the effects of early-age oven curing, it may present dual effects on the compressive strength of the L20-OC group. On one hand, oven curing may facilitate hydration and the subsequent strength development of clay samples. On the other hand, since the hydration rate of quicklime is very fast, which causes a low efficiency of expansion, the oven curing (or drying) may bring about the occurrence of micro-cracking within the samples containing quicklime at a later curing age, which would deteriorate their overall compressive strength. Nevertheless, the chances of micro-cracks formation within the M20-OC samples were reduced by the delayed volume expansion of magnesia hydration. Mo et al. [220] reported that the hydration of MgO can be found on the exterior surface of their particles, inner pore surface as well as at the boundary, and the $Mg(OH)_2$ precipitates adjacent to the MgO particles resulting from the short diffusion distance of Mg^{2+} ions gradually, then the delayed expansion of magnesia particles can be observed consequently. Since the expansive process (i.e. hydration) of magnesia particles occurs within a confined area, which is previously dominated by the initial ones, the expansive stress is generated owing to the confined expansion, hence, the cement samples are expanded subsequently. Therefore, considering the absence of micro-cracks, when magnesia is

incorporated in clay solidification, the effect of oven curing at an early stage on the strength development of clay samples could be strengthened. An illustration of chemical reactions that occurred in the L20-OC and M20-OC groups is presented in **Fig. 6.9**, which also explained the strength variations between these two groups.
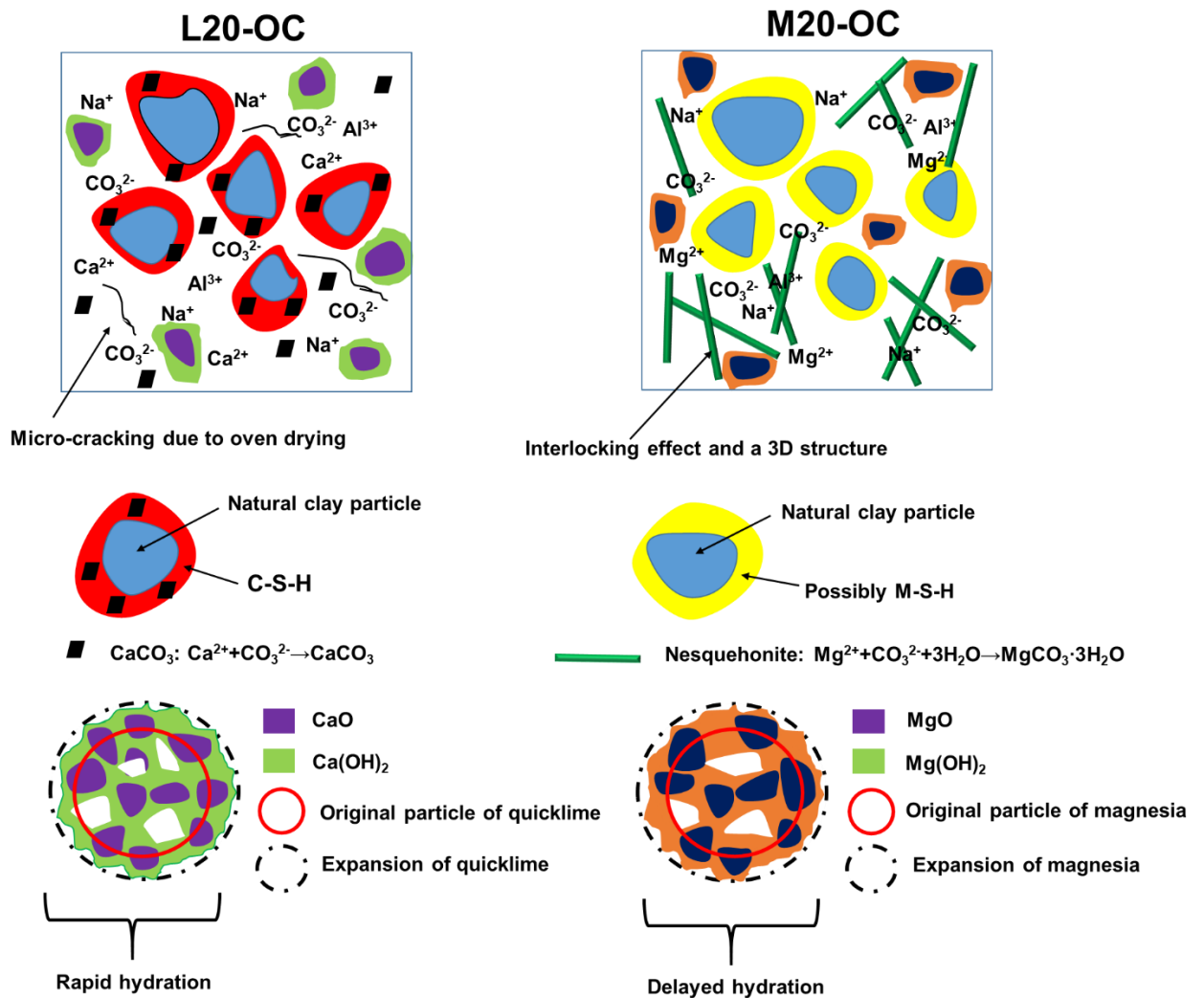
Fig. 6.9 Illustration of chemical reactions in the L20-OC and M20-OC groups after 28 days of mixed curing

6.2.4. Conclusions

This section solidified waste excavation clay via the incorporation of reactive magnesia, quicklime and sodium carbonate, and the efficiency of clay

solidification was further enhanced using oven curing at an early stage. Overall, the findings obtained will provide some guidance on the solidification of contaminated clay as well as the manufacturing of clay-based products such as masonry bricks. Besides, some major conclusions can be drawn as follows:

1. In addition to a pH increment in clay samples, which promoted the dissolution of clay particles, the use of quicklime and magnesia also provided additional Ca^{2+} and Mg^{2+} ions to produce several types of hydration phases within the clay samples, thus their strength development was boosted accordingly owing to the formation of a more compacted structure.

2. Under the early-age oven curing, the morphology of hydration phases could be possibly more critical than their quantity and sample porosity for the strength development of clays samples investigated in this study. As a result, compared with the CaO-based clay samples, greater compressive strength was revealed in the MgO-based counterparts, which could be possibly ascribed to the interlocking effects and a 3D structure of fibrous nesquehonite produced in this group.

3. The strength variation between the CaO- and MgO-based clay samples may be enlarged by the oven curing (or drying), as the chances of micro-crack formation within the M20-OC group could be reduced due to the delayed expansion of MgO hydration, however, CaO failed to eliminate the occurrence of micro-cracks within the clay samples at a later age due to its rapid hydration possibly, and the micro-cracks in these samples deteriorated the compressive strength.

6.3. Use of Magnesia to Recycle Milled Waste Glass Powders by Forming Magnesium-Silicate-Hydrate (M-S-H) Binder

6.3.1. Introduction

The development of a circular economy exerts enormous economic benefits. The Department for Environment, Food and Rural Affairs [238] provided an estimation that UK businesses could benefit by up to £23 billion annually by implementing measures involving the efficient use of resources and waste management in a low-cost way. Similarly, the European Union aims to achieve a 65% recycling rate for municipal solid waste and a reduction in the municipal landfill to 10% or lower by the year 2035 [239]. One potential use that can contribute to cutting down the environmental loads and preserving natural resources involves the recycling and utilization of potential waste materials (e.g. metal, plastics and glass, etc.) as raw materials in other industrial procedures.

In the UK, 5 billion glass bottles are consumed annually [240], with a significantly lower recycling rate (i.e. around 71% of container glass) when compared to some other major developed countries (i.e. 99%, 98%, 96% and 85% of the waste glass is recycled and reused in Sweden, Switzerland, Belgium, and Germany, respectively) [241]. The large consumption of glass and low recycling rates result in 1.5 billion glass bottles being sent to landfills in the UK [240]. As glass is produced via the combination of sand, soda ash, limestone and other additives, the recyclable and reprocessed glass with no loss of quality could reduce the energy consumption and the amount of harmful gases from the carbonate raw materials emitted into the environment [242]. The standard process used in recycling glass involves the crushing and removal of contaminants, blending with the raw materials to colour and/or enhance performance, and melting in a furnace for molding or recycling into new bottles or jars [241,243]. Despite the initiatives in this area, currently, 200,000 tonnes of glass generated by businesses such as bars, restaurants, and pubs are estimated to be landfilled annually in the UK.

One potential area that provides a reuse opportunity for WG is concrete mixes, where WG can be introduced as aggregates or raw material [244,245]. Numerous studies have reported that the utilization of WG as fine aggregates in cement mortars and traditional concrete mixtures presents an alternative method for the production of cement-based construction products [246]. However, the alkali-silica reaction (ASR) between the highly alkaline pore solution in cement paste and reactive silica in WG can lead to harmful expansion in concrete, which can weaken the concrete and shorten its lifespan [122,247]. This issue can be overcome with the use of alternative binder systems, which can present lower pH values, and can thereby accommodate WG in their formulations. For instance, magnesium-silicate-hydrate (M-S-H)-based binders can be considered as an alternative binder to reuse WG, in which M-S-H formation is enabled by the reaction between a magnesium (e.g. magnesium oxide (MgO)) and silica (e.g. silica fume or microsilica) source within a $MgO-SiO_2-H_2O$ system.

The most commonly used silica source, microsilica (MS), can present some environmental challenges associated with its production and use of natural resources. Moreover, the supply chain of some widely used supplementary cementitious materials (SCMs), such as fly ash which contains a variety of glassy phases, is threatened. In the UK, all the coal-fired power plants are planned to be retired by 2025 and in the Netherlands by 2030 [80]. However, a few studies [123,125,248] were performed in this area reported that a higher reaction degree was obtained in the presence of amorphous silica sources. The reaction between amorphous silica sources and reactive MgO led to a higher strength than that obtained with crystalline silica. Within these mixes, the compressive strength increased with increasing silica content in the range of 0–50% [123]. Therefore, to enhance the sustainability of $MgO-SiO_2$ systems and produce mixes with lower environmental impacts, alternative materials used in $MgO-SiO_2$ mixes need to be investigated. In this respect, with its high amorphous silica content soluble in alkaline conditions, and relatively homogeneous nature, municipal WG powder could present a promising silica source in the production of M-S-H. Reusing WG can also contribute to

reducing the environmental burden provided by the landfilling of WG. In addition to the chemical composition, the increasing municipal solid waste production also makes the use of WG feasible and imperative. Soares et al. [249] investigated the early-age compressive strength of magnesium silicate binders involving WG powder subjected to carbonation curing and reported that samples containing 0-50% (by mass) WG could reach a satisfactory mechanic performance (i.e. all of the specimens achieved more than 25 MPa of compressive strength after 2 hours of CO_2 curing and 3 days in room conditions). While these findings revealed the potential of WG to be used as a silica source in MgO-SiO_2 formulations subjected to CO_2 curing, there is a gap in the literature regarding the suitability of WG as a silica source in M-S-H systems without the use of any special curing regimes. This study also derives an adequate mixture proportion for the M-S-H binder containing WG by investigating the effects of low reactivity silica-to-high reactivity silica ratio on the mechanical strength. Due to the low cost of the WG, the higher WG content can reduce both cost and environmental impact. A more sustainable MSH binder can be produced by using WG without scarifying the strength properties. Therefore, a balance between the mechanical strength and the low-cost silica content (i.e. waste glass) needs to be established.

In line with this need to identify the feasibility of potentially more sustainable silica sources for the development of alternative binders, the involvement and influence of WG in the formation of M-S-H binders were investigated in this study. Accordingly, the effects of WG as a silica source in MgO-SiO_2 binders were evaluated via a measurement of the mechanical performance of the prepared samples for up to 28 days. These results were further supported by microstructural analysis including x-ray diffraction (XRD), thermogravimetric analysis/derivative thermogravimetry (TG/DTG) and Fourier-transform infrared spectroscopy (FTIR).

6.3.2. Mix Design and Sample Preparation

The details of the mix formulations investigated in this study are presented in **Table. 6.3**. Except for the control sample containing 100% MgO, the other mixtures contained 50 wt.% MgO (M) as the main binder and 50 wt.% of MS and/or WG. Accordingly, sample 100M, which contained 100% MgO, was selected as the control group. Samples 50M50MS, 50M50WG, and 50M25MS25WG contained 50% MS, 50% WG, and 25% MS and 25% WG for their silica source, respectively. In all sample groups, the water/binder (w/b) ratio was kept constant at 0.6. NaHMP was introduced at 2% of the total solid (by mass) as a superplasticizer.

Table. 6.3 Mix formulations used in this study

Mixture	Binder component (%)			w/b ratio
	MgO	Microsilica	Waste glass	
50M50MS	50	50	-	0.6
50M25MS25WG	50	25	25	0.6
50M50WG	50	-	50	0.6
100M	100	-	-	0.6
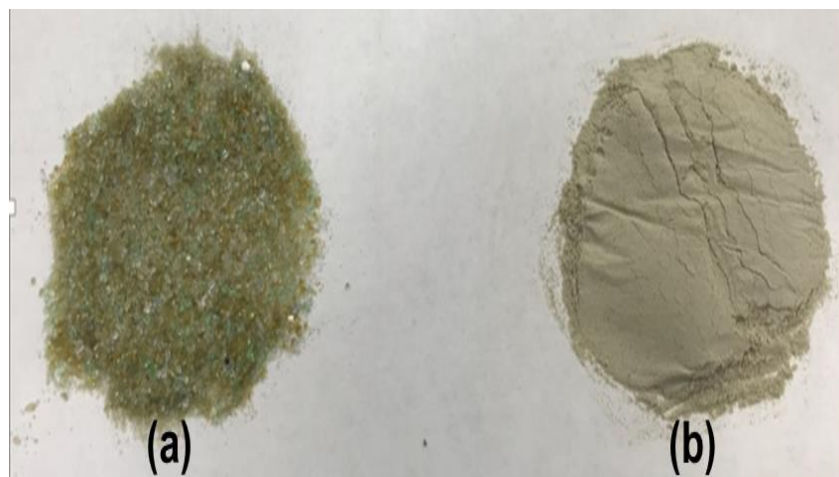
Fig. 6.10 Images of WG (a) as received and (b) after milling

WG was milled at 500 rpm for 20 minutes using a planetary ball milling machine (Retsch, PM 100, Germany) to achieve a powder consistency. The

images of received and milled waste glass are shown in **Fig. 6.10 (a)** and **(b)**. The particle size distribution (PSD) curve of the raw materials, i.e. MgO, MS, and WG, is illustrated in **Fig. 6.11**. Between the two silica sources, WG, which was used to substitute MS in this study, had a larger particle size than MS. When compared to other amorphous silica sources presented in the relevant literature [125], WG had a smaller median particle size ($d_{(50)}$) value of 30.2 μm (in comparison to 63.3 μm of rice husk ash). To prevent alkali-silica reactions due to the high alkali-silica reactivity of milled glass, particle size was preferably maintained below 100 μm [250]. The XRD diffractograms of milled WG, shown in **Fig. 6.12**, revealed a broad peak, which suggested a high amorphous silica content.
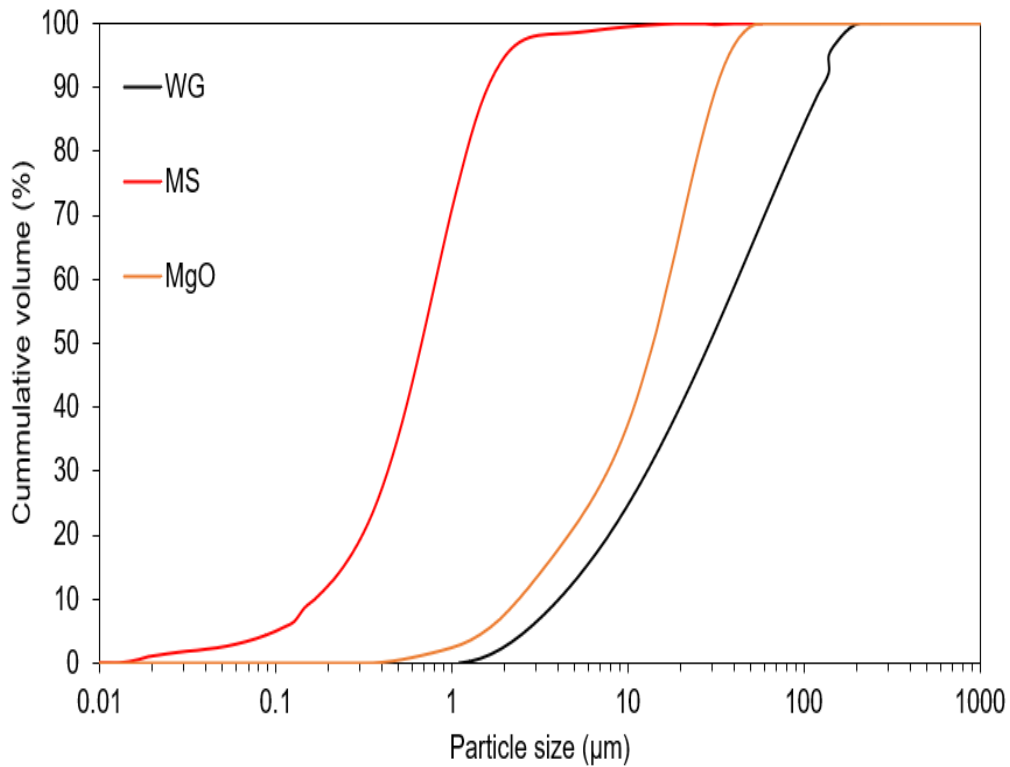
Fig. 6.11 Particle size distribution of the raw material (i.e. MgO, MS and WG)
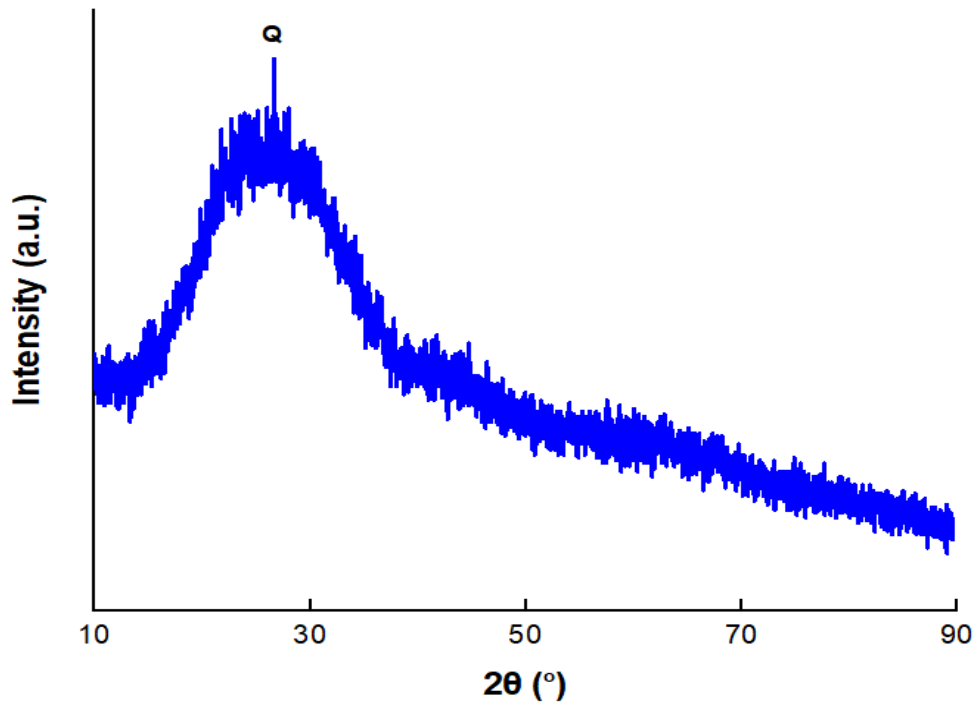
Fig. 6.12 X-ray diffraction pattern of milled WG powder (Q: Quartz)

NaHMP was mixed with water to form a solution, after which MgO was gradually added in during mixing. The silica source was then slowly added into the mix and followed by a further 3 minutes of mixing. The paste was cast into cubic moulds with the dimensions of 50 x 50 x 50 mm^3, compacted via a vibrating table, and trowel finished. All samples were demolded after 24 hours and subjected to ambient curing conditions (i.e. temperature: 25 ± 1 °C and relative humidity: 60 ± 5%) for up to 28 days.

6.3.3. Results and Discussion

6.3.3.1. Setting Times

For engineering applications, setting time is a crucial property of cementitious materials which should be noted. The effect of the silica source on the setting time of the magnesium silicate-based blend is shown in **Fig. 6.13**. Among all of the samples, the 100M samples showed the shortest initial setting time and final setting time, which indicates the high-water demand of MgO. The setting

times were extended with the addition of a silica source. This is related to the reduced MgO content, which led to a limited formation of $Mg(OH)_2$. The longest setting times were found in 50M50WG samples, which could be ascribed to the lower reactivity of WG compared to the microsilica. The reactivity of the silica source plays an important role in the formation of M-S-H gel, which dominates the paste's setting and hardening. In terms of practical applications, it is desirable to have a relatively longer initial setting and a shorter final setting time, in this case, the 50M25MS25WG samples show the best hardening property amongst all samples, which has the second highest initial setting time but much shorter final setting time compared to those of 50M50WG samples.
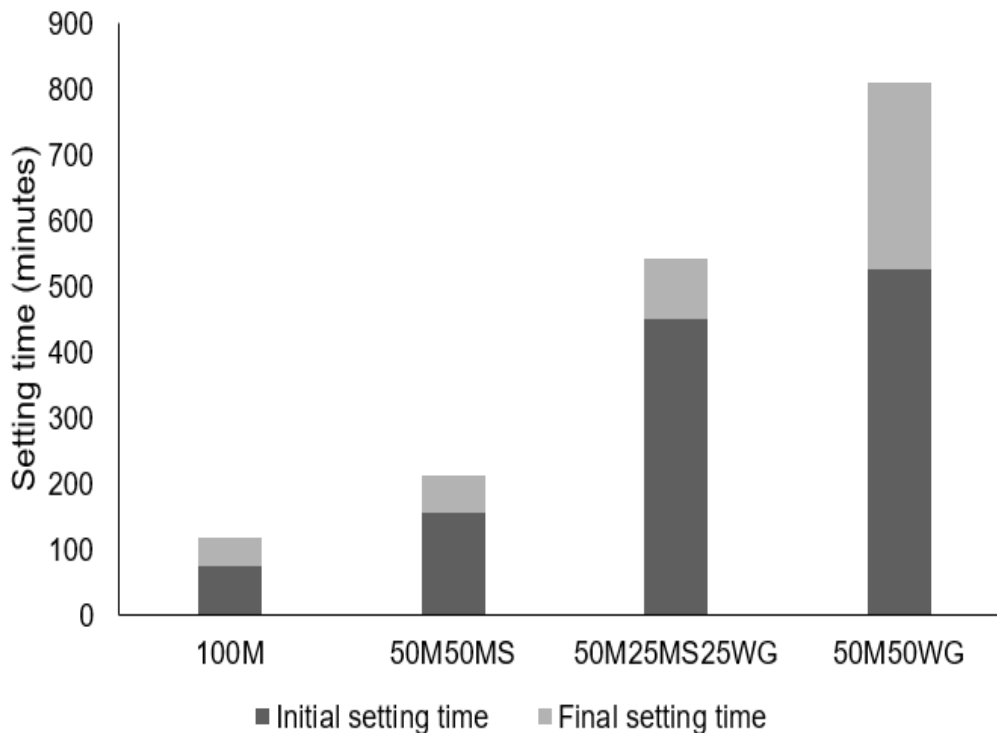
Fig. 6.13 Setting times of all samples

6.3.3.2. pH Values

For MgO-SiO_2 formulations, the reaction between Mg^{2+} and dissolved silica complexes can lead to the formation of M-S-H. Above a pH of 9, the hydrated surfaces of silica particles are ionized to form $SiO(OH)_3^-$ or $SiO(OH)_2^{2-}$, which

can instantly react with metallic cations (i.e. Mg^{2+}) in the solution. The formation of M-S-H is associated with a decrease in the pH value due to the consumption of OH^- ions. Therefore, the pH of the $MgO–SiO_2$ system plays a significant role in the formation of M-S-H, as the change in the pH is attributed to the formation of hydrate phases (i.e. brucite and M-S-H). According to other studies [123,125], the pH value of the high purity MgO (i.e. MgO content over 93%) only varied over a range of 0.5. Therefore, in this study, the effect of different silica sources on the pH values of blends was investigated only by measuring the pH values of MgO-SiO_2 mixes (i.e. 50M50MS, 50M50WG and 50M25MS25WG samples) up to 28 days.
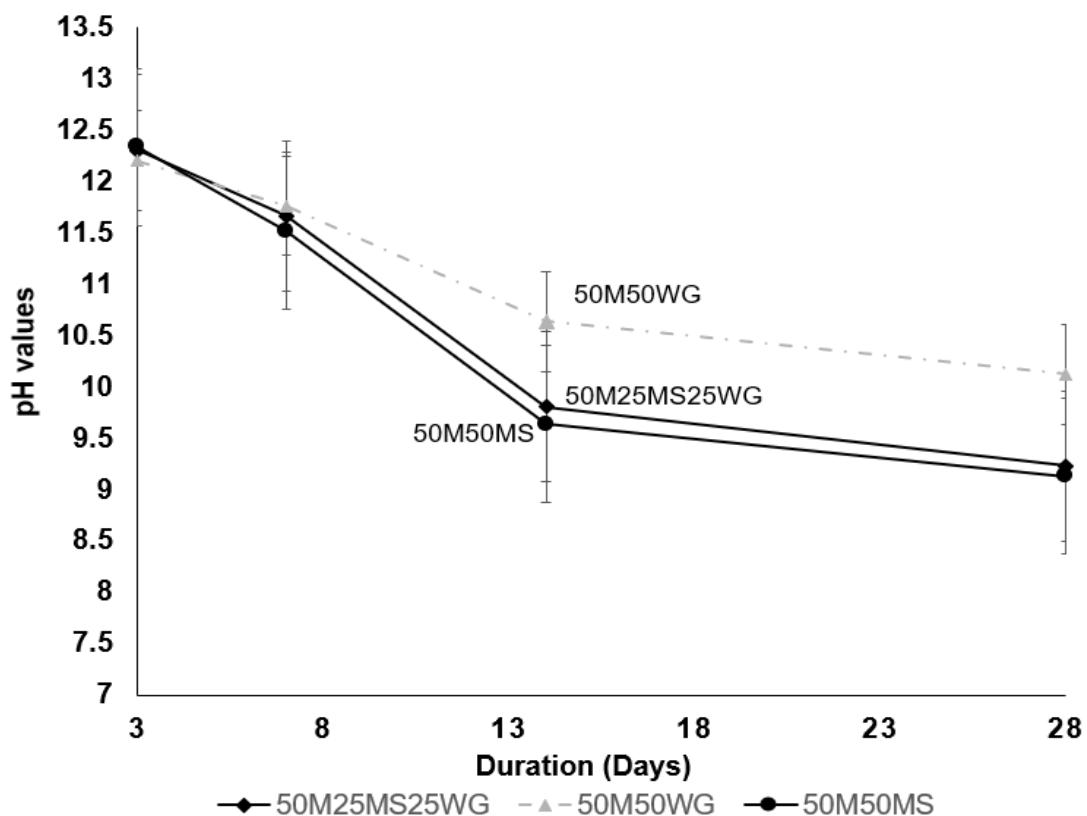
Fig. 6.14 pH values for all samples measured for up to 28 days

Fig. 6.14 shows that 50M25MS25WG and 50M50MS samples both revealed lower pH values than that of 50M50WG samples, while 50M50MS samples revealed the lowest pH value, which could be due to the solubility of MS. On the other hand, 50M50WG samples exhibited the highest pH values, which was related to the use of an undesirable silica source. The pH values of

50M50WG > 50M25MS25WG > 50M50MS throughout the entire measurement period indicates the role that the silica source plays in determining the pH. As shown in **Table. 6.4,** the initial pH values of all samples were around 12.3, which was higher than the pH value of brucite (i.e. ~10.5). The higher pH values of the prepared samples could be related to the use of NaHMP and the presence of impurities in MgO. The dissolution of silica sources and subsequent formation of M-S-H can lead to a decrease in the pH in all samples, which was observed after three days. The pH value of samples 50M50MS and 50M25MS25WG varied between 12.3 and 9.13 through the 28 days of analysis. Different from other samples, no significant change was observed in the pH value of 50M50WG samples, which may be due to the lack of reaction between the Mg-phase and WG.

Table. 6.4 pH values and standard deviation of all samples for up to 28 days

Mixture	3 days		7 days		14 days		28 days	
	pH	STD	pH	STD	pH	STD	pH	STD
50M50MS	12.33	0.16	11.51	0.01	9.63	0.07	9.13	0.03
50M50WG	12.20	0.12	11.76	0.04	10.63	0.02	10.12	0.12
50M25MS25WG	12.30	0.20	11.66	0.04	9.80	0.05	9.22	0.05

6.3.3.3. Compressive Strength

Fig. 6.15 shows the compressive strengths of all samples cured for up to 28 days. Unlike PC blends, all samples investigated in this study exhibited a poor strength gain between 0 to 3 days, which was ascribed to the low rate of dissolution of MgO under the ambient temperature [126,251]. Meanwhile, unreacted MgO particles were covered by the hydration products, resulting in a reduced surface area available for further hydration. The rapid gain in compressive strength was observed in all samples at early ages (3 to 7 days), which was associated with the formation of hydration products (i.e. M-S-H and brucite). During 3 to 7 days, as the hydration further progressed, the Brucite surrounding layer tended to break up due to its volume increase; thereby, the previously covered unhydrated MgO particles were exposed again for

hydration, which promoted the strength gain as observed. After 7 days, the strength increase slowed down, which could still be ascribed to the covering of the surface of unreacted MgO particles by the newly formed hydration products, resulting in a reduced amount of available surface area for further hydration and obstructing further interaction with unhydrated zones [47,232]. The inhibited hydration of MgO could be also proved by XRD results, which will be explained in the later sections.
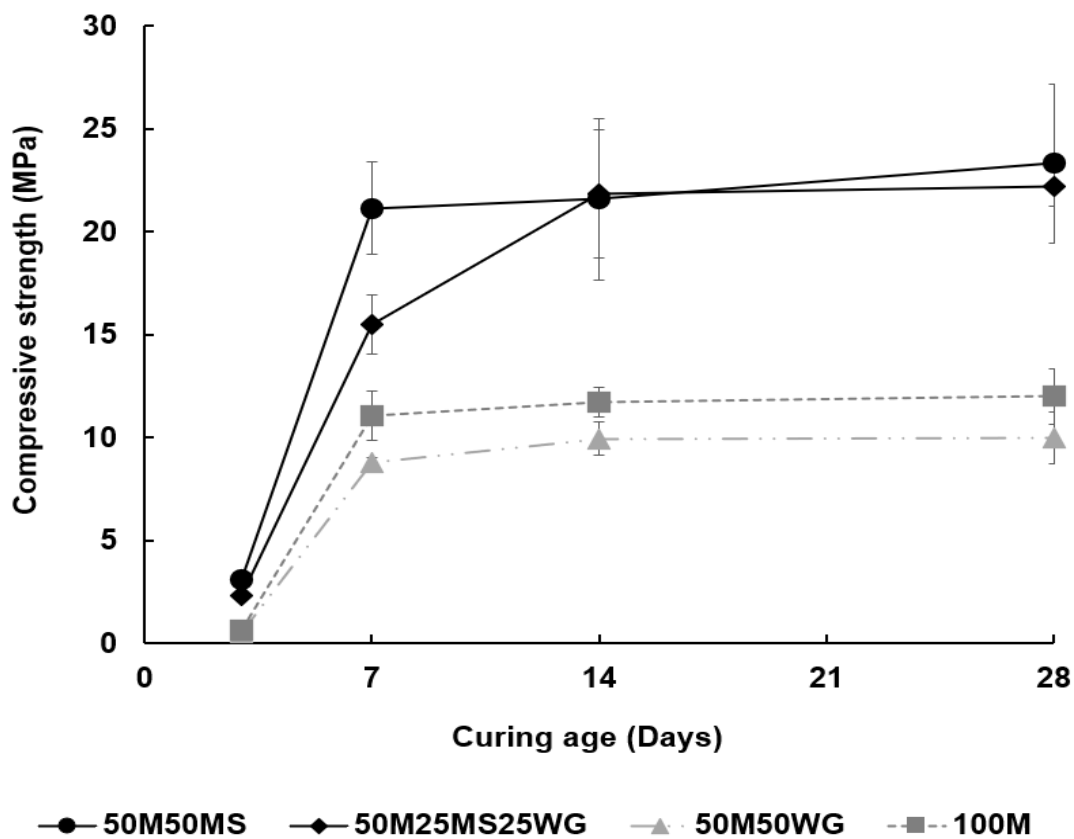
Fig. 6.15 Compressive strengths of all samples for up to 28 days

The 50M50WG sample, which involved the use of WG, exhibited the lowest strengths amongst all samples throughout the 28 days of analysis, reaching only 8.8 MPa and 10 MPa at 7 and 28 days, respectively (as shown in **Table. 6.5**). This limitation in strength development was related to the low reactivity of silica (i.e. WG) with the Mg-phase, which was in line with the high pH results of the 50M50WG samples shown in **Fig. 6.14**. The low reactivity of WG can be related to its relatively large particle size, when compared to MS,

shown in **Fig. 6.11**. Demonstrating comparable performance with 50M50WG samples, the 100M samples, which were introduced as a control group, revealed relatively low compressive strength. This limited strength development was related to the formation of brucite, which has a porous structure, thereby resulting in inferior mechanical performance [66,173]. A pure diluting effect caused by the replacement of WG that led to a lower compressive strength than the pure MgO sample revealed the relatively low interaction between the two components in 50M50WG samples [123].

Table. 6.5 Compressive strength (in MPa) and standard deviation (in MPa) of all samples for up to 28 days

Mixture	3 days		7 days		14 days		28 days	
	Compressive strength	STD	Compressive strength	STD	Compressive strength	STD	Compressive strength	STD
100M	0.66	0.32	11.09	1.20	11.72	0.74	12.00	1.64
50M50MS	3.13	0.09	21.20	2.23	21.60	3.94	23.30	3.86
50M50WG	0.52	0.01	8.80	0.29	9.90	0.82	10.00	1.26
50M25MS25WG	2.36	0.16	15.50	1.44	21.80	3.13	22.20	0.90

Alternatively, the 50M50MS sample, which contained MS as its silica source, showed consistent strength development and the highest strength (i.e. 23.3 MPa) over 28 days, which was 94.2% and 133% higher than the corresponding strengths of 100M and 50M50WG samples, respectively. This consistent strength gain was associated with the continuation of the hydration reaction within the 50M50MS sample due to the formation of M-S-H [118,215,252], and was in line with the most significant change in the pH values demonstrated by this sample.

The 50M25MS25WG sample, which consisted of a combination of MS and WG at equal amounts as its silica source, revealed a similar compressive strength development as the 50M50MS sample after 14 days of curing. The rapid increase in strength observed during the first 14 days of curing could be

attributed to the rapid formation of M-S-H. In terms of physical effect, WG can act as an inert filler, resulting in a denser microstructure that contributes to strength [253]. Furthermore, while maintaining its layered structure, brucite can react with the dissolved silica to form M-S-H, during which WG powders could act as nucleation sites, allowing M-S-H to form through the deposition of silicon–oxygen layers onto the WG layers. This nucleation effect could also be proven by the trend of the pH value of the 50M25MS25WG samples. Theoretically, the pH value of the M-S-H sample will be highly affected by the reactivity of the silica source, where the silica source with high amorphic shows a higher capacity to form M-S-H gel through the consumption of $Mg(OH)_2$ [248]. However, unlike sample 50M50WG, the pH value of samples 50M25MS25WG and 50M50MS were leveled at a similar range (<0.2) at all ages and exhibited a similar trend, which could be related to the nucleation effect provided by the WG leading the formation of M-S-H on the WG layers. Considering the comparable strength gain rate and 28-day strength of the 50M25MS25WG samples with that of the 50M50MS samples, WG could be considered as a feasible partial replacement of MS in $MgO-SiO_2$ systems.

6.3.3.4. XRD

The XRD patterns of 100M, 50M50WG, 50M25MS25WG and 50M50MS samples cured for 7 and 28 days are shown in **Fig. 6.16**. The peaks at 42.9°, 62.3°, 74.7° and 78.6° 2θ indicated the presence of crystalline MgO (periclase); while the main peaks at 18.6°, 38.0°, 50.8°, 58.6° and 68.2° 2θ were assigned to brucite. It is noted that the amorphous silica peak within the 50M50MS and 50M25MS25WG samples, located at around 17-25° 2θ as shown in **Fig. 6.16 (a)**, disappeared after 28 days of curing, indicating the complete reaction of silica source. In all samples, the presence of MgO and brucite were observed even after 28 days of curing which was an indication of the incomplete dissolution and hydration of MgO even after 28 days of curing, revealing the potential of the $MgO-SiO_2$ system to achieve further strength gain after hydration is completed. It is interesting to point out that the 100M samples exhibit the highest periclase peaks after 7 days of curing, which is

the indication of the highest amount of unreacted MgO, showing the hindered hydration of MgO due to the covering of MgO particles by the hydration products (i.e. brucite).
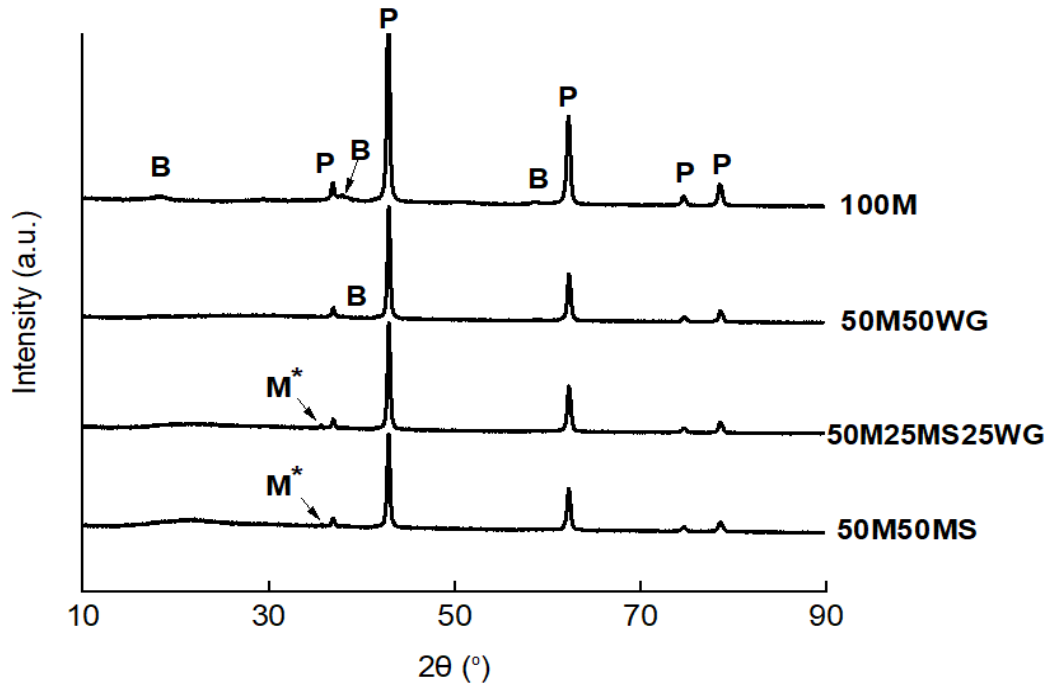
(a)
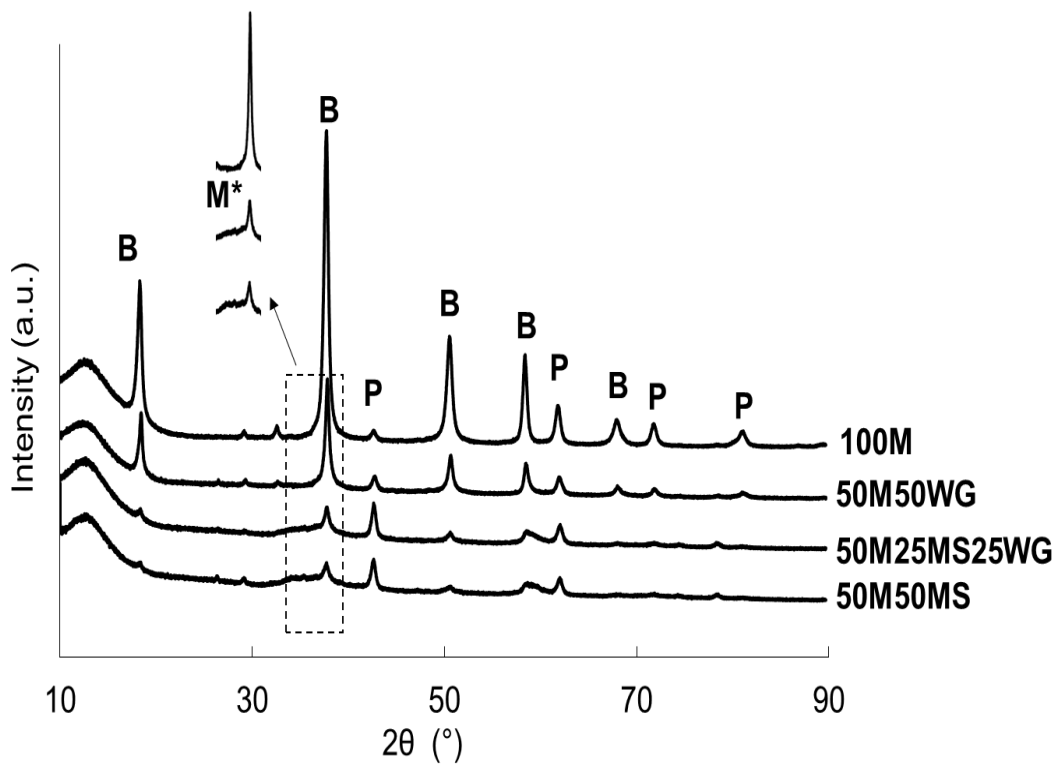
(b)

Fig. 6.16 XRD patterns of all samples after (a) 7 days; (b) 28 days of curing
(B: Brucite; P: Periclase; M*: M-S-H)

Within all samples cured for 7 days, the brucite peaks, as the main peaks of the product, were identified in 100M and 50M50WG samples, which can explain the similar strength performances of these two samples. The formation of porous brucite as the main hydration product in 100M and 50M50WG samples led to low early strength. No M-S-H peaks were observed in the 50M5WG sample, suggesting the low reactivity of WG due to the larger particle size compared to microsilica. When compared to XRD curves of 28 days, alternatively, samples 50M50MS and 50M25MS25WG only revealed a peak of M-S-H without the formation of brucite, which could be an indication of the higher strength compared to sample100M and 50M50WG.

The XRD diffractograms of all samples cured for 28 days are shown in **Fig. 6.16 (b)**. The 100M sample, containing only MgO for its binder component, demonstrated markedly higher intensities of brucite peaks when compared to other samples. This was attributed to the higher initial MgO content of the 100M sample. Differing from the other samples containing silica sources, no obvious M-S-H peaks, but comparatively high-intensity brucite peaks were observed in the 50M50WG sample, which was ascribed to the lack of silica dissolution and the low reactivity between WG and Mg-bearing phases even after 28 days. The main hydration phase in 100M and 50M50WG samples was brucite, which could explain their limited early strengths shown in **Fig. 6.15**. The differences observed in the brucite peaks among different samples could also be attributed to the higher degree of consumption of the brucite. Accordingly, within MgO-SiO$_2$ formulations, brucite can react with the dissolved silica to form M-S-H, which reduces the amount of brucite. Amongst the broad peaks of M-S-H located at around 20-30°, 35-39° and 58-62° 2θ [121,254], the presence of M-S-H was evident at 35-39° 2θ in the 50M25MS25WG and 50M50MS samples [188]. The intensities of the MgO and brucite in these samples were both much lower than those of the other two samples, indicating the transition from MgO to brucite and the concurrent consumption of brucite by its reaction with silica to form M-S-H. Further, some

Mg^{2+} ions can react with silica source directly instead of hydration, due to the involvement of NaHMP which can inhibit the formation of $Mg(OH)_2$ [255]. In the blend, MgO adsorbed the phosphate species released by the dissolution of NaHMP, therefore, the nucleation of the $Mg(OH)_2$ was hindered, increasing the concentration of Mg^{2+} in the solution [255]. This increased reaction degrees of $MgO\text{-}SiO_2$ mixes were reflected by the more pronounced decrease in the rate of pH values of the 50M25MS25WG and 50M50MS samples, as well as their higher strengths. When comparing the 7 days and 28 days XRD curves of the 50M25MS25WG and 50M50MS samples (**Fig. 6.16 (a)** vs **(b)**), it is clear that after the complete dissolution of the silica source, unreacted MgO continued to hydrate to form the brucite, which could contribute to the minor strength gain. With an increase in the amount of amorphous silica source content, the intensities of the brucite peaks were reduced, almost disappearing in the 50M50MS sample, whose silica source was MS. The differences in the phase compositions of these four samples revealed that the formation of different hydration phases and the hydration reactivity were highly affected by the type and properties of the silica source used in the mix design.

6.3.3.5. TG/DTG

Fig. 6.17 shows the TG/DTG plots of all samples cured for 28 days. Even though their amorphous silica source contents were different, the comparable TG curves of the 50M50MS and 50M25MS25WG samples revealed similar total mass loss at 28 days (16.61% vs 17%), which were in line with their comparable mechanical performances. Significantly, 50M50WG samples only showed a slightly higher total mass loss compared to that of the 50M25MS25WG sample (20.3% vs 17%), however, in this sample, the second stage of mass loss (as shown in **Table. 6.6**) contributes to the majority of total mass loss, which is different from those of 50M50MS and 50M25MS25WG samples, resulting in the different mechanical performance. For the three specimens containing silica sources, the compressive strength increased with the increase in total mass loss. The figure also shows a

smaller peak in the 100M samples at around 110 ⁰C when compared to other samples, which could be the result of the dehydration of absorbed water, occurring at a temperature below 150 ⁰C [125]. This observation suggests that mechanical performance is not only correlated to the total mass loss but is also linked to differences in the types and contents of the formed hydration phases, which could be demonstrated from the various DTG peaks.

The TG data of 50M50MS and 50M25MS25WG samples show multi-step weight loss curves for the M-S-H up to 900 °C, which is in line with other studies reporting TGA results for M-S-H [119]. For these 2 groups of samples, the TG curves in the temperature range of 320 to 430 °C present lower slopes than other samples, suggesting the transition from brucite to M-S-H. However, a sudden weight loss due to brucite decomposition at around 400 °C could be observed due to the unreacted brucite [123], which is also in line with the XRD results from **Fig. 6.16**. In terms of DTG curves, the sharp peaks at around 110 °C and 400 °C could be seen in the 50M50MS and 50M25MS25WG samples owing to the loss of interlayer water, separation of hydroxyl groups in M-S-H and the decomposition of a small amount of brucite [120]. For the 100M sample, a large peak at around 400 °C was likely ascribed to the decomposition of a large amount of brucite, which is in close agreement with the XRD pattern of the 100M sample.

According to [118-120], three stages of mass loss that are involved during the thermal decomposition of the M-S-H based samples can be summarized as follows:

1. 110 to 320 °C: Mass loss due to the loss of interlayer water in M-S-H gel.

2. 320 to 430 °C: Mass loss due to the removal of water bound to M-S-H gel and decomposition of brucite.

3. 430 to 900 °C: Mass loss due to the decomposition of hydroxyl groups bound to Mg^{2+} and silanol groups in M-S-H gel.
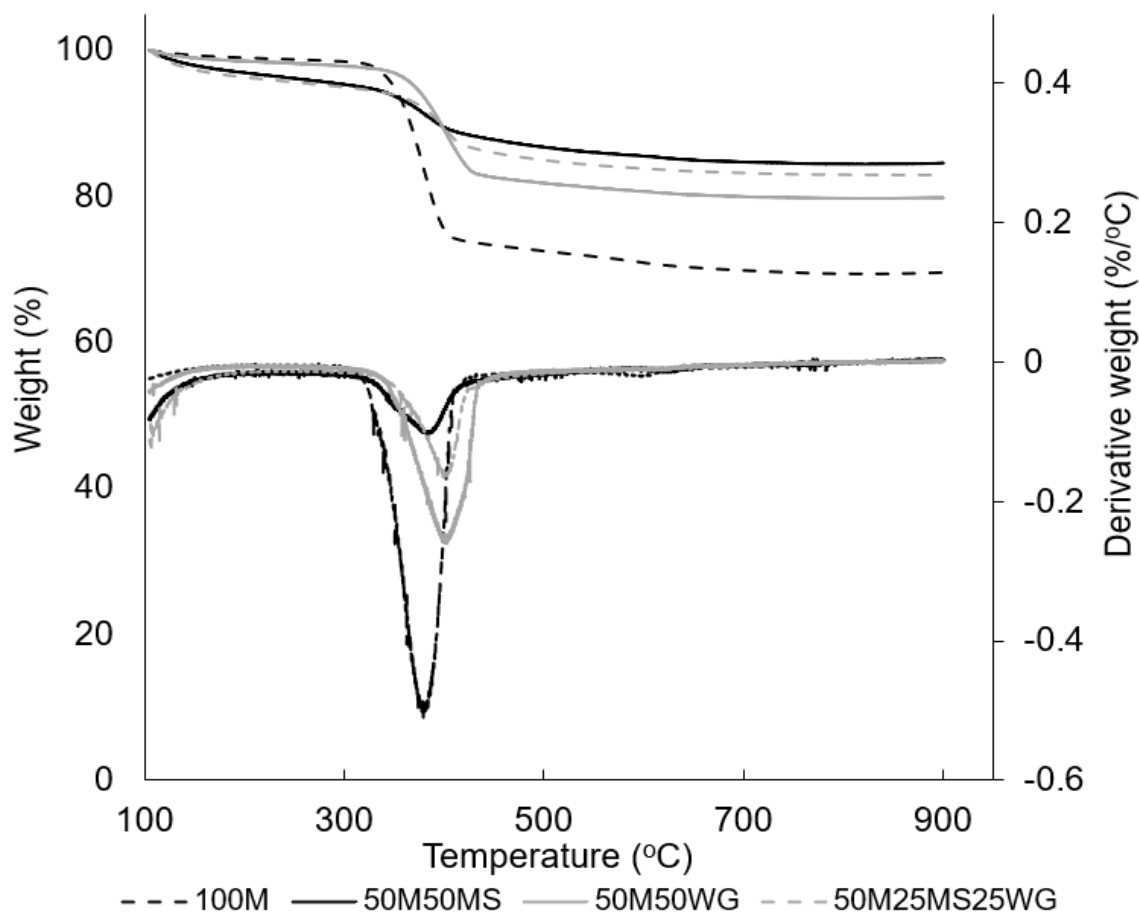
Fig. 6.17 Thermogravimetric analysis of all samples after 28 days of curing

These three mass loss stages can be seen and agree well with the TG results (shown in **Fig. 6.17**) obtained in this study. The first stage represents the weight loss of interlayer water in M-S-H gel, which is related to the mass of M-S-H gels. The second stage, attributed to the de-hydroxylation of $Mg(OH)_2$, can be observed clearly in DTG curves, and is in line with XRD results. The last stage of weight loss is led by the removal of silanol groups of M-S-H gel and is consistent with M-S-H gel formation, which is identified in XRD and TG/DTG results. Though there was no M-S-H gel formed in the 100M samples, the high mass loss was shown, which is related to the higher amount of unreacted MgO compared to other groups. For instance, the impurities in MgO (e.g. magnesite) will also contribute to the mass loss in this stage, as shown by a small peak at ~600 °C on the DTG curve of the 100M samples.

188

Table. 6.6 shows the mass loss ratios in three stages for all samples cured for 28 days. The 100M sample exhibited the lowest mass loss between 110 and 320 °C among all samples, ascribed to the lack of M-S-H formation due to a lack of a silica source. A similar scenario was observed in the 50M50WG samples, suggesting the limited reaction between MgO and the low-reactivity silica, albeit there was a small mass loss in the first stage, indicating its low amount of M-S-H, which is also in line with the previous sections. The samples containing an amorphous silica source (i.e. 50M50MS and 50M25MS25WG samples) revealed a higher mass loss in this temperature range (i.e. 110 to 320 °C), which included the loss of interlayer water from M-S-H and the dehydration of adsorbed water from the air, accounting for their much higher compressive strength compared to the other two specimens.

Table. 6.6 Mass loss (wt.%) of samples analyzed at 28 days by thermogravimetric analysis

Mixture	110-320 ºC	320-430 ºC	430-900 ºC
50M50MS	6.1	6.7	3.7
50M25MS25WG	5.4	8.1	3.5
50M50WG	2.4	14.4	3.5
100M	1.8	24.6	4.1

The mass loss within the temperature range of 320 to 430 °C can be mainly related to the decomposition of brucite. Not surprisingly, the 100M sample exhibited the highest weight loss from brucite dihydroxylation (24.6%). The weight loss between 320 to 430 °C of the 50M50WG sample (14.4%), being much lower than that of the 100M sample (24.6%), indicates the pure diluting effect and the presence of a small amount of M-S-H formed in this group. This value is much higher than the groups 50M50MS (i.e. 6.7%) and 50M25MS25WG (i.e. 8.1%), indicating a substantially higher degree of reaction between brucite and silica, which is in line with their respective XRD patterns. In terms of mixtures with high Mg/Si ratios, exothermic transition around 840–860 °C is normally observed in DTG curves, which is ascribed to the decomposition of amorphous M-S-H and the recrystallization to SiO_2 [119]. It is worth noting that, the decomposition peak of MSH failed to appear at 840-860 °C in the groups of 50M50MS and 50M25MS25WG, which might be related to the relatively lower Mg/Si ratio since the periclase peaks can still be detected in XRD after 28 days of curing, as shown in **Fig. 6.16 (b)**. A similar phenomenon was also found in other studies [125,256].

6.3.3.6. FTIR

FTIR is sensitive to vibrational modes, thereby absorption bands can indirectly provide information on the hydration phases, which can reflect XRD and TGA analyses. **Fig. 6.18** shows the FTIR spectra of all samples cured for 28 days. The 50M50MS and 50M25MS25WG samples demonstrated similar patterns within the wide range of ~980 to 1120 cm^{-1}, which can be associated with the presence of SiO_2 or the chains within M-S-H [125], and also agree well with their compressive strength results. A small peak at ~890 cm^{-1} can be assigned to the Si-OH group of layered M-S-H [123]. The absorption band at ~800 cm^{-1} can be attributed to the Si-O stretching vibrations in the SiO_2 [125,257], which is absent in the raw material, MgO. Therefore, given the foregoing, the figure indicates that very similar hydration phases, i.e. M-S-H, formed within the 50M50MS and 50M25MS25WG samples, as reflected by

the band range ~920 to 1120 cm^{-1}. Typically, the band at 1150 cm^{-1} shifts toward 1100 cm^{-1} and can be assigned to the anti-symmetric stretching vibration of Si–O–Mg, which suggests the formation of layer-structured magnesium silicate hydrate [256]. Meanwhile, indicated by the band at 920 cm^{-1} from the figure (shifted from 890 cm^{-1}), there is still some M-S-H formed in the 50M50WG samples, which is in line with the weight loss of the 50M50WG samples between 110 and 320 °C, but the reaction between brucite and SiO$_2$ is quite limited.
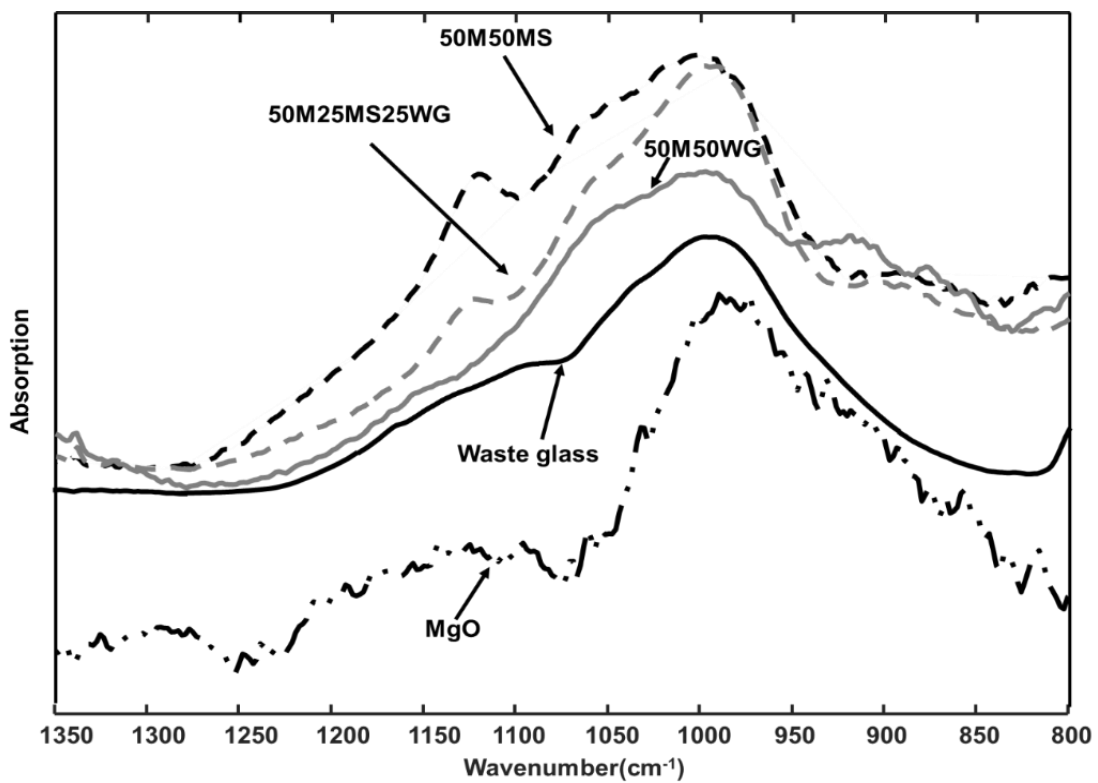
Fig. 6.18 FTIR results of all samples after 28 days of curing

The reactivity of MgO indicates the amount of brucite available for the reaction [151]. However, the pH of brucite is still not enough to dissolve the waste glass. Also, according to Golubeva et al. [258], the high reactivity of MgO may lead to the rapid formation of brucite, which significantly exceeds the dissolution rate of waste glass resulting in a slower reaction rate by the formed silicon tetrahedral sites, which is also confirmed with the curves shown in **Fig. 6.18**.

6.3.4. Conclusions

This section aimed to discover the effect of different silica sources in the form of microsilica and waste glass, and a combination of the two on the mechanical properties, phase compositions and environmental impacts of MgO-SiO$_2$ formulations. The main findings can be drawn as follows:

1. Due to the comparatively low solubility and larger particle size of waste glass powders, complete reliance on the waste glass as a silica source significantly sacrifices the performance of MgO-SiO$_2$ binders and therefore should be avoided. However, partial substitution of microsilica with waste glass is feasible to maintain the mechanical efficiency of MgO-SiO$_2$ binders, reduce the cost of raw material, and achieve a satisfactory hardening property (i.e. setting times).

2. The main hydrate phase in the 100M and 50M50WG samples was brucite, along with a small amount of M-S-H in the 50M50WG samples, resulting in relatively lower early strength in these systems. Alternatively, M-S-H was more pronounced in systems containing microsilica, explaining the satisfactory strength results of these mixes.

WG, considered a waste material, can partially replace MS in MgO-SiO$_2$ formulations, making it an alternative for providing economic, engineering and environmental benefits in the production of low-cost construction material. Further studies on the optimum mix designs of the mixture by using WG with other particle sizes (i.e. high reactivity) and curing regimes can further improve the mechanical properties of MgO-SiO$_2$ formulations, especially for large-scale structural applications.

7. Chapter 7 Conclusions and Future Works

7.1. A Summary of Key Findings of Thesis

The use of amino acids improved carbon sequestration, compressive strength and sustainability of magnesia-based formulations. The enhanced mechanical properties of the Portland metakaolin cement blends with the use of amino acid-controlled hydrated magnesium carbonates (HMCs) were also achieved. Meanwhile, two practice applications of magnesia in alumina silicate hydrate binder systems were assessed in terms of mechanical properties, suggesting the high potential of magnesia used in some typical construction sector to improve the mechanical performance of binder. Based on the conclusions, it appears that the objectives of the project have been adequately achieved. The following is a brief summary of the main conclusions derived from each chapter conducted in this research.

7.1.1. Performance-controlling Additives in Magnesium-based Binder

Overall, the results suggest that amino acids can be used as chemical admixtures to improve the mechanical performance of magnesium-based composites and capture more CO_2. For instance, the sample containing 0.2M of L-Asp sequestrated 46.7% more CO_2 than the plain MgO. Meanwhile, amino acids improved the stabilisation of the typical polymorph of HMCs, i.e. nesquehonite, in carbonated MgO composites. Regarding enhancing carbonation degree, the effectiveness of L-Asp increases with increasing concentration. Because of its superior morphology, nesquehonite was considered as the most effective HMC which can contribute more to compressive strength, compared with other HMCs (e.g. dypingite). The

samples containing 0.2M of L-Asp showed up to a 34.2% increase in compressive strengths at 14 days, compared to the control batch.

The morphology of both hydration and carbonation products was modified by the L-Asp. The amount of amorphous products increased by the application of L-Asp, leading to higher reactivity of the products. This feature provides the high potential for performance-controlled HMCs to apply to a wide range of binder systems due to their high reactivity.

7.1.2. Use of Magnesium-based Carbonates in Development of a Portland Metakaolin Cement with Enhanced Properties

The properties of Portland metakaolin cement, in terms of mechanical strength, microstructure, and durability are affected by the addition of different carbonate sources, especially when the cations are different. This is mainly through changing the hydration product in the binder. Magnesite ($MgCO_3$), hydromagnesite ($4MgCO_3 \cdot Mg(OH)_2 \cdot 4H_2O$), and dypingite ($4MgCO_3 \cdot Mg(OH)_2 \cdot 5H_2O$) are not considered as the desirable carbonates sources in this binder system. When using them as carbonate sources in Portland metakaolin cement, inferior mechanical strength, microstructure, and durability were observed. The formation of carboaluminates (i.e. Hc and Mc) provided a distinct advantage of carbonate addition in terms of compressive strength. LC3 exhibited the highest compressive strength, as it formed the highest amount of carboaluminates. The portlandite ($Ca(OH)_2$) was maintained by the formation of carboaluminates in the Portland metakaolin cement binders.

However, the lab-made HMCs (contain nesquehonite ($MgCO_3 \cdot 3H_2O$) and unreacted MgO) can improve the early-age strength of the binders. In comparison with the LC3 mix, AMC3 showed a 7-day compressive strength of 32.4 MPa, which was 8% higher than that of the LC3 mix. In the Portland metakaolin carbonate binder systems, the carboaluminates contribute more to compressive strength before 28 days, while strätlingite plays a more important role in controlling the late-age strength. The microstructure of the AMC3 sample was enhanced by the involvement of metakaolin, which limited the formation of $Mg(OH)_2$, subsequently, densified the binder matrix, leading to an outstanding mechanical performance.

7.1.3. Magnesia in Alumina Silicate Hydrate Binder Systems

Using magnesium-based material in alumina silicate hydrate binder systems has been investigated. To extend the range of applications, this thesis studied the feasibility of MgO in the alumina-silicate/silicate (i.e. waste excavation clay and water glass) binder systems. It provides two applications to reuse the alumina-silicate/silicate based waste material.

The first application introduced reactive magnesia (i.e. MgO) and sodium carbonate, together with an early-age oven curing regime as an approach to clay solidification. In this study, compared with the CaO-based clay samples, greater compressive strength was revealed in the MgO-based counterparts, which could be possibly ascribed to the interlocking effects and a 3D structure of fibrous nesquehonite produced in this group. A similar finding was also observed in **Chapter 4**, thereby, it is concluded that instead of the content, the morphology of hydration phases could be more crucial in controlling the compressive strength of clay samples investigated in this study. The strength variation between the CaO- and MgO-based clay samples may be enlarged

by the oven curing (or drying), as the micro-crack development within the M20-OC group could be limited due to the delayed expansion of MgO hydration, however, CaO failed to eliminate the occurrence of micro-cracks within the clay samples at a later age because of its rapid hydration possibly, and the micro-cracks in these samples deteriorated the compressive strength.

In the second application, the involvement and influence of waste glass in the formation of magnesium-silicate-hydrated (M-S-H) binders were investigated. Due to the comparatively low solubility and larger particle size of waste glass powders, complete reliance on the waste glass as a silica source significantly sacrificed the performance of $MgO-SiO_2$ binders and therefore should be avoided. However, partial substitution of microsilica (i.e. 50%) with waste glass is feasible to maintain the mechanical efficiency of $MgO-SiO_2$ binders, reduce the cost of raw material, and achieve a satisfactory mechanical strength and hardening property (i.e. compressive strength and setting times).

7.2. Future Work

It is a novel concept to control the phase polymorphs of hydrated and carbonated magnesia composites with organic matrices. Amino acids are proved to enable the enhancement of the performance of these composites. When L-Asp reached supersaturation, a strong attraction exists between the excess negative charge of L-Asp and Mg^{2+}, increasing the ions concentration and promoting the precipitation of carbonate. This theory may also explain the outstanding performance-controlling effects led by the high concentration L-Asp. Moreover, due to its double negative carboxyl groups, the L-Asp could bind to the specific crystal plane, inhibiting crystal growth. Further investigation of the mechanism of improved performance and the stabilisation of polymorphs of the composites when containing amino acids is also required.

Since the formed 'organic-inorganic' hybrid phases demonstrated outstanding strength, the reaction between the organic matrices (i.e. amino acids) and inorganic composite (i.e. magnesium-based carbonate) needs to be extensively studied to develop materials with extraordinary performance. For instance, broader ranges of amino acids can be adopted to control the crystallisation of other inorganic matrices, such as other hydrated magnesium-based carbonates or $CaCO_3$ in the future. Moreover, a comprehensive LCA is also needed. Since magnesia-based cement can absorb CO_2 during its service life, the LCA should adopt a cradle-to-grave approach. If carbonation curing is used to prepare the block or other elements, the environmental impact of the industrial CO_2 used in curing should also be considered.

Even though several carbonates were applied in this study and found a noticeable difference between the calcium carbonate and magnesium-based carbonates, there was no clear distinct difference between the various magnesium-based carbonates. Therefore, the role of cations (e.g. Mg^{2+} and Ca^{2+}) in carbonate sources seems to be critical and needs to be further investigated. In other words, the true benefits of calcium carbonate in the LC3 binder system remain to be determined. The formation mechanisms of carboaluminates and strätlingite are still unclear, which play important roles in the development of strength, and required to be clarified by a series of deeper investigations. Specificlly, the contributions of hemi- carboaluminate (Hc) and mono-carboaluminate (Mc) phases to the development of strength are vital to study.

Magnesia can involve in the utilisation of large quantities of waste and industrial by-products, due to its lower sensitivity to impurities. Even though it cannot gain a comparable strength with PC occasionally, magnesia can apply to some specific scenarios such as road pavement construction, soil

solidification, etc. Although the mechanical performance of the samples may be the most important property, several other properties of the clay-based samples developed such as the setting time, the durability or the geotechnical properties (e.g. atterberg limits) are also of great importance, which needs to be investigated in the future. Moreover, the reaction mechanism of reactive magnesia in the ternary phase still needs to be further investigated, which can provide a broader prospect for the practical applications.

8. Reference

Reference List

[1] P.J.M. Monteiro, S.A. Miller, A. Horvath, Towards sustainable concrete, Nature Materials. 16 (2017) 698-699.

[2] N. Chatziaras, C.S. Psomopoulos, N.J. Themelis, Use of waste derived fuels in cement industry: a review, Management of Environmental Quality: An International Journal. 27 (2016) 178-193.

[3] IEA, WBCSD, world business council on sustainable development & CSI, cement sustainability initiative. Technology Roadmap: Low-Carbon Transition in the Cement Industry, (2018).

[4] F. Pearce, Can the World's Most Polluting Heavy Industries Decarbonize? (2021).

[5] EPBD, Energy performance of buildings: climate neutrality by 2050, (2012).

[6] J.M. Allwood, J.M. Cullen, R.L. Milford, Options for Achieving a 50% Cut in Industrial Carbon Emissions by 2050, Environ. Sci. Technol. 44 (2010) 1888-1894.

[7] A. Josa, A. Aguado, A. Heino, E. Byars, A. Cardim, Comparative analysis of available life cycle inventories of cement in the EU, Cement and concrete research. 34 (2004) 1313-1320.

[8] Heavy Minerals Limited: 2021 USGS Mineral Commodity Summary, (2022).

[9] P. Busch, A. Kendall, C.W. Murphy, S.A. Miller, Literature review on policies to mitigate GHG emissions for cement and concrete, Resour. Conserv. Recycling. 182 (2022) 106278.

[10] T. Gonçalves, R.V. Silva, J. De Brito, J.M. Fernández, A.R. Esquinas, Hydration of reactive MgO as partial cement replacement and its influence on the macroperformance of cementitious mortars, Advances in Materials Science and Engineering. 2019 (2019).

[11] Y. Yi, M. Liska, A. Al-Tabbaa, Initial investigation into the use of GGBS-MgO in soil stabilisation, in: Anonymous Grouting and Deep Mixing 2012, , 2012, pp. 444-453.

[12] U.S. Geological Survey (USGS), Cement Statistics and Information, (2018).

[13] M. Schneider, M. Romer, M. Tschudin, H. Bolio, Sustainable cement production—present and future, Cem. Concr. Res. 41 (2011) 642-650.

[14] J. An, R.S. Middleton, Y. Li, Environmental Performance Analysis of Cement Production with CO2 Capture and Storage Technology in a Life-Cycle Perspective, Sustainability. 11 (2019).

[15] M.S. Imbabi, C. Carrigan, S. McKenna, Trends and developments in green cement and concrete technology, International Journal of Sustainable Built Environment. 1 (2012) 194-216.

[16] W. Shen, L. Cao, Q. Li, Z. Wen, J. Wang, Y. Liu, R. Dong, Y. Tan, R. Chen, Is magnesia cement low carbon? Life cycle carbon footprint comparing with Portland cement, J. Clean. Prod. 131 (2016) 20-27.

[17] World Business Council for Sustainable Development, The cement sustainability initiative: getting the numbers right, (2009).

[18] L. Mo, D.K. Panesar, Accelerated carbonation–A potential approach to sequester CO2 in cement paste containing slag and reactive MgO, Cement and Concrete Composites. 43 (2013) 69-77.

[19] C. Unluer, A. Al-Tabbaa, Enhancing the carbonation of MgO cement porous blocks through improved curing conditions, Cement and concrete research. 59 (2014) 55-65.

[20] L. Mo, D.K. Panesar, Effects of accelerated carbonation on the microstructure of Portland cement pastes containing reactive MgO, Cement and concrete research. 42 (2012) 769-777.

[21] M.A. Shand, The Chemistry and Technology of Magnesia, John Wiley & Sons, 2006.

[22] C. Sonat, C.H. Lim, M. Liska, C. Unluer, Recycling and reuse of reactive MgO cements – A feasibility study, Constr. Build. Mater. 157 (2017) 172-181.

[23] K. Hirota, N. Okabayashi, K. Toyoda, O. Yamaguchi, Characterization and sintering of reactive MgO, Mater. Res. Bull. 27 (1992) 319-326.

[24] S. Ruan, E. Yang, C. Unluer, Production of reactive magnesia from desalination reject brine and its use as a binder, Journal of CO2 Utilization. 44 (2021) 101383.

[25] Segall, R. L., Smart, R. St. C., and Turner, P. S., In Surface and Near-Surface Chemistry of Oxide Materials, , (1988).

[26] Fruhwirth, O., Herzog, G. W., Hollerer, I., and Rachetti, A., Surf. Tech, (1985) 301 – 317.

[27] G.L. Smithson, N.N. Bakhshi, Kinetics and mechanism of carbonation of magnesium oxide slurries, 12 (1973) 99-106.

[28] S. Liang, X. Zhou, P. Hou, Impact of amino acids as performance-controlling additives on the hydration of reactive MgO, 2423 (2023) 12029.

[29] G.W. Stephan, C.H. MacGillavry, The crystal structure of nesquehonite, $MgCO_3. 3H_2O$, 28 (1972) 1031-1033.

[30] R.J. Hill, J.H. Canterford, F.J. Moyle, New Data for Lansfordite, 46 (1982) 453-457.

[31] M. Akao, S. Iwai, The hydrogen bonding of artinite, 33 (1977) 951−3953.

[32] M. Akao, S. Iwai, The hydrogen bonding of hydromagnesite, 33 (1977) 1273−1275.

[33] G. Raade, Dypingite, a new hydrous basic carbonate of magnesium, from Norway, 55 (1970) 1457-1465.

[34] E.G. Soares, J. Castro-Gomes, Carbonation curing influencing factors of Carbonated Reactive Magnesia Cements (CRMC)–A review, J.Clean.Prod. 305 (2021) 127210.

[35] G.W. Groves, D.I. Rodway, I.G. Richardson, The carbonation of hardened cement pastes, 3 (1990) 117-125.

[36] H.F. Taylor, Cement Chemistry, Thomas Telford London, 1997.

[37] G. Rimmelé, V. Barlet-Gouédard, O. Porcherie, B. Goffé, F. Brunet, Heterogeneous porosity distribution in Portland cement exposed to CO2-rich fluids, Cem.Concr.Res. 38 (2008) 1038-1048.

[38] A. Fabbri, J. Corvisier, A. Schubnel, F. Brunet, B. Goffé, G. Rimmele, V. Barlet-Gouédard, Effect of carbonation on the hydro-mechanical properties of Portland cements, Cem.Concr.Res. 39 (2009) 1156-1163.

[39] P. De Silva, L. Bucea, V. Sirivivatnanon, Chemical, microstructural and strength development of calcium and magnesium carbonate binders, Cem.Concr.Res. 39 (2009) 460-465.

[40] L.J. Vandeperre, A. Al-Tabbaa, Accelerated carbonation of reactive MgO cements, 19 (2007) 67-79.

[41] M. Liska, A. Al-Tabbaa, Ultra-green construction: reactive magnesia masonry products, 162 (2009) 185-196.

[42] V. Ferrini, C. De Vito, S. Mignardi, Synthesis of nesquehonite by reaction of gaseous CO2 with Mg chloride solution: Its potential role in the sequestration of carbon dioxide, J.Hazard.Mater. 168 (2009) 832-837.

[43] I.M. Power, S.A. Wilson, J.M. Thom, G.M. Dipple, G. Southam, Biologically induced mineralization of dypingite by cyanobacteria from an alkaline wetland near Atlin, British Columbia, Canada, 8 (2007) 1-16.

[44] S. Teir, R. Kuusik, C. Fogelholm, R. Zevenhoven, Production of magnesium carbonates from serpentinite for long-term storage of CO2, Int.J.Miner.Process. 85 (2007) 1-15.

[45] R. Gruppo, Finding of Volcanic Artinite Overall of Alban Hells, (2003).

[46] N.T. Dung, A. Lesimple, R. Hay, K. Celik, C. Unluer, Formation of carbonate phases and their effect on the performance of reactive MgO cement formulations, Cem.Concr.Res. 125 (2019) 105894.

[47] Z. Xing, L. Bai, Y. Ma, D. Wang, M. Li, Mechanism of magnesium oxide hydration based on the multi-rate model, 11 (2018) 1835.

[48] M. Liska, L.J. Vandeperre, A. Al-Tabbaa, Influence of carbonation on the properties of reactive magnesia cement-based pressed masonry units, 20 (2008) 53-64.

[49] Z. Li, Q. Yu, X. Chen, H. Liu, J. Zhang, J. Zhang, Y. Yang, J. Wei, The role of MgO in the thermal behavior of MgO–silica fume pastes, 127 (2017) 1897-1909.

[50] J. Chen, T. Li, X. Li, K. Chou, X. Hou, Some new perspective on the reaction mechanism of MgO–SiO2–H2O system, 13 (2016) 1164-1172.

[51] L. Pu, C. Unluer, Investigation of carbonation depth and its influence on the performance and microstructure of MgO cement and PC mixes, Constr.Build.Mater. 120 (2016) 349-363.

[52] D.K. Panesar, L. Mo, Properties of binary and ternary reactive MgO mortar blends subjected to CO2 curing, 38 (2013) 40-49.

[53] N.T. Dung, R. Hay, A. Lesimple, K. Celik, C. Unluer, Influence of CO2 concentration on the performance of MgO cement mixes, 115 (2021) 103826.

[54] C. Unluer, A. Al-Tabbaa, The role of brucite, ground granulated blastfurnace slag, and magnesium silicates in the carbonation and performance of MgO cements, Constr.Build.Mater. 94 (2015) 629-643.

[55] A.P. Weber, Focus Group S-6: Using plants for carbon sequestration, 111 (2021).

[56] N.T. Dung, C. Unluer, Improving the performance of reactive MgO cement-based concrete mixes, Constr.Build.Mater. 126 (2016) 747-758.

[57] D. Meng, C. Unluer, E. Yang, S. Qian, Recent advances in magnesium-based materials: CO2 sequestration and utilization, mechanical properties and environmental impact, 138 (2023) 104983.

[58] R. Hay, K. Celik, Accelerated carbonation of reactive magnesium oxide cement (RMC)-based composite with supercritical carbon dioxide (scCO2), 248 (2020) 119282.

[59] L. Mo, F. Zhang, M. Deng, D.K. Panesar, Effectiveness of using CO2 pressure to enhance the carbonation of Portland cement-fly ash-MgO mortars, 70 (2016) 78-85.

[60] K. Rausis, A. Ćwik, I. Casanova, Phase evolution during accelerated CO2 mineralization of brucite under concentrated CO2 and simulated flue gas conditions, 37 (2020) 122-133.

[61] L. Wang, L. Chen, J.L. Provis, D.C.W. Tsang, C.S. Poon, Accelerated carbonation of reactive MgO and Portland cement blends under flowing CO2 gas, 106 (2020) 103489.

[62] R. Dheilly, Y. Sebaibi, J. Tudo, M. Queneudec, Importance de la présence de magnésie dans le stockage de la chaux: carbonatation de l'oxyde et de l'hydroxyde de magnésium, Can.J.Chem. 76 (1998) 1188-1196.

[63] N.T. Dung, C. Unluer, Carbonated MgO concrete with improved performance: The influence of temperature and hydration agent on hydration, carbonation and strength gain, 82 (2017) 152-164.

[64] P. Liyun, U. Cise, Effect of Preconditioning on Carbonated Reactive MgO-Based Concrete Samples, J.Mater.Civ.Eng. 32 (2020) 04020314.

[65] P. Liyun, U. Cise, Performance and Microstructure of Carbonated MgO Samples under High Temperatures, J.Mater.Civ.Eng. 31 (2019) 04019003.

[66] S. Ruan, C. Unluer, Effect of air entrainment on the performance of reactive MgO and PC mixes, 142 (2017) 221-232.

[67] R. Hay, K. Celik, Hydration, carbonation, strength development and corrosion resistance of reactive MgO cement-based composites, Cem.Concr.Res. 128 (2020) 105941.

[68] N.T. Dung, C. Unluer, Development of MgO concrete with enhanced hydration and carbonation mechanisms, Cem.Concr.Res. 103 (2018) 160-169.

[69] N.T. Dung, C. Unluer, Potential additives for magnesia-based concrete with enhanced performance and propensity for CO_2 sequestration, 56 (2022) 101834.

[70] K.P. Matabola, E.M. van der Merwe, C.A. Strydom, F.J.W. Labuschagne, The influence of hydrating agents on the hydration of industrial magnesium oxide, 85 (2010) 1569-1574.

[71] N.T. Dung, C. Unluer, Improving the carbonation of reactive MgO cement concrete via the use of $NaHCO_3$ and NaCl, J.Mater.Civ.Eng. 30 (2018) 04018320.

[72] S. Ma, A.H. Akca, D. Esposito, S. Kawashima, Influence of aqueous carbonate species on hydration and carbonation of reactive MgO cement, 41 (2020) 101260.

[73] N.T. Dung, C. Unluer, Sequestration of CO_2 in reactive MgO cement-based mixes with enhanced hydration mechanisms, 143 (2017) 71-82.

[74] N.T. Dung, C. Unluer, Influence of nucleation seeding on the performance of carbonated MgO formulations, 83 (2017) 1-9.

[75] N.T. Dung, T. Hooper, C. Unluer, Improving the carbonation resistance of Na2CO3-activated slag mixes via the use of reactive MgO and nucleation seeding, 115 (2021) 103832.

[76] C. Unluer, A. Al-Tabbaa, Impact of hydrated magnesium carbonate additives on the carbonation of reactive MgO cements, Cem.Concr.Res. 54 (2013) 87-97.

[77] C. Kuenzel, F. Zhang, V. Ferrandiz-Mas, C.R. Cheeseman, E.M. Gartner, The mechanism of hydration of MgO-hydromagnesite blends, Cem.Concr.Res. 103 (2018) 123-129.

[78] F. Winnefeld, E. Epifania, F. Montagnaro, E.M. Gartner, Further studies of the hydration of MgO-hydromagnesite blends, Cem.Concr.Res. 126 (2019) 105912.

[79] N.T. Dung, C. Unluer, Performance of reactive MgO concrete under increased CO2 dissolution, Cem.Concr.Res. 118 (2019) 92-101.

[80] M.C.G. Juenger, R. Snellings, S.A. Bernal, Supplementary cementitious materials: New sources, characterization, and performance insights, 122 (2019) 257-273.

[81] R. Snellings, Assessing, Understanding and Unlocking Supplementary Cementitious Materials, RILEM Tech Lett. 1 (2016) 50-55.

[82] Q.D. Nguyen, M.S.H. Khan, A. Castel, Engineering properties of limestone calcined clay concrete, 16 (2018) 343-357.

[83] G. Mishra, A. Emmanuel, S. Bishnoi, Studies on the Influence of Limestone-Calcined Clay Blend on the Hydration of Cement, (2018) 322-326.

[84] Y. Briki, F. Avet, M. Zajac, P. Bowen, M.B. Haha, K. Scrivener, Understanding of the factors slowing down metakaolin reaction in limestone calcined clay cement (LC3) at late ages, Cem.Concr.Res. 146 (2021) 106477.

[85] EPFL, Limestone Calcined Clay Cement, (2023).

[86] F. Avet, K. Scrivener, Influence of pH on the chloride binding capacity of Limestone Calcined Clay Cements (LC3), Cem.Concr.Res. 131 (2020) 106031.

[87] Y. Dhandapani, M. Santhanam, Investigation on the microstructure-related characteristics to elucidate performance of composite cement with limestone-calcined clay combination, Cem.Concr.Res. 129 (2020) 105959.

[88] A. Machner, M. Zajac, M.B. Haha, K.O. Kjellsen, M.R. Geiker, K. De Weerdt, Limitations of the hydrotalcite formation in Portland composite cement pastes containing dolomite and metakaolin, Cem.Concr.Res. 105 (2018) 1-17.

[89] C.S. Poon, L. Lam, S.C. Kou, Y.-. Wong, R. Wong, Rate of pozzolanic reaction of metakaolin in high-performance cement pastes, Cem.Concr.Res. 31 (2001) 1301-1306.

[90] R. Fernandez, F. Martirena, K.L. Scrivener, The origin of the pozzolanic activity of calcined clay minerals: A comparison between kaolinite, illite and montmorillonite, Cem.Concr.Res. 41 (2011) 113-122.

[91] Z. Dai, T.T. Tran, J. Skibsted, Aluminum Incorporation in the C–S–H Phase of White Portland Cement–Metakaolin Blends Studied by 27Al and 29Si MAS NMR Spectroscopy, J Am Ceram Soc. 97 (2014) 2662-2671.

[92] B. Lothenbach, G. Le Saout, E. Gallucci, K. Scrivener, Influence of limestone on the hydration of Portland cements, Cem.Concr.Res. 38 (2008) 848-860.

[93] W. Kunther, Z. Dai, J. Skibsted, Thermodynamic modeling of hydrated white Portland cement–metakaolin–limestone blends utilizing hydration kinetics from 29Si MAS NMR spectroscopy, Cem.Concr.Res. 86 (2016) 29-41.

[94] F. Avet, E. Boehm-Courjault, K. Scrivener, Investigation of C-A-S-H composition, morphology and density in Limestone Calcined Clay Cement (LC3), Cem.Concr.Res. 115 (2019) 70-79.

[95] F. Zunino, K. Scrivener, The reaction between metakaolin and limestone and its effect in porosity refinement and mechanical properties, Cem.Concr.Res. 140 (2021) 106307.

[96] M. Antoni, J. Rossen, F. Martirena, K. Scrivener, Cement substitution by a combination of metakaolin and limestone, Cem.Concr.Res. 42 (2012) 1579-1589.

[97] M. Antoni, Investigation of Cement Substitution by Blends of Calcined Clays and Limestone, (2013).

[98] F. Avet, K. Scrivener, Investigation of the calcined kaolinite content on the hydration of Limestone Calcined Clay Cement (LC3), Cem.Concr.Res. 107 (2018) 124-135.

[99] S. Krishnan, D. Gopala Rao, S. Bishnoi, Why Low-Grade Calcined Clays Are the Ideal for the Production of Limestone Calcined Clay Cement (LC 3), (2020) 125-130.

[100] K. Scrivener, F. Martirena, S. Bishnoi, S. Maity, Calcined clay limestone cements (LC3), Cem.Concr.Res. 114 (2018) 49-56.

[101] S. Krishnan, S. Bishnoi, Understanding the hydration of dolomite in cementitious systems with reactive aluminosilicates such as calcined clay, Cem.Concr.Res. 108 (2018) 116-128.

[102] V. Shah, A. Parashar, A. Scott, Understanding the importance of carbonates on the performance of Portland metakaolin cement, Constr.Build.Mater. 319 (2022) 126155.

[103] Y. Dhandapani, T. Sakthivel, M. Santhanam, R. Gettu, R.G. Pillai, Mechanical properties and durability performance of concretes with Limestone Calcined Clay Cement (LC3), Cem.Concr.Res. 107 (2018) 136-151.

[104] S. Bishnoi, S. Maity, A. Mallik, S. Joseph, S. Krishnan, Pilot scale manufacture of limestone calcined clay cement: the Indian experience, 88 (2014) 22-28.

[105] M. Sharma, S. Bishnoi, F. Martirena, K. Scrivener, Limestone calcined clay cement and concrete: A state-of-the-art review, Cem.Concr.Res. 149 (2021) 106564.

[106] P. Hou, T.R. Muzenda, Q. Li, H. Chen, S. Kawashima, T. Sui, H. Yong, N. Xie, X. Cheng, Mechanisms dominating thixotropy in limestone calcined clay cement (LC3), Cem.Concr.Res. 140 (2021) 106316.

[107] T.R. Muzenda, P. Hou, S. Kawashima, T. Sui, X. Cheng, The role of limestone and calcined clay on the rheological properties of LC3, 107 (2020) 103516.

[108] M.T. Palou, E. Kuzielová, M. Žemlička, M. Boháč, R. Novotný, The effect of curing temperature on the hydration of binary Portland cement: Slag and Portland cement—metakaolin-blended cements, 125 (2016) 1301-1310.

[109] S. Mohammed, O. Safiullah, Optimization of the SO3 content of an Algerian Portland cement: Study on the effect of various amounts of gypsum on cement properties, Constr.Build.Mater. 164 (2018) 362-370.

[110] G. Mishra, A.C. Emmanuel, S. Bishnoi, Influence of temperature on hydration and microstructure properties of limestone-calcined clay blended cement, Mater.Struct. 52 (2019) 1-13.

[111] S. Krishnan, A. Singh, S. Bishnoi, Impact of alkali salts on the hydration of ordinary portland cement and limestone–calcined clay cement, J.Mater.Civ.Eng. 33 (2021) 04021223.

[112] S. Krishnan, S. Bishnoi, A numerical approach for designing composite cements with calcined clay and limestone, Cem.Concr.Res. 138 (2020) 106232.

[113] R. Lin, S. Oh, W. Du, X. Wang, Strengthening the performance of limestone-calcined clay cement (LC3) using nano silica, Constr.Build.Mater. 340 (2022) 127723.

[114] L. Chen, K. Zheng, T. Xia, G. Long, Mechanical property, sorptivity and microstructure of steam-cured concrete incorporated with the combination of metakaolin-limestone, 11 (2019) e00267.

[115] F. Zunino, K. Scrivener, The influence of the filler effect on the sulfate requirement of blended cements, Cem.Concr.Res. 126 (2019) 105918.

[116] Z. Shi, B. Lothenbach, M.R. Geiker, J. Kaufmann, A. Leemann, S. Ferreiro, J. Skibsted, Experimental studies and thermodynamic modeling of the carbonation of Portland cement, metakaolin and limestone mortars, Cem.Concr.Res. 88 (2016) 60-72.

[117] R. Bucher, P. Diederich, G. Escadeillas, M. Cyr, Service life of metakaolin-based concrete exposed to carbonation: Comparison with blended cement containing fly ash, blast furnace slag and limestone filler, Cem.Concr.Res. 99 (2017) 18-29.

[118] T. Zhang, L.J. Vandeperre, C.R. Cheeseman, Formation of magnesium silicate hydrate (M-S-H) cement pastes using sodium hexametaphosphate, 65 (2014) 8-14.

[119] D. Nied, K. Enemark-Rasmussen, E. L;Hopital, J. Skibsted, B. Lothenbach, Properties of magnesium silicate hydrates (M-S-H), 79 (2016) 323-332.

[120] B. Lothenbach, D. Nied, E. L;Hôpital, G. Achiedo, A. Dauzères, Magnesium and calcium silicate hydrates, 77 (2015) 60-68.

[121] E. Bernard, B. Lothenbach, C. Chlique, M. Wyrzykowski, A. Dauzères, I. Pochard, C. Cau-Dit-Coumes, Characterization of magnesium silicate hydrate (M-S-H), 116 (2019) 309-330.

[122] H. Tran, Development of magnesium silicate hydrate binder systems, (2019).

[123] F. Jin, A. Al-Tabbaa, Strength and hydration products of reactive MgO–silica pastes, 52 (2014) 27-33.

[124] F. Jin, A. Abdollahzadeh, A. Al-Tabbaa, Effect of different MgO on the hydration of MgO-activated granulated ground blastfurnace slag paste, (2013).

[125] C. Sonat, C. Unluer, Development of magnesium-silicate-hydrate (M-S-H) cement with rice husk ash, 211 (2019) 787-803.

[126] F. Jin, A. Al-Tabbaa, Thermogravimetric study on the hydration of reactive magnesia and silica mixture at room temperature, 566 (2013) 162-168.

[127] P. Sherwood, Soil Stabilization with Cement and Lime, , 1993.

[128] S.E. Schulze, J. Rickert, Suitability of natural calcined clays as supplementary cementitious material, 95 (2019) 92-97.

[129] L. Wang, D. Cho, D.C.W. Tsang, X. Cao, D. Hou, Z. Shen, D.S. Alessi, Y.S. Ok, C.S. Poon, Green remediation of As and Pb contaminated soil using cement-free clay-based stabilization/solidification, 126 (2019) 336-345.

[130] L. Wang, L. Chen, D. Cho, D.C.W. Tsang, J. Yang, D. Hou, K. Baek, H.W. Kua, C. Poon, Novel synergy of Si-rich minerals and reactive MgO for stabilisation/solidification of contaminated sediment, 365 (2019) 695-706.

[131] R. Gmür, K. Thienel, N. Beuntner, Influence of aging conditions upon the properties of calcined clay and its performance as supplementary cementitious material, 72 (2016) 114-124.

[132] O. Cuisinier, D. Deneele, F. Masrouri, Shear strength behaviour of compacted clayey soils percolated with an alkaline solution, 108 (2009) 177-188.

210

[133] K. Hossain, L. Mol, Some engineering properties of stabilized clayey soils incorporating natural pozzolans and industrial wastes, Constr.Build.Mater. 25 (2011) 3495-3501.

[134] F. Slaty, H. Khoury, J. Wastiels, H. Rahier, Characterization of alkali activated kaolinitic clay, 75-76 (2013) 120-125.

[135] G. Kastiukas, S. Ruan, S. Liang, X. Zhou, Development of precast geopolymer concrete via oven and microwave radiation curing with an environmental assessment, 255 (2020) 120290.

[136] A. Haque, C.K. Tang, S. Islam, P.G. Ranjith, H.H. Bui, Biochar sequestration in lime-slag treated synthetic soils: A green approach to ground improvement, J.Mater.Civ.Eng. 26 (2014) 06014024.

[137] S. Islam, A.A. Haque, S.A. Wilson, Effects of Curing Environment on the Strength and Mineralogy of Lime-GGBS–Treated Acid Sulphate Soils, J. Mater. Civ. Eng. 26 (2014) 1003.

[138] J.E. Oti, J.M. Kinuthia, Stabilised unfired clay bricks for environmental and sustainable use, Appl.Clay.Sci. 58 (2012) 52-59.

[139] N.C. Consoli, R.A.Q. Samaniego, N.M.K. Villalba, Durability, Strength, and Stiffness of Dispersive Clay–Lime Blends, J. Mater. Civ. Eng. 28 (2016).

[140] K. Gu, F. Jin, A. Al-Tabbaa, B. Shi, C. Liu, L. Gao, Incorporation of reactive magnesia and quicklime in sustainable binders for soil stabilisation, 195 (2015) 53-62.

[141] H. Wu, F. Jin, Y. Bo, Y. Du, J. Zheng, Leaching and microstructural properties of lead contaminated kaolin stabilized by GGBS-MgO in semi-dynamic leaching tests, 172 (2018) 626-634.

[142] H. Wu, F. Jin, J. Ni, Y. Du, Engineering properties of vertical cutoff walls consisting of reactive magnesia-activated slag and bentonite: workability, strength, and hydraulic conductivity, J.Mater.Civ.Eng. 31 (2019) 04019263.

[143] Y. Yi, L. Gu, S. Liu, F. Jin, Magnesia reactivity on activating efficacy for ground granulated blastfurnace slag for soft clay stabilisation, 126 (2016) 57-62.

[144] Y. Yi, K. Lu, S. Liu, A. Al-Tabbaa, Property changes of reactive magnesia–stabilized soil subjected to forced carbonation, 53 (2015) 314-325.

[145] Y. Yi, M. Liska, F. Jin, A. Al-Tabbaa, Mechanism of reactive magnesia – ground granulated blastfurnace slag (GGBS) soil stabilization, Can.Geotech.J. 53 (2016) 773-782.

[146] M. Atkins, F.P. Glasser, J.J. Jack, Zeolite P in cements: Its potential for immobilizing toxic and radioactive waste species, 15 (1995) 127-135.

[147] W. Li, P. Ni, Y. Yi, Comparison of reactive magnesia, quick lime, and ordinary Portland cement for stabilization/solidification of heavy metal-contaminated soils, 671 (2019) 741-753.

[148] W. Li, Y. Yi, Stabilization/solidification of lead- and zinc-contaminated soils using MgO and CO2, 33 (2019) 215-221.

[149] H. Wu, D. Zhang, B.R. Ellis, V.C. Li, Development of reactive MgO-based Engineered Cementitious Composite (ECC) through accelerated carbonation curing, 191 (2018) 23-31.

[150] R. Zhang, D.K. Panesar, Mechanical properties and rapid chloride permeability of carbonated concrete containing reactive MgO, 172 (2018) 77-85.

[151] S. Ruan, C. Unluer, Influence of mix design on the carbonation, mechanical properties and microstructure of reactive MgO cement-based concrete, 80 (2017) 104-114.

[152] S. Ruan, C. Unluer, Comparison of the Environmental Impacts of Reactive Magnesia and Calcined Dolomite and Their Performance under Different Curing Conditions, J. Mater. Civ. Eng. 30 (2018).

[153] J.L. Provis, J.S. Van Deventer, Alkali Activated Materials: State-of-the-Art Report, RILEM TC 224-AAM, Springer Science & Business Media, 2013.

[154] BS EN 1015-3:1999, Methods of test for mortar for masonry Determination of consistence of fresh mortar (by flow table), (2007).

[155] American Society for Testing and Materials. Committee C-1 on Cement, Standard Test Method for Compressive Strength of Hydraulic Cement Mortars (using 2-in. Or [50-mm] Cube Specimens), ASTM International, 2013.

[156] A. ASTM, Standard test methods for time of setting of hydraulic cement by Vicat needle, (2013).

[157] BS EN 12390-7:2019, Testing hardened concrete. Density of hardened concrete, (2019).

[158] ASTM C642, Standard test method for density, absorption, and voids in hardened concrete, Annual book of ASTM standards, 4 (2006).

[159] K. De Weerdt, G. Plusquellec, A.B. Revert, M.R. Geiker, B. Lothenbach, Effect of carbonation on the pore solution of mortar, Cem.Concr.Res. 118 (2019) 38-56.

[160] N. Du, R. Guan, P. Hou, New fluorescent pH indicators for characterizing cement carbonation, Constr.Build.Mater. 388 (2023) 131662.

[161] X. Ye, T. Chen, J. Chen, Carbonation of cement paste under different pressures, Constr.Build.Mater. 370 (2023) 130511.

[162] ASTM C25-19, Standard test methods for chemical analysis of limestone, quicklime, and hydrated lime, (2011).

[163] ASTM C1702-17, Standard Test Method for Measurement of Heat of Hydration of Hydraulic Cementitious Materials Using Isothermal Conduction Calorimetry, (2017).

[164] S. Ruan, C. Unluer, Comparative life cycle assessment of reactive MgO and Portland cement production, 137 (2016) 258-273.

[165] J. Li, Y. Zhang, S. Shao, S. Zhang, Comparative life cycle assessment of conventional and new fused magnesia production, 91 (2015) 170-179.

[166] P. He, M.U. Hossain, C.S. Poon, D.C.W. Tsang, Mechanical, durability and environmental aspects of magnesium oxychloride cement boards incorporating waste wood, 207 (2019) 391-399.

[167] Yan Zhao, H. Wang, W. Lu, A. Damgaard, T.H. Christensen, Life-cycle assessment of the municipal solid waste management system in Hangzhou, China (EASEWASTE), 27 (2009) 399-406.

[168] M. Spielmann, C. Bauer, R. Dones, M. Tuchschmid, Life cycle inventories of transport services Ecoinvent v 2.0, (2004).

[169] D. Kellenberger, H.J. Althaus, N. Jungbluth, T. Künniger, M. Lehmann, P. Thalmann, Life cycle inventories of building products, 7 (2007).

[170] M.E. Boesch, S. Hellweg, Identifying Improvement Potentials in Cement Production with Life Cycle Assessment, 44 (2010) 9143-9149.

[171] C. Chen, G. Habert, Y. Bouzidi, A. Jullien, A. Ventura, LCA allocation procedure used as an incitative method for waste recycling: An application to mineral additions in concrete, 54 (2010) 1231-1240.

[172] G. Habert, E. Denarié, A. Šajna, P. Rossi, Lowering the global warming impact of bridge rehabilitations by using Ultra High Performance Fibre Reinforced Concretes, 38 (2013) 1-11.

[173] M. LISKA, A. AL-TABBAA, K. CARTER, J. FIFIELD, Scaled-up commercial production of reactive magnesium cement pressed masonry units. Part I: Production, 165 (2012) 211-223.

[174] D. Langmuir, Stability of carbonates in the system MgO-CO2-H2O, J.Geol. 73 (1965) 730-754.

[175] R.I. Khan, W. Ashraf, J. Olek, Amino acids as performance-controlling additives in carbonation-activated cementitious materials, Cem.Concr.Res. 147 (2021) 106501.

[176] BS EN 771-5:2011+A1:2015, Specification for masonry units, (2015).

[177] S. Ruan, S. Liang, G. Kastiukas, W. Zhu, X. Zhou, Solidification of waste excavation clay using reactive magnesia, quicklime, sodium carbonate and early-age oven curing, 258 (2020) 120333.

[178] T. Hoang, N.T. Dung, C. Unluer, J. Chu, Use of microbial carbonation process to enable self-carbonation of reactive MgO cement mixes, 143 (2021) 106391.

[179] E. Grünhäuser Soares, J. Castro-Gomes, M. Sitarz, T. Zdeb, I. Hager, K. Hassan, M. Saif Al-Kuwari, Feasibility for co-utilisation of Carbonated Reactive Magnesia Cement (CRMC) and industrial wastes in circular economy and CO2 mineralisation, Constr.Build.Mater. 323 (2022) 126488.

[180] R. Chaliulina, J. Galvez-Martos, A. Hakki, A. Elhoweris, J. Mwanda, Y. Al-Horr, Eco materials from CO2 capture: Compressive strengths of a plasterboard alternative, Constr.Build.Mater. 312 (2021) 125276.

[181] H. Tong, W. Ma, L. Wang, P. Wan, J. Hu, L. Cao, Control over the crystal phase, shape, size and aggregation of calcium carbonate via a L-aspartic acid inducing process, 25 (2004) 3923-3929.

[182] K. Maruyama, T. Yoshino, H. Kagi, Synthesizing a composite material of amorphous calcium carbonate and aspartic acid, Mater Lett. 65 (2011) 179-181.

[183] Y. Kim, J.D. Carloni, B. Demarchi, D. Sparks, D.G. Reid, M.E. Kunitake, C.C. Tang, M.J. Duer, C.L. Freeman, B. Pokroy, Tuning hardness in calcite by incorporation of amino acids, 15 (2016) 903-910.

[184] Z. Zou, L. Bertinetti, Y. Politi, P. Fratzl, W.J. Habraken, Control of polymorph selection in amorphous calcium carbonate crystallization by poly (aspartic acid): Two different mechanisms, 13 (2017) 1603100.

[185] R. Hay, N.T. Dung, A. Lesimple, C. Unluer, K. Celik, Mechanical and microstructural changes in reactive magnesium oxide cement-based concrete mixes subjected to high temperatures, 118 (2021) 103955.

[186] H. Nguyen, H. Santos, H. Sreenivasan, W. Kunther, V. Carvelli, M. Illikainen, P. Kinnunen, On the carbonation of brucite: Effects of Mg-acetate on the precipitation of hydrated magnesium carbonates in aqueous environment, Cem.Concr.Res. 153 (2022) 106696.

[187] G. Socrates, Infrared and Raman Characteristic Group Frequencies: Tables and Charts, John Wiley & Sons, 2004.

[188] G.V.P. Bhagath Singh, C. Sonat, E.H. Yang, C. Unluer, Performance of MgO and MgO–SiO2 systems containing seeds under different curing conditions, 108 (2020) 103543.

[189] H.A. Abdel-Gawwad, S.A. El-Enein, M. Heikal, S. Abd El-Aleem, A.A. Amer, I.M. El-Kattan, Synergistic effects of curing conditions and magnesium oxide addition on the physico-mechanical properties and firing resistivity of Portland cement mortar, Constr.Build.Mater. 176 (2018) 676-689.

[190] A. Ansari, A. Ali, M. Asif, Microwave-assisted MgO NP catalyzed one-pot multicomponent synthesis of polysubstituted steroidal pyridines, 42 (2018) 184-197.

[191] R.L. Frost, S. Bahfenne, Raman and mid‐IR spectroscopic study of the magnesium carbonate minerals—brugnatellite and coalingite, 40 (2009) 360-365.

[192] H.G. Edwards, S.E.J. Villar, J. Jehlicka, T. Munshi, FT–Raman spectroscopic study of calcium-rich and magnesium-rich carbonate minerals, 61 (2005) 2273-2280.

[193] H. Han, S. Hu, J. Feng, H. Gao, Effect of stearic acid, zinc stearate coating on the properties of synthetic hydromagnesite, Appl.Surf.Sci. 257 (2011) 2677-2682.

[194] A.L. Harrison, V. Mavromatis, E.H. Oelkers, P. Bénézeth, Solubility of the hydrated Mg-carbonates nesquehonite and dypingite from 5 to 35° C: Implications for CO2 storage and the relative stability of Mg-carbonates, Chem.Geol. 504 (2019) 123-135.

[195] A. Rodriguez-Navarro, C. Jimenez-Lopez, A. Hernandez-Hernandez, A. Checa, J.M. García-Ruiz, Nanocrystalline structures in calcium carbonate biominerals, 2 (2008) 021935.

[196] L. Štajner, J. Kontrec, B.N. Džakula, N. Maltar-Strmečki, M. Plodinec, D.M. Lyons, D. Kralj, The effect of different amino acids on spontaneous precipitation of calcium carbonate polymorphs, J.Cryst.Growth. 486 (2018) 71-81.

[197] A. Xie, Y. Shen, C. Zhang, Z. Yuan, X. Zhu, Y. Yang, Crystal growth of calcium carbonate with various morphologies in different amino acid systems, J.Cryst.Growth. 285 (2005) 436-443.

[198] C. Rodriguez-Navarro, M. Rodriguez-Gallego, K. Ben Chekroun, M.T. Gonzalez-Muñoz, Conservation of ornamental stone by Myxococcus xanthus-induced carbonate biomineralization, Appl.Environ.Microbiol. 69 (2003) 2182-2193.

[199] R. Zhang, A. Arrigoni, D.K. Panesar, Could reactive MgO cement be a green solution? The effect of CO2 mineralization and manufacturing route on the potential global warming impact, 124 (2021) 104263.

[200] R. Snellings, P. Suraneni, J. Skibsted, Future and emerging supplementary cementitious materials, Cem.Concr.Res. 171 (2023) 107199.

[201] G. Xu, X. Shi, Characteristics and applications of fly ash as a sustainable construction material: A state-of-the-art review, Resour.Conserv.Recycling. 136 (2018) 95-109.

[202] A.F.(.). Karen Scrivener, Calcined Clays for Sustainable Concrete, RILEM Bookseries 10, Springer, 2015.

[203] K. Scrivener, F. Avet, H. Maraghechi, F. Zunino, J. Ston, W. Hanpongpun, A. Favier, Impacting factors and properties of limestone calcined clay cements (LC3), 7 (2019) 3-14.

[204] V.L. Bonavetti, V.F. Rahhal, E.F. Irassar, Studies on the carboaluminate formation in limestone filler-blended cements, Cem.Concr.Res. 31 (2001) 853-859.

[205] A. Parashar, S. Bishnoi, Hydration behaviour of limestone-calcined clay and limestone-slag blends in ternary cement, 6 (2021) 17-24.

[206] S. Teir, S. Eloneva, C. Fogelholm, R. Zevenhoven, Stability of calcium carbonate and magnesium carbonate in rainwater and nitric acid solutions, 47 (2006) 3059-3068.

[207] J.H. Canterford, G. Tsambourakis, B. Lambert, Some observations on the properties of dypingite, Mg5 (CO3) 4 (OH) 2· 5H2O, and related minerals, 48 (1984) 437-442.

[208] Y. Dhandapani, M. Santhanam, G. Kaladharan, S. Ramanathan, Towards ternary binders involving limestone additions — A review, Cem.Concr.Res. 143 (2021) 106396.

[209] R. Lin, H. Lee, Y. Han, X. Wang, Experimental studies on hydration–strength–durability of limestone-cement-calcined Hwangtoh clay ternary composite, Constr.Build.Mater. 269 (2021) 121290.

[210] S. Krishnan, A.C. Emmanuel, S. Bishnoi, Hydration and phase assemblage of ternary cements with calcined clay and limestone, Constr.Build.Mater. 222 (2019) 64-72.

[211] K. Scrivener, R. Snellings, B. Lothenbach, A Practical Guide to Microstructural Analysis of Cementitious Materials, Crc Press, 2018.

[212] C.K. Chau, J. Chan, Z. Li, Influences of fly ash on magnesium oxychloride mortar, 31 (2009) 250-254.

[213] S.A. Walling, J.L. Provis, Magnesia-Based Cements: A Journey of 150 Years, and Cements for the Future? 116 (2016) 4170-4204.

[214] T. Zhang, C.R. Cheeseman, L.J. Vandeperre, Development of low pH cement systems forming magnesium silicate hydrate (M-S-H), 41 (2011) 439-442.

[215] A.M. Neville, Properties of Concrete, Longman London, 1995.

[216] P. Duxson, G.C. Lukey, J.S.J. van Deventer, The thermal evolution of metakaolin geopolymers: Part 2 – Phase stability and structural development, 353 (2007) 2186-2200.

[217] X. Lingling, D. Min, Dolomite used as raw material to produce MgO-based expansive agent, 35 (2005) 1480-1485.

[218] P. Gao, X. Lu, F. Geng, X. Li, J. Hou, H. Lin, N. Shi, Production of MgO-type expansive agent in dam concrete by use of industrial by-products, 43 (2008) 453-457.

[219] L. Mo, M. Deng, M. Tang, A. Al-Tabbaa, MgO expansive cement and concrete in China: Past, present and future, 57 (2014) 1-12.

[220] L. Mo, M. Deng, M. Tang, Effects of calcination condition on expansion property of MgO-type expansive agent used in cement-based materials, 40 (2010) 437-446.

[221] R. Wang, Q. Tian, S. Zhang, H. Li, A. Lu, J. Cheng, L. Li, J. Liu, Improving efficiency of calcium oxide expansive additives by polylactic acid film, 68 (2016) 1070-1078.

[222] C. Sonat, N.T. Dung, C. Unluer, Performance and microstructural development of MgO–SiO2 binders under different curing conditions, 154 (2017) 945-955.

[223] Y. Yi, L. Gu, S. Liu, Microstructural and mechanical properties of marine soft clay stabilized by lime-activated ground granulated blastfurnace slag, 103 (2015) 71-76.

[224] Y. Yi, X. Zheng, S. Liu, A. Al-Tabbaa, Comparison of reactive magnesia- and carbide slag-activated ground granulated blastfurnace slag and Portland cement for stabilisation of a natural soil, 111 (2015) 21-26.

[225] Y. YI, C. LI, S. LIU, A. AL-TABBAA, Resistance of MgO–GGBS and CS–GGBS stabilised marine soft clays to sodium sulfate attack, 64 (2014) 673-679.

[226] I. García Lodeiro, D.E. Macphee, A. Palomo, A. Fernández-Jiménez, Effect of alkalis on fresh C–S–H gels. FTIR analysis, 39 (2009) 147-153.

[227] Z. Zhang, Y. Zhu, H. Zhu, Y. Zhang, J.L. Provis, H. Wang, Effect of drying procedures on pore structure and phase evolution of alkali-activated cements, 96 (2019) 194-203.

[228] F. Jin, K. Gu, A. Al-Tabbaa, Strength and drying shrinkage of reactive MgO modified alkali-activated slag paste, 51 (2014) 395-404.

[229] W. Zhu, X. Chen, L.J. Struble, E. Yang, Characterization of calcium-containing phases in alkali-activated municipal solid waste incineration bottom ash binder through chemical extraction and deconvoluted Fourier transform infrared spectra, 192 (2018) 782-789.

[230] E. Gallucci, X. Zhang, K.L. Scrivener, Effect of temperature on the microstructure of calcium silicate hydrate (CSH), Cem.Concr.Res. 53 (2013) 185-195.

[231] S. Ruan, J. Qiu, Y. Weng, Y. Yang, E. Yang, J. Chu, C. Unluer, The use of microbial induced carbonate precipitation in healing cracks within reactive magnesia cement-based blends, 115 (2019) 176-188.

[232] S. Özen, M.C. Göncüoğlu, Sequential formation of natrolite-group zeolites in amygdules of basaltic lavas, 53 (2015) 757-765.

[233] S. Wang, X. Peng, L. Tang, L. Zeng, C. Lan, Influence of Hydrothermal Synthesis Conditions on the Formation of Calcium Silicate Hydrates: from Amorphous to Crystalline Phases, J. Wuhan Univ. Technol.-Mat. Sci. Edit. 33 (2018) 1150-1158.

[234] K. Okano, M. Uemoto, J. Kagami, K. Miura, T. Aketo, M. Toda, K. Honda, H. Ohtake, Novel technique for phosphorus recovery from aqueous solutions using amorphous calcium silicate hydrates (A-CSHs), 47 (2013) 2251-2259.

[235] J. Qiu, S. Ruan, C. Unluer, E. Yang, Autogenous healing of fiber-reinforced reactive magnesia-based tensile strain-hardening composites, Cem.Concr.Res. 115 (2019) 401-413.

[236] J. Ke, M. McNeil, L. Price, N.Z. Khanna, N. Zhou, Estimation of CO_2 emissions from China's cement production: Methodologies and uncertainties, 57 (2013) 172-181.

[237] Department for Environment, Food and Rural Affairs, Our waste,our resources: A strategy for England, (2018).

[238] EU (European Union), Directive (EU) 2018/850 of the European Parliament and of the Council of 30 May 2018 amending Directive1999/31/EC on the landfill of waste, (2018).

[239] Voluntary & Economic Incentives Working Group, Voluntary and economics incentives working group report in February 2018, (2018).

[240] Recyclenow, How are glass bottles recycled? (2020).

[241] J. Lu, H. Zheng, S. Yang, P. He, C.S. Poon, Co-utilization of waste glass cullet and glass powder in precast concrete products, 223 (2019) 210-220.

[242] J. Lu, Y. Zhou, P. He, S. Wang, P. Shen, C.S. Poon, Sustainable reuse of waste glass and incinerated sewage sludge ash in insulating building products: Functional and durability assessment, 236 (2019) 117635.

[243] G. Kastiukas, X. Zhou, J. Castro-Gomes, Preparation Conditions for the Synthesis of Alkali-Activated Binders Using Tungsten Mining Waste, J. Mater. Civ. Eng. 29 (2017).

[244] M. Rakshvir, S.V. Barai, Studies on recycled aggregates-based concrete, 24 (2006) 225-233.

[245] J. Lu, X. Yan, P. He, C.S. Poon, Sustainable design of pervious concrete using waste glass and recycled concrete aggregate, 234 (2019) 1102-1112.

[246] M. Mirzahosseini, K.A. Riding, Influence of different particle sizes on reactivity of finely ground glass as supplementary cementitious material (SCM), 56 (2015) 95-105.

[247] H.A. Abdel-Gawwad, S. Abd El-Aleem, A.A. Amer, H. El-Didamony, M.A. Arif, Combined impact of silicate-amorphicity and MgO-reactivity on the performance of Mg-silicate cement, 189 (2018) 78-85.

[248] E. Grünhäuser Soares, J. Castro-Gomes, Early Age Compressive Strength of Waste-based-glass-powder Magnesium Silicate Binders on Initial Carbonation Curing, (2020).

[249] G. Kastiukas, X. Zhou, Effects of waste glass on alkali-activated tungsten mining waste: composition and mechanical properties, Mater Struct. 50 (2017) 1.

[250] S.D.F. Rocha, M.B. Mansur, V.S.T. Ciminelli, Kinetics and mechanistic analysis of caustic magnesia hydration, J.Chem.Technol.Biotechnol. 79 (2004) 816-821.

[251] J. Szczerba, R. Prorok, E. Śnieżek, D. Madej, K. Maślona, Influence of time and temperature on ageing and phases synthesis in the MgO–SiO2–H2O system, 567 (2013) 57-64.

[252] C.H. Chen, R. Huang, J.K. Wu, C.C. Yang, Waste E-glass particles used in cementitious mixtures, 36 (2006) 449-456.

[253] D.R.M. Brew, F.P. Glasser, Synthesis and characterisation of magnesium silicate hydrate gels, 35 (2005) 85-98.

[254] Y. Jia, B. Wang, Z. Wu, J. Han, T. Zhang, L.J. Vandeperre, C.R. Cheeseman, Role of sodium hexametaphosphate in MgO/SiO2 cement pastes, 89 (2016) 63-71.

[255] T. Zhang, J. Zou, B. Wang, Z. Wu, Y. Jia, C.R. Cheeseman, Characterization of magnesium silicate hydrate (MSH) gel formed by reacting MgO and silica fume, 11 (2018) 909.

[256] C. Sonat, C. Unluer, Investigation of the performance and thermal decomposition of MgO and MgO-SiO2 formulations, 655 (2017) 251-261.

[257] O. Golubeva, E. Korytkova, V. Gusarov, Hydrothermal Synthesis of Magnesium Silicate Montmorillonite for Polymer-Clay Nanocomposites, 78 (2005) 26-32.

[258] S. Ruan, G. Kastiukas, S. Liang, X. Zhou, Waste Glass Reuse in Foamed Alkali-Activated Binders Production: Technical and Environmental Assessment, 7 (2020).